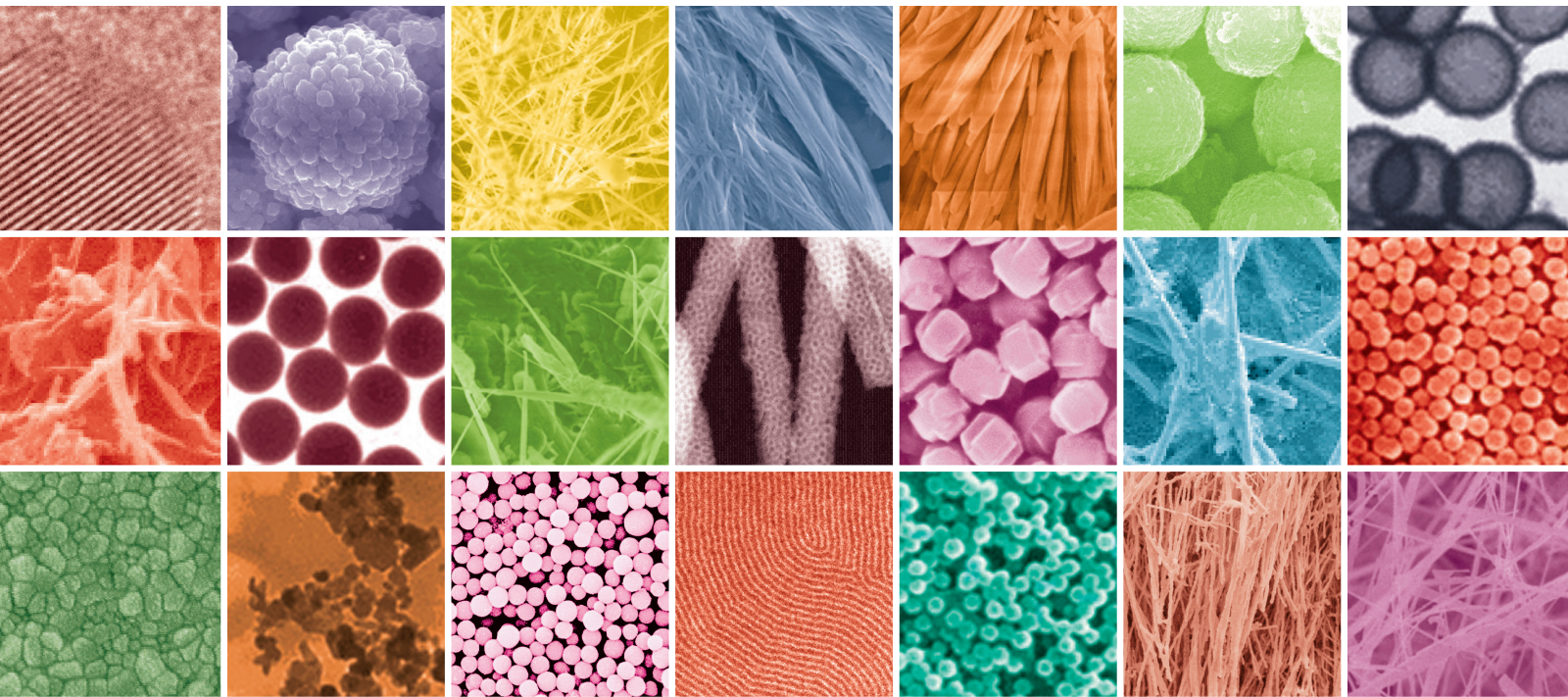


Engineered Nanoparticles and Their Applications

Guest Editors: Themis Matsoukas, Tapan Desai, and Kangtaek Lee





Engineered Nanoparticles and Their Applications

Journal of Nanomaterials

Engineered Nanoparticles and Their Applications

Guest Editors: Themis Matsoukas, Tapan Desai,
and Kangtaek Lee



Copyright © 2015 Hindawi Publishing Corporation. All rights reserved.

This is a special issue published in "Journal of Nanomaterials." All articles are open access articles distributed under the Creative Commons Attribution License, which permits unrestricted use, distribution, and reproduction in any medium, provided the original work is properly cited.

Editorial Board

Domenico Acierno, Italy
Katerina Aifantis, USA
Nageh K. Allam, USA
Margarida Amaral, Portugal
Martin Andersson, Sweden
Raul Arenal, Spain
Ilaria Armentano, Italy
Vincenzo Baglio, Italy
Lavinia Balan, France
Thierry Baron, France
Andrew R. Barron, USA
Reza Bayati, USA
Hongbin Bei, USA
Daniel Bellet, France
Stefano Bellucci, Italy
Enrico Bergamaschi, Italy
Samuel Bernard, France
D. Bhattacharyya, New Zealand
Sergio Bietti, Italy
Giovanni Bongiovanni, Italy
Theodorian Borca-Tasciuc, USA
Mohamed Bououdina, Bahrain
Torsten Brezesinski, Germany
C. Jeffrey Brinker, USA
Christian Brosseau, France
Philippe Caroff, Australia
Victor M. Castaño, Mexico
Albano Cavaleiro, Portugal
Bhanu P. S. Chauhan, USA
Shafiu Chowdhury, USA
Jin-Ho Choy, Republic of Korea
Kwang-Leong Choy, UK
Yu-Lun Chueh, Taiwan
Elisabetta Comini, Italy
Giuseppe Compagnini, Italy
David Cornu, France
Miguel A. Correa-Duarte, Spain
Pantaleo D. Cozzoli, Italy
Shadi A. Dayeh, USA
Luca Deseri, USA
Yong Ding, USA
Philippe Dubois, Belgium
Zehra Durmus, Turkey
Joydeep Dutta, Oman
Ali Eftekhari, USA
Jeffrey Elam, USA
Samy El-Shall, USA
Ovidiu Ersen, France
Claude Estournès, France
Andrea Falqui, KSA
Matteo Ferroni, Italy
Elena J. Foster, USA
Ilaria Fratoddi, Italy
Alan Fuchs, USA
Miguel A. Garcia, Spain
Siddhartha Ghosh, Singapore
P. K. Giri, India
Russell E. Gorga, USA
Jihua Gou, USA
Jean M. Greneche, France
Smrati Gupta, Germany
Kimberly Hamad-Schifferli, USA
Simo-Pekka Hannula, Finland
Michael Harris, USA
Yasuhiko Hayashi, Japan
F. Hernandez-Ramirez, Spain
Michael Z. Hu, USA
Nay Ming Huang, Malaysia
Shaoming Huang, China
David Hui, USA
Zafar Iqbal, USA
Balachandran Jeyadevan, Japan
Xin Jiang, Germany
Rakesh Joshi, Australia
Jeong-won Kang, Republic of Korea
Hassan Karimi-Maleh, Iran
Antonios Kelarakis, UK
Alireza Khataee, Iran
Ali Khorsand Zak, Iran
Philippe Knauth, France
Ralph Krupke, Germany
Christian Kübel, Germany
Prashant Kumar, UK
Michele Laus, Italy
Eric Le Bourhis, France
Burtrand Lee, USA
Jun Li, Singapore
Meiyong Liao, Japan
Shijun Liao, China
Silvia Licocchia, Italy
Wei Lin, USA
Nathan C. Lindquist, USA
Jun Liu, USA
Zainovia Lockman, Malaysia
Nico Lovergine, Italy
Jim Low, Australia
Jue Lu, USA
Songwei Lu, USA
Ed Ma, USA
Laura M. Maestro, Spain
Gaurav Mago, USA
Muhamamd A. Malik, UK
Devanesan Mangalaraj, India
Sanjay R. Mathur, Germany
Tony McNally, UK
Yogendra Mishra, Germany
Paulo Cesar Morais, Brazil
Paul Munroe, Australia
Jae-Min Myoung, Republic of Korea
Rajesh R. Naik, USA
Albert Nasibulin, Russia
Toshiaki Natsuki, Japan
Koichi Niihara, Japan
Natalia Noginova, USA
Sherine Obare, USA
Won-Chun Oh, Republic of Korea
Atsuto Okamoto, Japan
Abdelwahab Omri, Canada
Ungyu Paik, Republic of Korea
Piersandro Pallavicini, Italy
Edward A. Payzant, USA
Alessandro Pegoretti, Italy
Ton Peijs, UK
O. Perales-Pérez, Puerto Rico
Jorge Pérez-Juste, Spain
Alexey P. Popov, Finland
Philip D. Rack, USA
Peter Reiss, France
Orlando Rojas, USA
Marco Rossi, Italy
Ilker S. Bayer, Italy
Cengiz S. Ozkan, USA
Sudipta Seal, USA
Shu Seki, Japan
Vladimir Šepelák, Germany



Huaiyu Shao, Japan
Prashant Sharma, USA
Donglu Shi, USA
Bhanu P. Singh, India
Surinder Singh, USA
Vladimir Sivakov, Germany
Ashok Sood, USA
Adolfo Speghini, Italy
Marinella Striccoli, Italy
Xuping Sun, KSA
Ashok K. Sundramoorthy, USA
Angelo Taglietti, Italy
Bo Tan, Canada

Leander Tapfer, Italy
Valeri P. Tolstoy, Russia
M. S. Toprak, Sweden
Ramon Torrecillas, Spain
Achim Trampert, Germany
Takuya Tsuzuki, Australia
Tamer Uyar, Turkey
Bala Vaidhyanathan, UK
Luca Valentini, Italy
Rajender S. Varma, USA
Ester Vazquez, Spain
Antonio Villaverde, Spain
Ajayan Vinu, Australia

Ruibing Wang, Macau
Shiren Wang, USA
Yong Wang, USA
Magnus Willander, Sweden
Ping Xiao, UK
Zhi Li Xiao, USA
Yangchuan Xing, USA
Doron Yadlovker, Israel
Yoke K. Yap, USA
Kui Yu, Canada
William Yu, USA
Michele Zappalorto, Italy
Renyun Zhang, Sweden

Contents

Engineered Nanoparticles and Their Applications, Themis Matsoukas, Tapan Desai, and Kangtaek Lee
Volume 2015, Article ID 651273, 2 pages

Passivation and Stabilization of Aluminum Nanoparticles for Energetic Materials, Matthew Flannery, Tapan G. Desai, Themis Matsoukas, Saba Lotfizadeh, and Matthew Oelschlager
Volume 2015, Article ID 682153, 12 pages

Formulation and Optimization of Eudragit RS PO-Tenofovir Nanocarriers Using Box-Behnken Experimental Design, Kefilwe Matlhola, Lebogang Katata-Seru, Lesego Tshweu, Indra Bahadur, Gertrude Makgatho, and Mohammed Balogun
Volume 2015, Article ID 630690, 11 pages

Preparation of $\text{Cu}_2\text{Sn}_3\text{S}_7$ Thin-Film Using a Three-Step Bake-Sulfurization-Sintering Process and Film Characterization, Tai-Hsiang Lui, Fei-Yi Hung, Truan-Sheng Lui, and Kuan-Jen Chen
Volume 2015, Article ID 969783, 7 pages

Comparative Aquatic Toxicity of Gold Nanoparticles and Ionic Gold Using a Species Sensitivity Distribution Approach, Tarryn L. Botha, Tanyin E. James, and Victor Wepener
Volume 2015, Article ID 986902, 16 pages

Sea-Urchin-Like ZnO Nanoparticle Film for Dye-Sensitized Solar Cells, Cheng-Wen Ma, Chia-Ming Chang, Po-Cheng Huang, and Yao-Joe Yang
Volume 2015, Article ID 679474, 6 pages

Functionalised Au Coated Iron Oxide Nanocomposites Based Reusable Immunosensor for AFBI Detection, Ruchika Chauhan and T. Basu
Volume 2015, Article ID 607268, 15 pages

Synthesis and Microwave Absorption Properties of Core-Shell Structured Co_3O_4 -PANI Nanocomposites, Hongyan Xu, Zhenyin Hai, Jiangtao Diwu, Qiang Zhang, Libo Gao, Danfeng Cui, Junbin Zang, Jun Liu, and Chenyang Xue
Volume 2015, Article ID 845983, 8 pages

The Effect of NaCl/pH on Colloidal Nanogold Produced by Pulsed Spark Discharge, Kuo-Hsiung Tseng, Chin-Liang Hsieh, Jen-Chuen Huang, and Der-Chi Tien
Volume 2015, Article ID 612324, 7 pages

Effect of Nanostructure on Thermal Conductivity of Nanofluids, Saba Lotfizadeh and Themis Matsoukas
Volume 2015, Article ID 697596, 7 pages

Influence of Monodisperse Fe_3O_4 Nanoparticle Size on Electrical Properties of Vegetable Oil-Based Nanofluids, Bin Du, Jian Li, Feipeng Wang, Wei Yao, and Shuhan Yao
Volume 2015, Article ID 560352, 9 pages

Recent Advances in FePt Nanoparticles for Biomedicine, Yujuan Shi, Mei Lin, Xingmao Jiang, and Shuai Liang
Volume 2015, Article ID 467873, 13 pages

Incorporation of Nanohybrid Films of Silica into Recycled Polystyrene Matrix, Genoveva Hernández-Padrón, Domingo Rangel-Miranda, Gerardo Cedillo, and Alejandra Blanco-Hernández
Volume 2015, Article ID 173949, 6 pages

Editorial

Engineered Nanoparticles and Their Applications

Themis Matsoukas,¹ Tapan Desai,² and Kangtaek Lee³

¹*Department of Chemical Engineering, The Pennsylvania State University, University Park, PA 16802, USA*

²*JLC Electromet, Jaipur 302013, India*

³*Department of Chemical and Biomolecular Engineering, Yonsei University, Seoul 03722, Republic of Korea*

Correspondence should be addressed to Themis Matsoukas; matsoukas@enr.psu.edu

Received 2 November 2015; Accepted 2 November 2015

Copyright © 2015 Themis Matsoukas et al. This is an open access article distributed under the Creative Commons Attribution License, which permits unrestricted use, distribution, and reproduction in any medium, provided the original work is properly cited.

Nanoparticles engineered for shape, size, and surface properties impart special functionalities including catalytic behavior, improved strength, enhanced thermal and electrical conductivity, and controlled release of host molecules. These advances have opened up applications in biomedicine, nanoenergetic materials, and functional nanocomposites. This special issue highlights successes in developing nanoparticles for a number of diverse applications.

A field in which nanoparticles are poised to play a significant role is biomedicine. Y. Shi and coworkers review recent advances in the use of FePt nanoparticles in the medical field. These alloy nanoparticles exhibit enhanced magnetic properties while also being chemically stable against oxidation. In addition to physical methods of preparation, which are scalable but suffer from poor control of morphology and size, several chemical methods have been shown to successfully produce monodisperse particles in the low nanometer range. These functionalizable and biocompatible particles find uses as MRI agents, fluorescence image probes, and targeted drug delivery, among others. This is clearly an area where much progress has been made and it is likely that in the near future FePt nanoparticles will make the transition from laboratory to clinical applications. One particularly promising biomedical application is targeted delivery. Drug losses in the gastrointestinal track are minimized and the half-life of the drug increases and allows release in a sustained manner. Thus higher bioavailability is possible with lower dosage and lower toxic side effects. K. Matlholo and coworkers study the targeted delivery of tenofovir, one of the first line drugs against HIV. The carrier particle in this study is Eudragit RS PO, a synthetic polymer that is widely used in tablets

and capsules to retard the release of the drug and allow delivery in a sustained manner. Size, encapsulation efficiency, and release profile depend on several processing parameters including amount of polymer, concentration of surfactant, amount of drug, stirring speed and time, and temperature. The authors used Box-Behnken Design (BBD) to optimize the drug formulation with respect to these process parameters. The size of the particles was found to depend strongly on the polymer-to-drug ratio, surfactant concentration, and sonication time. The optimized formulation that resulted from the statistical design was characterized by very high encapsulation efficiency (98%), good particle stability, as indicated by its zeta potential, and a sustained release profile of the drug over a period of 80 hours.

Gold nanoparticles (nAu) have been used in biomedical research quite extensively but one issue is colloidal stability in the presence of salts at physiological pH. K.-H. Tseng and coworkers studied the stability of nAu produced by pulse spark discharge. The authors report that carboxymethyl cellulose and polyvinyl pyrrolidone are quite effective in stabilizing nAu. Sensing of biological molecules is another area of application for gold nanostructures. R. Chauhan and T. Basu report on a highly sensitive sensor for aflatoxin B1, a toxin and potent carcinogen that is of major concern in the food processing industry. The authors describe a successful implementation of a piezoelectric sensor based on a gold coated iron oxide core-shell nanostructure functionalized to immobilize the toxin and sensed via a piezoelectric mechanism. An overlooked aspect of nAu is the potential environmental impacts and toxic effects to aquatic organisms when nanoparticles are released to the environment. T. L.

Botha and coworkers used species sensitivity distribution (SSD) to address this question. SSD is a statistical tool routinely used in assessing environmental risks by quantifying the sensitivity of aquatic species to a particular stressor. The toxicity of Au nanoparticles was examined with respect to concentration, size distribution, surface charge, surface functionality, and level of agglomeration. The toxicity of gold nanoparticles was found to be generally low. Only one species (*T. sparrmanii*) displayed a maximum mortality of 48% after 96 h. Nanoparticles that are stabilized by nitrate capping lose their stability when diluted in aquatic environments and this leads to aggregation. The size of the aggregates depends on pH and the presence of other ionic species, but, generally, larger aggregates are more difficult to be taken up by organisms. This highlights an intricate interplay between colloidal chemistry and toxicity.

Nanoparticles and nanocomposites find new applications in sustainable energy research. J. Lui and coworkers discuss the synthesis of $\text{Cu}_2\text{Sn}_3\text{S}_7$ as the light absorbing layer for thin-film solar cells. This material, produced by the powder, baking, sulfur, and sintering (PBSS) process, exhibits an improved energy band gap and increases carrier concentration and mobility. C.-W. Ma and coworkers show how ZnO needle-shaped nanoparticles may be used to fabricate dye-sensitized solar cells. In this example, ZnO produced by a chemical solution method was deposited on a fluorine-doped tin oxide (FTO) glass to form the working electrode, against a platinized FTO glass as the counter electrode. As the authors show, this system yielded a high power conversion efficiency and enhanced electron transport. H. Xu and coworkers discuss the fabrication of a core-shell structured Co_3O_4 -PANI nanocomposite to produce a low cost but highly efficient nanomaterial for microwave absorption. In an interesting application, G. Hernández-Padrón and coworkers produced antifog coatings from recycled polystyrene. They used silica particles to produce a nanocomposite material with hydrophobic properties and variable optical transparency.

A final application discussed in this issue is the use of nanoparticles to enhance the electric and thermal properties of colloidal suspensions. J. Li and coworkers prepared Fe_3O_4 particles with an oleate coating which were then suspended in oil to produce a highly stable nanofluid with improved dielectric breakdown behavior. Both the electric and thermal properties of suspensions are influenced very strongly by the presence of nanoparticles. S. Lotfizadeh and T. Matsoukas demonstrate these effects in a numerical study of thermal conductivity in suspensions containing colloidal clusters of various structures and shapes. The authors show that chain aggregates and nonspherical particles in general enhance the thermal conductivity.

The collection of studies in this special issue highlights the importance of engineered nanoparticles and points to multiple areas in which nanoparticle research has the potential to make new contributions.

*Themis Matsoukas
Tapan Desai
Kangtaek Lee*

Research Article

Passivation and Stabilization of Aluminum Nanoparticles for Energetic Materials

Matthew Flannery,¹ Tapan G. Desai,¹ Themis Matsoukas,²
Saba Lotfizadeh,² and Matthew Oelschlager³

¹Advanced Cooling Technologies, Inc., 1046 New Holland Avenue, Lancaster, PA 17601, USA

²Penn State University, 150 Fenske Laboratory, University Park, PA 16802, USA

³Rensselaer Polytechnic Institute, 110 8th Street, Troy, NY 12180, USA

Correspondence should be addressed to Tapan G. Desai; tapandesai06@gmail.com

Received 17 June 2015; Accepted 13 October 2015

Academic Editor: Paulo Cesar Morais

Copyright © 2015 Matthew Flannery et al. This is an open access article distributed under the Creative Commons Attribution License, which permits unrestricted use, distribution, and reproduction in any medium, provided the original work is properly cited.

In aircraft applications, fuel is used not only as a propellant but also as a coolant and improving both the thermal conductivity and combustion enthalpy of the fuel is beneficial in these applications. These properties can be enhanced by dispersing aluminum nanoparticles into the fuel; however, the nanoparticles require stabilization from agglomeration and passivation from oxidation in order for these benefits to be realized in aircraft applications. To provide this passivation and stabilization, aluminum nanoparticles were encapsulated with a coating by the plasma enhanced chemical vapor deposition (PE-CVD) method from toluene precursors. The thermal conductivity, combustion and ignition properties, and stability of the nanoparticles dispersed in RP-2 fuel were subsequently evaluated. In addition, the effect of dispersing aluminum nanoparticles in RP-2 fuel on the erosion rate of fuel nozzles was evaluated. The dispersion of PE-CVD coated aluminum nanoparticles at a concentration of 3.0% by volume exhibited a 17.7% and 0.9% increase in thermal conductivity and volumetric enthalpy of combustion, respectively, compared to the baseline RP-2 fuel. Additionally, particle size analysis (PSA) of the PE-CVD coated aluminum nanofuel exhibited retention of particle size over a five-month storage period and erosion testing of a 1 mm stainless steel nozzle exhibited a negligible 1% change in discharge coefficient after 100 hours of testing.

1. Introduction

Increasing the mission capability of aircraft is a never ending objective for the military. Critical to achieving this objective is improving the thermal performance and energy density of the fuel aboard the aircraft, which is used as both a propellant and coolant [1]. Thus, improving the thermal conductivity and energy density of the fuel is one way to reach this objective. The improvement in thermal conductivity of oil-based fluids has been demonstrated by dispersing metallic nanoparticles into the base fluid in numerous research efforts [2]. Additionally, metals have higher combustion energy than carbon based fuels [3]. Thus, creating a metallic nanofuel for aircraft applications can improve both the thermal performance and

combustion energy of the fuel to meet the objective of increasing mission capability.

Due to its low density compared to other metals and larger combustion enthalpy than the base fuel [4], aluminum is a preferred candidate nanoparticle for the development of nanofuels. The improvement in the volumetric enthalpy of combustion of ethanol by Jones et al. shows that additions of 50 nm diameter aluminum nanoparticles at concentrations ranging from 1 to 10% by volume exhibited improvements in the volumetric enthalpy of combustion up to 15%. This increase in heat release upon combustion was also demonstrated by Mitchell et al. for aluminum nanoparticle/diesel fuel systems [5]. Despite the potential for combustion improvements, the aluminum rapidly oxidizes to form aluminum

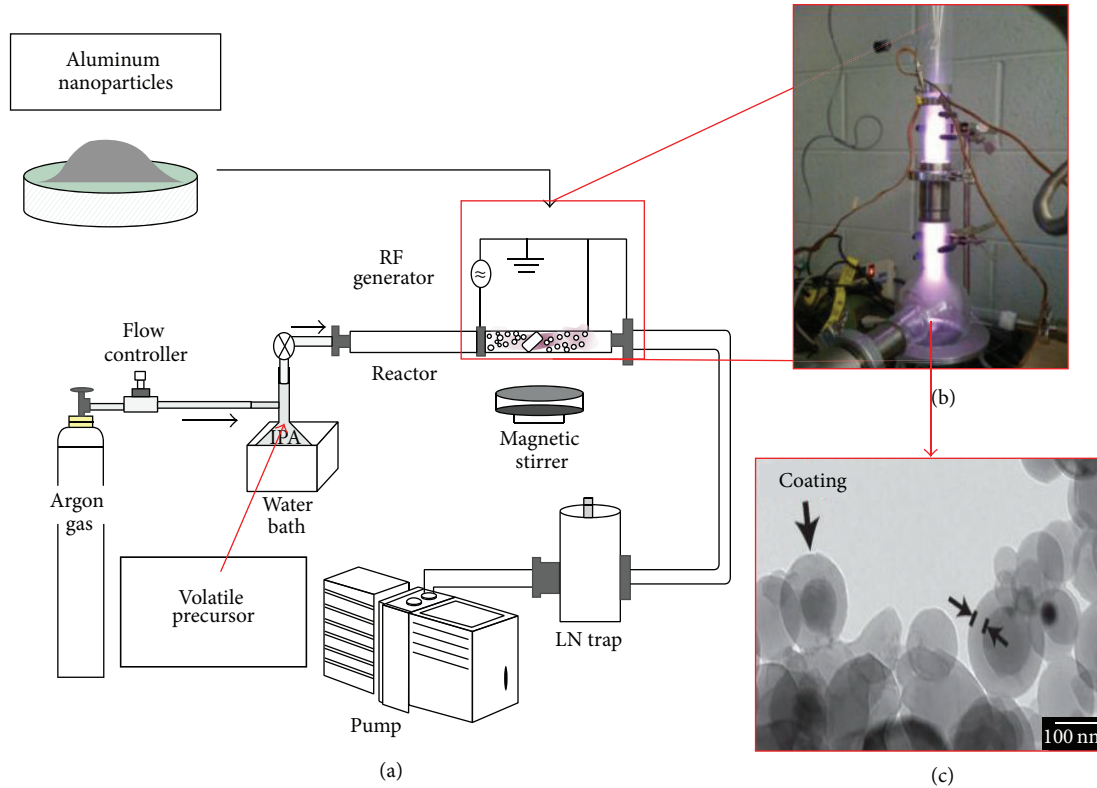


FIGURE 1: PE-CVD coating process wherein metallic nanoparticles are coated by a deeply fragmented volatile organic precursor.

oxide, which reduces the combustion enthalpy of the nanoparticles. Additionally, in the dispersed phase, the aluminum nanoparticles can agglomerate due to strong attractive forces and increase the average particle size of the aluminum, which causes the subsequent settling of the nanoparticles. This not only reduces the stability of the nanofuel, but could increase the erosion damage of fuel system components.

Reduction from agglomeration can be accomplished by a combination of electrostatic and steric stabilization [6], which can be achieved by the use of surfactants, coatings, or ionic fluids. The surface agents acting to stabilize the nanoparticles from agglomeration simultaneously protect the nanoparticle from oxidation. Meziani et al. developed stabilized aluminum nanoparticles in organic solvents using a wet-chemical synthesis approach from alane precursors with carboxylic acid molecules for surface passivation. These methods demonstrated an average aluminum particle size of 48 nm with a 15 nm standard deviation and low oxygen concentration consistent with passivation from oxidation [7]. While the wet-chemical approach has been shown to produce small diameter nanoparticles that are stabilized and passivated during synthesis [7, 8], application of passivating and stabilizing coatings has been conducted in the dry state [9].

To prevent the oxidation and agglomeration of the aluminum nanoparticles, the PE-CVD coating method was utilized to develop a 6 nm thick coating that encapsulates individual metallic nanoparticles. This coating passivates the aluminum nanoparticle to protect from oxidation and reduces the strong attractive forces to weak attractive forces

to eliminate agglomeration, thereby stabilizing the nanofuel. Through previous research, this coating method has demonstrated the successful passivation of aluminum, which increased the combustion enthalpy of the aluminum [9]. In this research effort, we present the coating of aluminum nanoparticles by the PE-CVD coating method, the evaluation of the stability of the nanofuel over a 5-month period by particle size analysis (PSA), and the evaluation of the thermal conductivity and combustion enthalpy of the nanofuel at concentrations of 0.7%, 1.5%, and 3.0% by volume by the transient hot-wire method and bomb calorimetry, respectively. Additionally, the erosion rate of a 1 mm stainless steel nozzle with aluminum nanofuel pumped at 200 PSID for 100 hours was evaluated in a custom built pumped loop, and the ignition delay time of the aluminum nanofuel was measured by spray injection of the fuel into an electrically heated, constant volume combustion chamber.

2. Materials and Methods

2.1. PE-CVD Coating Deposition. The PE-CVD coating process is a dry, one-step coating method that applies a nanometer thin plasma coating to the surface of the aluminum nanoparticles, which is outlined in Figure 1.

As is shown in Figure 1(a), the PE-CVD process is comprised of a volatile organic precursor, which is carried by inert argon gas to a plasma reaction chamber that contains aluminum nanoparticles (99.9% purity, 80 nm diameter particles from Nanostructured and Amorphous Materials, Inc.,

Houston, TX). The toluene precursor is deeply fragmented by radio frequency (RF) glow discharge, as depicted in Figure 1(b). The deeply fragmented precursors react on the surface of the nanoparticles creating a coating that mimics the chemistry of the initial precursor material [10]. The volatile organic precursor chosen for this research effort was toluene due to its chemical similarity to RP-2 fuel. In order to achieve uniform coating, as is shown in Figure 1(c), the aluminum nanoparticles are agitated by a magnetic stirrer. The growth of the coating is linear with respect to time, and therefore, it is controlled by adjusting the residence time of the nanoparticles in the reaction chamber. The target coating thickness of the toluene PE-CVD coating was 6 nm and was confirmed by transmission electron microscopy (TEM).

2.2. Nanoparticle Storage Stability Evaluation. To evaluate the stability of the aluminum nanofuel, the particle size distribution of PE-CVD coated aluminum nanofuel samples at concentrations of 0.7% by volume was evaluated after initial dispersion in RP-2 fuel and was reevaluated in one-month intervals for five months. At each month interval, the samples were sonicated and well mixed, and an aliquot of the nanofuel was analyzed by dynamic light scattering (DLS). A baseline nanofuel sample produced from uncoated aluminum nanoparticles at equivalent concentration was evaluated to determine whether the coating provided stability from agglomeration during the five-month storage period.

Additionally, to evaluate the ability to redisperse the aluminum nanoparticles after the first month of storage, the particle size distribution of an aliquot of PE-CVD coated and uncoated aluminum nanofuel was evaluated with and without sonication.

2.3. Nanofuel Thermal Conductivity Measurements. The thermal conductivity of the aluminum nanofuel was evaluated by the transient hot-wire method. The transient hot-wire apparatus consists of a thin diameter platinum wire, as is shown in Figure 2, immersed in a stagnant fluid sample. Current is passed through the wire generating heat and the temperature of the wire is monitored throughout the duration of the test by measuring the electrical resistance of the wire.

The temperature of the wire was determined through the resistance-temperature relationship of platinum. The working equation of the transient hot-wire test is presented in (1), where q is the applied electrical power to the wire, k is the thermal conductivity of the fluid, ΔT is the temperature change of the wire, t is time, α is the thermal diffusivity of the fluid, r is the radius of the wire, and C is a constant of the apparatus [11]:

$$T(t) - T_{\text{ref}} = \Delta T = \frac{q}{4\pi k} \ln\left(\frac{4\alpha t}{r^2 C}\right). \quad (1)$$

Equation (1) demonstrates that plotting ΔT versus $\ln(t)$ produces a linear plot which can be fitted to determine the thermal conductivity of the fluid. However, prior to analyzing nanofuel samples, the constant of the transient hot-wire test

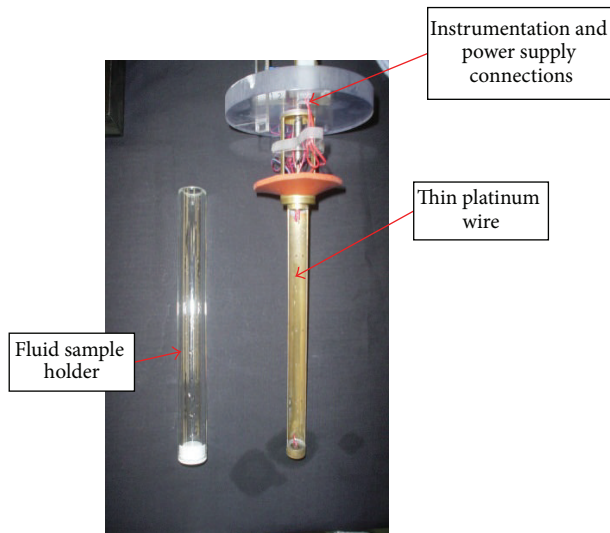


FIGURE 2: Transient hot-wire apparatus for evaluating the thermal conductivity of nanofuels.

apparatus, C , in (1), was determined by calibrating the apparatus with baseline RP-2 fuel using a thermal conductivity of 0.15 W/mK.

A programmable potentiostat was used to apply power and record electrical data in the transient hot-wire test apparatus, and the data was processed to calculate the thermal conductivity of the nanofuel. The potentiostat was programmed to conduct six consecutive runs in a single trial, which enables the thermal conductivity to be observed over a five-minute time period. This method not only measured the absolute thermal conductivity of the nanofuel but also provided indication of the stability of the PE-CVD coated aluminum nanoparticles.

2.4. Combustion Enthalpy Evaluations. To quantify the increase in combustion energy of the PE-CVD coated aluminum nanofuel, the volumetric enthalpy of combustion was evaluated by bomb calorimetry. The evaluations were conducted at concentrations of 0.7%, 1.5%, and 3.0% by volume using a Parr 1341 oxygen bomb calorimeter. To evaluate the ability of the coating to passivate the aluminum nanoparticles from oxidation, the volumetric enthalpy of combustion of baseline uncoated aluminum nanoparticles dispersed in RP-2 fuel at equivalent concentrations was evaluated.

Prior to evaluating the combustion energy of nanofuel samples, the heat capacity of the bomb calorimeter was determined using National Institute of Standards and Technology (NIST) certified benzoic acid tablets. Additionally, combustible gelatin capsules were used to handle the liquid nanofuel samples and the combustion energy of the capsules was evaluated prior to conducting combustion energy evaluations on nanofuel samples.

2.5. Nozzle Erosion Testing. Adding aluminum nanoparticles to RP-2 fuel to increase the thermal conductivity and combustion energy presents risks to erosion of fuel system

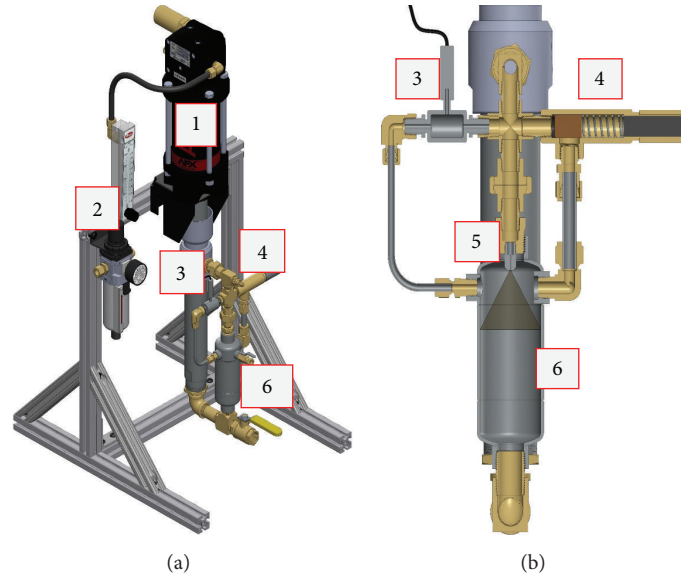


FIGURE 3: (a) CAD model of custom nozzle erosion pumped loop. (b) Cross section of the nozzle and reservoir. (1) Air Driven Piston Pump, (2) Air Pressure Regulator and Flow Meter, (3) High-Accuracy Differential Pressure Sensor, (4) Adjustable Pressure Relief Valve, (5) 1 mm stainless steel nozzle, and (6) Nanofuel Reservoir.

components. The most vulnerable area was suspected to be the injectors where the nanofuel is forced through a small diameter orifice and atomized. Nanofluids that are unstable will agglomerate during storage and when pumped through the nozzle could severely erode the nozzle or even clog the nozzle. To evaluate the effect of the addition of PE-CVD coated aluminum particles to RP-2 fuel, a custom-made pumped loop was designed and fabricated to pump the PE-CVD coated nanofuel at a concentration of 0.7% by volume through a 1 mm stainless steel nozzle at 200 PSID for 100 hours, as shown in Figure 3.

The nozzle erosion pumped loop was designed with an Air Driven Piston Pump that delivered nanofuel to a removable 1 mm nozzle. A differential pressure transducer was connected to the inlet and outlet of the nozzle to measure and monitor the differential pressure across the nozzle. A pressure relief valve was incorporated into the pumped loop to ensure fluid bypass in the event of clogging.

Erosion of the nozzle would cause a change in the flow characteristics of the nozzle. Thus, a nozzle evaluation loop was developed, as shown in Figure 4, to measure the discharge coefficient of the nozzle at 25-hour intervals. Additionally, optical microscopy evaluations were conducted to measure the diameter of the nozzle and observe the nozzle for signs of erosion.

At 25-hour intervals, the nozzle was removed from the erosion test pumped loop, cleaned thoroughly in acetone, and placed into the nozzle evaluation loop. Water was pumped through the nozzle at flow rates varying from 2.5 GPH to 15 GPH in 2.5 GPH increment and the pressure differential across the nozzle at steady state was measured. The flow performance and erosion of the nozzle were compared to a baseline RP-2 fuel tested for 100 hours under the same

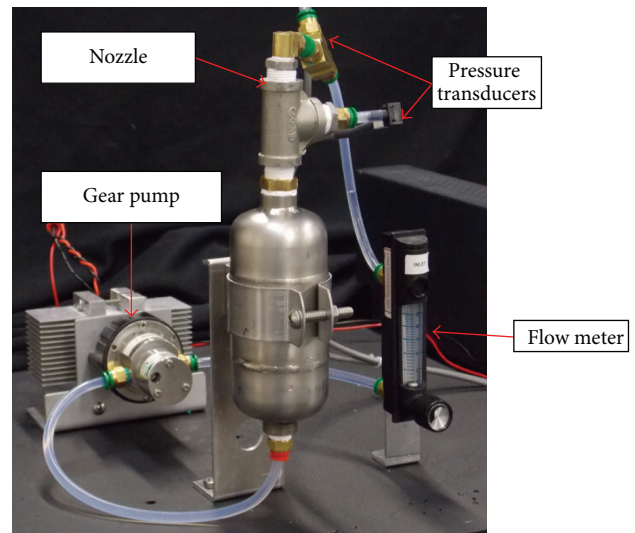


FIGURE 4: Nozzle evaluation test loop developed to characterize the discharge coefficient of the nozzle at 25-hour intervals.

condition in order to determine how the addition of metallic nanoparticles effects the erosion of fuel system components.

2.6. Ignition Delay Time Measurements. To evaluate the effect of the addition of the aluminum nanoparticles on the combustion kinetics of the fuel, the ignition delay time of baseline RP-2 fuel, uncoated aluminum nanofuel, and PE-CVD coated aluminum nanofuel, each at a concentration of 1.5% by volume, was evaluated in a constant volume, electrically heated combustion chamber, shown in Figure 5.

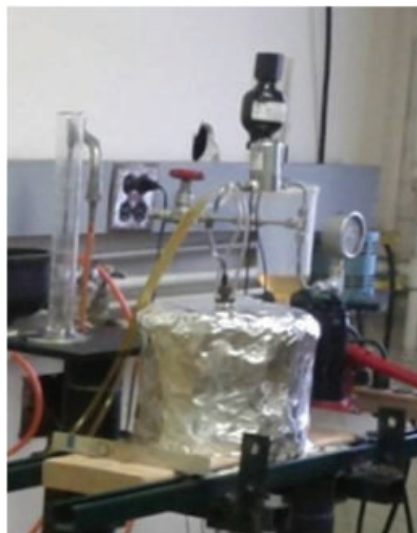
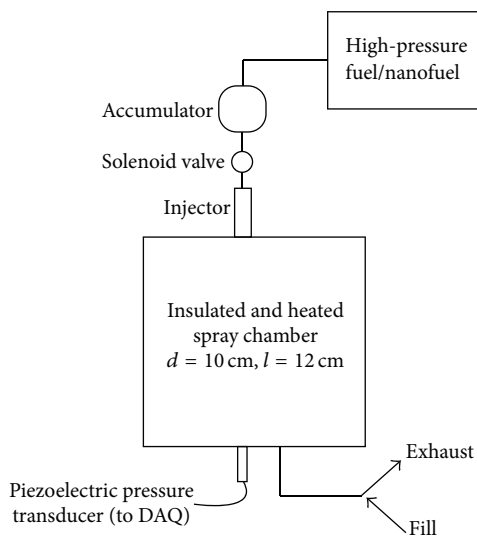


FIGURE 5: Spray combustion apparatus for evaluating the ignition delay time of RP-2 fuel and aluminum nanofuel.

The combustion chamber was heated with electric-resistance heaters embedded into the chamber walls and was insulated with 5 cm of high-temperature ceramic fiber, mineral wool insulation. The chamber was instrumented with K-type thermocouples for chamber wall temperature measurements and a water-cooled Kistler pressure transducer (model 6041A) for measurement of chamber pressure during the spray ignition event and determination of the ignition delay time. At the top of the cylindrical combustion chamber, a low-pressure diesel, single-hole, pintle-style injector (Bosch W0133-1827210) atomized the fuel samples into the chamber. The injector was cooled by circulating diesel fuel, which flows through the injector body. The fuel sample was pressurized in a hydraulic accumulator, and the duration of injection was controlled by a solenoid valve located between the high-pressure accumulator and the injector. The pressure of the fuel delivered to the injector was set to 2200 psia for a duration of 3 ms.

Prior to ignition delay time measurements, the mass of the fuel injected was characterized to ensure consistent injector performance. High-pressure fuel was injected into a container and the mass of single injections was measured over ten trials using a high-accuracy scale (Mettler PM6100). The mass per injection for the three fuel samples studied is presented in Figure 6.

As is shown in Figure 6, the mass of fuel injected with a 2200 psia injection pressure and a 3 ms pulse duration was consistent over the 10 trials and deviated by less than 3% between fuel samples. Additionally, the consistent injection performance between the baseline RP-2 fuel and the nanofuel samples demonstrated that injector performance was not affected by the addition of toluene PE-CVD coated aluminum nanoparticles.

To carry out a series of spray ignition delay time measurements, the combustion chamber was heated to a temperature of approximately 800 K, and the heaters were turned off. As the combustion chamber cooled over the course of several

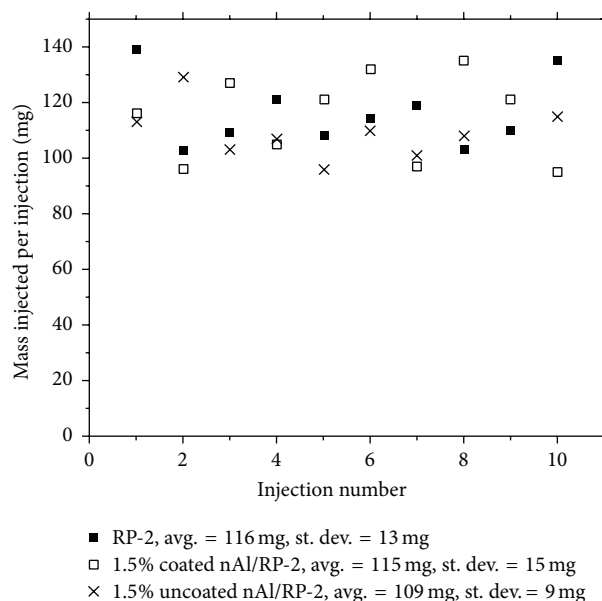


FIGURE 6: Characterization of fuel mass injection during spray combustion testing demonstrating consistent spray performance.

hours, spray injection measurements were conducted at temperatures ranging from 800 to 600 K with a temperature uniformity of ± 3 K. The evacuated chamber was filled with high-purity air to 20 atm from a compressed gas cylinder, and the fuel sample was injected into the high-temperature, high-pressure air, which initiates the combustion experiment. The pressure of the chamber was monitored using a Kistler pressure transducer, as shown in Figure 7.

As is shown in Figure 7, at injection, the pressure in the chamber immediately decreases due to evaporative cooling of the chamber air as the fuel evaporates in the chamber and mixes. After an induction period, a partially mixed fuel/air

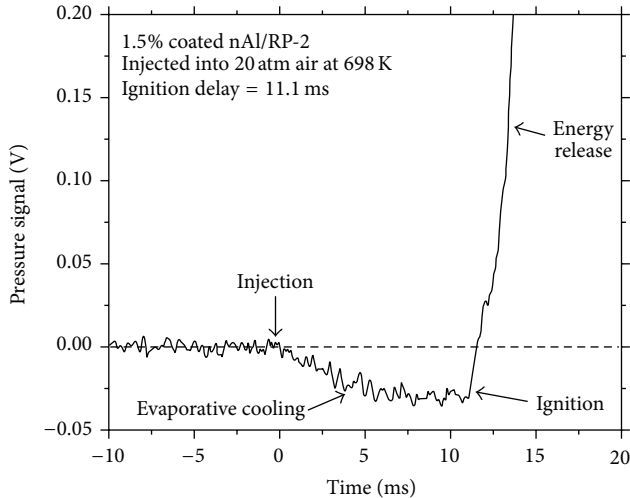


FIGURE 7: Sample pressure profile for spray ignition delay measurements.

region locally ignites causing the chamber pressure to rise rapidly. The ignition delay time was determined by comparing the time interval between spray injection, defined as the time at which the chamber pressure first decreases due to spray evaporation, and the onset of ignition, defined as the time at which the pressure gradient first becomes positive due to ignition-related heat release.

3. Results and Discussion

3.1. PE-CVD Coating Deposition. The target coating thickness of the PE-CVD coating from toluene precursor was 6 nm. To ensure the coating thickness met this target and encapsulated individual nanoparticles, the coating thickness of dry aluminum nanoparticles was characterized by transmission electron microscopy (TEM). As is shown in Figure 8, the toluene PE-CVD coating encapsulates the individual aluminum nanoparticles and has an average thickness of 6.21 nm, which demonstrates that PE-CVD coating met the target coating thickness specification.

3.2. Nanoparticle Stability Evaluation. During storage, nanoparticles will settle due to the relative density of the particle and the base fuel. However, a stabilized nanofluid will redispersed after settling without increasing particle size (i.e., will not agglomerate). The ability to redispersed the PE-CVD coated aluminum nanofuels compared to the uncoated counterpart was evaluated by measuring the median particle size with and without sonication of the respective sample by dynamic light scattering (DLS) after one month of storage at room temperature.

As is shown in Figure 9, the PE-CVD coated nanofuel sample increases particle size over the one-month period but is easily redispersed with sonication. This indicates that weak bonding forces are present between agglomerated aluminum nanoparticles. Alternatively, the uncoated aluminum nanofuel sample demonstrated a consistent particle size that

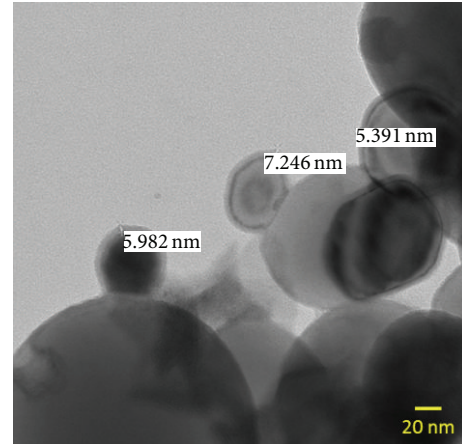


FIGURE 8: TEM micrograph of toluene PE-CVD coated aluminum nanoparticles exhibiting a 6 nm coating thickness that encapsulates individual aluminum nanoparticles.

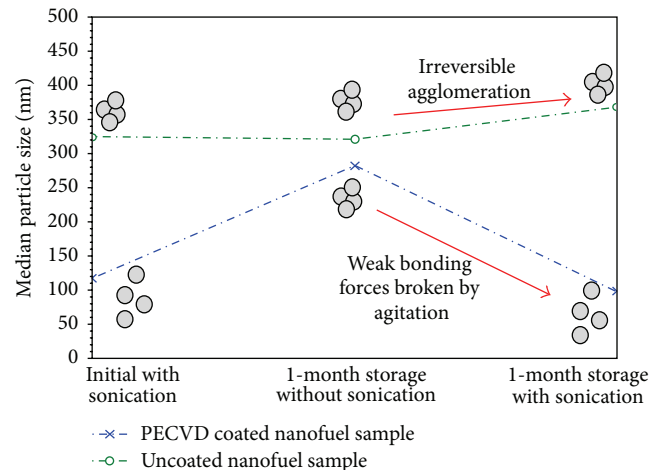


FIGURE 9: Median particle size of PE-CVD coated and uncoated aluminum nanofuel after one month of storage before and after sonication demonstrating that the PE-CVD coated nanoparticles are able to be redispersed.

could not be redispersed due to strong bonding forces between aluminum nanoparticles which leads to agglomeration. The ability to redispersed the PE-CVD coated aluminum nanofuel sample by sonication demonstrates that the coating provides stabilization from agglomeration, which improves storage stability of the nanofuel.

In order to quantify the extent of agglomeration of PE-CVD coated and uncoated aluminum nanoparticles, dynamic light scattering (DLS) was conducted to evaluate the particle size distribution of each sample. Particle size distributions were determined by the number of particles of a given diameter. Moreover, the samples were stored at room temperature and the DLS analysis was repeated at one-month intervals over a 5-month period to determine the growth rate of particle size due to agglomeration. DLS results at the one-month intervals are presented in Figure 10.

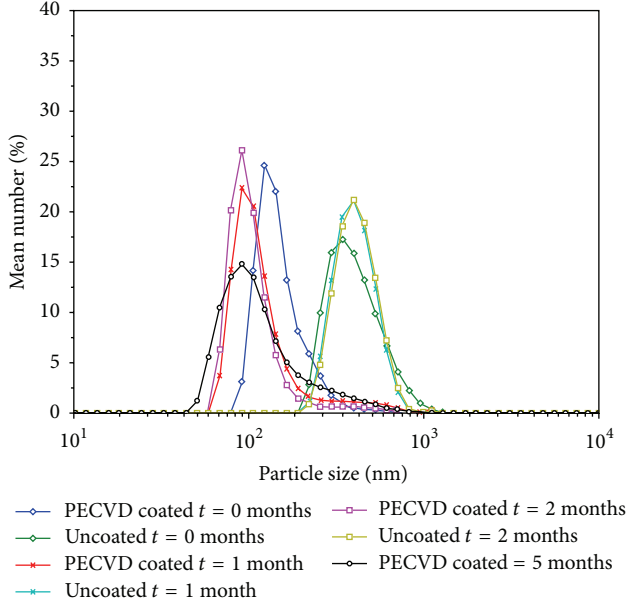


FIGURE 10: Dynamic light scattering results of PE-CVD coated and uncoated aluminum nanoparticles dispersed in RP-2 fuel demonstrating that the PE-CVD coated nanofuel maintained a reduced median particle size over a five-month storage period.

As is shown in Figure 10, the smallest nanoparticle size present in the uncoated sample distribution was greater than 200 nm, while the PE-CVD coated aluminum nanoparticle distribution exhibited the smallest aluminum nanoparticle size at ~ 80 nm. Moreover, the median particle size of the PE-CVD coated aluminum nanoparticle sizes was ~ 150 nm, which was 30% of the median particle size of the uncoated counterpart. After being stored for five months at room temperature, the PE-CVD coated aluminum nanoparticles maintained a smaller particle size than the uncoated counterpart sample with 90% of the particles being less than 235 nm in diameter indicating that the PE-CVD coating prevents agglomeration of the aluminum nanoparticles.

3.3. Nanofuel Thermal Conductivity Measurements. The thermal conductivity of PE-CVD coated aluminum nanofuel samples at a concentration of 0.7%, 1.5%, and 3.0% by volume was determined by the transient hot-wire method in nine trials spanning a three-month period and results are presented in Figure 11. The measured thermal conductivity was plotted with the upper and lower bounds of the Hashin and Shtrikman (H-S) model for thermal conductivity in nanofluids, which is presented in (2), where k_f is the thermal conductivity of the base fluid RP-2 fuel, k_p is the thermal conductivity of the aluminum particle, ϕ is the volume fraction of nanoparticles, $[k] = k_p - k_f$, and k_{nf} is the thermal conductivity of the nanofuel [12]:

$$k_f \left[1 + \frac{3\phi [k]}{3k_f + (1 - \phi) [k]} \right] \leq k_{nf} \leq \left[1 - \frac{3(1 - \phi) [k]}{3k_p - \phi [k]} \right] k_p. \quad (2)$$

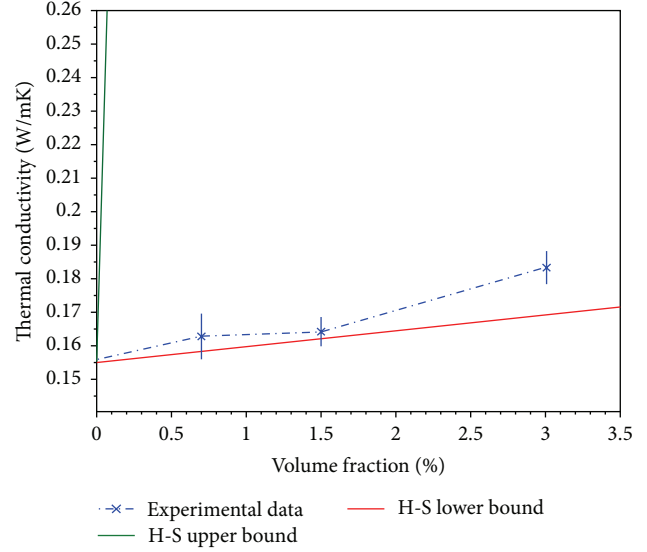


FIGURE 11: Thermal conductivity of PE-CVD coated aluminum nanoparticles dispersed in RP-2 fuel at 0.7%, 1.5%, and 3.0% volume fractions.

As is shown in Figure 11, the thermal conductivity of PE-CVD coated aluminum nanofuel increases with increasing nanoparticle concentration and reaches a 17.7% improvement in thermal conductivity over the baseline RP-2 fuel at a 3.0% volume fraction. The error bars in Figure 11 represent one standard deviation in the thermal conductivity measured over multiple trials. This indicates that addition of aluminum nanoparticles improves the thermal performance of RP-2 fuel and, as a result, increases the heat transfer properties of the fuel as a coolant. Furthermore, agreement of the thermal conductivity of the PE-CVD coated aluminum nanofuel samples with the lower bound of the H-S model indicates that there is no anomalous improvement in thermal performance. The well-known H-S model bounds the thermal conductivity of a nanofluid based on the configuration of the nanoparticles. The lower bound of the model corresponds to a nanofluid configuration in which the nanoparticles are discretely dispersed, while the upper bound of the model corresponds to a nanofluid configuration in which nanoparticles form chains that increase the thermal conduction path, as shown in Figure 12 [12]. The agreement with the lower bound of the H-S model provides supporting evidence that the PE-CVD coated aluminum nanofuels have increased stability that can be attributed to lack of agglomeration and support the PSA results presented in Figure 10.

As nanoparticles settle, the thermal conductivity of the nanofuel will decrease, approaching that of the RP-2 fuel. Hence, a consistent thermal conductivity throughout the six consecutive runs indicates a low settling rate and demonstrates a stable nanoparticle suspension. The experimentally determined thermal conductivity of six consecutive runs for the RP-2 baseline, 0.7%, 1.5%, and 3.0% by volume PE-CVD coated aluminum nanofuel is presented in Figure 13.

As is shown in Figure 13, the thermal conductivity of the nanofuel samples is consistent over six consecutive runs,

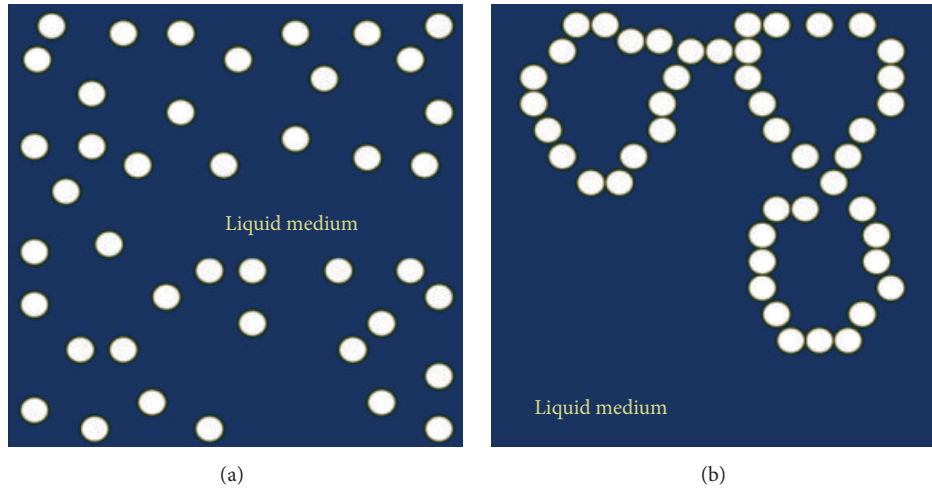


FIGURE 12: Depiction of nanoparticle configurations that correspond to the (a) lower bounds and (b) upper bounds of the H-S model [12].

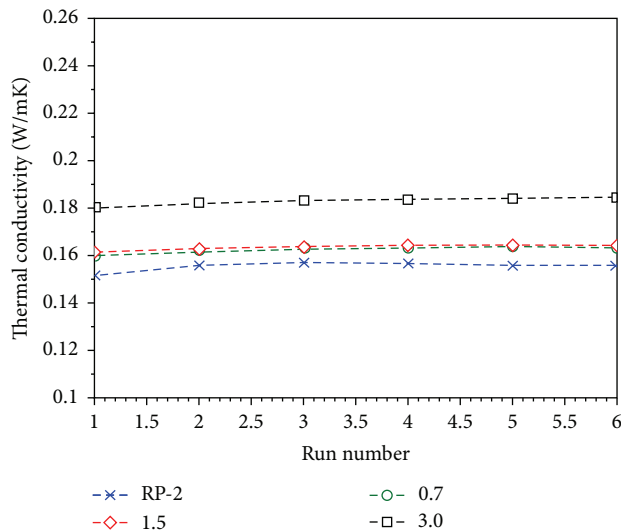


FIGURE 13: Thermal conductivity measurements of baseline RP-2, 0.7%, 1.5%, and 3.0% PE-CVD coated aluminum nanofuel over six consecutive runs spanning a five-minute period exhibiting consistent thermal conductivity and indicating low settling rate of the aluminum PE-CVD nanoparticles.

which indicates a low settling rate. The consistent thermal conductivity between consecutive runs provides evidence to support enhanced stabilization of the PE-CVD coated aluminum nanoparticles.

PE-CVD coated aluminum nanoparticle stability in storage conditions was also determined by repeating the thermal conductivity analysis over three consecutive months. Agglomerating nanoparticles will increase the diameter of the nanoparticles causing them to settle out of solution, which reduces the thermal conductivity of the nanofuel, according to the H-S model. Consistent thermal conductivity readings

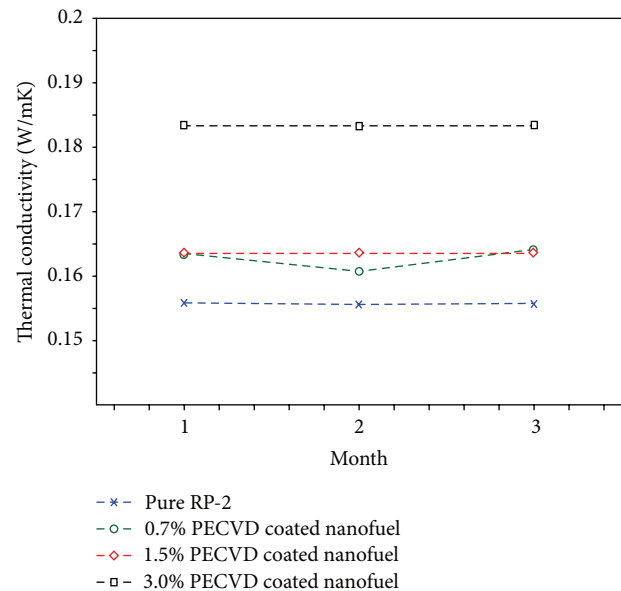


FIGURE 14: Thermal conductivity of baseline RP-2, 0.7%, 1.5%, and 3.0% PE-CVD coated aluminum nanofuel after three months of storage indicating the ability to easily redisperse the nanoparticles after storage.

over a three-month period would demonstrate a stable nanoparticle suspension that resists agglomeration and subsequent settling. Thermal conductivity data conducted over the three-month period is presented in Figure 14.

As is shown in Figure 14, the thermal conductivity of the baseline RP-2, 1.5%, and 3.0% samples was repeatable over the three-month period and exhibited a 2.6% relative standard deviation at 3.0% volume fraction. The repeatable thermal conductivity over a three-month storage period demonstrated a nanoparticle suspension that was easily redispersed due to stabilizing the aluminum nanoparticles from agglomeration and supports the data presented in Figure 9.

3.4. Combustion Enthalpy Evaluation. The volumetric enthalpy of combustion, $\Delta H_{\text{fuel,vol}}$, of PE-CVD coated and uncoated aluminum nanofuel samples at a concentration of 0.7%, 1.5%, and 3.0% by volume was determined by bomb calorimetry and was calculated from (3), where C_{cal} is the heat capacity of the bomb calorimeter, ΔT is the temperature change of the bomb calorimeter, m_{gel} is the mass of the gelatin capsule used to hold the liquid sample, ΔU_{gel} is the internal energy of combustion of the gelatin capsule, L_{wire} is the length of ignition wire combusted during the bomb calorimetry trials, γ_{wire} is the combustion energy of the wire per unit length, Δn is the change in the number of moles of gaseous species, R is the universal gas constant (8.3145 J/molK), ρ_{fuel} is the density of the fuel sample, and m_{fuel} is the mass of the fuel sample:

$$\Delta H_{\text{fuel,vol}} = \frac{(C_{\text{cal}}\Delta T - m_{\text{gel}}\Delta U_{\text{gel}} - L_{\text{wire}}\gamma_{\text{wire}} + \Delta nRT)\rho_{\text{fuel}}}{m_{\text{fuel}}} \quad (3)$$

Experimentally determined volumetric combustion enthalpies of PE-CVD coated and uncoated aluminum nanofuel samples that were stored for one month are presented in Figure 15.

As shown in Figure 15, the volumetric enthalpy of combustion of the PE-CVD coated aluminum nanofuels increased with increasing volume concentration, reaching 0.9% enhancement at 3.0% volume fraction. Conversely, uncoated 0.7% and 1.5% volume fractions did not improve the volumetric combustion enthalpy of the RP-2 fuel, while the uncoated 3.0% nanofuel sample exhibited 0.3% improvement in volumetric combustion enthalpy. Furthermore, statistical analysis of the combustion energy data using a t -test, assuming unequal variance, suggests that the measured improvement of the 3.0% volume fraction PE-CVD coated sample is within a 90% confidence interval. Thus, the statistical analysis of the volumetric enthalpy of combustion suggests that the observed improvement in energy density of the PE-CVD coated samples was statistically significant.

3.5. Nozzle Erosion Testing. After 25 hours of erosion testing, the nozzle was placed in the evaluation test loop and water was pumped through the nozzle at flow rates varying from 2.5 to 15 GPH in 2.5 GPH increments. The pressure differential across the nozzle was measured in three trials. The discharge coefficient, C_d , of the nozzle was determined by (4), where ΔP_{theor} is the theoretical pressure difference of the nozzle at the given flow rate and ΔP_{meas} was the measured pressure difference. The theoretical pressure difference was calculated from (5), where \dot{m} is the mass flow rate of water, D is the diameter of the nozzle (1 mm), ρ is the density of water, and d is the ratio of the nozzle diameter to the upstream pipe diameter (0.16):

$$C_d = \frac{\sqrt{\Delta P_{\text{theor}}}}{\sqrt{\Delta P_{\text{meas}}}} \quad (4)$$

$$\Delta P_{\text{theor}} = \left(\frac{4\dot{m}}{\pi D^2 \rho}\right)^2 \frac{\rho(1-d^4)}{2}. \quad (5)$$

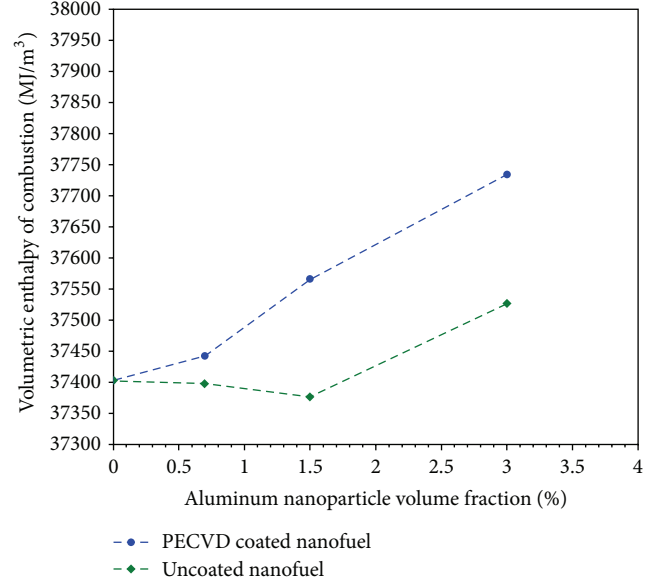


FIGURE 15: Volumetric combustion enthalpy of PE-CVD coated and uncoated aluminum nanofuel samples.

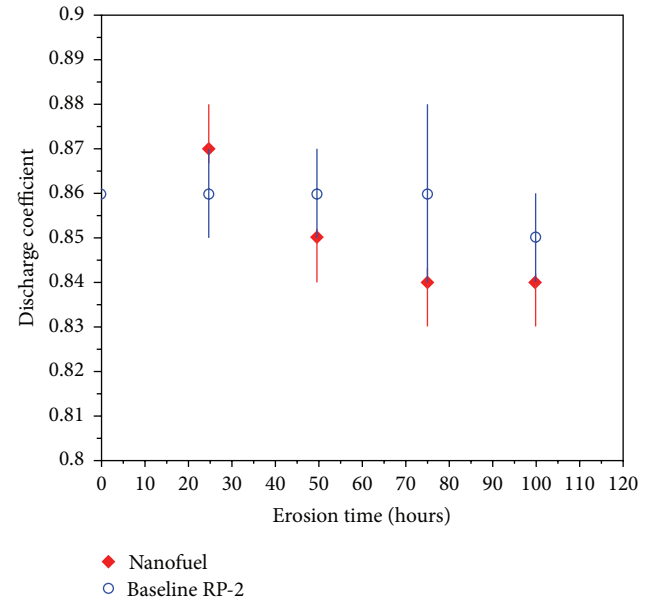


FIGURE 16: Nozzle discharge coefficients throughout the 100 hours of erosion testing indicating negligible change in discharge coefficient.

The discharge coefficients of the nozzle tested with baseline RP-2 fuel and 0.5% volume fraction nanofuel throughout the 100-hour erosion test are presented in Figure 16.

As is shown in Figure 16, after 100 hours of erosion testing, the discharge coefficient of the nozzle tested with nanofuel reduced by 2% while the baseline RP-2 fuel decreased by 1% indicating a negligible change in discharge coefficient for both samples. The error bars in Figure 16 represent one standard deviation in the measured discharge coefficient over multiple experimental trials. Optical microscopy images of

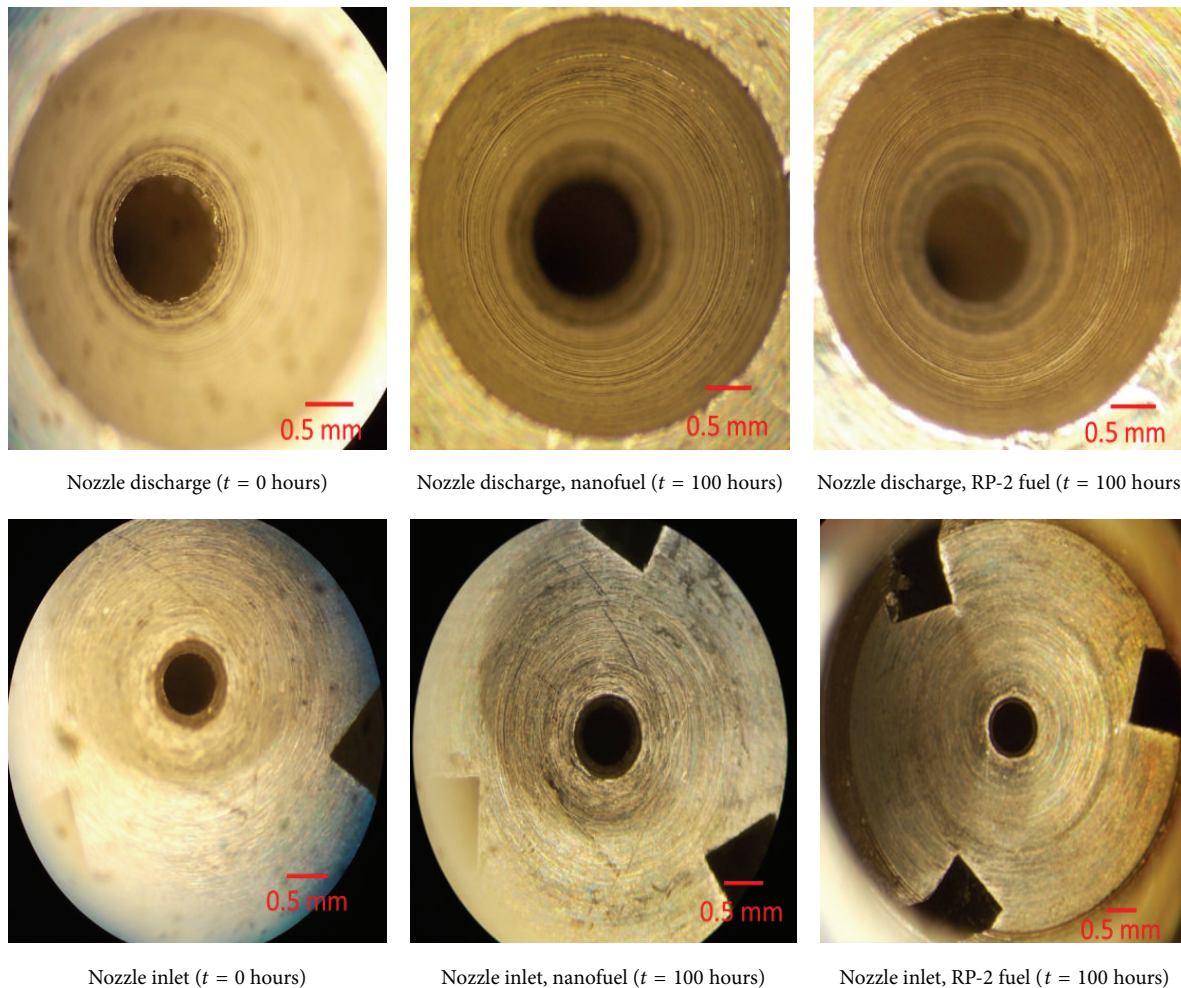


FIGURE 17: Optical microscopy images of nozzle discharge and inlets at initial conditions and after 100 hours of erosion testing exhibiting no significant erosion damage.

the nozzle discharge and inlet, prior to testing and after 100 hours of erosion testing, are presented in Figure 17.

As is shown in Figure 17, the diameter of the nozzle discharge and inlet remained constant after 100 hours of erosion testing. However, additional wear was noticed in the inlet of the nanofuel tested nozzle after 100 hours of erosion testing. The additional wear in the nozzle inlet was suspected to increase the roughness of the inlet, thereby increasing the coefficient of friction and subsequently reducing the discharge coefficient, as is observed in Figure 16. However, the change in discharge coefficient between the nanofuel tested nozzle and baseline RP-2 tested nozzle was insignificant after 100 hours of pumping the fuel at a pressure differential of 200 PSI indicating that the nanofuel did not increase the erosion rate of fuel injector components.

3.6. Ignition Delay Time Measurements. To evaluate the effect of adding aluminum nanoparticles to the combustion kinetics of RP-2 fuel, spray ignition delay times were measured in a constant volume combustion chamber. Spray ignition delay

times at temperatures ranging from 600 to 800 K for baseline RP-2 fuel, 1.5% PE-CVD coated aluminum nanofuel, and 1.5% uncoated aluminum nanofuel are presented in Figure 18.

The spray ignition delay time for the PE-CVD coated aluminum nanofuels is 10–20% longer than baseline RP-2 fuel, which is considered within an acceptable deviation. The ignition delay times of the uncoated RP-2 nanofuel samples were approximately 50–100% longer than the baseline RP-2. The combustion process is divided into three major steps: evaporation, mixing, and gas-phase chemical reaction. It was hypothesized that the uncoated sample formed agglomerates that reduced the evaporation rate of the RP-2 fuel, which reduces the kinetics of the combustion process. On the other hand, the negligible change in ignition delay time for the PE-CVD coated aluminum nanofuel sample provides evidence to support the conclusion that the PE-CVD coating reduces agglomeration and permits the fuel to evaporate and maintain combustion kinetic characteristics while simultaneously releasing more energy as determined in the combustion enthalpy evaluations.

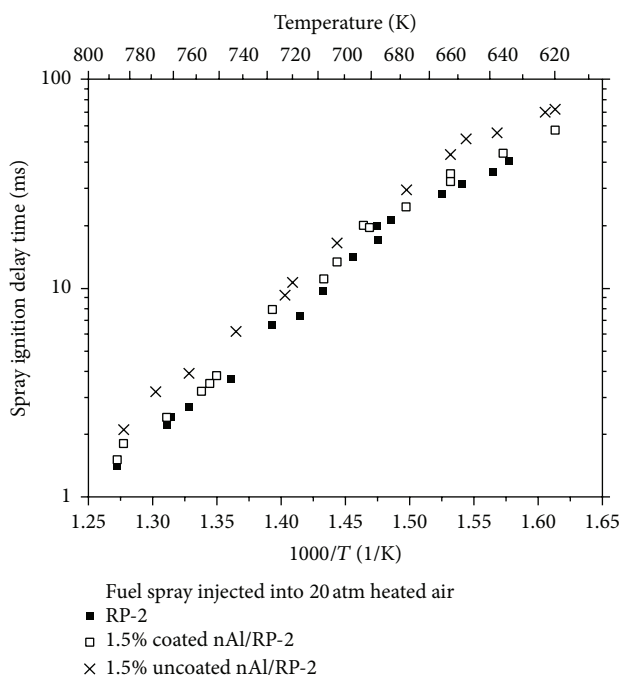


FIGURE 18: Spray ignition delay time results demonstrating a 10–20% increase in ignition delay time for the PE-CVD coated aluminum nanofuel and a 50–100% increase in ignition delay time for the uncoated counterpart.

4. Conclusions

Utilizing nanoparticle technology to improve the thermal performance and energy density of fuels can help meet the objectives of improving mission capabilities of aircraft but must be passivated from oxidation and stabilized from agglomeration to ensure the functionality of the fuel is not compromised. Through our research, a passivating 6 nm thick coating that stabilizes individual nanoparticles was demonstrated by the PE-CVD coating process. Once dispersed into RP-2 base fuel, the nanoparticles exhibited retention of particle size over a five-month storage period, thereby demonstrating stability from agglomeration. Additionally, the thermal conductivity and volumetric enthalpy of combustion of the PE-CVD coated aluminum nanofuel at a concentration of 3.0% by volume exhibited 17.7% and 0.9% improvement, respectively, compared to the baseline RP-2 fuel. At an equivalent concentration, uncoated aluminum nanofuel exhibited 0.3% improvement in volumetric enthalpy of combustion compared to the baseline RP-2 fuel. The greater improvement in the volumetric enthalpy of combustion between the PE-CVD coated and uncoated aluminum nanofuel indicates that the PE-CVD coating protected the aluminum from oxidation, thereby providing a greater amount of combustible aluminum per mass of nanofuel. Furthermore, the PE-CVD coated aluminum nanofuel exhibited a negligible 1% reduction in the discharge coefficient of a 1 mm stainless steel nozzle compared to baseline RP-2 fuel after 100 hours of erosion testing at pressure differential across the nozzle of 200 PSID. Finally, the ignition delay time of the PE-CVD coated aluminum nanofuel and

uncoated aluminum nanofuel at a concentration of 1.5% by volume exhibited an increase in ignition delay time of 10–20% and 50–100%, respectively, compared to the baseline RP-2 fuel. Thus, the larger increase in ignition delay time for the uncoated sample compared to the PE-CVD coated sample indicates that the agglomeration of the uncoated nanoparticles affected the ignition process. As a result, the passivation and stabilization of aluminum nanoparticles by the PE-CVD coating method demonstrated that nanoparticle technology can be utilized to improve the thermal performance and energy density of fuels.

Conflict of Interests

The authors declare that there is no conflict of interests regarding the publication of this paper.

Acknowledgments

The authors thank the United States Air Force for their support of these developments under Contract no. FA9300-13-M-1007. Additional support was provided by the National Science Foundation under Grant no. CBET GOALI no. 1132220.

References

- [1] P. De Bock and B. Gerstler, *Thermal Challenges in Today's Commercial and Military Aircraft*, Electronics Cooling, 2011.
- [2] R. A. Bhogare and B. S. Kothawale, "A review on applications and challenges of nano-fluids as coolant in automobile radiator," *International Journal of Scientific and Research Publications*, vol. 3, no. 8, 2013.
- [3] Y. Gan and L. Qiao, "Combustion characteristics of fuel droplets with addition of nano and micron-sized aluminum particles," *Combustion and Flame*, vol. 158, no. 2, pp. 354–368, 2011.
- [4] M. Jones, C. H. Li, A. Afjeh, and G. Peterson, "Experimental study of combustion characteristics of nanoscale metal and metal oxide additives in biofuel (ethanol)," *Nanoscale Research Letters*, vol. 6, no. 1, article 246, 2011.
- [5] M. R. Mitchell, R. E. Link, M.-J. Kao, C.-C. Ting, B.-F. Lin, and T.-T. Tsung, "Aqueous aluminum nanofluid combustion in diesel fuel," *Journal of Testing and Evaluation*, vol. 36, no. 2, Article ID 100579, 2008.
- [6] A. Kraynov and T. E. Müller, *Concepts for the Stabilization of Metal Nanoparticles in Ionic Liquids*, InTech Open Access, 2011.
- [7] M. J. Meziani, C. E. Bunker, F. Lu et al., "Formation and properties of stabilized aluminum nanoparticles," *ACS Applied Materials & Interfaces*, vol. 1, no. 3, pp. 703–709, 2009.
- [8] R. J. Helmich and K. S. Suslick, "Chemical aerosol flow synthesis of hollow metallic aluminum particles," *Chemistry of Materials*, vol. 22, no. 17, pp. 4835–4837, 2010.
- [9] A. Shahravan, T. Desai, and T. Matsoukas, "Passivation of aluminum nanoparticles by plasma-enhanced chemical vapor deposition for energetic nanomaterials," *ACS Applied Materials & Interfaces*, vol. 6, no. 10, pp. 7942–7947, 2014.
- [10] A. Shahravan, T. Desai, and T. Matsoukas, "Controlled manipulation of wetting characteristics of nanoparticles with dry-based plasma polymerization method," *Applied Physics Letters*, vol. 101, no. 25, Article ID 251603, 2012.

- [11] H. M. Roder, "A transient hot wire thermal conductivity apparatus for fluids," *Journal of Research of the National Bureau of Standards*, vol. 86, no. 5, pp. 457–493, 1981.
- [12] J. Eapen, R. Rusconi, R. Piazza, and S. Yip, "The classical nature of thermal conduction in nanofluids," *Journal of Heat Transfer*, vol. 132, no. 10, Article ID 102402, 2010.

Research Article

Formulation and Optimization of Eudragit RS PO-Tenofovir Nanocarriers Using Box-Behnken Experimental Design

Kefilwe Matlhola,¹ Lebogang Katata-Seru,¹ Lesego Tshweu,² Indra Bahadur,¹ Gertrude Makgatho,³ and Mohammed Balogun²

¹Chemistry Department, Faculty of Agriculture, Science and Technology, North West University, Mafikeng Campus, Private Bag X2046, Mmabatho 2735, South Africa

²Council for Scientific and Industrial Research, Materials Science and Manufacturing, Polymers and Composites, P.O. Box 395, Meiring Naude Road, Brummeria, Pretoria 0001, South Africa

³Council for Scientific and Industrial Research, Materials Science and Manufacturing, DST/CSIR National Centre for Nanostructured Materials, P.O. Box 395, Meiring Naude Road, Brummeria, Pretoria 0001, South Africa

Correspondence should be addressed to Lebogang Katata-Seru; lebzakate@yahoo.com

Received 22 May 2015; Revised 11 September 2015; Accepted 14 September 2015

Academic Editor: Tapan Desai

Copyright © 2015 Kefilwe Matlhola et al. This is an open access article distributed under the Creative Commons Attribution License, which permits unrestricted use, distribution, and reproduction in any medium, provided the original work is properly cited.

The objective of present study was to develop an optimized polymeric nanoparticle system for the antiretroviral drug tenofovir. A modified nanoprecipitation method was used to prepare Eudragit RS PO nanoparticles of the drug. The effect of amount of polymer, surfactant concentration, and sonication time on particle size, particle distribution, encapsulation efficiency (EE), and zeta potential were assessed and optimized utilizing a three-factor, three-level Box-Behnken Design (BBD) of experiment. Fifteen formulations of nanoparticles were prepared as per BBD and evaluated for particle size, polydispersity index (PDI), EE, and zeta potential. The results showed that the measured mean particle sizes were in the range of 233 to 499 nm, PDI ranged from 0.094 to 0.153, average zeta potential ranged from -19.9 to -45.8 mV, and EE ranged between 98 and 99%. The optimized formulation was characterized for *in vitro* drug release and structural characterization. The mean particle size of this formulation was 233 nm with a PDI of 0.0107. It had a high EE of 98% and average zeta potential of -35 mV, an indication of particle stability. The FTIR showed some noncovalent interactions between the drug and polymer but a sustained release was observed *in vitro* for up to 80 hours.

1. Introduction

Tenofovir is one of the first-line drugs used in the treatment of the human immunodeficiency virus (HIV) infected adults. It is a potent inhibitor of the virus nucleotide reverse transcriptase and was approved for clinical use in 2001 [1]. Its relatively low toxicity, long plasma half-life of 17 hours, and convenient dosing of 300 mg per day has made it favoured in HIV/AIDS-burdened countries like South Africa [2]. It is also an important component of the fixed dose antiretroviral combinations Truvada, Atripla, and Complera [3]. However, tenofovir suffers from nephrotoxicity, high aqueous solubility and is characterized by low gastrointestinal membrane penetration, which lowers its bioavailability to 25% [4]. Therefore, to maintain the oral delivery route, formulating the drug

into polymeric nanoparticles is essential for improving the bioavailability.

Nanoparticles present significant advantages over conventional free drug dosing [5, 6]. There is minimal drug loss during transit through the gastrointestinal tract while the particles evade degradation in the acidic environment of the stomach. Their size and surface properties allow for uptake, without disrupting the particles' integrity, by M cells in the Peyer's patches of the small intestine [7]. The lymphoid tissue associated with these patches facilitates distribution of the nanoparticles through the systemic circulations. While in the systemic circulation the nanoparticles extend the half-life of the drug and release it in a sustained manner. The resultant benefit is a reduction of therapeutic dose, increased bioavailability, and limitation of toxic side-effects.

The selection of a polymer for encapsulation is informed by several factors including the desired nanoparticle design and its biocompatibility [8]. Eudragit polymers are commercially available synthetic polymers used in drug delivery. They are copolymers of acrylic and methacrylic esters compatible with oral drug administration [9]. Eudragit RS PO is a derivative with quaternary ammonium functional group [10]. It is insoluble at the physiological pH but the cationic charge facilitates rapid permeation through the intestinal mucosa [10]. This means that the drug payload can be transported by diffusion. Eudragit RS PO is used in the pharmaceutical industry as a film-coating agent for tablets and capsule [11]. It has also been used in the preparations of time-controlled drug delivery formulations [12]. Tenofovir was encapsulated in Eudragit RS PO in this study intended for oral administration since most studies are based on the prevention of HIV transmission [13].

The most important characteristics of drug-bearing nanoparticles are size, encapsulation efficiency (EE), zeta potential, and drug release [14]. Various formulation and process variables such as amount of polymer, concentration of surfactant, amount of drug, stirring speed, stirring time, and temperature play a key role in determining the final physical and mechanical characteristics of nanoparticles. These parameters are often screened and optimized using highly automated statistical tools and design of experiment. Box-Behnken Design (BBD) is an experimental design of response surface methodology. It is one of the most popular experimental designs which is used for the development and optimization of drug delivery systems [8] and it offers the advantage of exploring more than three formulation variables to minimize the number of wet experiments to be carried out [15]. Apart from this, BBD was chosen in this study because it is a more cost-effective technique than other similar experimental designs like central composite design, D-optimal design, and Latin square design which require 20 runs and 5 levels of the factor [13]. It also does not contain any points at the corners, which helps to avoid unreasonable results [16].

More than 50% of the nanoparticles reported in the literature are prepared by nanoprecipitation [17]. It is also known as solvent displacement or interfacial deposition method and was developed about 40 years ago [18]. Compared to other methods like emulsion [19], desolvation [20], salting out, and supercritical fluid technology it involves an economy of energy and steps and does not require specialized equipment. Particles synthesized by nanoprecipitation are typically of the size 200 nm [21]. In this project we used a modified nanoprecipitation method to encapsulate tenofovir.

2. Materials and Methods

2.1. Materials. Polyvinyl alcohol (PVA) (molecular weight 13–23 kDa, 87–89% hydrolyzed), sodium dodecyl sulphate (SDS), Pluronic F127, Poloxamer 188, and acetone were purchased from Sigma-Aldrich (South Africa). Tenofovir was purchased from DB Fine Chemicals (South Africa). Eudragit RS PO (average molecular weight, 35 kDa) was received as

a gift from Evonik (South Africa). All other chemicals used were of analytical grade and purchased from Sigma-Aldrich (South Africa).

2.2. Solubility Studies. Solubility experiments were carried out by adding excess amount of tenofovir (134 mg) in 5 mL of surfactants (PVA, SDS, Poloxamer 188, and Pluronic F127) in stoppered vials and agitated on a shaker at 100 rpm for 24 hours at room temperature. The solution was filtered through a 0.45 μm membrane filter and the concentration of the drug was determined using UV/Vis spectrophotometer at 260 nm (Perkin Elmer, Lambda 35, Singapore).

2.3. Experimental Design and Analysis. The BBD (three factors, Quantum XL, Sigma) was used to study the influence of formulation parameters in optimizing the preparation of nanoparticles. Effects of three independent parameters, namely, ratio of a polymer to a drug (X_1), concentration of surfactant (X_2), and sonication time (X_3) on average particles size (Y_1), particle size distribution (expressed as polydispersity index, PDI) (Y_2), encapsulation efficiency (EE) (Y_3), and zeta potential (Y_4) were studied. They were selected at their low, medium, and high levels with replicated centre points as shown in Table 1. The completed design consisted of 15 experimental runs, which were done in triplicate.

Analysis of variation (ANOVA) helps to identify the significant independent factors that affect the responses [22] and the fitness of the model. It was applied to determine the significance and the magnitude of the effects of the main variable and their interactions by applying probability value (p value). The fitness of the model was checked by coefficient of determination (R^2) and signal to noise (F -test). A nonlinear quadratic model correlating the relationship between the independent and dependent variables were generated and shown in

$$Y = b_0 + b_1X_1 + b_2X_1 + b_3X_3 + b_{12}X_1X_2 + b_{13}X_1X_3 + b_{23}X_2X_3 + X_3^2, \quad (1)$$

where Y is the dependent variable, b_0 is the intercept, b_1 to b_{23} are the regression coefficients, and X_1 , X_2 , and X_3 are the independent variables. To graphically demonstrate the influence of each factor on the response, the surface plots for each response were generated results using BBD [23].

2.4. Preparation of Nanoparticles. Tenofovir nanoparticles were prepared using modified nanoprecipitation method [24] in accordance with BBD (Table 2). Fifteen different amounts of Eudragit RS PO were dissolved in acetone (3 mL) and diluted with distilled water (2 mL) under sonication for 5 min. The prepared solutions were added into 10 mL of the aqueous phases containing 50 mg of tenofovir and different percentages of SDS, which were previously sonicated for 10 minutes. Subsequently, nanoparticles were formed which turned the aqueous phase slightly milky with bluish opalescence. However, the mixtures were continued to be sonicated at different time frames and were left to stir overnight to aid size reduction and to evaporate solvent present.

TABLE 1: BBD experimental parameters and levels for preparation of nanoparticles.

	Levels		
	Low (-1)	Medium (0)	High (+1)
Independent variables			
X_1 = ratio of a polymer to a drug (mg)	50	75	100
X_2 = SDS (%)	3	4	5
X_3 = sonication time (min)	30	45	60
Dependant variables			
	Constraints		
Y_1 = PS (nm)	Minimum		
Y_2 = PDI	Minimum		
Y_3 = EE (%)	Maximum		
Y_4 = zeta potential (mV)	Maximum		

TABLE 2: BBD experimental parameters and levels for preparation of nanoparticles.

Run	X_1 Ratio of a polymer to a drug (mg)	X_2 Concentration of a surfactant (% SDS)	X_3 Sonication time (min)
1	50	3	45
2	50	5	45
3	100	3	45
4	100	5	45
5	50	4	30
6	50	4	60
7	100	4	30
8	100	4	60
9	75	3	30
10	75	3	60
11	75	5	30
12	75	5	60
13	75	4	45
14	75	4	45
15	75	4	45

2.5. Particle Size, Particle Size Distribution, and Zeta Potential.

The mean particle size, particle size distribution (PDI), and zeta potential of nanoparticles were determined using Malvern Zetasizer Nano ZS (Malvern Instruments, United Kingdom). Each sample was measured in triplicate. The results are expressed as mean standard deviation (SD).

2.6. Encapsulation Efficiency and Drug Loading of Nanoparticles. The encapsulation efficiency and drug loading of nanoparticles were determined by UV/Vis spectrophotometry. The prepared samples were centrifuged at 20 000 rpm for one hour, to separate nanoparticles from aqueous medium.

The supernatant was taken and quantified by measuring at 260 nm. The encapsulated drug was calculated using

$$\begin{aligned} & \text{Encapsulation efficiency (\%)} \\ & = \left(\frac{\text{total amount of drug} - \text{amount of the free drug}}{\text{total drug}} \right) \\ & \quad \times 100, \end{aligned} \quad (2)$$

Drug loading (%)

$$= \left(\frac{\text{amount of drug in nanoparticles}}{\text{total weight of nanoparticles}} \right) \times 100.$$

2.7. Fourier Transform Infrared Spectroscopy (FTIR). FTIR spectra of pure drug, Eudragit RS PO polymer, and nanoparticles were recorded using Perkin Elmer Spectrum 100 FTIR spectrophotometer, USA. The samples were placed onto sample holder and scanned in the spectral region between 4000 cm^{-1} and 650 cm^{-1} .

2.8. Morphology. The morphology of the nanoparticles was studied using a scanning electron microscope, SEM (Field Emission Electron Microscope, JEOL JSM-7500F, Japan). The samples were prepared using a double adhesive tape stuck to an aluminium stub. Drops of nanoparticles dispersion were applied on the stub and dried overnight. They were then coated with gold under an argon atmosphere using a gold sputter in a high vacuum evaporator.

2.9. In Vitro Drug Release. The *in vitro* drug release studies were carried out using dialysis bag method [25]. Briefly, 20 mg of freeze-dried samples was suspended in 10 mL of PBS (pH 7.4 and 1.5) and filled in dialysis bags with the molecular weight cut-off value of 12 000 Da. The bags were placed separately in 50 mL PBS (pH 7.4 and 1.5), respectively, and agitated in a 37°C water bath shaker at 100 rpm. At predetermined time intervals, 5 mL aliquots were drawn and the dissolution media were then replaced by 5 mL of fresh PBS to maintain a constant volume. Concentration of drug

TABLE 3: Observed responses in BBD for Eudragit RS PO nanoparticles.

Formulation code	Variable levels in coded form			Dependent variables			
	X_1	X_2	X_3	PS (nm \pm SD)	PDI (\pm SD)	ZP (mv \pm SD)	EE (%)
1	-1	-1	0	233.5 \pm 7.973	0.107 \pm 0.019	-35.2 \pm 4.47	98
2	-1	+1	0	307.65 \pm 4.59	0.094 \pm 0.022	-35.7 \pm 6.19	99
3	+1	-1	0	283.0 \pm 6.545	0.131 \pm 0.021	-32.2 \pm 9.19	99
4	+1	+1	0	404.5 \pm 6.382	0.153 \pm 0.028	-26.2 \pm 2.43	99
5	-1	0	-1	258.85 \pm 9.14	0.109 \pm 0.018	-36.5 \pm 4.14	99
6	-1	0	+1	260.5 \pm 9.589	0.094 \pm 0.017	-45.8 \pm 6.93	99
7	+1	0	-1	408.6 \pm 5.150	0.132 \pm 0.056	-19.9 \pm 2.62	99
8	+1	0	+1	317.1 \pm 8.567	0.120 \pm 0.019	-40.6 \pm 6.19	99
9	0	-1	-1	321.4 \pm 9.140	0.108 \pm 0.018	-39.8 \pm 4.14	99
10	0	-1	+1	305.95 \pm 3.87	0.132 \pm 0.041	-28.4 \pm 3.07	99
11	0	+1	-1	553.35 \pm 9.79	0.104 \pm 0.027	-25.6 \pm 1.32	99
12	0	+1	+1	301.4 \pm 13.51	0.117 \pm 0.028	-32.5 \pm 12.7	99
13	0	0	0	373.05 \pm 10.6	0.123 \pm 0.077	-37.5 \pm 0.97	99
14	0	0	0	329.65 \pm 5.36	0.099 \pm 0.019	-29.9 \pm 4.44	99
15	0	0	0	358.7 \pm 19.33	0.124 \pm 0.030	-36.0 \pm 12.3	99

released was determined using UV spectrophotometer. The percent drug release was determined by

$$\text{Drug release} = \frac{\text{release drug}}{\text{total drug}} \times 100. \quad (3)$$

3. Results and Discussion

3.1. Solubility Study. Nanoprecipitation of hydrophobic drugs is more facile than the hydrophilic ones. Hydrophilic drugs tend to rapidly equilibrate from the organic to the outer aqueous phase leaving very little drug in the precipitating nanoparticles [26]. Modification of the traditional method with the use of surfactants improves the EE. Thus the purpose of solubility study was to identify suitable surfactant that possesses good solubilizing capacity for tenofovir to increase entrapment of the drug. A number of surfactants (SDS, PVA, Pluronic F127, and Poloxamer 188) were employed. It was found that the drug exhibited maximum solubility of 226 mg·mL⁻¹ in SDS, followed by Pluronic F127 (151 mg/mL) (Figure 1). It was also found that SDS was able to increase the drug solubility by threefold when compared to the solubility of tenofovir in water. Divya et al. [18] also determined the solubility of tenofovir in different oils and surfactants (Tween 20 and Tween 80) by employing the same method [18]. Their results indicated that the drug had a solubility of 33.3 mg·mL⁻¹ in Tween 20, which is much less when compared to our results.

3.2. Preparation and Optimization of Nanoparticles. Three-level, three-factor BBD was used to study the effect of variables in the preparation steps of nanoparticles. Modified nanoprecipitation method was used to prepare 15 formulations as per BBD. On the basis of the results obtained from solubility study, SDS was chosen as surfactant to stabilize

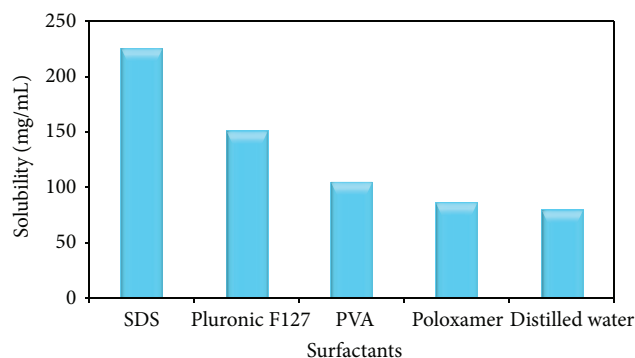


FIGURE 1: Solubility study of tenofovir in different surfactants.

nanoparticles and acetone was chosen as an organic phase. As shown in Table 3, the measured mean particle sizes are in the range of 233 to 499 nm, PDI 0.094 to 0.153, average zeta potential -19.9 to -45.8 mv, and EE 98-99%.

3.3. Statistical Analysis of the Model. ANOVA was performed to test the significance and adequacy of the model. The criteria followed in this model are if the calculated value of the F -ratio (signal to noise ratio) of the regression model is more than the standard value specified (f -table) for 95% confidence level and the model is considered adequate within the confidence limit [27]. Normally the ratio greater than 4 is desirable for the model to be used effectively [28]. Factors with p values that are less than 0.05 are considered to be statistically significant to the response [29]. Any terms in the models with high f -value and small p value indicate more significant effect on the respective response variables. Moreover, coefficient of determination (R^2) indicates the proportion of variation in the data that is explained by the

TABLE 4: The result of ANOVA for mean particle size.

Variables	Coefficient	<i>t</i> -test	<i>p</i> value	R^2	R^2 adj.	<i>F</i> -test
Constant	351.778	70.589	0.000	0.9446	0.9152	32.191
X_1	50.367	11.67	0.000			
X_2	35.525	7.9997	0.000			
X_3	-15.475	-3.5857	0.002			
X_1X_3	-23.275	-3.1136	0.006			
X_2X_3	-38.35	-5.1303	0.000			
X_2X_2	-20.1	-2.6889	0.016			
X_3X_3	-29.171	-4.9361	0.000			

TABLE 5: The result ANOVA for EE.

Variables	Coefficient	<i>t</i> -test	<i>p</i> value	R^2	R^2 adj.	<i>F</i> -test
Constant	99.0	216.748	0.000	0.9328	0.9126	46.254
X_1	-3.2667	-6.3969	0.000			
X_1	-0.7333	-1.436	0.166			
X_1	-0.8333	-1.6319	0.118			
X_1X_2	-7.3	-8.2533	0.000			
X_1X_3	-7.5	-8.4794	0.000			
X_1X_1	-6.5667	-9.5846	0.000			

TABLE 6: ANOVA results for zeta potential.

Variables	Coefficient	<i>t</i> -test	<i>p</i> value	R^2	R^2 adj.	<i>F</i> -test
Constant	34.98	39.156	0.000	0.8167	0.7352	10.023
X_1	-2.533	-3.1841	0.005			
X_2	-1.1167	-1.4305	0.177			
X_3	2.1667	2.7233	0.014			
X_1X_3	5.55	4.0275	0.001			
X_2X_3	6.45	4.6806	0.036			
X_1X_1	-2.4133	-2.2609	0.036			

TABLE 7: The result of ANOVA for PDI.

Variables	Coefficient	<i>t</i> -test	<i>p</i> value	R^2	R^2 adj.	<i>F</i> -test
Constant	0.1163	57.983	0.000	0.654	0.59	10.396
X_1	0.0183	6.0683	0.000			
X_2	0.0011	0.3602	0.722			

model. An R^2 closer to 1 or 0.9 indicates that the model fits the data perfectly. Tables 4–7 show results of the ANOVA model for mean particle size, EE, average zeta potential, and PDI, respectively.

The significant effects of the independent variables were graphically demonstrated by 3D surface plots. These kinds of plots are useful in studying the effects of two independent factors on the response at one time [30]. Since the model has more than two factors, one factor was held constant for each diagram [31]. The 3D surface plots illustrating the effects of independent variables on mean particle size, EE, average zeta potential, and PDI are shown in Figures 2–5, respectively.

Mathematical models were developed to understand the nature of the true relationship between the input variables and the output variables of the system [32]. The equation is

composed of linear and interaction terms. The linear terms are coded independent variables ranging between -1 and $+1$ [33] while interaction terms are second-order terms which are useful to estimate nonlinearity of response [34] and how response changes when two variables are simultaneously changed [8]. The negative sign for the coefficients in the equation indicates a negative effect on responses, while the positive sign indicates a positive effect [8]. The reduced mathematical models for mean particle size, EE, average zeta potential, and PDI are presented by (4) to (7), respectively.

3.4. Effect of Independent Variables on Particle Size. The results presented in ANOVA Table 4 indicate that all the studied factors (X_1 = ratio of polymer to a drug, X_2 = concentration of surfactant, and X_3 = sonication time) were found to have significant effect on mean particle size. The coefficient of determination (R^2) of the model for mean particle size was 0.9446 with adjusted R^2 of 0.9152 indicating that 94.46% and 91.52% of the model can be predicted. The equation derived for mean particle size is given in

$$\begin{aligned} \text{Mean particle size} = & 351.778 + 50.369X_1 + 35.525X_2 \\ & - 15.475X_3 - 23.275X_1X_3 \\ & - 38.35X_2X_3 - 20.1X_2^2 \\ & - 29.171X_3^2, \end{aligned} \quad (4)$$

where X_1 , X_2 , and X_3 are ratio of a polymer to a drug, concentration of a surfactant, and sonication time, respectively, and X_1X_3 and X_2X_3 are interaction effects between ratio of a polymer to a drug and sonication time, concentration of a surfactant, and sonication time while X_1^2 and X_3^2 are quadratic effect on mean particle size.

From equation, it was observed that ratio of a polymer and concentration of a surfactant had positive effect on mean particle size whereas sonication time had negative effect. Figure 2 provides the 3D response surface plots showing the change of particles size corresponding to the change of independent variables. Figure 2(a) shows the effect of ratio of a polymer to a drug and concentration of a surfactant at a constant sonication time. It can be seen from the plot that an increase in ratio of a polymer and concentration of a surfactant resulted in an increased mean particle size. It was explained that an increase in polymer concentration leads to an increase in viscous force resisting droplet breakdown by sonication [35]. Small mean particle size was obtained by low polymer to a drug having ratio of 1:1 (50 mg of a polymer to 50 mg of a drug). These results are in good agreement with the results reported by Gannu et al. [36] where they showed that smaller particle size was observed with the formulation having drug polymer ratio 1:1 due to the surfactant concentration enough to maintain the stability of the particles [36]. Small mean particle size was observed in Figure 2(b) when sonication time was increased. This may be due to the increase erosion effect on the surface of large particle and particle agglomerates resulting in small particles [37].

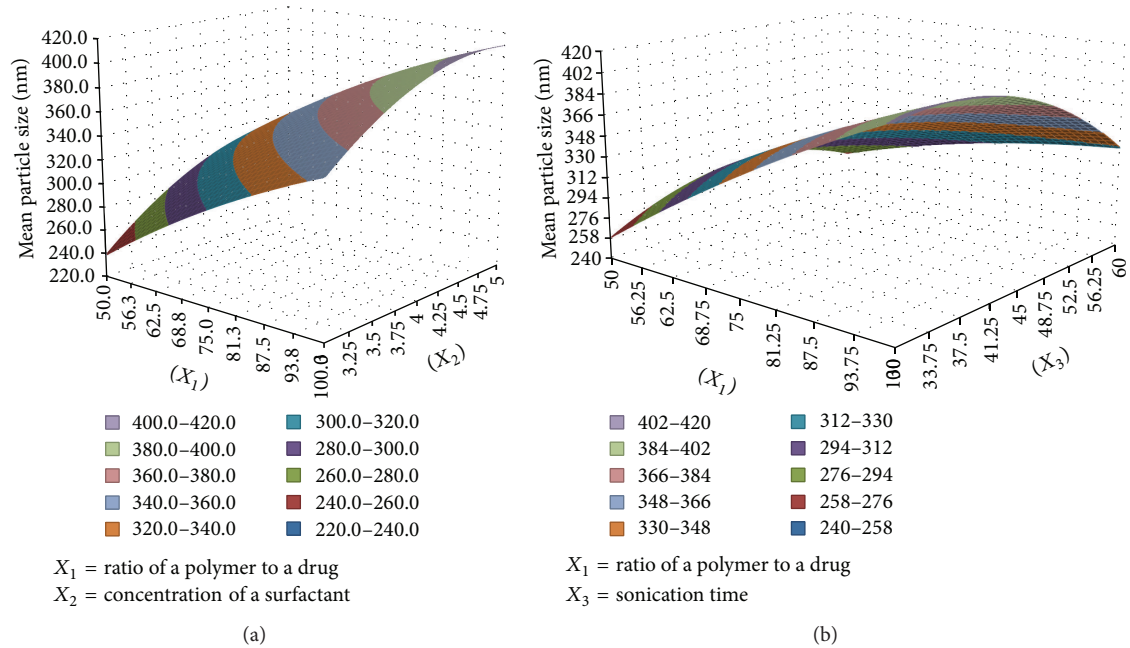


FIGURE 2: 3D response surface plots showing the effect of (a) ratio of a polymer to a drug (X_1) and concentration of a surfactant (X_2) at constant sonication time (X_3) and (b) ratio of a polymer to a drug (X_1) and sonication time (X_3) at constant concentration of a surfactant (X_2).

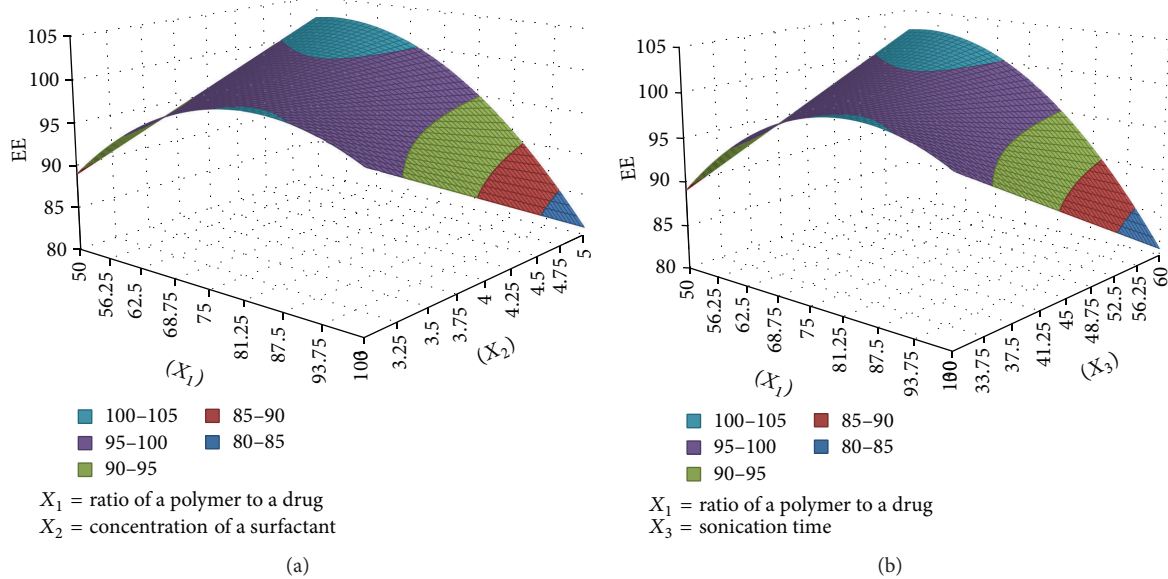


FIGURE 3: 3D response surface plots showing the effect of (a) ratio of a polymer to a drug (X_1) and concentration of a surfactant (X_2) at constant sonication time (X_3) and (b) ratio of a polymer to a drug (X_1) and sonication time (X_3) at constant concentration of a surfactant (X_2).

3.5. Effect of Independent Variables on EE. Table 5 provides ANOVA results for EE. It was observed that ratio of a polymer to a drug (X_1) has significant effect whereas other factors do not have an effect on EE. The interactions between ratio of a polymer to a drug and concentration of a surfactant and ratio of a polymer to a drug and sonication time were also

statistically significant ($p < 0.05$) on EE. The reduced model for EE is presented in

$$EE = 99.0 - 3.2667X_1 - 0.7333X_2 - 0.8333X_3 - 7.38X_1X_2 - 7.5X_1X_3 - 6.5667X_1^2 \quad (5)$$

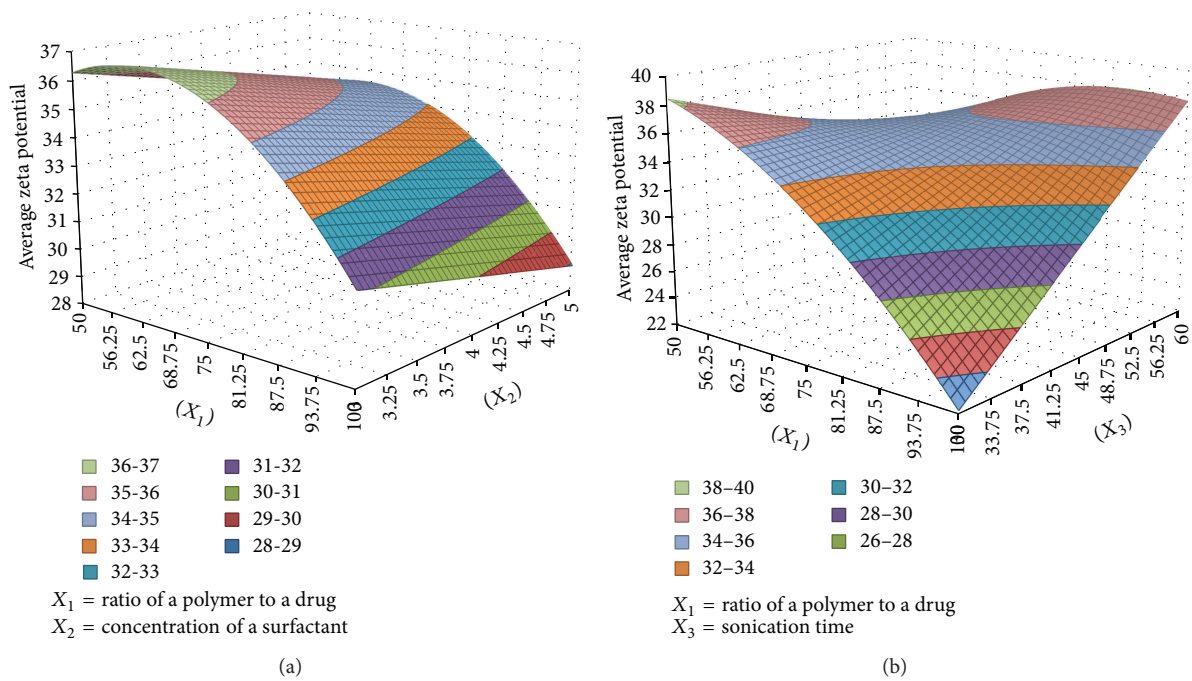


FIGURE 4: 3D response surface plots showing the effect of (a) ratio of a polymer to a drug (X_1) and concentration of a surfactant (X_2) at constant sonication time (X_3) and (b) ratio of a polymer to a drug (X_1) and sonication time (X_3) at constant concentration of a surfactant (X_2).

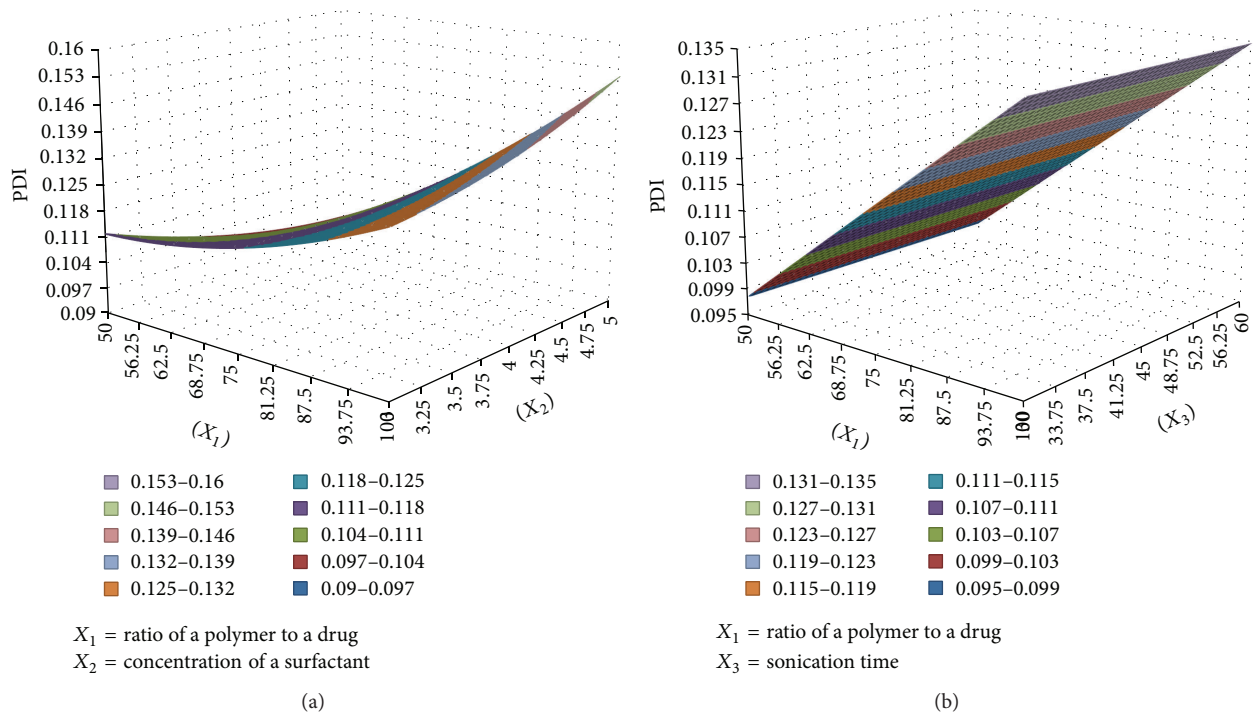


FIGURE 5: 3D response surface plots showing the effect of (a) ratio of a polymer to a drug (X_1) and concentration of a surfactant (X_2) at constant sonication time (X_3) and (b) ratio of a polymer to a drug (X_1) and sonication time (X_3) at constant concentration of a surfactant (X_2).

where X_1 , X_2 , and X_3 are ratio of a polymer to a drug, concentration of a surfactant, and sonication time, respectively, and X_1X_2 and X_1X_3 are interaction effects between ratio of a polymer to a drug and sonication time while X_1^2 is quadratic effect on EE.

The direction of the magnitude of significance as shown in (5) was negative for ratio of a polymer to a drug indicating an inverse relationship between ratio of a polymer to a drug and EE. This can further be seen from 3D surface plots in Figure 3. From Figure 3(a), a higher EE was attained with decrease in ratio of polymer to a drug and a maximum concentration of a surfactant at a constant sonication time. Similarly in Figure 3(b), a higher EE was obtained with a decrease in ratio of a polymer to a drug and a maximum sonication time at a constant concentration of a surfactant. This can be due to the fact that an increase in polymer concentration led to an enhancement of the concentration gradient between emulsion droplets and the continuous phase, as a result increasing the amount of drug partitioning into the continuous phase [38].

3.6. Effect of Independent Variables on Zeta Potential. Table 6 shows that zeta potential is significantly influenced by ratio of a polymer to a drug and sonication time. It was also found that the interaction between ratio of a polymer and sonication time and concentration of surfactant and sonication time significantly influence zeta potential. The coefficient of determination (0.8167) for the response was found to be close with adj. R^2 (0.7352), indicating that the model has predicted the response values well. The quadratic model of zeta potential is shown in

$$\begin{aligned} \text{Average zeta potential} \\ = 34.98 - 2.5333X_1 - 1.1167X_2 + 2.1667X_3 \\ + 5.55X_1X_3 + 6.45X_2X_3 - 2.4133X_1^2 \end{aligned} \quad (6)$$

where X_1 , X_2 , and X_3 represent ratio of a polymer to a drug, concentration of a surfactant, and sonication time, respectively, and X_1X_3 and X_2X_3 are interaction effects between ratio of a polymer to a drug and sonication time and concentration of a surfactant and sonication time while X_1^2 are quadratic effect.

3D surface plots corresponding to zeta potential are illustrated in Figure 4. From Figure 4(a), it was observed that decreasing the ratio of a polymer to a drug from 100 mg to 50 mg resulted in an increased zeta potential with an increased concentration of a surfactant. The results are similar to the results published by various researchers [22] that the zeta potential decreases at high level of ratio of a polymer to a drug. The reduction in zeta potential is attributed to the effect of the shift in the plane of shear away from the particle surface [39]. Figure 5(b) also shows that a decrease in ratio of a polymer resulted in an increased zeta potential with an increased sonication time.

3.7. Effect of Independent Variables on PDI. In case of PDI, ratio of polymer to a drug has shown statistically significant

TABLE 8: Predicted and observed values for the model.

Dependent variable	Predicted	Observed	Percentage prediction error
PS (Y_1)	240.3	233.5	-2.83
PDI (Y_2)	0.108	0.107	-0.93
EE (Y_3)	99	98	-1.01
Zeta potential (Y_4)	-34.6	-35.2	1.73

influence ($p < 0.05$) on PDI as shown in Table 7. All other tested factors and their interaction did not have an effect on PDI. The reduced model for PDI is presented in

$$\text{PDI} = 0.1163 + 0.0183X_1 + 0.0011X_2, \quad (7)$$

where X_1 and X_2 are ratio of a polymer to a drug and concentration of a surfactant, respectively. Figure 4 shows 3D response surface plots showing the change of PDI corresponding to the change of independent variables. As shown in Figure 4(a) increasing an amount of polymer resulted in an increase in PDI. The same profile was observed in Figure 3(b). The equation explaining the effect of independent factors on PDI is shown in (7) below.

3.8. Validation of the Model. The aim of the optimization was to obtain small particles size, small PDI, high EE, and high zeta potential. The optimal formulation was found to be 50 mg of polymer, 3% concentration of surfactant (SDS), and 45 minutes of sonication time. In order to confirm the predicted results, the predicted and experimental results were compared as shown in Table 8. The percentage prediction error was calculated which helps in the validation of generated regression by using (8). The percentage errors between measured and predicted values were found to be insignificant. A graphical representation of an optimized mean particle size is given in Figure 6:

$$\begin{aligned} \text{Percentage prediction error} \\ = \frac{\text{Observed} - \text{Predicted}}{\text{Predicted}} \times 100. \end{aligned} \quad (8)$$

3.9. FTIR and SEM Analysis of Optimized Nanoparticles. The FTIR spectra of tenofovir, Eudragit RS PO, and Eudragit RS PO-tenofovir nanoparticles are shown in Figure 7. FTIR spectra of pure tenofovir drug showed a weak intensity broad band at 3225 cm^{-1} corresponding to O-H of aromatic ring, a sharp peak at 1600 cm^{-1} which is due to phosphoric P=O group and N-H wagging bands at 660 and 900 cm^{-1} [40]. Eudragit spectra showed peaks at 1260, 1736, and 1340 cm^{-1} which are due to C-O, C=O, and C-N, respectively. A stronger, wide peak was observed in the final nanoparticles without major shift in the structure of Eudragit. This could be attributed to an ionic electrostatic interaction between the drug and the polymer during formation of nanoparticles. Additionally, there was compatibility between drug and the polymer, meaning that, during the process of formulation,

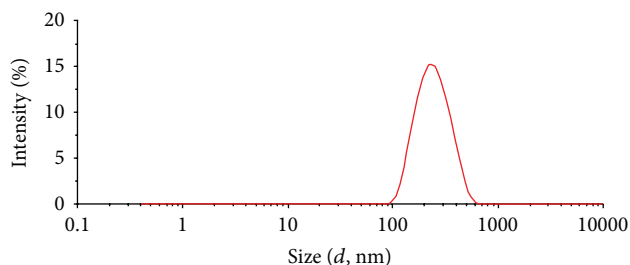


FIGURE 6: Mean particle size of optimized nanoparticles.

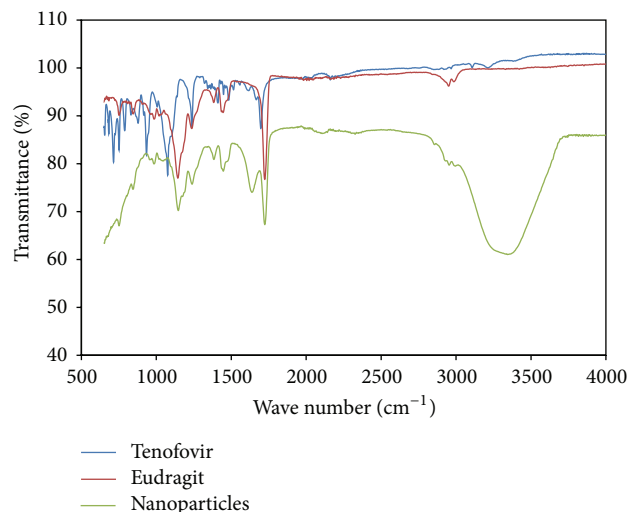


FIGURE 7: FTIR spectra of tenofovir, Eudragit RS PO, and Eudragit RS PO-tenofovir nanoparticles.

polymer has not reacted with the drug to give rise to reactant products; it is only physical mixture. A spherical morphology of the prepared nanoparticles was observed in the SEM images (Figure 8).

3.10. In Vitro Drug Release Studies. The *in vitro* drug release studies were carried out in dissolution media pH (7.4 and 1.5) within a period of one week. The release profiles for both pH 7.4 and 1.5 are displayed in Figure 9. An identical release profiles were observed in both dissolution media, which is due to the fact that Eudragit RS PO is pH independent; the release of drug is dependent on the diffusion of the drug from the matrix of the polymer. After 80 hours about 90% of the drug was able to be released in both media. However, the release of a drug in acidic media pH 1.5 was slightly higher than that of the alkaline media; this is attributed to the fact that Eudragit RS PO contains quaternary ammonium groups and solubilisation of these quaternary ammonium groups in acidic pH leads to formation of pores in the matrix, thereby releasing more drug in the acidic pH [41]. Long term release of the drug may be due to the charge interactions between the cationic polymer and anionic drug resulting in a gradual drug release. These results demonstrated that the nanoparticles were able to sustain the release of tenofovir

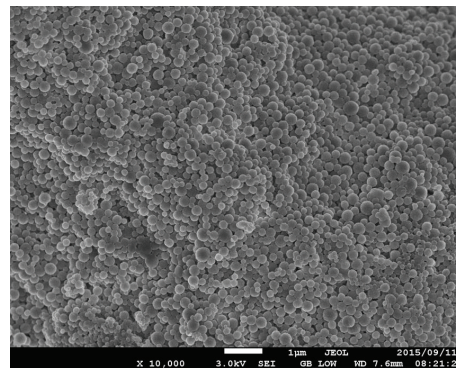


FIGURE 8: Scanning electron microscope image of Eudragit RS PO-tenofovir nanoparticles.

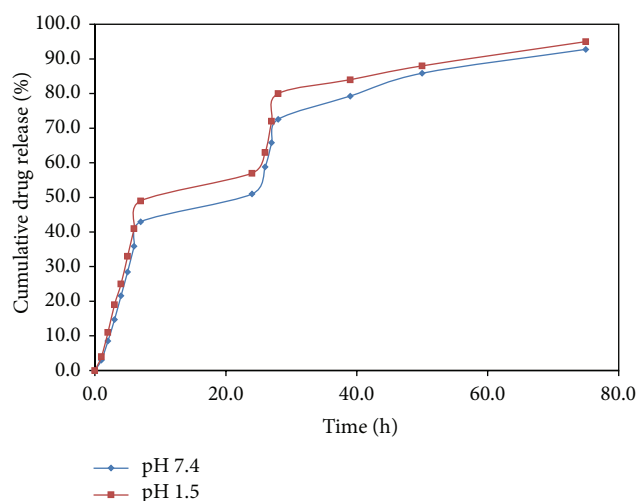


FIGURE 9: The release curves of tenofovir from nanoparticles in various pH (7.4 and 1.5).

by showing slow absorption rate and therefore were more suitable for controlling the release of the drug.

4. Conclusion

The encapsulation of tenofovir in Eudragit RS PO nanoparticles was successful with the aid of an optimal design based on BDD. The characteristics of the designed nanoparticles are attractive for pharmaceutical use as they showed high EE, physical stability, narrow size distribution, and prolonged drug release.

Conflict of Interests

The authors declare that there is no conflict of interests regarding the publication of this paper.

References

- [1] J. Meng, T. F. Sturgis, and B.-B. C. Youan, "Engineering tenofovir loaded chitosan nanoparticles to maximize microbicide

- mucoadhesion," *European Journal of Pharmaceutical Sciences*, vol. 44, no. 1-2, pp. 57–67, 2011.
- [2] S. Tokar, "Tenofovir, leading HIV medication, linked with risk of kidney damage," February 2012, <https://www.ucsf.edu/news/2012/02/11508/tenofovir-leading-hiv-medication-linked-risk-kidney-damage>.
 - [3] T. M. Viread, *Tenofovir Disoproxile Fumarate*, Gilead Sciences, Foster City, Calif, USA, 2009.
 - [4] A. Pozniak, "Tenofovir: what have over 1 million years of patient experience taught us?" *International Journal of Clinical Practice*, vol. 62, no. 8, pp. 1285–1293, 2008.
 - [5] L. Tshweu, L. Katata, L. Kalombo, and H. Swai, "Nanoencapsulation of water-soluble drug, lamivudine, using a double emulsion spray-drying technique for improving HIV treatment," *Journal of Nanoparticle Research*, vol. 15, article 2040, 2013.
 - [6] L. Katata, L. Tshweu, S. Naidoo, L. Kalombo, and H. Swai, "Design and formulation of nano-sized spray dried efavirenz-part I: influence of formulation parameters," *Journal of Nanoparticle Research*, vol. 14, no. 11, article 1247, 2012.
 - [7] S. Mitragotri, P. A. Burke, and R. Langer, "Overcoming the challenges in administering biopharmaceuticals: formulation and delivery strategies," *Nature Reviews Drug Discovery*, vol. 13, no. 9, pp. 655–672, 2014.
 - [8] H. M. Ibrahim, H. R. Ismail, and A. E. A. Lila, "Formulation and optimization of ocular poly-D, L-lactic acid nano drug delivery system of amphotericin-B using box behnken design," *International Journal of Pharmacy and Pharmaceutical Sciences*, vol. 4, no. 2, pp. 342–349, 2012.
 - [9] M. H. Abdallah, O. A. Sammour, H. A. El-Ghamry, H. M. El-Nahas, and W. Barakat, "Development and characterization of controlled release ketoprofen microspheres," *Journal of Applied Pharmaceutical Science*, vol. 2, no. 3, pp. 60–67, 2012.
 - [10] R. Kola and B. P. Kumar, "A detailed description of synthetic and natural polymers which are used in the formulation of sustained release drug delivery system: a review," *Journal of Chemical and Pharmaceutical Sciences*, vol. 6, no. 3, pp. 161–169, 2013.
 - [11] K. Animesh, M. Afrasim, R. R. Bommareddy, A. Ayaz, R. Shruthi, and H. G. Shivakumar, "Applicability and approaches of (Meth) acrylate copolymers (Eudragits) in novel drug delivery systems," *Current Drug Therapy*, vol. 7, no. 4, pp. 219–234, 2012.
 - [12] F. Hoobakht, F. Ganji, E. Vasheghani-Farahani, and S. M. Mousavi, "Eudragit RS PO nanoparticles for sustained release of pyridostigmine bromide," *Journal of Nanoparticle Research*, vol. 15, article 1912, 2013.
 - [13] T. Zhang, C. Zhang, V. Agrahari, J. B. Murowchick, N. A. Oyler, and B.-B. C. Youan, "Spray drying tenofovir loaded mucoadhesive and pH-sensitive microspheres intended for HIV prevention," *Antiviral Research*, vol. 97, no. 3, pp. 334–346, 2013.
 - [14] S. Arora, S. Gupta, R. K. Narang, and R. D. Budhiraja, "Amoxicillin loaded chitosan-alginate polyelectrolyte complex nanoparticles as mucopenetrating delivery system for *H. pylori*," *Scientia Pharmaceutica*, vol. 79, no. 3, pp. 673–694, 2011.
 - [15] D. C. Montgomery, *Design and Analysis of Experiments*, Wiley-Interscience, Montréal, Canada, 5th edition, 2001.
 - [16] G. E. P. Box and J. S. Hunter, *Statistics for Experimenters*, John Wiley & Sons, New York, NY, USA, 1978.
 - [17] S. Schubert, J. T. Delaney Jr., and U. S. Schubert, "Nanoprecipitation and nanof ormulation of polymers: from history to powerful possibilities beyond poly(lactic acid)," *Soft Matter*, vol. 7, no. 5, pp. 1581–1588, 2011.
 - [18] C. E. Mora-Huertas, H. Fessi, and A. Elaissari, "Polymer-based nanocapsules for drug delivery," *International Journal of Pharmaceutics*, vol. 385, no. 1-2, pp. 113–142, 2010.
 - [19] A. Divya, P. Kumar, K. Gnanaprakash, and M. Gobinath, "Design, formulation and characterization of tenofovir microemulsion as oral drug delivery," *International Journal of Pharmacy Review & Research*, vol. 4, pp. 1–5, 2014.
 - [20] L. Jenita, J. Josephine, C. Vijaya, B. Wilson, B. K. Savitha, and R. Suma, "Design and characterization of bovine serum albumin nanocarriers for tenofovir by modified desolvation method," *Journal of Pharmacy Research*, vol. 5, no. 9, pp. 4663–4667, 2012.
 - [21] U. Bilati, E. Allémann, and E. Doelker, "Nanoprecipitation versus emulsion-based techniques for the encapsulation of proteins into biodegradable nanoparticles and process-related stability issues," *AAPS PharmSciTech*, vol. 6, no. 4, pp. E594–E604, 2005.
 - [22] L. Julianna and R. T. Eniko, "Nanomedicine applications towards the cure of HIV," *Nanomedicine: Nanotechnology, Biology, and Medicine*, vol. 9, no. 1, pp. 28–38, 2013.
 - [23] D. Alukda, T. Sturgis, and B.-B. C. Youan, "Formulation of tenofovir-loaded functionalized solid lipid nanoparticles intended for HIV prevention," *Journal of Pharmaceutical Sciences*, vol. 100, no. 8, pp. 3345–3356, 2011.
 - [24] S. H. Syed, S. U. Premnath, and K. Muddu, "Development and validation of stability indicating RP-HPLC method for tenofovir nanoparticle formulation," *International Journal of Pharmacy and Pharmaceutical Sciences*, vol. 5, no. 2, pp. 245–248, 2013.
 - [25] A. S. Zidan, C. Spinks, J. Fortunak, M. Habib, and M. A. Khan, "Near-infrared investigations of novel anti-HIV tenofovir liposomes," *The AAPS Journal*, vol. 12, no. 2, pp. 202–214, 2010.
 - [26] P. Sharma and S. Garg, "Pure drug and polymer based nanotechnologies for the improved solubility, stability, bioavailability and targeting of anti-HIV drugs," *Advanced Drug Delivery Reviews*, vol. 62, no. 4-5, pp. 491–502, 2010.
 - [27] T. Zhang, T. F. Sturgis, and B.-B. C. Youan, "pH-responsive nanoparticles releasing tenofovir intended for the prevention of HIV transmission," *European Journal of Pharmaceutics and Biopharmaceutics*, vol. 79, no. 3, pp. 526–536, 2011.
 - [28] T. J. Johnson, K. M. Gupta, J. Fabian, T. H. Albright, and P. F. Kiser, "Segmented polyurethane intravaginal rings for the sustained combined delivery of antiretroviral agents dapivirine and tenofovir," *European Journal of Pharmaceutical Sciences*, vol. 39, no. 4, pp. 203–212, 2010.
 - [29] D. S. Singare, S. Marella, K. Gowthamrajan, G. T. Kulkarni, R. Vooturi, and P. S. Rao, "Optimization of formulation and process variable of nanosuspension: an industrial perspective," *International Journal of Pharmaceutics*, vol. 402, no. 1-2, pp. 213–220, 2010.
 - [30] S. H. Shah, M. J. Shan, and J. R. Sharma, "An overview on brain targeting drug delivery system," *Pharmaceutical Reviews*, vol. 7, no. 1, 2009.
 - [31] M. Chidambaram and K. Krishnasamy, "Modifications to the conventional nanoprecipitation technique: an approach to fabricate narrow sized polymeric nanoparticles," *Advanced Pharmaceutical Bulletin*, vol. 4, no. 2, pp. 205–208, 2014.
 - [32] Q. Y. Tan, N. Wang, H. Yang et al., "Characterization, stabilization and activity of uricase loaded in lipid vesicles," *International Journal of Pharmaceutics*, vol. 384, no. 1-2, pp. 165–172, 2010.
 - [33] M. Alauddin, M. A. Mazid, M. A. El Baradi, and M. S. J. Hashmi, "Cutting forces in the end milling of Inconel 718," *Journal of*

- Materials Processing Technology*, vol. 300, no. 3-4, pp. 153–159, 1998.
- [34] M. Manohar, J. Jomy, T. Selvaraj, and D. Sivakumar, “Application of Box Behnken design to optimize the parameters for turning Inconel 718 using coated carbide tools,” *International Journal of Scientific and Engineering Research*, vol. 4, no. 4, pp. 2229–5518, 2013.
- [35] W.-L. Guo, Y.-B. Zhang, J.-H. Lu et al., “Optimization of fermentation medium for nisin production from *Lactococcus lactis* subsp. *lactis* using response surface methodology (RSM) combined with artificial neural network-genetic algorithm (ANN-GA),” *African Journal of Biotechnology*, vol. 9, no. 38, pp. 6264–6272, 2010.
- [36] R. Gannu, V. V. Yamsani, S. K. Yamsani, C. R. Palem, and M. R. Yamsani, “Optimization of hydrogels for transdermal delivery of lisinopril by box-behnken statistical design,” *AAPS PharmSciTech*, vol. 10, no. 2, pp. 505–514, 2009.
- [37] R. Ragonese, M. Macka, J. Hughes, and P. Petocz, “The use of the Box-Behnken experimental design in the optimisation and robustness testing of a capillary electrophoresis method for the analysis of ethambutol hydrochloride in a pharmaceutical formulation,” *Journal of Pharmaceutical and Biomedical Analysis*, vol. 27, no. 6, pp. 995–1007, 2002.
- [38] J. P. Maran, S. Manikandan, B. Priya, and P. Gurumoorthi, “Box-Behnken design based multi-response analysis and optimization of supercritical carbon dioxide extraction of bioactive flavonoid compounds from tea (*Camellia sinensis* L.) leaves,” *Journal of Food Science and Technology*, vol. 52, no. 1, pp. 92–104, 2015.
- [39] M. A. Tekindal, H. Bayrak, B. Ozkaya, and Y. Genc, “Box-behnken experimental design in factorial experiments: the importance of bread for nutrition and health running head,” *Turkish Journal of Field Crops*, vol. 17, no. 2, pp. 115–123, 2012.
- [40] M. S. Gambhire, M. R. Bhalekar, and V. M. Gambhire, “Simvastatin loaded Solid lipid nanoparticles: formulation optimization using Box Behnken design, characterization and in vitro evaluation,” *Current Pharma Research*, vol. 1, pp. 157–164, 2011.
- [41] N. T. Anh, N. T. Chi, T. K. Tran et al., “Preparation and characterization of ketoprofen loaded eudragit RS polymeric nanoparticles for controlled release,” *Advances in Natural Sciences: Nanoscience and Nanotechnology*, vol. 3, no. 4, Article ID 045015, 2012.

Research Article

Preparation of $\text{Cu}_2\text{Sn}_3\text{S}_7$ Thin-Film Using a Three-Step Bake-Sulfurization-Sintering Process and Film Characterization

Tai-Hsiang Lui,¹ Fei-Yi Hung,¹ Truan-Sheng Lui,¹ and Kuan-Jen Chen²

¹Department of Materials Science and Engineering, National Cheng Kung University, Tainan 701, Taiwan

²The Instrument Center, National Cheng Kung University, Tainan 701, Taiwan

Correspondence should be addressed to Fei-Yi Hung; fyhung@mail.ncku.edu.tw

Received 2 March 2015; Accepted 14 June 2015

Academic Editor: Tapan Desai

Copyright © 2015 Tai-Hsiang Lui et al. This is an open access article distributed under the Creative Commons Attribution License, which permits unrestricted use, distribution, and reproduction in any medium, provided the original work is properly cited.

$\text{Cu}_2\text{Sn}_3\text{S}_7$ (CTS) can be used as the light absorbing layer for thin-film solar cells due to its good optical properties. In this research, the powder, baking, sulfur, and sintering (PBSS) process was used instead of vacuum sputtering or electrochemical preparation to form CTS. During sintering, Cu and Sn powders mixed in stoichiometric ratio were coated to form the thin-film precursor. It was sulfurized in a sulfur atmosphere to form CTS. The CTS film metallurgy mechanism was investigated. After sintering at 500°C, the thin film formed the $\text{Cu}_2\text{Sn}_3\text{S}_7$ phase and no impurity phase, improving its energy band gap. The interface of CTS film is continuous and the formation of intermetallic compound layer can increase the carrier concentration and mobility. Therefore, PBSS process prepared CTS can potentially be used as a solar cell absorption layer.

1. Introduction

For thin-film solar cells, copper indium gallium selenide (CIGS) materials are expensive, and thus copper zinc tin sulfide (CZTS) materials have been developed [1, 2]. Studies [3, 4] have shown that it is difficult to control the Cu, Zn, Sn, and S atomic ratio of the four-element CZTS system. For upper ZnS junction solar modules, interactions during the crystallization process cause Zn atoms to easily diffuse into the CZTS system (insufficient or excess Zn). The present study uses the Cu, Sn, and S (CTS) ternary system, mainly formed by colloidal baking and powder sintering, as a light absorbing layer material [5, 6].

Studies have reported that CuS and SnS_2 coevaporation [7, 8] and sputtering [9] can be used to form CTS ternary films whose energy band gap is close to the ideal energy band gap of $\text{Cu}_2\text{Sn}_3\text{S}_7$ (1.2~1.3 eV). However, this process is easy to produce much secondary degradation like $\text{Cu}_{10}\text{Sn}_2\text{S}_{13}$ and Cu_4SnS_4 of nature, reducing the energy conversion efficiency. This study coated Cu and Sn powders at a set atomic percentage mix on a Mo substrate with spin-coater and formed powder film. Baking, sulfurizing (sulfur vapor), and liquid-phase sintering were then applied to form

the Cu-Sn-S compound and a crystalline thin film. The powder, baking, sulfur, and sintering (PBSS) process can reduce the solar film process (sputtering and deposition) costs [10] and avoid the reliability problems of chemical solutions such as forming oxide phase and atomic ratio control problem [11].

Comparing with other literatures processes [12, 13], PBSS process has potential applications due to its easy fabrication, lower cost, and easy-controlling atomic ratio procedure. In addition, no previous studies have been conducted on CTS/Mo metallurgy and the interfacial diffusion mechanism. This research determines the CTS crystalline phase and optical and electrical properties. The PBSS process was adopted according to temperature effects. The interface diffusion behavior of atoms between absorption layer and Mo substrate was explored to understand relationship between structure and optoelectric properties. The results may be used as a reference for solar cell manufacturing.

2. Experimental Procedure

Cu (~500 nm) and Sn (~1000 nm) powders were mixed in a 2 : 3 molar ratio in colloid and deposited onto Mo substrates with spin coater (3000 rpm). Cu-Sn prefilms were obtained

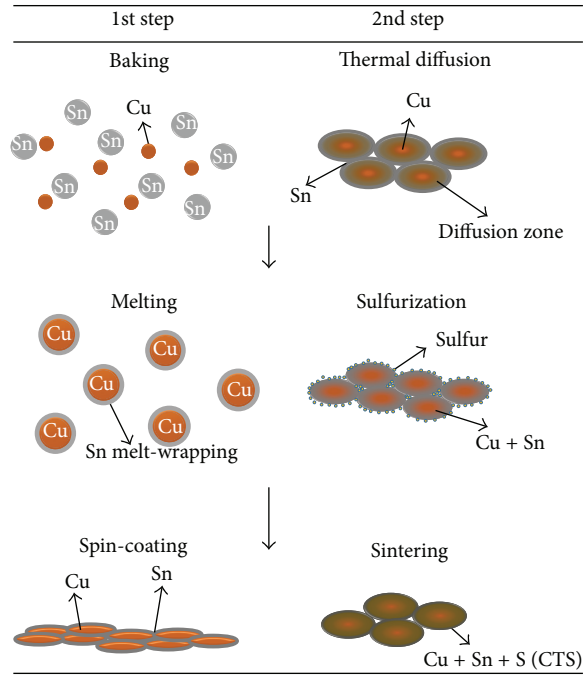


FIGURE 1: Schematic procedure of CTS film.

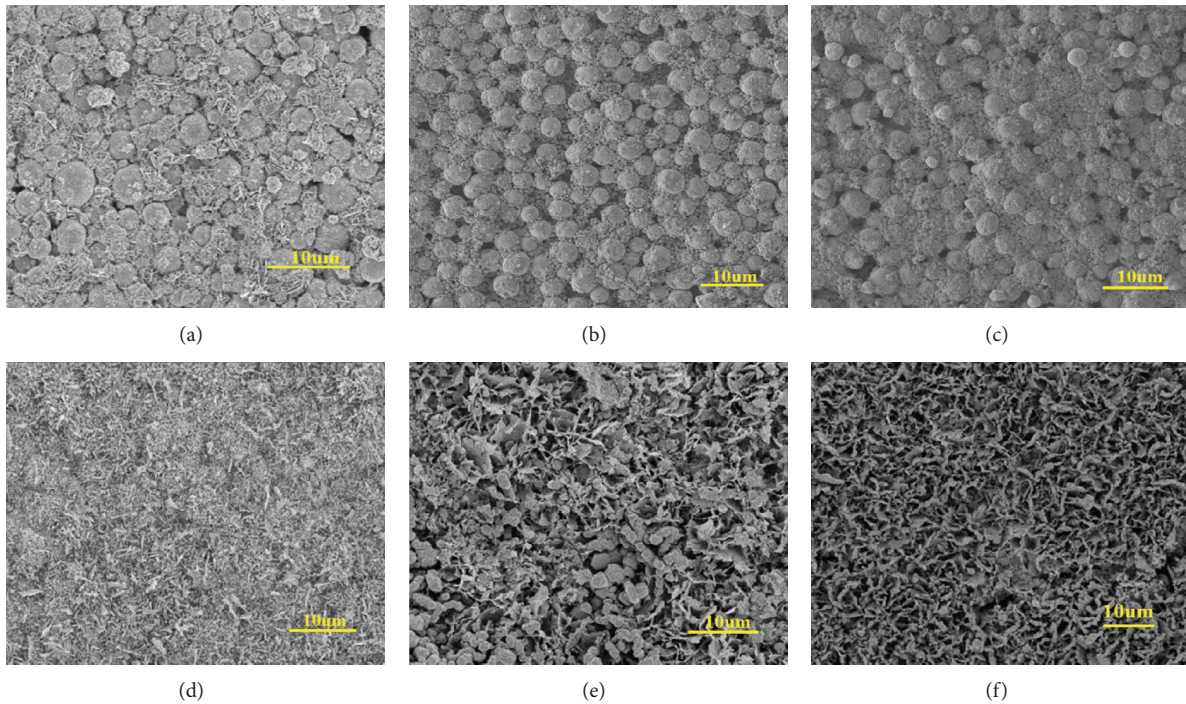


FIGURE 2: Morphology of CTS films sintered at (a) 200, (b) 300, (c) 400, (d) 500, (e) 600, and (f) 700°C.

by vacuum baking (200°C, 10^{-2} Torr, 8 h). Subsequently, the films were subjected to sulfur vapor in an oven (240°C, 1 h) and followed by different sintering temperatures at 300, 400, 500, 600, and 700°C (4 h for each) to form CTS film in vacuum process. All the procedure is schematically shown in Figure 1.

The specimens were observed using scanning electron microscopy (SEM, Hitachi SU8000), energy-dispersive X-ray spectroscopy (EDS), and atomic-scale surface topography. X-ray diffraction (XRD, Bruker AXS, Germany) was conducted at a scanning rate of $1^\circ/\text{min}$ in the 2θ range of 20° – 60° to determine phase composition. A photoluminescence-

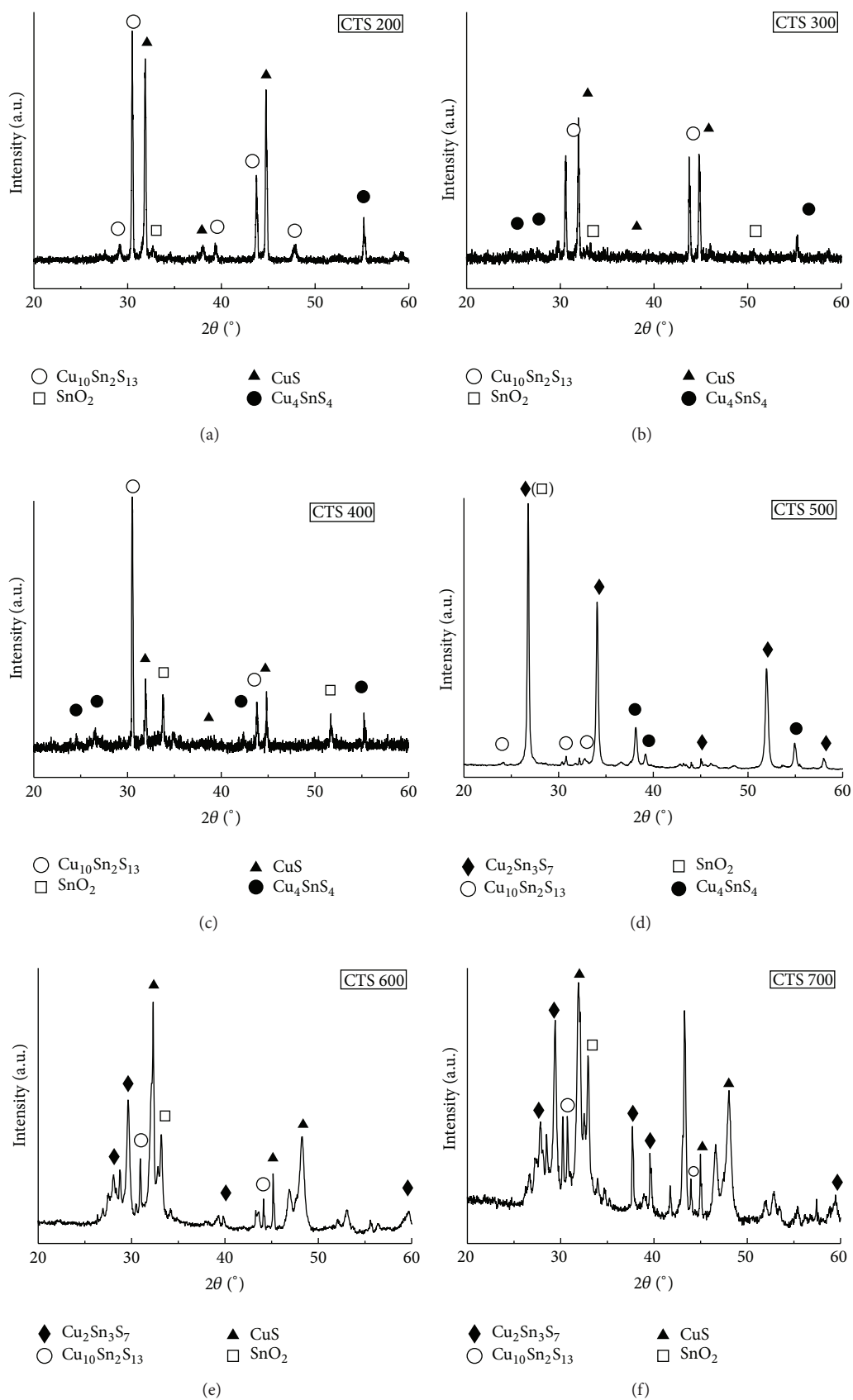


FIGURE 3: XRD patterns of CTS sintered at (a) 200, (b) 300, (c) 400, (d) 500, (e) 600, and (f) 700°C.

(PL-) ultraviolet (UV) spectrometer (ULVAC) was used to determine the sintering temperatures and the absorption layer specifications. Hall measurements were conducted for samples sintered at 200, 500, and 600°C to determine the resistance value and carrier mobility. The interfacial diffusion behavior study of samples sintered at 500°C was chosen because the sample had flattening surface and less second phases. It possessed the best morphology and phase composition. The sample sintered at 500°C was observed by transmission electron microscopy (TEM, JEM-2100F). The interface structure characteristics caused by atoms diffusion between absorption layer and Mo substrate are discussed by the atomic and structure change between CTS and Mo.

3. Results and Discussion

In the PBSS process (vulcanization condition), for sintering temperatures of 200°C to 400°C, the specimen surface was coarse and Sn particles had not completely melted. The particle size was approximately 3~5 μm (Figure 2). When the sintering temperature was increased to 500°C, melting and solidification film were evenly distributed on the substrate surface. When the temperature was 600°C or 700°C, the surface of the sample had sheet-like deposition on CTS film surface which was regarded as CuS precipitates. The XRD patterns (Figure 3) for samples sintered at between 200°C and 400°C show that CuS and $\text{Cu}_{10}\text{Sn}_2\text{S}_{13}$ formed, without the $\text{Cu}_2\text{Sn}_3\text{S}_7$ phase. At 500°C, $\text{Cu}_2\text{Sn}_3\text{S}_7$ began to become the main phase. At 600°C or 700°C, most of the CuS transformed into a liquid phase that coagulated and precipitated on the surface. The XRD patterns show multiple CuS diffraction peaks. The phases of specimens sintered at various temperatures identified from XRD patterns are shown in Table 1. The films are divided into three broad categories: (I), (II), and (III), corresponding to the experiment in the choice of 200, 500, and 600°C specimens. The chosen specimen with best optical properties is regarded as ideal sintering condition for CTS. And it will be taken in interface characteristics discussion.

In the analysis of spectral absorption and excitation properties of Cn-Sn-S materials, the conversion results of UV spectrometer measurements are shown in Figure 4. The specimens sintered at 200, 500, and 600°C have energy band gaps of about 3.77, 1.25, and 2.08 eV, respectively. The energy band gap of the specimen sintered at 500°C is close to the ideal range of a solar absorption layer (1.3–1.5 eV). To determine the absorption of various wavelengths of light, PL measurements (Figure 5) were taken. The PL spectra show three absorption peaks. The specimens sintered at 200, 500, and 600°C have absorption peaks at a short wavelength (607.1 nm) near a clear continuous peak region, a long wavelength (859.0 nm) near the infrared region, and short wavelengths (577.1 and 611.5 nm) and a long wavelength (871.7 nm), respectively. From the phase composition (Table 1), the $\text{Cu}_{10}\text{Sn}_2\text{S}_{13}$ and CuS phases contributed to the short wavelength absorption waves. The long wavelength absorption is contributed by $\text{Cu}_2\text{Sn}_3\text{S}_7$. Overall, the UV and

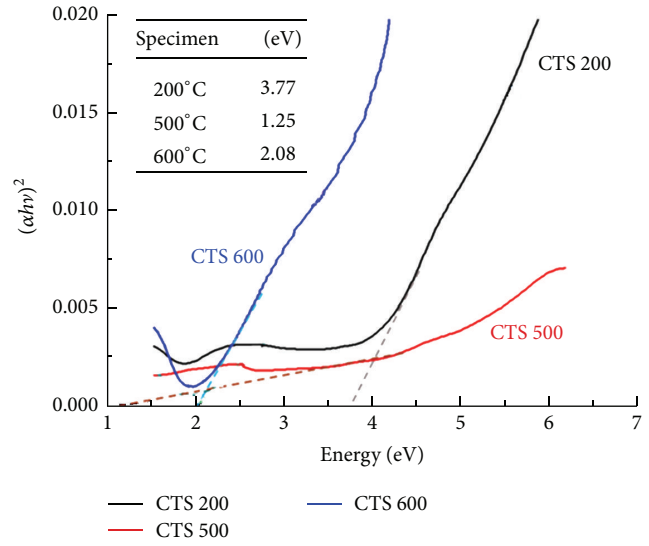


FIGURE 4: CTS band gap of 200, 500, and 600°C sintering temperatures.

TABLE 1: Phase composition of samples sintered at various temperatures.

	(I)		(II)		(III)	
	200°C	300°C	400°C	500°C	600°C	700°C
$\text{Cu}_2\text{Sn}_3\text{S}_7$				○	○	○
SnO_2	○	○	○	○	○	○
CuS	○	○	○		○	○
Cu_4SnS_4	○	○	○	○		
$\text{Cu}_{10}\text{Sn}_2\text{S}_{13}$	○	○	○	○	○	○

PL spectra show similar trends, confirming that the specimen sintered at 500°C possesses an ideal band gap.

In addition to the light absorption characteristics, the characteristics of the absorption layer and substrate interface affect the material conversion efficiency. Figure 6 shows TEM image and selected area electron diffraction (SAED) pattern of the specimen sintered at 500°C. The structure change of the intermetallic compound (IMC) layer was showing at the interface that the SAED pattern changed from (b) and (c) Mo-rich IMC to (d) and (e) CTS layer and from (d) and (e) CTS layer to (f) and (g) Mo layer. At the IMC interface, there is a face centered cubic (FCC) structure (thickness: about 38 nm), the upper CTS is orthorhombic, and the lower Mo substrate has a body centered cubic (BCC) structure. Therefore, we got the whole structure of “CTS/IMC (38 nm)/Mo” by PBSS processes.

Hall measurement values of samples are shown in Table 2. The average thickness of the CTS films was approximately 50 μm . Each specimen was measured by four probes on sample surface corners. The formula $[\rho = R_s \times T = [C.F. \times (V/I)] \times T]$ was used to calculate bulk resistivity, where ρ is resistivity ($\mu \omega\text{-cm}$); R_s is sheet resistance (ω); T is thickness (cm); C.F. is correction factor (=4.532); V is voltage; I is current.

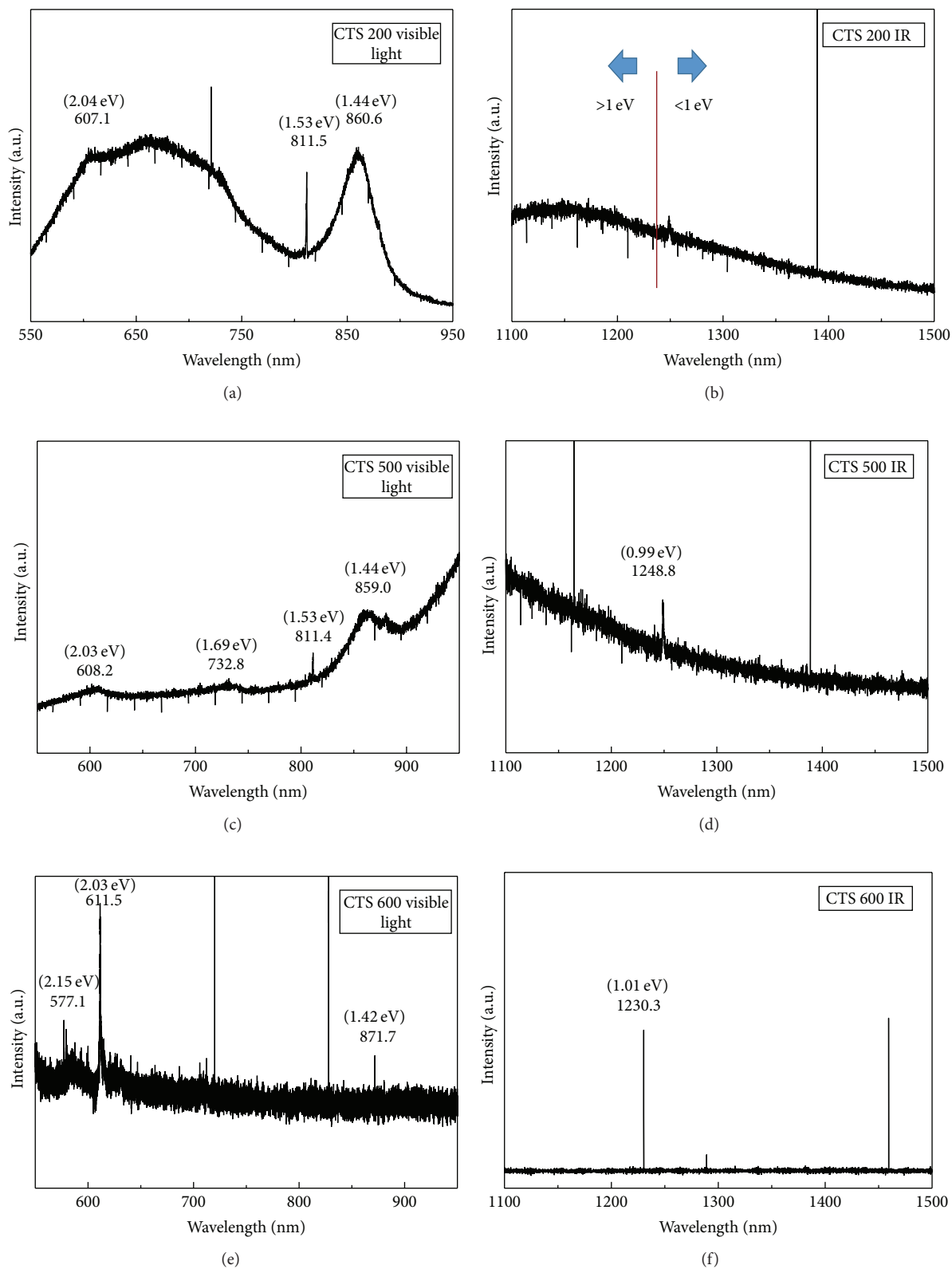


FIGURE 5: PL characteristics of specimens. (a) 200°C and visible light, (b) 200°C and infrared, (c) 500°C and visible light, (d) 500°C and infrared, (e) 600°C and visible light, and (f) 600°C and infrared.

TABLE 2: Hall 4-point measurements of CTS after sintering at various temperatures.

CTS	200°C	500°C	600°C
Bulk resistivity (Ohm·cm)	3.3899×10^{-2}	1.6038×10^{-1}	1.8678
Sheet resistivity (Ohm·Sq.)	3.3899	1.6038×10	1.8678×10^2
Bulk carrier concentration (cm^{-3})	2.6494×10^{20}	2.1088×10^{17}	9.7608×10^{15}
Sheet carrier concentration (cm^{-2})	2.6494×10^{18}	2.1088×10^{15}	9.7608×10^{13}
Mobility (cm^2/Vs)	6.9590×10^{-1}	1.8479×10^2	3.4282×10^2
Conductivity	P-type	P-type	P-type

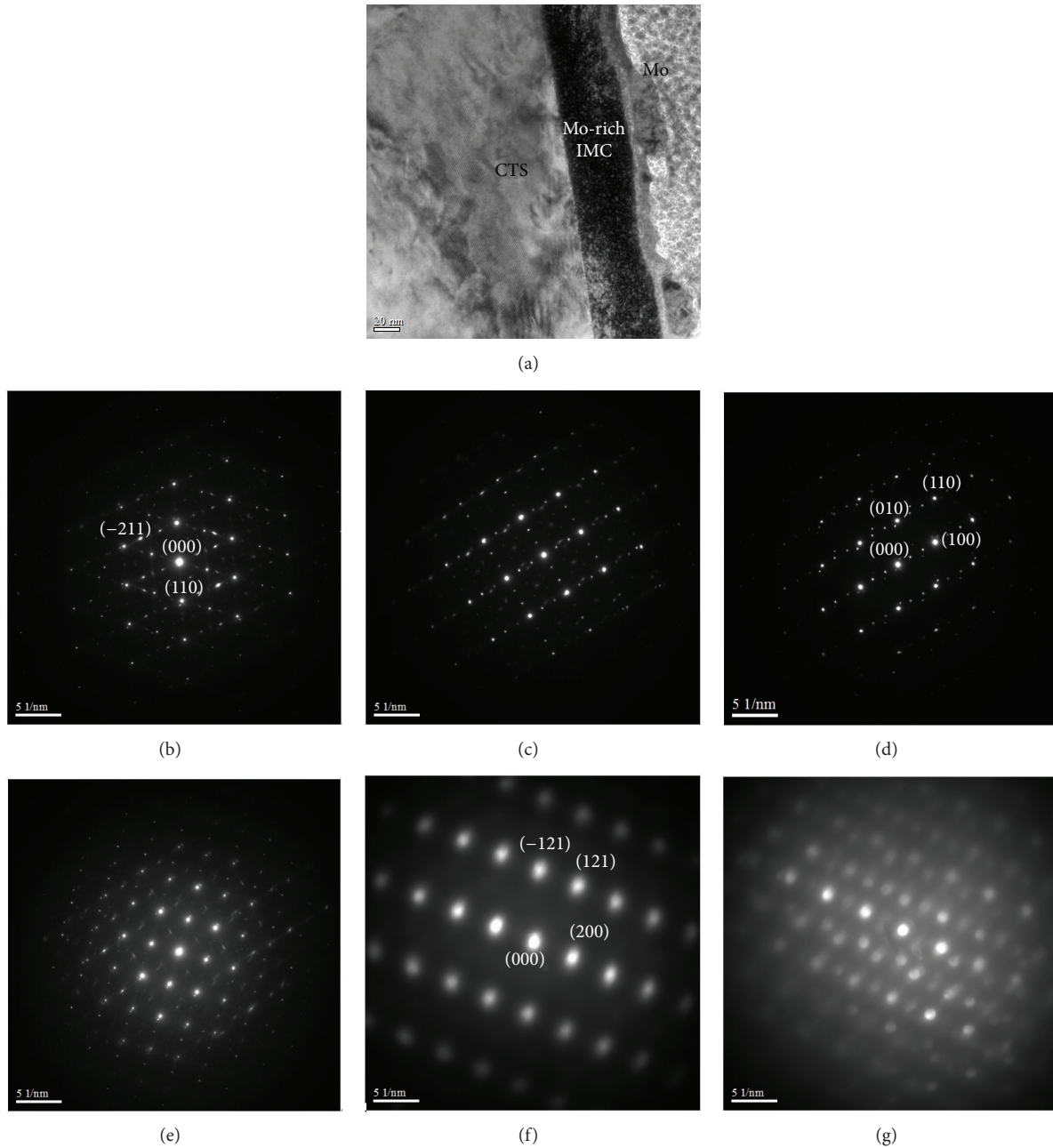


FIGURE 6: TEM morphology and SAED patterns of CTS sintered at 500°C. (a) Morphology of CTS-Mo interface and SAED patterns, (b) and (c) Mo-rich IMC, (d) and (e) CTS layer, and (f) and (g) Mo layer.

The sample sintered at 200°C has the lowest carrier mobility. With increasing sintering temperature, the carrier mobility significantly increases. The ideal migration rate is $10^1 \sim 10^2 \text{ cm}^2/\text{Vs}$ [14]. The specimen sintered at 600°C has a lower carrier concentration than that of the specimen sintered at 500°C and the highest resistance value mainly due to the formation of CuS. Therefore, CuS not only affected light absorption, but also affected carrier concentration and resistance. It could be presumed that the specimen sintered at 500°C melted evenly and contained more $\text{Cu}_2\text{Sn}_3\text{S}_7$ phase than the other sintering conditions. Also, the CTS/IMC (38 nm)/Mo structure improves carrier mobility which can be found that 500°C and 600°C specimens were both better than 200°C specimen.

4. Conclusion

CTS material was obtained by the PBSS process. For a given sulfurizing condition, sintering at 500°C led to surface melting and formation of $\text{Cu}_2\text{Sn}_3\text{S}_7$ possesses positive benefits in spectral absorption and electrical properties. When temperatures are too high, forming sheet specimen surface structure (CuS) deteriorates characteristics. Thus, an appropriate sintering temperature is needed for absorption layer preparation. From the study, the 500°C temperature possessed the best morphology and optoelectric properties which is ideal for further research.

The PBSS process is continuous formation at the absorption layer and substrate interface. The cross-section structure is CTS/IMC/Mo. The crystal structure of the IMC layer is rich-Mo and has a face centered cubic arrangement (nonvoid doped). This interface mechanism is dominated by Cu and Sn thermal diffusion and leads to improvements in optoelectric properties.

Conflict of Interests

The authors declare that there is no conflict of interests regarding the publication of this paper.

Acknowledgments

The authors are grateful to The Instrument Center of National Cheng Kung University and the National Science Council, Taiwan, for financial support under Grants nos. 102-2221-E-006-061 and 103-2221-E-006-066.

References

- [1] S. Abermann, "Non-vacuum processed next generation thin film photovoltaics: towards marketable efficiency and production of CZTS based solar cells," *Solar Energy*, vol. 94, pp. 37–70, 2013.
- [2] N. M. Shinde, C. D. Lokhande, J. H. Kim, and J. H. Moon, "Low cost and large area novel chemical synthesis of $\text{Cu}_2\text{ZnSnS}_4$ (CZTS) thin films," *Journal of Photochemistry and Photobiology A: Chemistry*, vol. 235, pp. 14–20, 2012.
- [3] T. P. Dhakal, C.-Y. Peng, R. R. Tobias, R. Dasharathy, and C. R. Westgate, "Characterization of a CZTS thin film solar cell grown by sputtering method," *Solar Energy*, vol. 100, pp. 23–30, 2014.
- [4] C. Malerba, F. Biccari, C. L. A. Ricardo et al., "CZTS stoichiometry effects on the band gap energy," *Journal of Alloys and Compounds*, vol. 582, pp. 528–534, 2014.
- [5] M. Monsefi and D.-H. Kuo, "Influence of Cu content on the $n \rightarrow p$ transition of 15% Sn-doped $\text{Cu}_x(\text{In,Ga})\text{Se}_2$ bulk materials," *Journal of Alloys and Compounds*, vol. 580, pp. 348–353, 2013.
- [6] S. Fiechter, M. Martinez, G. Schmidt, W. Henrion, and Y. Tomm, "Phase relations and optical properties of semiconducting ternary sulfides in the system Cu-Sn-S," *Journal of Physics and Chemistry of Solids*, vol. 64, no. 9-10, pp. 1859–1862, 2003.
- [7] V. P. G. Vani, M. V. Reddy, and K. T. R. Reddy, "Thickness-dependent physical properties of coevaporated Cu_4SnS_4 films," *ISRN Condensed Matter Physics*, vol. 2013, Article ID 142029, 6 pages, 2013.
- [8] T. Tanaka, A. Yoshida, D. Saiki et al., "Influence of composition ratio on properties of $\text{Cu}_2\text{ZnSnS}_4$ thin films fabricated by co-evaporation," *Thin Solid Films*, vol. 518, no. 21, pp. S29–S33, 2010.
- [9] T. Ericson, J. J. Scragg, T. Kubart, T. Törndahl, and C. Platzer-Björkman, "Annealing behavior of reactively sputtered precursor films for $\text{Cu}_2\text{ZnSnS}_4$ solar cells," *Thin Solid Films*, vol. 535, no. 1, pp. 22–26, 2013.
- [10] A. I. Inamdar, S. Lee, K.-Y. Jeon et al., "Optimized fabrication of sputter deposited $\text{Cu}_2\text{ZnSnS}_4$ (CZTS) thin films," *Solar Energy*, vol. 91, pp. 196–203, 2013.
- [11] N. M. Shinde, P. R. Deshmukh, S. V. Patil, and C. D. Lokhande, "Aqueous chemical growth of $\text{Cu}_2\text{ZnSnS}_4$ (CZTS) thin films: air annealing and photoelectrochemical properties," *Materials Research Bulletin*, vol. 48, no. 5, pp. 1760–1766, 2013.
- [12] S. M. Pawar, A. I. Inamdar, B. S. Pawar et al., "Synthesis of $\text{Cu}_2\text{ZnSnS}_4$ (CZTS) absorber by rapid thermal processing (RTP) sulfurization of stacked metallic precursor films for solar cell applications," *Materials Letters*, vol. 118, pp. 76–79, 2014.
- [13] A. V. Moholkar, S. S. Shinde, G. L. Agawane et al., "Studies of compositional dependent CZTS thin film solar cells by pulsed laser deposition technique: an attempt to improve the efficiency," *Journal of Alloys and Compounds*, vol. 544, pp. 145–151, 2012.
- [14] O. J. Weiß, R. K. Krause, and A. Hunzea, "Hole mobility of 1-NaphDATA," *Journal of Applied Physics*, vol. 103, no. 4, Article ID 043709, 6 pages, 2008.

Research Article

Comparative Aquatic Toxicity of Gold Nanoparticles and Ionic Gold Using a Species Sensitivity Distribution Approach

Tarryn L. Botha,¹ Tanyn E. James,¹ and Victor Wepener²

¹Department of Zoology, University of Johannesburg, P.O. Box 534, Auckland Park 2006, South Africa

²Unit for Environmental Sciences and Management, Water Research Group (Ecotoxicology), North-West University, Private Bag X6001, Potchefstroom 2520, South Africa

Correspondence should be addressed to Tarryn L. Botha; tlbothanano@gmail.com

Received 22 May 2015; Accepted 23 June 2015

Academic Editor: Kangtaek Lee

Copyright © 2015 Tarryn L. Botha et al. This is an open access article distributed under the Creative Commons Attribution License, which permits unrestricted use, distribution, and reproduction in any medium, provided the original work is properly cited.

Gold nanoparticles (nAu) are used in drug delivery systems allowing for targeted cellular distribution. The effects of increased use and release of nanoparticles into the environment are not well known. A species sensitivity distribution (SSD) allows for the ecotoxicological hazard assessment of a chemical based on single species toxicity tests. Aquatic toxicity needs to be related to particle characterization in order to understand the effects. The behaviour of nAu in the medium changed as the concentration increased. The toxic potential of ionic gold and nAu was expressed as a hazardous concentration where 5% of species will be harmed (HC5). The HC5 for nAu was much higher (42.78 mg/L) compared to the ionic gold (2.44 mg/L). The differences between the hazard potentials of nAu and ionic gold were attributed to the nAu not releasing any Au ions into solution during the exposures and following an aggregation theory response. Exposures to ionic gold on the other hand followed a clear dose dependent response based on the concentration of the ionic metal. Although SSDs present an indication of the relative hazard potential of nanoparticles, the true worth can only be achieved once other nanoparticle characteristics and their behavior in the environment are also considered.

1. Introduction

In recent years, gold nanoparticles (nAu) have been studied and developed within the biological and photothermal therapeutic contexts. The major clinical interest is within the application of novel drug delivery systems and targeted delivery into cells [1–4] as well as microelectromechanical systems [5] and diagnostic systems [6]. Exposure of nanoparticles can occur in different stages of the lifecycle of the product, from their synthesis, application (which can include ingestion or intravenously), and weathering to their waste disposal. Due to little research within this field there are currently no guidelines for their use; therefore, the previously mentioned exposure routes could build up in the environment [1, 7–10].

To manage environmental resources such as water quality, laboratory toxicity tests are used worldwide and are deemed as the first step in a tiered approach to set up guidelines for acceptable maximum concentrations of specific pollutants [11–14]. Bioassays are employed to find toxicity which could come from complex mixtures and are a complementary tool

to assess toxic effects overcoming certain limitations and are relatively rapid, cost effective, and simple to perform [15–17]. Bioassays can detect synergistic, antagonistic, and additive effects and also explain both point and diffuse sources of aquatic pollution since they are site specific [15, 18–20]. Several different bioassays are used simultaneously at different trophic levels of different biological complexity to sufficiently assess whether a potential hazard exists [11, 21] since no single test is suitable to measure all ecological risks due to different sensitivities by organisms [17, 22–24].

Species sensitivity distributions (SSDs) are being integrated into ecological risk assessments to evaluate the toxicity of particular chemicals [25]. An SSD is a distribution of statistical data approximated from a set of toxicity data and observed as a function of accumulative distribution [26, 27]. Species sensitivity distributions are used to calculate the concentration at which a specified proportion of species will be affected. The SSD provides a plot of logarithmic toxicity endpoints, specifically LC50 (the lethal concentration of toxicant that causes 50% death of test organisms at a specific

period of time) against rank-assigned percentiles for each endpoint value to which a statistical distribution is fitted [28]. A resulting hazard concentration (HCP) is produced from the SSD which is expressed as the percentage (p) of all species that are presumed to become affected [28, 29]. Toxicological databases are key factors in the derivation of water quality guidelines; thus SSDs are more commonly used in ecological risk assessments and generating water quality guidelines [28, 30]. The application of SSDs to evaluate the hazard of nanoparticles is fairly new since the database for nanoparticle toxicity data is relatively small compared to bulk chemical equivalents. Adam et al. [31] and Garner et al. [32] made use of SSDs to compare the relative toxicity of nanoparticles for which data are available, for example, CuO, ZnO, TiO₂, and carbon nanotubes. Many nanoparticle ecotoxicity studies highlight the importance of physicochemical nanoparticle characterization in the exposure media to be able to link exposure to effect [11, 33–35]. However there are very limited data for nAu. Therefore the aim of this study was to determine the comparative toxicity of aquatic organisms exposed to nAu and ionic gold using an SSD approach. The study also aimed to link mortality to the nAu particle characteristics.

2. Materials and Methods

2.1. Gold Nanoparticle and Ionic Gold Stock Solutions. The nAu stock solution (14 ± 2 nm nAu with product code TMU14G, batch numbers 20130304FKP49b, 20130308FKP52, and 20140905BM001) was prepared by standard citrate reduction techniques according to Murphy et al. [36] and Fren [37] and was sterilized using the filtration method. Gold used for ionic exposures was purchased in powder form from Aldrich (USA) as gold(III) chloride and was dissolved in standard OECD medium to a stock solution concentration of 1 g/L of Au³⁺ prior to the preparation of exposure concentrations.

2.2. Preparation of Environmental Media as Diluent for nAu Suspensions of Varying Concentrations. The reconstituted water for *Daphnia* toxicity testing was performed by making a standard OECD [38] medium (NaHCO₃, CaSO₄·2H₂O, KCl, and MgSO₄·7H₂O). The standard OECD medium [38] for fish toxicity testing contained CaCl₂·2H₂O, MgSO₄·7H₂O, NaHCO₃, and KCl. The reconstituted water media were aerated for 24 hours prior to use [39]. The nAu stock solution was placed in an ultrasonic bath and sonicated for two hours prior to use. To make up the required exposure concentrations, relevant volumes of the nAu stock were added to the environmental media water.

2.3. Physicochemical Water Quality. Physicochemical water quality parameters were measured according to standard test protocols [36]. Measurements were taken at the start of the test and at 24-hour (h) intervals until the tests were concluded. The pH, electrical conductivity (EC), total dissolved solids (TDS), oxygen saturation (% O₂), and dissolved oxygen (DO) concentration (mg/L) were measured using a handheld Eutech pH 110 RS232C meter, Eutech CON 110 RS232C conductivity and TDS meter, and Eutech DO6 DO

meter. The oxygen saturation was maintained above 60% for the duration of the test by bubbling compressed air into the exposure beakers.

2.4. Nanoparticle Exposure Concentration. Total gold concentrations were determined at the start of the toxicity bioassay (0 h) as well as at the conclusion of the assay (48 h or 96 h where relevant) to verify nominal concentrations in both ionic and nAu exposures. Samples (11 mL) were acidified with 3 mL Suprapur 30% hydrochloric acid (Merck) and 1 mL 65% HNO₃ to ensure that all of the gold was in ionic form. Inductively coupled plasma atom emission spectroscopy (ICP-OES) (Spectro Arcos FSH12) techniques were used to analyse the water samples.

2.5. Characterization of nAu Particles. Based on the recommendations by von der Kammer et al. [42], Stone et al. [43], and Klaine et al. [35], the following characteristics were determined: concentration, size distribution, surface charge, surface functionality, and agglomeration patterns. Dynamic light scattering (Malvern Zetasizer Nano series, NanoZS) was used to measure the hydrodynamic size distribution and zeta potential of the nAu in solution. Fourier transform infrared spectrometry (FTIR) (Perkin Elmer FTIR-spectrometer, Spectrum 100) was used to determine the nAu surface functionality and provide insight into possible reasons of particle aggregation. These measurements were taken at 0 h as well as at the conclusion of the test; that is, for fish this was after 96 h while for *Daphnia* this was 48 hours. Transmission electron microscopy (TEM) (FEI Tecnai G2) was used to quantify nAu diameter and nAu surface morphology as well as show particle aggregation patterns. One drop of nAu medium was dropped onto a carbon coated copper grid and allowed to settle for a few minutes. The excess water was removed using a filter paper by touching only the edge of the droplet and the grid was allowed to dry before examination at high resolution (200 kV).

2.6. *Daphnia pulex* and *Daphnia magna* 48-Hour Acute Immobilisation Test. The arthropods *Daphnia pulex* and *D. magna* were used for acute testing. Adults were kept in 2.5 L tanks in *Daphnia* media which were replaced three times per week and kept at a temperature of 20°C. Five milliliters of *Daphnia* food was suspended in the *Daphnia* media at each water cycle change. Prior to testing approximately thirty adults were transferred to a new tank and neonates less than 24 hrs old were used for the test.

For nAu a concentration range of 0.5 mg/L, 2 mg/L, 5 mg/L, 10 mg/L, 15 mg/L, 20 mg/L, 25 mg/L, 35 mg/L, and 45 mg/L was used. A separate dispersant control (the citrate buffer in which the nAu particles were dispersed) was made up in the same concentration range as the nAu. The ionic gold exposure concentration range was 0.0005 mg/L, 0.005 mg/L, 0.5 mg/L, 1 mg/L, 2 mg/L, and 5 mg/L. A positive control consisting of 1 g/L potassium dichromate solution was also conducted. The test organisms were not fed during the assay.

Twenty-one neonates were used for each concentration and tests were carried out in triplicate with each of the three

50 mL beakers per concentration containing seven organisms. A 16 h light and 8 h dark cycle was applied for the duration of the test and the temperature was maintained at $20 \pm 2^\circ\text{C}$. After each 24 h exposure period, the number of immobilized *Daphnia*, that is, any animal that was immobilized for more than 15 seconds, was counted. Any abnormal behaviour was also noted. The test was concluded after 48 h.

2.7. Fish 96-Hour Acute Lethality Test. Acute toxicity tests were conducted using two standard toxicity test fish species, that is, *Danio rerio* (zebrafish) and *Poecilia reticulata* (guppy), and four indigenous fish species, that is, *Labeobarbus aeneus* (smallmouth yellowfish), *Pseudocrenilabrus philander* (southern mouthbrooder), *Tilapia sparrmanii* (banded tilapia), and *Oreochromis mossambicus* (Mozambique tilapia). All fish were maintained and cultured in the research laboratories of the University of Johannesburg. The fish acute lethality test [36] was performed on 14-day-old juveniles. Similar to the *Daphnia* exposures a concentration range of 5 mg/L, 10 mg/L, 15 mg/L, 20 mg/L, 25 mg/L, 30 mg/L, 35 mg/L, 40 mg/L, 45 mg/L, 50 mg/L, 100 mg/L, and 200 mg/L was used for nAu. A range of 50 mg/L, 100 mg/L, and 200 mg/L was used to conduct a solvent (dispersant) control assay on the citric buffer dispersant. A concentration range of 1 mg/L, 2 mg/L, 5 mg/L, and 10 mg/L was used for the ionic gold (in the form of chloroauric acid) bioassay. Potassium dichromate (1g/L) was used as a positive control. Three replicates of seven fish per concentration were conducted in 500 mL beakers containing exposure medium. A 16 h light and 8 h dark cycle was maintained for the duration of the test and the temperature was maintained between 21°C and 25°C . The physicochemical water quality parameters were taken at the start of the test and again at 24 h intervals until the test was concluded after 96 h. The oxygen saturation was maintained above 60% for the duration of the test. If more than 10% of the juveniles died in the control the test was discarded and repeated. At 24 h intervals mortalities were recorded. Mortality was regarded if no visible movement was seen including gill movement. All dead fish were removed from the exposure beaker.

2.8. Statistical Analysis

2.8.1. Acute Toxicity. Data from the acute bioassays were analysed to calculate LC50/EC50 values using the Probit or Trimmed Spearman-Kärber methods where appropriate [44]. To determine whether there were any significant differences between the LC50 values for the different species, the following formula was used [45]: $f_{1,2} = \text{antilog}\sqrt{((\log f_1)^2 + (\log f_2)^2)}$, where f is the factor for 95% confidence limits of the LC50 and is calculated by dividing the upper confidence limit by the LC50. If the ratio of the higher LC50 to the lower LC50 exceeds the value for $f_{1,2}$ for both the upper and lower 95% confidence limits the LC50s are considered to be significantly different. The nominal concentrations were used to determine the LC50 values. In the absence of chronic data, the lowest observed effect concentration (LOEC) and no observed effect concentration (NOEC) can be useful in

deriving water quality criteria. The NOEC was taken as the maximum concentration of the test materials that produced no significant harmful effect on the test organisms. The LOEC was determined as the lowest concentration that has a significant harmful effect on test organisms.

2.8.2. Species Sensitivity Distributions. The results obtained from the bioassays were used to compare the tolerances of standard test species and indigenous arthropod and fish species using an SSD approach [27]. The SSDs were produced using the CADDIS SSD Generator [44]. Separate distribution models were constructed with the acute toxicity data collected for a range of species for nAu and ionic gold from which the average hazard concentration (HC_p) endpoint was extrapolated. The HC5 (hazard concentration where 5% of species are affected) was determined for freshwater fish and arthropods with exposure durations from 48 to 96 hrs. The comparisons in sensitivity were drawn between toxic responses of indigenous organisms and the standard test organisms. The taxonomic groups were analysed separately for the SSD model to illustrate the difference in tolerance between the taxa. A cumulative SSD model of all data for fish and arthropod's endpoints was also constructed for both nAu and ionic gold to ascertain the hazard threshold values.

3. Results

3.1. Physicochemical Water Parameters. The physicochemical water parameters were maintained within the OECD guidelines [38] as shown in Table 1. The temperature ranged between 20 and 23.9°C across all exposures; the pH was maintained between 7 and 8 but had a minimum of 6.24 and a maximum of 8.95 for chloroauric acid exposures. The DO concentration ranged between 4.44 mg/L and 9.78 mg/L and as previously discussed the oxygen percentage ($\text{O}_2\%$) was well maintained above 60% according to standard protocol. The *Daphnia* medium had a lower EC and TDS when compared to the fish medium. This was expected as the reconstituted water is made up of different salts at higher concentrations. The EC ranged between 198 and 420 $\mu\text{S}/\text{cm}$ for the *Daphnia* medium and 621 and 809 $\mu\text{S}/\text{cm}$ for the fish medium. The TDS ranged between 104 and 267 mg/L for the *Daphnia* medium, while for the fish medium the range was between 309 and 485 mg/L.

3.2. Nanoparticle Exposure Concentration. To verify the concentrations added to each exposure group, total gold concentrations were measured. The nominal ionic gold concentrations and measured concentrations were in close agreement (Figure 1). After a 48 h and 96 h period the concentrations were maintained within the start concentration limits. The total gold concentrations in the nAu exposures showed up to a 20% difference between nominal and measured gold concentrations.

3.3. Particle Size Distribution. The largest proportion of nAu (i.e., >90%) in the *Daphnia* medium across all exposure concentrations showed agglomerations greater than 566 nm

TABLE 1: Physicochemical water quality means for selected species in toxicity exposure bioassays with nAu, chloroauric acid, and citrate buffer.

Species	pH (min–max)	D.O. (mg/L) (min–max)	O ₂ (%) (min–max)	EC (μ S/cm) (min–max)	Temp. ($^{\circ}$ C) (min–max)	TDS (mg/L)
Citrate buffer						
<i>D. pulex</i>	7.85 (6.57–8.36)	5.43 (4.44–6.08)	64.6 (61.7–67.4)	339 (309–374)	20.5 (20–21.2)	171 (156–189)
<i>D. magna</i>	7.70 (7.6–8.37)	7.26 (6.63–8.72)	77.0 (62.6–91.4)	310 (297–362)	19.3 (20–21.9)	155 (148–181)
<i>D. rerio</i>	8.26 (7.10–8.65)	4.77 (4.0–6.15)	69.6 (60.0–87.2)	708 (621–809)	23.3 (22.7–23.9)	350 (309–398)
<i>O. mossambicus</i>	7.98 (7.39–8.34)	5.04 (4.26–5.9)	66.9 (60.2–78.08)	708 (530–841)	21.4 (20.6–22.1)	365 (321–407)
<i>P. reticulata</i>	7.74 (6.57–8.22)	4.85 (3.5–5.77)	67.7 (60–77.1)	748 (696–810)	22.2 (21.6–23.03)	373 (316–405)
<i>P. philander</i>	6.93 (6.01–7.75)	5.62 (4.3–6.47)	71.7 (60–89.5)	732 (665–874)	23.1 (22.9–23.2)	366 (333–402)
<i>T. sparrmanii</i>	6.57 (5.81–7.39)	4.85 (4.00–5.77)	67.9 (60–77.1)	674 (612–704)	22.1 (21.3–22.6)	372 (313–595)
<i>L. aeneus</i>	7.06 (5.99–7.93)	5.93 (4.89–7.07)	67.0 (60.3–80.5)	680 (638–729)	22.5 (21.5–23)	346 (324–369)
nAu						
<i>D. pulex</i>	7.66 (7.05–8.7)	5.05 (4.4–6.1)	63.1 (60.7–72.6)	328 (208–420)	20.7 (20–21.9)	167 (104–220)
<i>D. magna</i>	7.78 (7.74–8.39)	7.23 (6.39–9.28)	78.4 (71.7–97.8)	309 (293–374)	20.2 (20.5–22.2)	155 (146–206)
<i>D. rerio</i>	7.88 (7.13–8.42)	4.49 (4.04–6.26)	68.1 (60.1–98.7)	674 (642–765)	22.6 (22.4–23.9)	336 (321–412)
<i>O. mossambicus</i>	7.43 (7.13–7.97)	4.68 (4.11–6.24)	63.9 (60.0–82.9)	681 (621–827)	20.8 (20.1–21.1)	340 (310–414)
<i>P. reticulata</i>	7.57 (6.31–8.19)	5.97 (4.84–8.26)	67.3 (60.0–79.6)	743 (658–824)	22.2 (21.3–22.6)	370 (329–412)
<i>P. philander</i>	7.24 (6.23–7.79)	5.89 (5.14–6.76)	73.9 (60.8–92.20)	699 (580–762)	23.0 (22.9–23.2)	350 (328–379)
<i>T. sparrmanii</i>	7.51 (6.85–8.01)	5.69 (4.37–8.26)	66.6 (60–79.6)	703 (617–754)	22.2 (21–22.7)	335 (308–378)
<i>L. aeneus</i>	7.55 (6.29–7.90)	5.55 (4.08–7.08)	55.9 (60.0–80.7)	556 (628–762)	22.9 (21.6–23.1)	275 (314–381)
Chloroauric acid						
<i>D. pulex</i>	7.90 (6.93–8.95)	5.35 (4.35–6.13)	66.3 (62.7–71.5)	344 (198–382)	20.6 (20–22)	176 (104–267)
<i>D. magna</i>	8.22 (7.59–8.43)	7.57 (6.4–9.78)	83.3 (62.5–99.7)	332 (296–381)	21.6 (20.4–22.4)	168 (148–259)
<i>D. rerio</i>	7.92 (6.24–8.67)	4.98 (4.2–6.044)	72.0 (62.8–85.3)	677 (621–739)	23.0 (21.8–23.7)	350 (311–485)
<i>O. mossambicus</i>	7.56 (6.45–7.98)	5.86 (4.23–7.85)	72.3 (60.2–84.8)	700 (620–806)	21.3 (20.6–21.6)	350 (310–403)
<i>P. reticulata</i>	7.33 (6.26–8.27)	5.63 (4.8–7.67)	73.6 (60.9–81)	711 (616–838)	21.7 (20.9–22.4)	355 (308–419)
<i>P. philander</i>	7.62 (7.36–8.04)	6.82 (4.49–8.26)	77.0 (62.1–99)	702 (603–736)	23.1 (22.3–23.5)	352 (301–400)
<i>T. sparrmanii</i>	7.24 (6.26–8.14)	5.61 (4.6–7.67)	73.4 (62.3–81)	633 (545–792)	21.6 (21.0–22.1)	388 (308–436)
<i>L. aeneus</i>	7.77 (7.36–8.04)	5.90 (4.46–8.24)	76.7 (61.8–99.4)	700 (603–794)	23.1 (22.3–23.6)	350 (301–398)

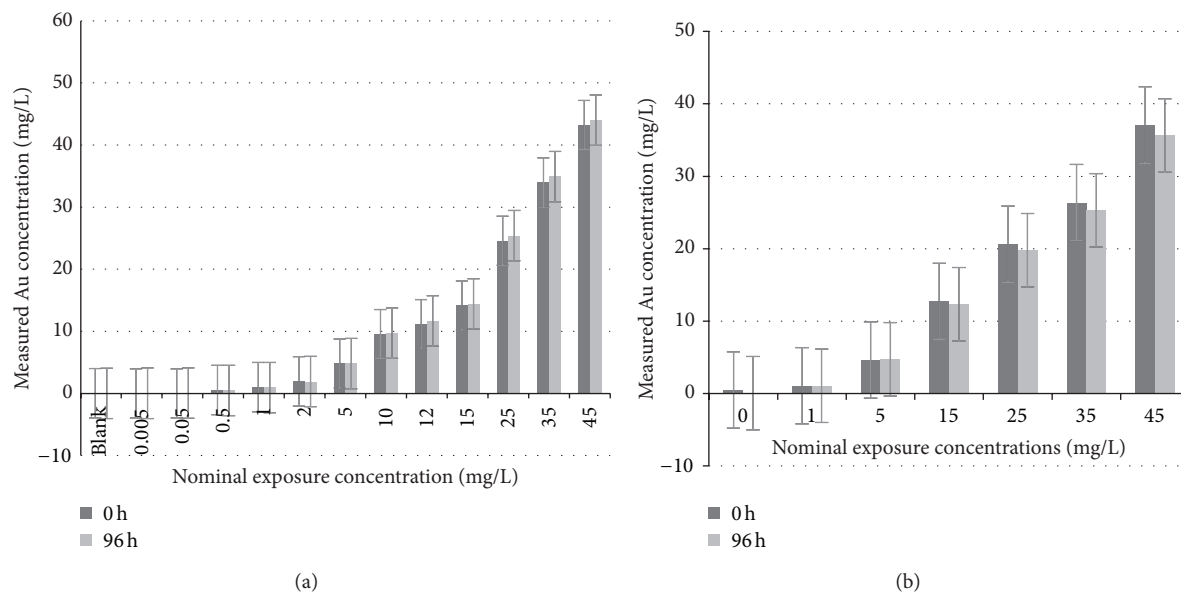


FIGURE 1: Mean measured gold concentrations (mg/L) \pm standard deviation of the (a) ionic gold (HAuCl₄) and (b) nAu exposures at all exposure concentrations used in this study.

TABLE 2: Size distribution of gold nanoparticles across all concentrations in *Daphnia* medium.

Concentration	nAu size <i>Daphnia</i> medium		
	nm	St. dev.	% intensity
25 mg/L	565.6	87.82	93.9
35 mg/L	827.45	56.50	92.5
45 mg/L	3175.5	443.35	93

(Table 2). As the exposure concentration increased, so did the average sizes of the agglomeration; for example, in the 45 mg/L exposure the average sizes were 3175.5 nm (Table 2).

In contrast to the nAu particle aggregation/agglomeration in *Daphnia* media, the dynamic light scattering (DLS) indicated that the size distribution in fish media is represented by two peaks in terms of percentage intensity (Figure 2). The particle size distribution is therefore not presented as the average size as there were distinct differences and this would not give an accurate indication of the sizes available for biological uptake. Therefore the size distribution is represented as two dominant size classes per concentration with the corresponding percentage intensities at 0 h as well as at 96 h.

The nanoparticle size distribution was determined at 0 h and again at 96 h to observe any changes in aggregation over time. Results are presented by indicating the main size distribution classes in terms of the percentage contribution after 0 h and 96 h. At 0 h nAu exposures there were two dominant size distribution classes, that is, sizes representing >60% intensity and less than 40% intensity (Figure 3). The same was shown at 96 h where more than 55% of nanoparticles had the indicated size. In four concentrations (10 mg/L, 20 mg/L, 25 mg/L, and 45 mg/L) the particles had less than 45% percentage intensity of the indicated size.

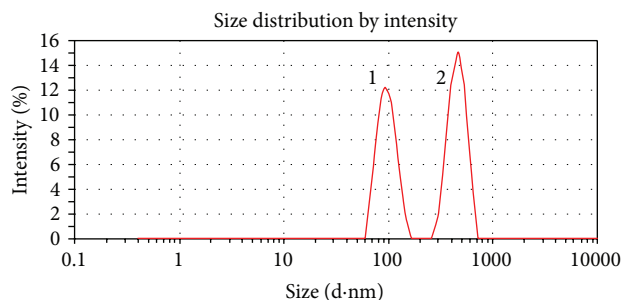


FIGURE 2: Raw data sheet showing two peaks of Z-average size (d-nm) of gold nanoparticles in aquatic medium where peak 1 shows a size of 96.89 nm (\pm 45.5 nm) and peak 2 shows a size of 455.6 nm (\pm 54.5 nm).

At 0 h in the 5 mg/L concentration 89% of the sample had a size distribution of 150.7 nm and 12% of nanoparticles were 12.64 nm. After 96 h more than 90% of particles were 133.7 nm in size. At 10 mg/L all particles measured in the sample were around 75.79 nm while after 96 h the particles (82.7%) had agglomerated to 986.4 nm while 17.3% remained approximately 79.64 nm in diameter. At 15 mg/L, 89% were in the size range of 89.49 nm, while 11% were at 15.51 nm. After 96 h particles had all aggregated to 96.6 nm. At the onset of the 20 mg/L exposure 88% of the particles had aggregated to 127.9 nm and 12.2% to 17.12 nm in diameter. After 96 h 64% of the sample had agglomerated to 894.5 nm and 36% of the sample was 121.5 nm in size. At the 25 mg/L concentration just over half (59.6%) of the sample was 298.4 nm in size while just under half (40.4%) of the sample was 71.48 nm. After 96 h the same ratio was maintained where 54.5% of the sample had a size of 455.6 nm and 45.5% had a size of 96.89 nm. At 30 mg/L the prevalence was 72.3% distribution of 163.1 nm particles and 27.7% at 40.27 nm, while after 96 h

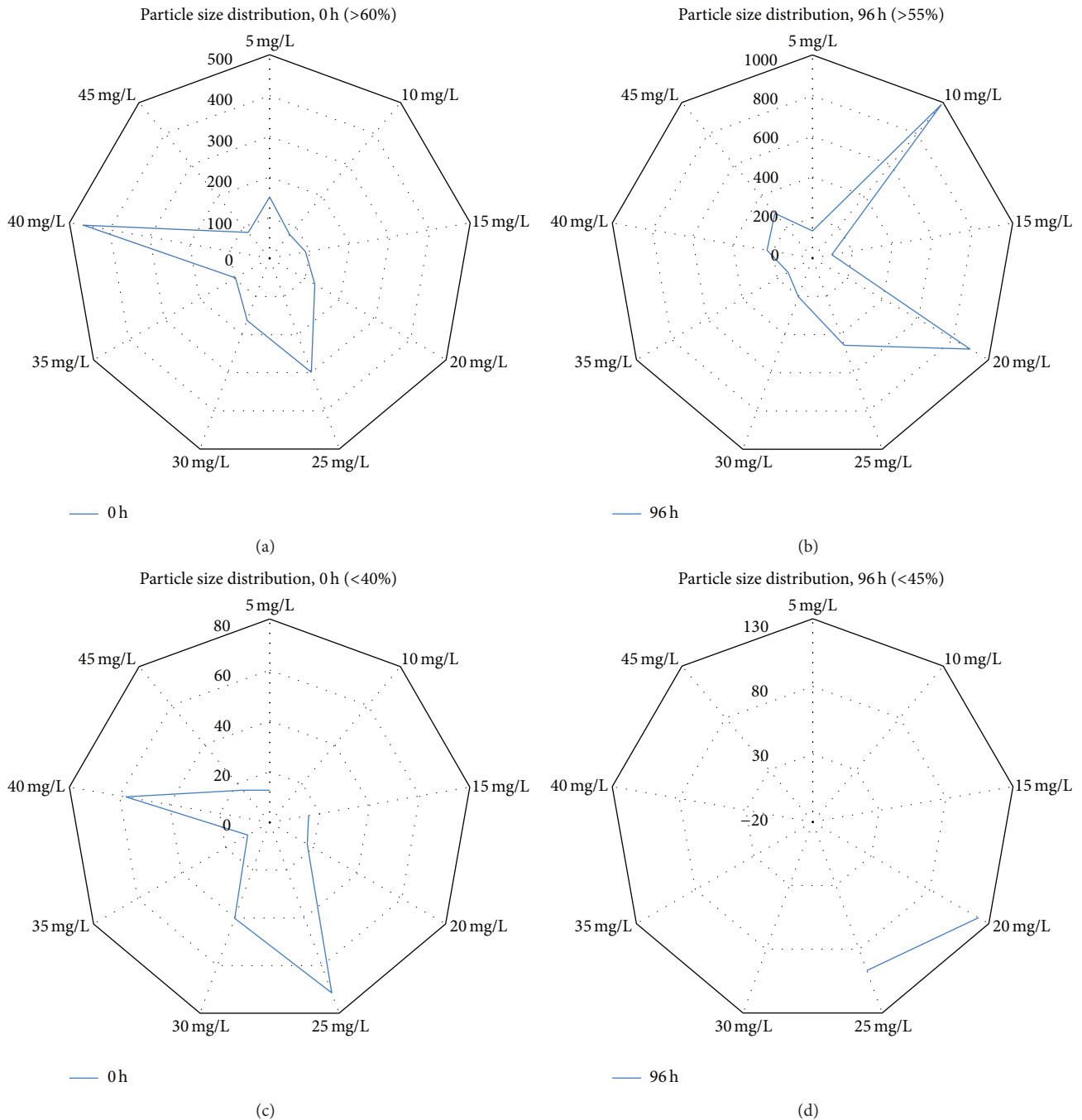


FIGURE 3: Particle size distribution (nm) of nAu with a percentage intensity of (a) more than 60% at 0 h and (b) less than 40% at 0 h as well as (c) more than 55% at 96 h and (d) less than 45% at 96 h.

all particles had agglomerated to 201.5 nm. The 35 mg/L concentration revealed that 91% of the sample had aggregated to 96.89 nm and 9% of the sample remained around 14 nm in size. After 96 h all particles had aggregated to 138.2 nm. The 40 mg/L concentration showed an immediate aggregation at 0 h where 57.4% of the sample was 464.9 nm and 42.6% of the sample was 57.55 nm in size. After 96 h all sample measured contained a uniform size of 226.9 nm. At the highest concentration, 45 mg/L, 79.9% of the sample had

particles 82.52 nm in size and 15% remained around the original size of 14 nm. After 96 h the prevalence of particles at 288 nm was 87.7% and 12.3% were 63.05 nm in size. In the 40 mg/L and 45 mg/L concentration nAu had precipitated out of solution and were visible to the naked eye. These agglomerates were in the millimetre size range and could not be measured on the DLS instrument.

At 0 h there was a clear increase in size of nAu aggregations and agglomeration at concentrations of 25 mg/L and

TABLE 3: Zeta potential (mV) of the nAu in the *Daphnia* medium across exposure concentrations.

nAu	1 mg/L	5 mg/L	15 mg/L	25 mg/L	35 mg/L	45 mg/L
	Zeta potential [mV]					
0 h	-8.74 ± 2.91	-3.07 ± 1.58	-8.13 ± 9.72	-17.16 ± 22.92	-10.27 ± 2.12	-9.40 ± 0.54
48 h	-2.03	-7.17 ± 4.30	-16.10	-8.50 ± 0.92	-2.78 ± 0.80	-4.14 ± 1.23

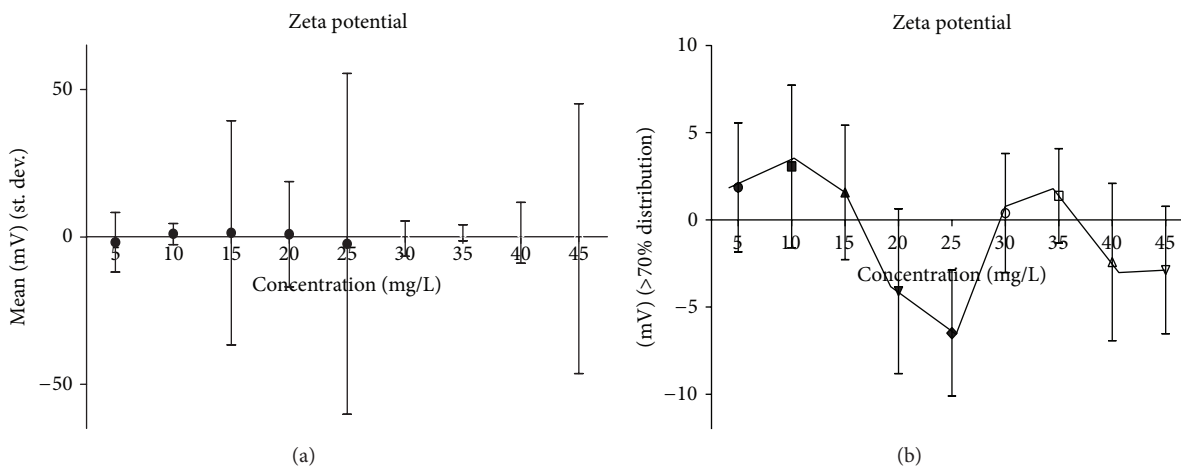


FIGURE 4: (a) The zeta potential (mV) average peak reading across all concentrations. (b) The zeta potential (mV) reading where the peak had greater-than-seventy-percent distribution measured across all concentrations.

40 mg/L when compared to other concentrations. But after 96 h the 20 mg/L and 25 mg/L concentrations still showed agglomerations increasing in size and dispersion in the media while concentrations 30 mg/L and above showed no or lower measured sizes, which is attributed to particle precipitation.

3.4. Particle Charge (Zeta Potential). The EC differed for the *Daphnia* and fish media based on the salts used to make up the reconstituted water. For the *Daphnia* medium the zeta potential ranged between -3.07 mV and -17.16 mV (Table 3) with all values across all time intervals being negative. At 5 mg/L and 15 mg/L exposures the zeta potential decreased even further after 48 h while at all other concentrations the zeta potential became more positive.

For the fish medium there was much greater variation (as observed in the increase in the standard deviation) of the measured zeta potential. The standard deviation (Figure 4(a)) ranged between 57.8 mV and -54.9 mV. This is related to the large difference in size distribution as shown in Figure 3. In Figure 4(b) the zeta potential data were limited to those that represent 70% of the dominant distribution (i.e., the outliers were removed). The dominant zeta potential at 20 mg/L, 25 mg/L, 40 mg/L, and 45 mg/L was negative, that is, -4.09 mV, -6.49 mV, -2.42 mV, and -2.88 mV, respectively. At all other concentrations the charge was positive with the highest at 10 mg/L (3.06 mV).

3.5. Surface Functionality. The FTIR results revealed two distinct peaks (Figure 5). One of the peaks was identified as a hydroxyl group and further analyses of the black particle aggregates were carried out on dried sample to eliminate any

interference in the spectrum of the water suspension. The first peak (± 1632 cm^{-1}) was identified as an organic nitrate or carbon double bond aromatic stretch. The second peak (± 3343 cm^{-1}) was identified as a hydroxyl group, H-bonded OH stretch (3570 – 3200 cm^{-1} (broad) 3400 – 3200 cm^{-1}) or a normal “polymeric” OH stretch, which indicates interaction with the water medium.

3.6. Gold Nanoparticle Aggregation and Agglomeration Patterns. The TEM results revealed a better understanding of the size distribution patterns. As defined by Klaine et al. [35] nanoparticle groupings of less than 150 nm were referred to as aggregates and those larger than 150 nm were seen as agglomerates. In the stock solution (1000 mg/L) the citrate capping was visible around the nAu especially at a higher magnification. It was clear that particles were separated from one another while present in the citrate buffer capping agent (Figure 6(a)). A live fast Fourier transform (FFT) image was taken to verify that the particles were aligned in a crystal lattice formation as is typical of nano metals (Figure 6(b)). At 0 h dispersed nAu were observed in all exposure concentrations. However, after 96 h this was only possible to identify dispersed particles at 5 mg/L and 10 mg/L exposure concentrations. For the 40 mg/L and 45 mg/L exposures it was apparent that after 24 h the nAu started to agglomerate and precipitate out of solution. At 5 mg/L nAu were much more difficult to find on the dried copper grid but were present and showed aggregations of small groups (Figure 6(c)) as well as string-like aggregates (Figure 6(d)), while at 10 mg/L the string-like aggregates were still present but more were present (Figure 6(e)) and had started aggregating at 122.87 nm onto

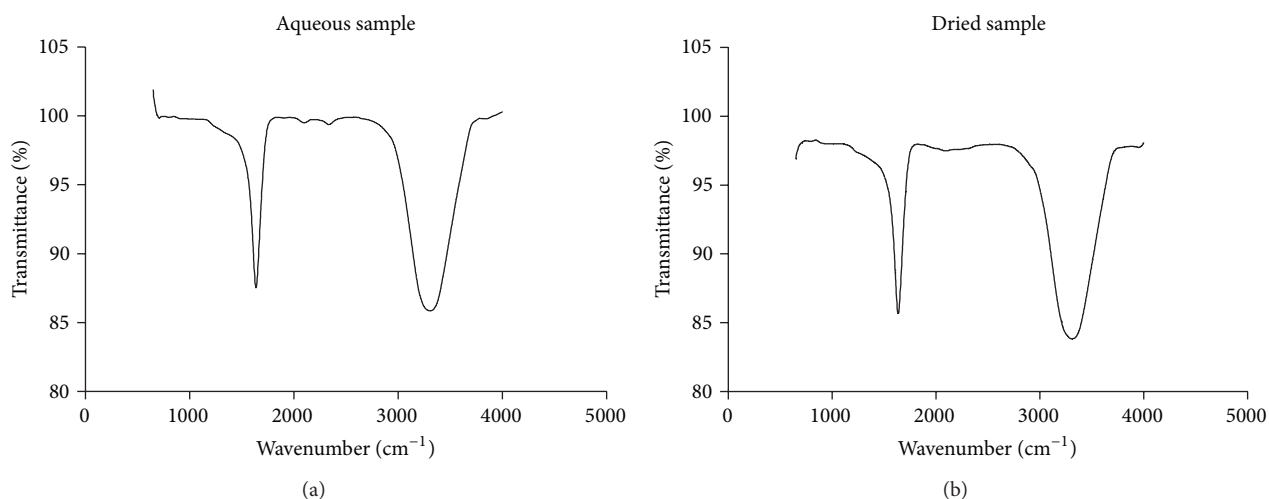


FIGURE 5: (a) The FTIR spectra results of the highest concentration of gold nanoparticle in an aqueous solution. (b) FTIR spectra results of the dried gold nanoparticle sample in the highest concentration to eliminate OH interference from the solution.

the string-like structures as though a skeletal backbone had been formed (Figure 6(f)).

In the 20 mg/L exposure there were two major types of agglomerates noted; these were skeletal-like agglomerates which reached approximately 352.1 nm in length (Figure 7(a)) and smaller aggregates which were quite prevalent and easy to find throughout the dried copper grid and which showed an approximate size of around 73.67 nm. When observing 30 mg/L nAu concentrations it was quite clear that the skeletal backbone structures were starting to attach to one another as seen in Figure 7(c). Seeing that the conformation was stable the smaller agglomerates (152.19 nm) started attaching the open spaces in between and particle agglomerates were as large as 430.78 nm (Figure 7(d)). It appears that at 40 mg/L the larger agglomerates as seen in 30 mg/L started attaching to one another (Figure 7(e)); the skeletal backbone has now been filled and the nAu aggregate into an accumulation of particles forming large agglomerates of up to 2000 nm visible on TEM. At these concentrations agglomerates were also visible to the naked eye.

3.7. Acute Toxicity Testing. No mortalities were recorded in the controls and the dispersant controls (i.e., mortalities were below 10%). It was not possible to calculate LC50 values for the 48 h *D. pulex* and 96 h *D. rerio*, *O. mossambicus*, *P. philander*, and *L. aeneus* nAu exposures (Table 4). The nAu LC50 values for *D. pulex*, *T. sparrmanii*, and *P. reticulata* were 7.31 mg/L, 12.08 mg/L, and 52.57 mg/L, respectively. The ionic gold LC50 values for the test organisms ranged between 0.01 mg/L for *D. pulex* and 20.58 mg/L for *P. reticulata*. For the nAu *T. sparrmanii* was the most sensitive, while for ionic gold *D. pulex* was the most sensitive aquatic organism tested. Based on the LC50 values it was evident that the species were much more sensitive to ionic gold than nAu exposure. The toxicity of ionic gold was significantly greater ($p < 0.05$) to *D. pulex* compared to all the species tested. Both *Daphnia* species were significantly more sensitive to ionic gold than the fish

species. The fish species *L. aeneus*, *D. rerio*, and *P. philander* were significantly ($p < 0.05$) more sensitive than the other species. The NOEC and LOEC data were established from the mortality results and are depicted in Table 4. The LOECs observed for nAu for *D. pulex*, *D. magna*, *D. rerio*, *P. reticulata*, *P. philander*, *T. sparrmanii*, and *L. aeneus* were 10, 5, >15, 35, 25, and 5 mg/L, respectively, with *O. mossambicus* showing no mortalities at any of the exposure concentrations. No effect concentrations were recorded at 1, 5, <15, and <35 mg/L, respectively. The LOECs for ionic gold were 0.0005, 0.01, 5, 5, 10, 10, 2, and 1 mg/L for *D. pulex*, *D. magna*, *D. rerio*, *O. mossambicus*, *P. reticulata*, *P. philander*, *T. sparrmanii*, and *L. aeneus*.

3.8. Species Sensitivity Distribution. The cumulative mortality rates of the organisms over the 48 h and 96 h exposure periods for both nAu and ionic gold are depicted in Figures 8 and 9, respectively. The cumulative percentages are based on the mortalities recorded at all exposure concentrations during the particular exposure period and provide further indication of the sensitivity of the particular species. The low toxicity of nAu exposure is clearly visible (Figure 8) with only *T. sparrmanii* displaying a 20% toxicity response after 36–48 h exposure and maximum mortality of 48% after 96 h. The rest of the species had a mortality rate lower than 10%. For most species exposed to ionic gold 50% mortality was reached between 12 h and 24 h with *O. mossambicus*, *D. rerio*, and *L. aeneus* displaying the highest immortality of 57%, 68%, and 78% (Figure 9). Both species of *Daphnia* show 75% mortality after 24 h.

Seven data points are generally required to generate a meaningful SSD for any given chemical [46]. Since it was not possible to calculate nAu LC50 values for all the species tested, an SSD was constructed based on the toxicity data that were available. The SSD for nAu (Figure 10) was generated based on the limited acute toxicity data generated during this study and the few data published in literature [40, 41].

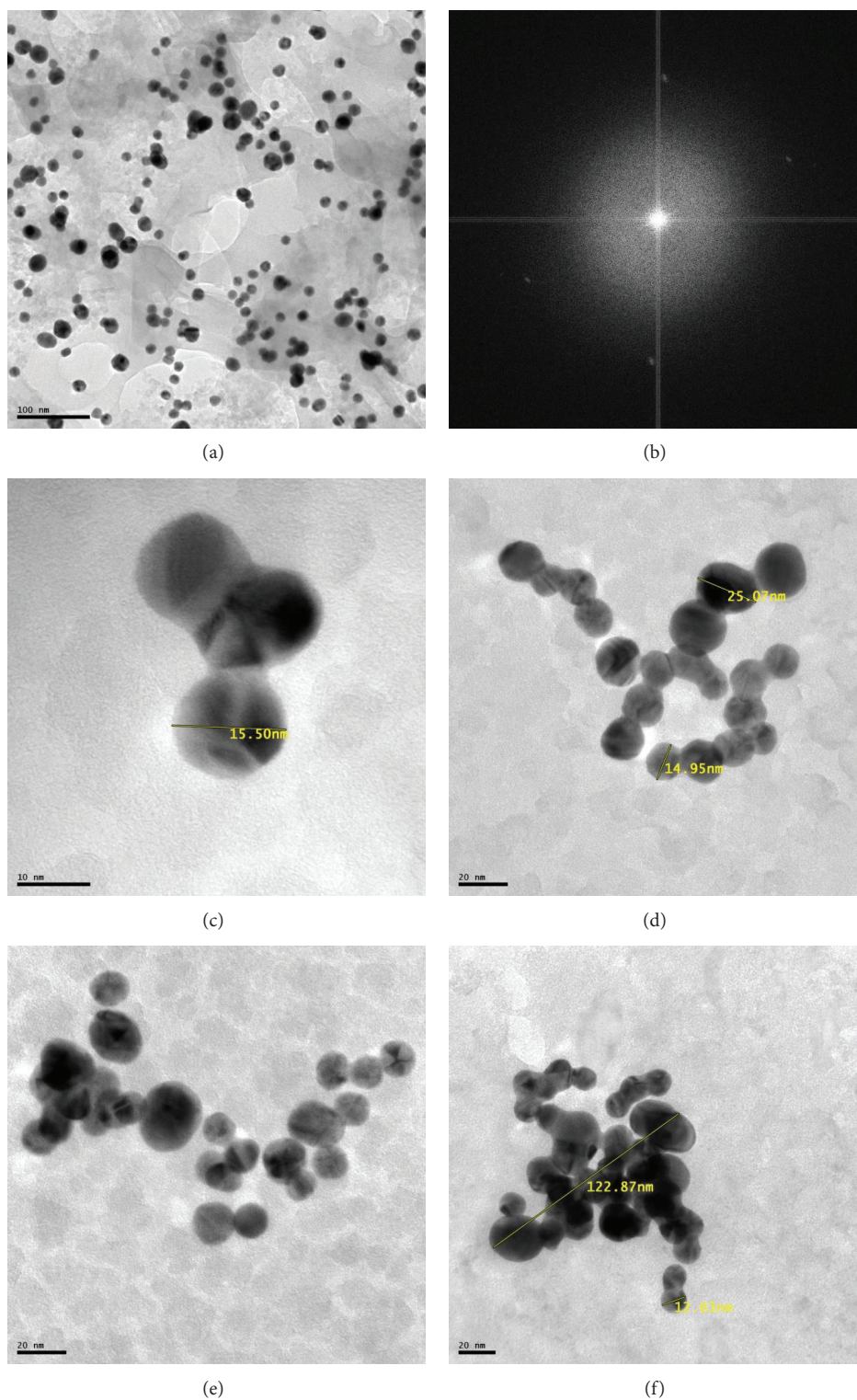


FIGURE 6: (a) A TEM micrograph of a drop of the concentrated citrate capped 1000 mg/L concentration gold nanoparticle stock solution. (b) An FFT image of the nAu to confirm the presence of a crystal lattice. ((c) and (d)) A TEM micrograph of the 5 mg/L gold nanoparticle concentration showing average aggregations and measurements. ((e) and (f)) A TEM micrograph of the 10 mg/L gold nanoparticle concentration showing average aggregations and measurements.

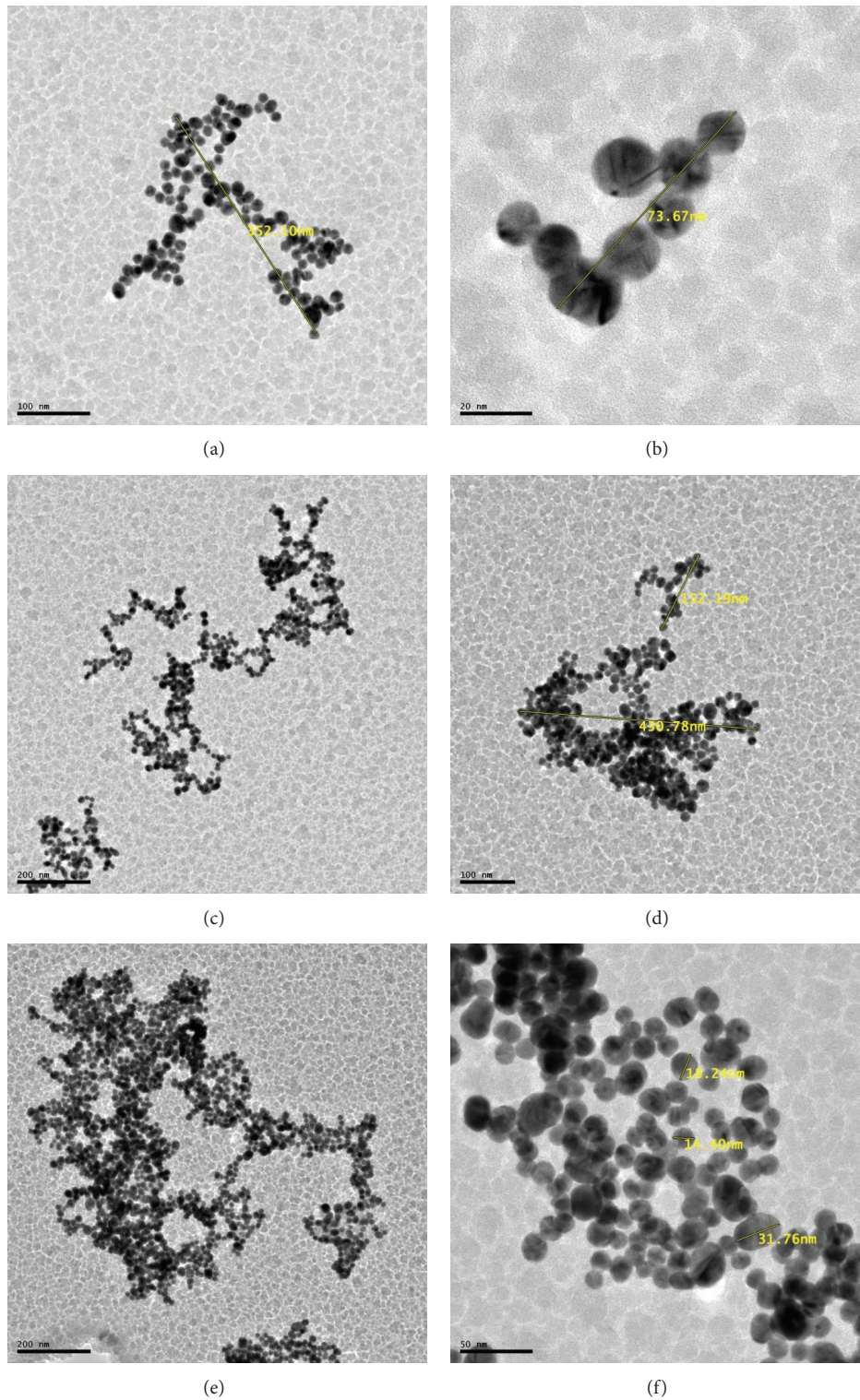


FIGURE 7: ((a) and (b)) A TEM micrograph of the 20 mg/L nAu concentration showing average aggregations and measurements. ((c) and (d)) A TEM micrograph of the 30 mg/L gold nanoparticle concentration showing average aggregations and measurements. ((e) and (f)) A TEM micrograph of the 40 mg/L gold nanoparticle concentration showing average aggregations and measurements.

TABLE 4: Median lethal concentrations for 50% (LC50) effect and the corresponding 95% confidence intervals for test organisms exposed to nAu and chloroauric acid.

Species	Duration/endpoint	Mean	LC50 (mg/L) (95% CI)		NOEC	LOEC
			Upper & lower confidence limits (mg/L)			
nAu						
<i>D. pulex</i>	48 h	75.31	*		1	10
<i>D. magna</i>	48 h		Could not be calculated		0	5
<i>D. rerio</i>	96 h		Could not be calculated		<15	>15
<i>O. mossambicus</i>	96 h		No mortalities			
<i>P. reticulata</i>	96 h	52.57	*		<35	35
<i>P. philander</i>	96 h		Could not be calculated		5	10
<i>T. sparrmanii</i>	96 h	12.08	*		5	25
<i>L. aeneus</i>	96 h		Could not be calculated		1	5
Chloroauric acid						
<i>D. pulex</i>	48 h	0.01	0	0.02	<0.0005	0.0005
<i>D. magna</i>	48 h	0.15	0.29	0.08	<0.005	0.01
<i>D. rerio</i>	96 h	4.85	3.62	6.49	<1	5
<i>O. mossambicus</i>	96 h	11.30	15.89	8.03	<1	5
<i>P. reticulata</i>	96 h	20.58	24.15	17.54	<10	10
<i>P. philander</i>	96 h	7.53	8.18	6.94	<10	10
<i>T. sparrmanii</i>	96 h	10.78	8.92	13.03	1.5	2
<i>L. aeneus</i>	96 h	0.93	1.08	0.80	<1	1

*No confidence levels could be calculated.

The ionic gold acute toxicity data from both published literature and this study (Table 5) were used to generate respective SSD toxicity plots (Figures 11 and 12). The HC5 based on the combined data sets (literature and this study) for nAu and ionic gold was 42.78 mg/L and 2.44 mg/L, respectively. The HC5 of the published literature was 4.46 mg/L, whilst the indigenous species were more sensitive with an HC5 of 1.83.

4. Discussion

4.1. Characterization of nAu. Nanoparticle ecotoxicity involves several factors to consider, the initial size of the particles, the capping agent, how particles aggregate in an aquatic medium, and the charge that exists. All these affect the toxicity and ability for particle uptake in organisms [3, 47, 48]. The changes in zeta potential and aggregation could be related to changes in conductivity and pH over time [49, 50]. These changes in ionic strength based on the physicochemical

water parameters allow for more binding sites on the particle surface due to an increased negative charge [51]. Therefore negative zeta potentials have the potential for aggregation to decrease. There is an increase in aggregation as the zeta potential becomes more positive as seen at 30 mg/L and above [52, 53].

When there is a change in any of these factors the behaviour of the nAu in an aquatic medium would also change. In *Daphnia* medium, there is uniform distribution of particle characteristics over the entire concentration range, while for fish medium there is a wide range of charges and size distributions which would affect particle uptake. Between 20 mg/L and 25 mg/L in the fish medium there was a diverse size distribution as nAu ranged from 17 nm to 890 nm and were present in equal intensities. The charge was negative at these concentrations and this could be adding to the smaller particles present because negative charges would cause aggregates to repel one another [52]. After 30 mg/L

TABLE 5: Acute toxicity data from the published literature that were included used to derive the SSDs.

Test species	Endpoint	Duration (h)	LC50 HAuCl ₄ (mg/L)	Reference
Arthropods				
<i>D. magna</i>	LC50	48	2	Li et al. [40]
<i>D. magna</i>	LC50	48	0.64	Nam et al. [41]
<i>D. magna</i>	LC50	48	0.15	This study
<i>D. pulex</i>	LC50	48	0.01	This study
<i>M. macrocopa</i>	LC50	48	0.62	Nam et al. [40]
Fish				
<i>D. rerio</i>	LC50	96	4.85	This study
<i>P. reticulata</i>	LC50	96	20.58	This study
<i>T. sparrmanii</i>	LC50	96	10.78	This study
<i>P. philander</i>	LC50	96	7.53	This study
<i>O. mossambicus</i>	LC50	96	11.3	This study
<i>L. aeneus</i>	LC50	96	0.93	This study
<i>T. arcticus</i>	LC50	96	14.4	Nam et al. [41]
<i>O. mykiss</i>	LC50	96	10.7	Nam et al. [41]
<i>O. kisutch</i>	LC50	96	14.1	Nam et al. [41]

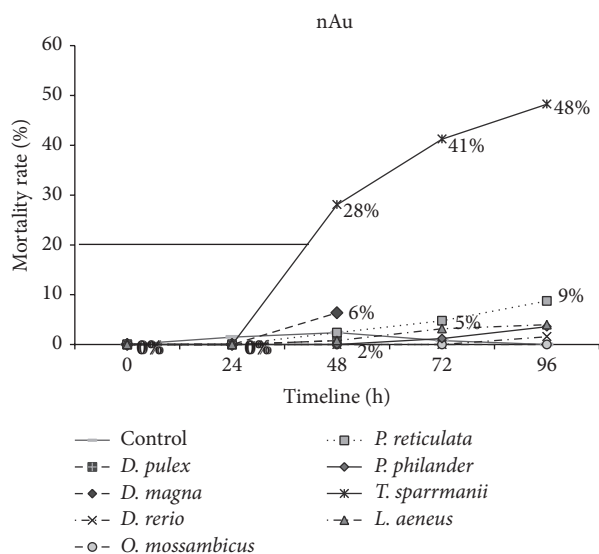


FIGURE 8: Cumulative mortalities of test organisms exposed to nAu over 48 h (daphnids) and 96 h (fish).

the nAu start forming large agglomerates, which, when observed under the TEM to reveal skeletal-like structures, may already be too large to be taken up by an organism [54–56]. Therefore there is a high enough concentration of nAu present for the aggregation to outweigh the charge and this would result in the nAu binding to one another and less are left in solution. However at 40 mg/L and 45 mg/L the agglomerates become so large that they are visible to the naked eye (up to 3 mm) and therefore when a drop is collected for TEM only those particles which have been unable to bind to the larger agglomerate are visible. This would also explain why after 96 h it becomes increasingly difficult using TEM to

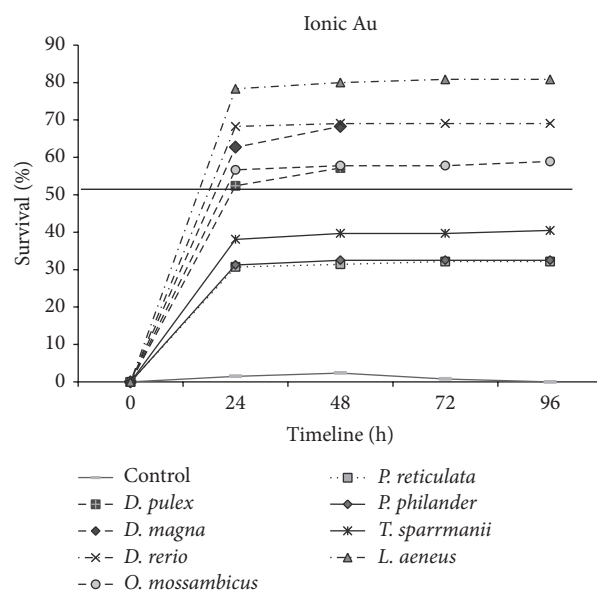


FIGURE 9: Cumulative mortalities of test organisms exposed to ionic gold over 48 h (daphnids) and 96 h (fish).

observe nAu in concentrations above 10 mg/L as they have already started to sediment out of solution.

As all citrate capped gold nanoparticles in the stock solution were around the 14 nm range it is evident that from the moment the particles were diluted in the respective environmental media they started to agglomerate to one another. This could also reflect the 10 mg/L loss of nanoparticle concentrations measured due to aggregations as the entire sample was not read but only a portion of it. The citrate capping is soluble and by the hydrolysis of

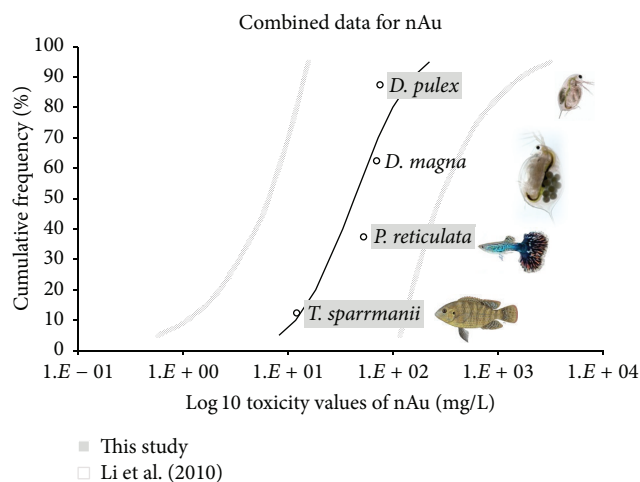


FIGURE 10: Species sensitivity distributions and confidence limits for nAu based on combined data from this study and the published literature.

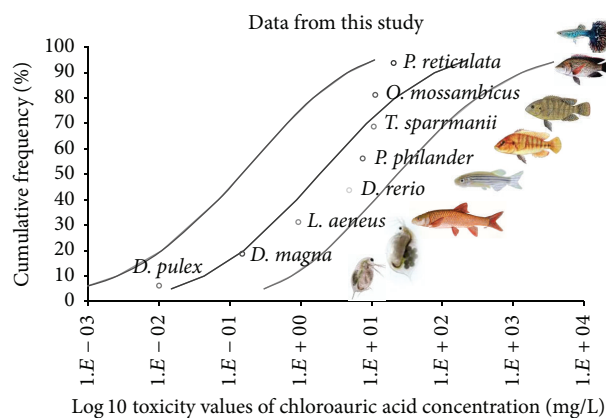


FIGURE 11: Species sensitivity distributions and confidence limits for ionic gold based on acute toxicity data from this study.

water is converted to citric acid [57]. Sections of the sodium citrate capping agent ($\text{Na}_3\text{C}_6\text{H}_5\text{O}_7$) are washed off in the medium and particles become functionalized and therefore gain a charge [1] which allows them to stick to one another through van der Waals forces [47]. Divalent cations such as Ca^{2+} and Mg^{2+} , which are present in the reconstituted OECD medium, effectively neutralize the surface charge of citrate coated nAu, thereby compressing the electric double layer (repulsive forces) and enhancing aggregation [58, 59]. This suggests that aggregates of nAu should be regulated by the type and concentration of the solvent and ionic strengths of reconstituted water medium [54, 60–62]. The zeta sizer indicated three peaks where the distribution of each size is represented as a percentage. It was found that to gain a better understanding of the particle behaviour at each concentration these percentages need to be taken into account.

Functional groups present on the nAu surface play a role in tissue distribution [63, 64]. When additional ligands are

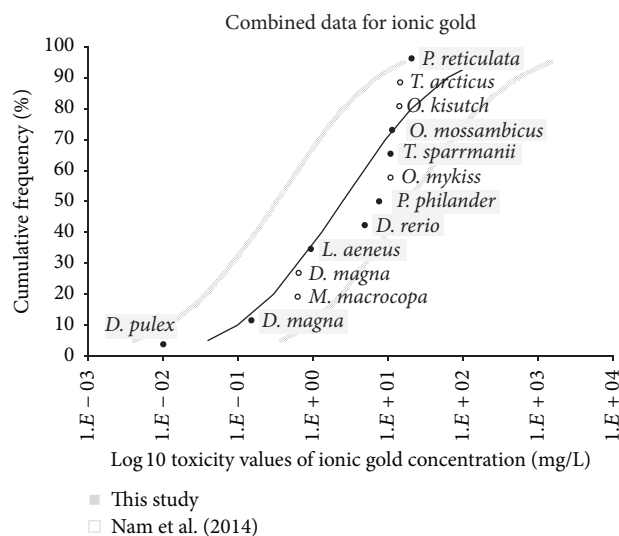


FIGURE 12: Species sensitivity distributions and confidence limits for ionic gold based on toxicity data from this study and the published literature [41].

not present as is the case with a controlled bioassay, the most stable form in solution for the nAu would be the hydrolyzed species, namely, functionalized to $\text{AuOH}(\text{H}_2\text{O})^0$ [65]. The OH frequency indicates that OH forms strong H-bonding with groups of citrate caps present on nAu [66]. However depending on the pH and presence of chloride species this could change, where a pH of less than 4 would cause AuCl_2 to form. However the neutral pH during these bioassays and FTIR results confirmed that this was not the case. When negative charges are present, as seen in 20 mg/L, 25 mg/L, 40 mg/L, and 45 mg/L, this may change the toxicity of the particle where at a pH above 6 the predominant charge in solution would be $\text{AuCl}(\text{OH})_3^-$. In cases where the pH was above 9 the functionality could change to $\text{Au}(\text{OH})_4^-$. Since the pH had a maximum of 8.7 for the duration of the experiment it can be concluded that negative charges were due to the presence of $\text{AuCl}(\text{OH})_3^-$ ions [61, 65, 67]. The cellular uptake is highly dependent on the functional groups attached to the particle, as these would affect the charge and aggregation patterns [1].

4.2. Acute Toxicity and SSDs. The nAu SSD revealed that fish were more sensitive to nAu with an LC50 (when calculable) of between 12.08 mg/L and 52.6 mg/L, while daphnids were less sensitive with an LC50 ranging from approximately 70 mg/L to 75.31 mg/L. Since arthropods are able to undergo molting they would be able to cope with the nAu particles adhered onto their carapace. Literature to date shows no evidence of nAu uptake in daphnids while gold ions would be taken up [40]. Fish species are unable to molt and since respiration takes place over the gill surface it provides a large surface area for nAu uptake within the nanometer range; therefore larger agglomerates could possibly be taken up [35]. Fish have a far more complex digestive, respiratory, and excretory system when compared to *Daphnia* since ionic gold ions

have evolved with organisms and nAu have not; the fish is unable to cope with increased uptake and reduced excretion. Surface area and particle uptake play an important role in toxicity; it is therefore proposed that a threshold value for exposure concentrations exists; this occurs between 20 mg/L and 25 mg/L in the fish medium. Based on particle size distributions particle uptake is possible and accumulates in the organism in high enough concentrations to have an effect. The nAu have a high enough concentration to have an effect in an organism but agglomerations are still small enough in the medium to move through the cellular membrane. At concentrations above 25 mg/L particle interactions in the medium increase which decreases particle uptake into the organism.

When comparing the SSD plots it becomes apparent that the nAu and ionic gold have different distributions in toxicity. Smaller organisms, like *Daphnia*, have a higher sensitivity to ionic gold when compared to fish while for nAu exposures the opposite trend is seen. Reasons for this could be attributed to different effect and uptake mechanisms. Ionic gold follows the dose dependent response while nAu follow an aggregation theory response.

The SSD plots for the nAu and the ionic gold clearly indicate that there was a difference in the hazard potential of the two substances with the latter being an order of magnitude more toxic. This is in contrast to studies where SSDs comparing nano metals (i.e., CuO, ZnO, nAg, and nAl₂O₃) to their bulk metal (ionic) equivalents revealed that the hazard potentials were very similar [31, 32, 35, 40]. These authors attributed similar toxic potentials to the dissolution of the ionic metals from the particle, causing the particle toxicity to be similar to the bulk metal. However compared to nano metals that have the potential for metal ion dissolution, more inert nanoparticles such as TiO₂ and carbon nanotubes are much less toxic [34]. The results for nAu from this study support these findings.

At this stage the toxicity and therefore hazard assessment of nanoparticles are still very much based on dose-response (i.e., exposure concentration) relationships. Only when more data becomes available on the relationship between nanoparticle characteristics (e.g., size, shape, charge, and functional group) and the exposure medium will predictors of toxicity other than the release of metal ions become apparent. Notwithstanding the limitations of using only concentration-based toxicity data, the information provided by the SSDs for nAu provides useful ecotoxicological comparisons with other nanomaterials.

Conflict of Interests

The authors declare that there is no conflict of interests regarding the publication of this paper.

Acknowledgments

The research is based upon work supported by the Department of Science and Technology. The authors wish to thank MINTEK for supplying the nAu stock solutions.

References

- [1] C. S. Yah, "The toxicity of gold nanoparticles in relation to their physicochemical properties," *Biomedical Research*, vol. 24, no. 3, pp. 400–413, 2013.
- [2] M. Janowski, J. W. M. Bulte, and P. Walczak, "Personalized nanomedicine advancements for stem cell tracking," *Advanced Drug Delivery Reviews*, vol. 64, no. 13, pp. 1488–1507, 2012.
- [3] F. K. Alanazi, A. A. Radwan, and I. A. Alsarra, "Biopharmaceutical applications of nanogold," *Saudi Pharmaceutical Journal*, vol. 18, no. 4, pp. 179–193, 2010.
- [4] D. Fernandes, H. Carmo, M. Bastos, and S. Fraga, "Influence of surface coating on the toxicity of gold nanoparticles in Caco-2 cells," *Toxicology Letters*, vol. 196, p. S277, 2010.
- [5] G. Voskerician, M. S. Shive, R. S. Shawgo et al., "Biocompatibility and biofouling of MEMS drug delivery devices," *Biomaterials*, vol. 24, no. 11, pp. 1959–1967, 2003.
- [6] I. H. El-Sayed, X. Huang, and M. A. El-Sayed, "Surface plasmon resonance scattering and absorption of anti-EGFR antibody conjugated gold nanoparticles in cancer diagnostics: applications in oral cancer," *Nano Letters*, vol. 5, no. 5, pp. 829–834, 2005.
- [7] S. Arora, J. M. Rajwade, and K. M. Paknikar, "Nanotoxicology and in vitro studies: the need of the hour," *Toxicology and Applied Pharmacology*, vol. 258, no. 2, pp. 151–165, 2012.
- [8] H. J. Byrne, I. Lynch, W. H. de Jong et al., *Protocols for Assessment of Biological Hazards of Engineered Nanomaterials*, The European Network on the Health and Environmental Impact of Nanomaterials, 2010.
- [9] G. C. Delgado, "Economics and governance of nanomaterials: potential and risks," *Technology in Society*, vol. 32, no. 2, pp. 137–144, 2010.
- [10] N. Lewinski, V. Colvin, and R. Drezek, "Cytotoxicity of nanoparticles," *Small*, vol. 4, no. 1, pp. 26–49, 2008.
- [11] D. Kühnel and C. Nickel, "The OECD expert meeting on ecotoxicology and environmental fate—towards the development of improved OECD guidelines for the testing of nanomaterials," *Science of the Total Environment*, vol. 472, pp. 347–353, 2014.
- [12] V. Wepener and P. M. Chapman, "South African ecotoxicology: present status and future prognosis," *African Journal of Aquatic Science*, vol. 37, no. 3, pp. 229–234, 2012.
- [13] J. C. Chapman, "The role of ecotoxicity testing in assessing water quality," *Australian Journal of Ecology*, vol. 20, no. 1, pp. 20–27, 1995.
- [14] K. D. Kimball and S. A. Levin, "Limitations of laboratory bioassays: the need for ecosystem-level testing," *BioScience*, vol. 35, no. 3, pp. 165–171, 1985.
- [15] J. Martins, L. O. Teles, and V. Vasconcelos, "Assays with *Daphnia magna* and *Danio rerio* as alert systems in aquatic toxicology," *Environment International*, vol. 33, no. 3, pp. 414–425, 2007.
- [16] D. R. Grothe, K. L. Dickson, and D. K. Reed-Judkins, *Whole Effluent Toxicity Testing: An Evaluation of Methods and Prediction of Receiving System Impacts*, SETAC Special Publications Series, SETAC Press, Pensacola, Fla, USA, 1996.
- [17] G. M. Rand, P. G. Wells, and L. S. McCarty, *Fundamentals of Aquatic Toxicology: Effects, Environmental Fate and Risk Assessment*, edited by: G. M. Rand, Taylor & Francis, 2nd edition, 1995.
- [18] P. B. Dorn, "An industrial perspective on whole effluent toxicity testing," in *Whole Effluent Toxicity Testing: An Evaluation of Methods and Predictions of Receiving Impacts*, D. R. Grothe,

- K. L. Dickson, and D. K. Reed-Judkins, Eds., Society of Environmental Toxicology and Chemistry Special Publications Series, Society of Environmental Toxicology and Chemistry, Pensacola, Fla, USA, 1996.
- [19] H. C. Sarakinos, N. Bermingham, P. A. White, and J. B. Rasmussen, "Correspondence between whole effluent toxicity and the presence of priority substances in complex industrial effluents," *Environmental Toxicology and Chemistry*, vol. 19, no. 1, pp. 63–71, 2000.
- [20] R. Smolders, L. Bervoets, V. Wepener, and R. Blust, "A conceptual framework for using mussels as biomonitors in whole effluent toxicity," *Human and Ecological Risk Assessment*, vol. 9, no. 3, pp. 741–760, 2003.
- [21] S. Jergentz, P. Pessacq, H. Mugni, C. Bonetto, and R. Schulz, "Linking in situ bioassays and population dynamics of macroinvertebrates to assess agricultural contamination in streams of the Argentine pampa," *Ecotoxicology and Environmental Safety*, vol. 59, no. 2, pp. 133–141, 2004.
- [22] P. M. Chapman, "Whole effluent toxicity testing—usefulness, level of protection, and risk assessment," *Environmental Toxicology and Chemistry*, vol. 19, no. 1, pp. 3–13, 2000.
- [23] Department of Water Affairs and Forestry (DWAF), "The management of complex industrial wastewater discharges: introducing the Direct Estimation of Ecological Effect Potential (DEEEP) approach," A Discussion Document, Department of Water Affairs and Forestry, Institute for Water Quality Studies, Pretoria, South Africa, 2003.
- [24] A. R. Fernández-Alba, L. H. Guil, G. D. López, and Y. Chisti, "Toxicity of pesticides in wastewater: a comparative assessment of rapid bioassays," *Analytica Chimica Acta*, vol. 426, no. 2, pp. 289–301, 2001.
- [25] C. G. Palmer, W. J. Muller, and H. D. Davies-Coleman, "Applied aquatic toxicology: sub-lethal methods, whole effluent testing and communication," WRC Report No. 1245/1/04, Water Research Commission, Pretoria, South Africa, 2004.
- [26] L. Maltby, N. Blake, T. C. M. Brock, and P. J. van den Brink, "Insecticide species sensitivity distributions: importance of test species selection and relevance to aquatic ecosystems," *Environmental Toxicology and Chemistry*, vol. 24, no. 2, pp. 379–388, 2005.
- [27] L. Posthuma, T. P. Traas, and G. W. Suter II, "General introduction to species sensitivity distributions," in *Species Sensitivity Distribution in Ecotoxicology*, L. Posthuma, T. P. Traas, and G. W. Suter II, Eds., Lewis Publishers, Boca Raton, Fla, USA, 2002.
- [28] J. R. Wheeled, E. P. M. Grist, K. M. Y. Leung, D. Morrith, and M. Crane, "Species sensitivity distributions: data and model choice," *Marine Pollution Bulletin*, vol. 45, no. 1-12, pp. 192–202, 2002.
- [29] M. C. Newman, D. R. Ownby, L. C. A. Mezin et al., "Applying species-sensitivity distribution in ecological risk assessment: assumptions of distribution type and sufficient numbers of species," *Environmental Toxicology and Chemistry*, vol. 19, no. 2, pp. 508–515, 2000.
- [30] S. Browne, *The role of acute toxicity data for South African freshwater macroinvertebrates in the derivation of water quality guidelines for salinity [M.S. thesis]*, Rhodes University, Grahamstown, South Africa, 2005.
- [31] N. Adam, C. Schmitt, L. de Bruyn, D. Knapen, and R. Blust, "Aquatic acute species sensitivity distributions of ZnO and CuO nanoparticles," *Science of The Total Environment*, vol. 526, pp. 233–242, 2015.
- [32] K. L. Garner, S. Suh, H. S. Lenihan, and A. A. Keller, "Species sensitivity distributions for engineered nanomaterials," *Environmental Science & Technology*, vol. 49, no. 9, pp. 5753–5759, 2015.
- [33] H. Johnston, D. Brown, A. Kermanizadeh, E. Gubbins, and V. Stone, "Investigating the relationship between nanomaterial hazard and physicochemical properties: informing the exploitation of nanomaterials within therapeutic and diagnostic applications," *Journal of Controlled Release*, vol. 164, no. 3, pp. 307–313, 2012.
- [34] B. J. Shaw and R. D. Handy, "Physiological effects of nanoparticles on fish: a comparison of nanometals versus metal ions," *Environment International*, vol. 37, no. 6, pp. 1083–1097, 2011.
- [35] S. J. Klaine, P. J. J. Alvarez, G. E. Batley et al., "Nanomaterials in the environment: behavior, fate, bioavailability, and effects," *Environmental Toxicology and Chemistry*, vol. 27, no. 9, pp. 1825–1851, 2008.
- [36] C. J. Murphy, A. M. Gole, J. W. Stone et al., "Gold nanoparticles in biology: beyond toxicity to cellular imaging," *Accounts of Chemical Research*, vol. 41, no. 12, pp. 1721–1730, 2008.
- [37] G. Fren, "Preparation of gold dispersions of varying particle size: controlled nucleation for the regulation of the particle size in monodisperse gold suspensions," *Nature Physics*, vol. 241, pp. 20–22, 1973.
- [38] OECD, *Oecd Guideline for Testing of Chemicals: Fish, Acute Toxicity Tests*, 1992.
- [39] E. Truter, *Method of Estimating the Chronic Toxicity of a Chemical or Water Sample to the Cladoceran Daphnia pulex*, Department of Water Affairs and Forestry, Department of Water Affairs & Forestry, Pretoria, South Africa, 1994.
- [40] T. Li, B. Albee, M. Alemayehu et al., "Comparative toxicity study of Ag, Au, and Ag-Au bimetallic nanoparticles on *Daphnia magna*," *Analytical and Bioanalytical Chemistry*, vol. 398, no. 2, pp. 689–700, 2010.
- [41] S.-H. Nam, W.-M. Lee, Y.-J. Shin et al., "Derivation of guideline values for gold (III) ion toxicity limits to protect aquatic ecosystems," *Water Research*, vol. 48, no. 1, pp. 126–136, 2014.
- [42] F. von der Kammer, P. L. Ferguson, P. A. Holden et al., "Analysis of engineered nanomaterials in complex matrices (environment and biota): general considerations and conceptual case studies," *Environmental Toxicology and Chemistry*, vol. 31, no. 1, pp. 32–49, 2012.
- [43] V. Stone, B. Nowack, A. Baun et al., "Nanomaterials for environmental studies: classification, reference material issues, and strategies for physico-chemical characterisation," *Science of the Total Environment*, vol. 408, no. 7, pp. 1745–1754, 2010.
- [44] M. A. Hamilton, R. C. Russo, and R. V. Thurston, "Trimmed Spearman-Kärber method for estimating median lethal concentrations in toxicity bioassays," *Environmental Science & Technology*, vol. 11, no. 7, pp. 714–719, 1977, Correction: vol. 12, p. 417, 1978.
- [45] American Public Health Association (APHA), *Standard Methods for the Examination of Water and Wastewater*, American Water Works Association (AWWA), Water Environment Federation (WEF), Washington, DC, USA, 1992.
- [46] United States Environmental Protection Agency (USEPA), *CADDIS Volume 4: Data Analysis*, United States Environmental Protection Agency (USEPA), 2012, <http://www.epa.gov/>.
- [47] N. Oh and J.-H. Park, "Endocytosis and exocytosis of nanoparticles in mammalian cells," *International Journal of Nanomedicine*, vol. 9, no. 1, pp. 51–63, 2014.

- [48] K. T. Kim, S. J. Klaine, J. Cho, S.-H. Kim, and S. D. Kim, "Oxidative stress responses of *Daphnia magna* exposed to TiO₂ nanoparticles according to size fraction," *Science of the Total Environment*, vol. 408, no. 10, pp. 2268–2272, 2010.
- [49] B. Fadeel and A. E. Garcia-Bennett, "Better safe than sorry: understanding the toxicological properties of inorganic nanoparticles manufactured for biomedical applications," *Advanced Drug Delivery Reviews*, vol. 62, no. 3, pp. 362–374, 2010.
- [50] A. M. Schrand, M. F. Rahman, S. M. Hussain, J. J. Schlager, D. A. Smith, and A. F. Syed, "Metal-based nanoparticles and their toxicity assessment," *Wiley Interdisciplinary Reviews: Nanomedicine and Nanobiotechnology*, vol. 2, no. 5, pp. 544–568, 2010.
- [51] W. Cui, J. Li, Y. Zhang, H. Rong, W. Lu, and L. Jiang, "Effects of aggregation and the surface properties of gold nanoparticles on cytotoxicity and cell growth," *Nanomedicine: NBM*, vol. 8, no. 1, pp. 46–53, 2011.
- [52] H. Weinberg, A. Galyean, and M. Leopold, "Evaluating engineered nanoparticles in natural waters," *TrAC Trends in Analytical Chemistry*, vol. 30, no. 1, pp. 72–83, 2011.
- [53] R. J. Griffitt, J. Luo, J. Gao, J.-C. Bonzongo, and D. S. Barber, "Effects of particle composition and species on toxicity of metallic nanomaterials in aquatic organisms," *Environmental Toxicology and Chemistry*, vol. 27, no. 9, pp. 1972–1978, 2008.
- [54] A. Elsaesser and C. V. Howard, "Toxicology of nanoparticles," *Advanced Drug Delivery Reviews*, vol. 64, no. 2, pp. 129–137, 2012.
- [55] R. N. Grass, L. K. Limbach, E. K. Athanassiou, and W. J. Stark, "Exposure of aerosols and nanoparticle dispersions to in vitro cell cultures: a review on the dose relevance of size, mass, surface and concentration," *Journal of Aerosol Science*, vol. 41, no. 12, pp. 1123–1142, 2010.
- [56] L. Treuel, M. Malissek, J. S. Gebauer, and R. Zellner, "The influence of surface composition of nanoparticles on their interactions with serum albumin," *ChemPhysChem*, vol. 11, no. 14, pp. 3093–3099, 2010.
- [57] A. Tabrizi, F. Ayhan, and H. Ayhan, "Gold nanoparticle synthesis and characterisation," *Hacettepe Journal of Biology and Chemistry*, vol. 37, no. 3, pp. 217–226, 2009.
- [58] M. Baalousha, Y. Nur, I. Römer, M. Tejamaya, and J. R. Lead, "Effect of monovalent and divalent cations, anions and fulvic acid on aggregation of citrate-coated silver nanoparticles," *Science of the Total Environment*, vol. 454–455, pp. 119–131, 2013.
- [59] M. Delay, T. Dolt, A. Woellhaf, R. Sembritzki, and F. H. Frimmel, "Interactions and stability of silver nanoparticles in the aqueous phase: influence of natural organic matter (NOM) and ionic strength," *Journal of Chromatography A*, vol. 1218, no. 27, pp. 4206–4212, 2011.
- [60] I. Römer, T. A. White, M. Baalousha, K. Chipman, M. R. Viant, and J. R. Lead, "Aggregation and dispersion of silver nanoparticles in exposure media for aquatic toxicity tests," *Journal of Chromatography A*, vol. 1218, no. 27, pp. 4226–4233, 2011.
- [61] J. Farkas, P. Christian, J. A. G. Urrea et al., "Effects of silver and gold nanoparticles on rainbow trout (*Oncorhynchus mykiss*) hepatocytes," *Aquatic Toxicology*, vol. 96, no. 1, pp. 44–52, 2010.
- [62] D. G. Abradelo, R. Cao, and R. Cea, "Self-aggregation of bilayer ferrocenyl termini gold nanoparticles," *Inorganic Chemistry Communications*, vol. 10, no. 5, pp. 511–513, 2007.
- [63] G. M. Fent, S. W. Casteel, D. Y. Kim, R. Kannan, K. Katti, and N. Chanda, "Biodistribution of maltose and gum arabic hybrid gold nanoparticles after intravenous injection in juvenile swine," *Nanomedicine: Nanotechnology, Biology, and Medicine*, vol. 5, no. 2, pp. 128–135, 2009.
- [64] Y.-J. Gu, J. Cheng, C.-C. Lin, Y. W. Lam, S. H. Cheng, and W.-T. Wong, "Nuclear penetration of surface functionalized gold nanoparticles," *Toxicology and Applied Pharmacology*, vol. 237, no. 2, pp. 196–204, 2009.
- [65] B. H. Stuart, *Modern Infrared Spectroscopy*, Analytical Chemistry by Open Learning Series, John Wiley & Sons, 1995.
- [66] R. Pal, S. Panigrahi, D. Bhattacharyya, and A. S. Chakraborti, "Characterization of citrate capped gold nanoparticle-quercetin complex: experimental and quantum chemical approach," *Journal of Molecular Structure*, vol. 1046, pp. 153–163, 2013.
- [67] A. Lapresta-Fernández, A. Fernández, and J. Blasco, "Nanocytotoxicity effects of engineered silver and gold nanoparticles in aquatic organisms," *Trends in Analytical Chemistry*, vol. 32, pp. 40–59, 2012.

Research Article

Sea-Urchin-Like ZnO Nanoparticle Film for Dye-Sensitized Solar Cells

Cheng-Wen Ma, Chia-Ming Chang, Po-Cheng Huang, and Yao-Joe Yang

Department of Mechanical Engineering, National Taiwan University, No. 1, Section 4, Roosevelt Road, Taipei 10617, Taiwan

Correspondence should be addressed to Yao-Joe Yang; yjy@ntu.edu.tw

Received 19 May 2015; Accepted 14 July 2015

Academic Editor: Tapan Desai

Copyright © 2015 Cheng-Wen Ma et al. This is an open access article distributed under the Creative Commons Attribution License, which permits unrestricted use, distribution, and reproduction in any medium, provided the original work is properly cited.

We present novel sea-urchin-like ZnO nanoparticles synthesized using a chemical solution method. Solution approaches to synthesizing ZnO nanostructures have several advantages including low growth temperatures and high potential for scaling up. We investigated the influence of reaction times on the thickness and morphology of sea-urchin-like ZnO nanoparticles, and XRD patterns show strong intensity in every direction. Dye-sensitized solar cells (DSSCs) were developed using the synthesized ZnO nanostructures as photoanodes. The DSSCs comprised a fluorine-doped tin oxide (FTO) glass with dense ZnO nanostructures as the working electrode, a platinized FTO glass as the counter electrode, N719-based dye, and I-/I³⁻-liquid electrolyte. The DSSC fabricated using such nanostructures yielded a high power conversion efficiency of 1.16% with an incident photo-to-current efficiency (IPCE) as high as 15.32%. Electrochemical impedance spectroscopy was applied to investigate the characteristics of DSSCs. An improvement in the electron transport in the ZnO photoanode was also observed.

1. Introduction

Dye-sensitized solar cells (DSSCs) provide efficient solar-energy conversion and have attracted substantial attention over the past decade because of their structural flexibility, low cost, and ease of fabrication [1–3]. In general, DSSCs comprise a porous TiO₂ nanoparticle photoanode [4–6]. Researchers in many recent studies have focused on improving performance through developing new substitutes for porous TiO₂ nanoparticle films for use in photoanodes, such as the TiO₂-nanowire type [7, 8] and TiO₂-nanotube type [9, 10]. However, a recombination problem usually occurs in TiO₂ nanocrystals because of the lack of a depletion layer on the TiO₂ surface. The severity of the recombination problem increases with the TiO₂ photoanode film thickness [11].

In recent years, ZnO-based materials have been widely studied for use as photoanodes for DSSC devices [12]. Although ZnO has a similar energy level of the conduction band as that of TiO₂, the ZnO-based DSSCs in general give lower efficiency as compared to TiO₂-based DSSCs. One of the reasons is caused by the precipitation of the sensitizing dye with Zn cations for the ZnO-based DSSCs. However, it

is relatively difficult to grow TiO₂ films on a substrate with controlled structure, which in turn limits the development of TiO₂-based DSSCs. Furthermore, in terms of material characteristics, ZnO has a few advantages over TiO₂, such as higher electronic mobility and more flexibility in high-area film morphologies. Therefore, ZnO is considered as one of the promising alternatives for TiO₂ as the core material of DSSCs.

Numerous types of ZnO nanostructures have been proposed for application in DSSCs. For example, Law et al. [13] proposed a DSSC including a dense array of oriented ZnO nanowires as a photoanode material with a 1.51% conversion efficiency. In [14], ZnO nanotube photoanodes templated using anodic aluminum oxide for use in DSSCs were reported. Anodic aluminum oxide templating and atomic layer deposition were employed to yield oriented arrays of electrically interconnected nanotubes. In addition, in [15], ZnO nanoforest photoanodes, which effectively increased the power conversion efficiency to approximately 2.63%, were introduced. The efficiency increase is due to the substantially enhanced surface area and reduced charge recombination. Kakiuchi et al. [16] proposed a DSSC with a ZnO nanosheet structure synthesized using Zn(NO₃)₂ and (NH₂)₂CO,

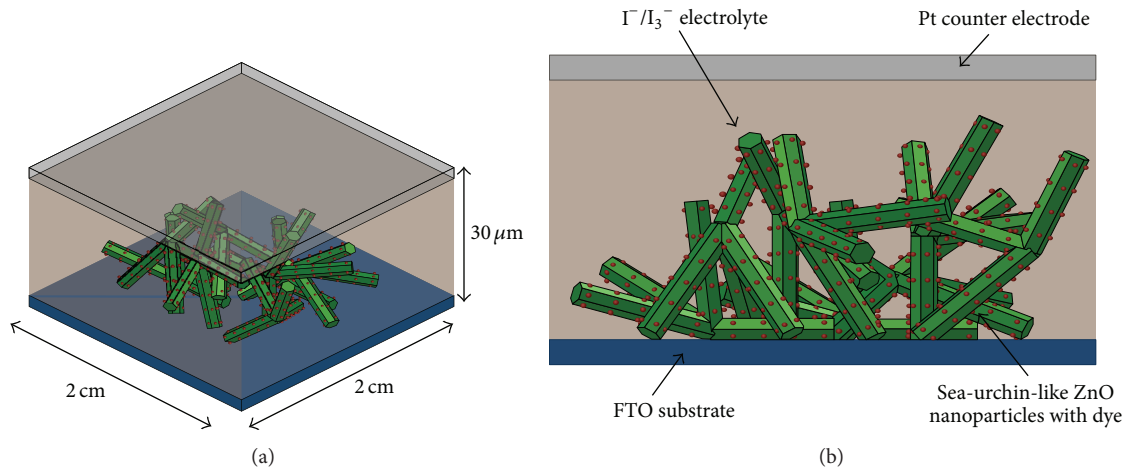


FIGURE 1: (a) Schematic of the dye-sensitized solar cell based on sea-urchin-like ZnO nanoparticles. (b) Schematic of the side view.

achieving a conversion efficiency of 3.3%. In [17], ZnO nanoarchitecture fabricated on a plastic substrate by using a facile room-temperature chemical-bath deposition method was presented. A notable efficiency of 5.24% was simply achieved using a low crystallization temperature and the anisotropic growth of ZnO. In addition, the synthesis of a DSSC with a sponge-like ZnO nanostructure was reported in [18]. By using a polymer gel electrolyte to stabilize the dye/ZnO/electrolyte interface, an improvement of the electron injection efficiency, photovoltaic conversion efficiencies, and the long-term durability of ZnO-based DSSCs was achieved.

In this work, we propose a DSSC in which the photoanode is based on sea-urchin-like ZnO nanoparticles that can be easily formed through chemical solution synthesis. We also studied the effects of nanoparticle morphologies on different synthesis parameters. In addition, the sea-urchin-like structures may potentially enhance the surface area to improve dye absorbance. Because of the branched characteristic of the sea-urchin-like structures, they can easily form strong conductive networks.

The remainder of this paper is organized as follows. Section 2 describes the synthesis, photoanode preparation, and DSSC fabrication. The measurement results are presented in Section 3. Conclusions are provided in Section 4.

2. Synthesis of Nanoparticles

Figure 1 shows a schematic of the proposed DSSC. From the lower to the upper layer, the cell comprises a fluorine-doped tin oxide (FTO) transparent conductive glass with a ZnO photoanode and platinized counter electrode. Organic dye molecules are absorbed on the photoanode, with the electrolyte positioned between the electrodes. This study proposes using novel sea-urchin-like ZnO nanoparticles as a photoanode material according to the following fabrication process.

The chemical solution method [19] was used to synthesize the sea-urchin-like ZnO nanoparticle structure. First,

a room-temperature solution was prepared. The solution was composed of 75 mM zinc nitrate hexahydrate, 25 mM HMTA, 5 mM PEI, and 0.80 M ammonium hydroxide. The reaction solution was heated in two steps [20]. In a container, the solution was first heated to 85°C in a water bath while covered by a watch glass. After 15 min, the glass was removed, exposing the solution to open air for another 15 min. The nondirectional ZnO nanostructures (sea-urchin-like ZnO nanoparticles) formed on the bottom of the container. Next, the container was covered with the watch glass to prevent further solution evaporation. The deposited ZnO structure continued to grow. Finally, the sea-urchin-like ZnO nanoparticles were deposited on the top of the FTO electrode.

After the synthesis reaction, the FTO covered with a sea-urchin-like ZnO nanoparticle film (the photoanode) was dried in N₂ for a few minutes and then heated in a tube furnace at 400°C for 30 min. The heating process enhanced the mechanical strength of the ZnO film and the adhesion between the film and the FTO substrate.

The FTO substrate with the sea-urchin-like ZnO nanoparticles (the fabricated photoanode) was immersed in an ethanol solution of N719 dye at 50°C for 2 h. After fully absorbing the dye molecules, the FTO substrate was washed with ethanol and then air dried. A FTO glass deposited with a platinum film served as the counter electrode. The photoanode and counter electrode were then sandwiched using Surlyn E185SB (Dupont). A liquid electrolyte was then injected into the cavity of the photoanode and counter electrode. The electrolyte contains 0.5 M LiI, 50 mM I₂, and 0.5 M 4-tert-butylpyridine in a 3-methoxypropionitrile solvent [13].

3. Results and Discussion

3.1. Morphology and Structure Characterization. Figures 2(a) and 2(b) show the SEM images of the sea-urchin-like ZnO nanoparticles with various deposition times. Figure 2(c) illustrates the detailed structural morphologies, indicating that the longer the deposition time, the longer the branch length of the ZnO nanoparticles because of the increased reaction time,

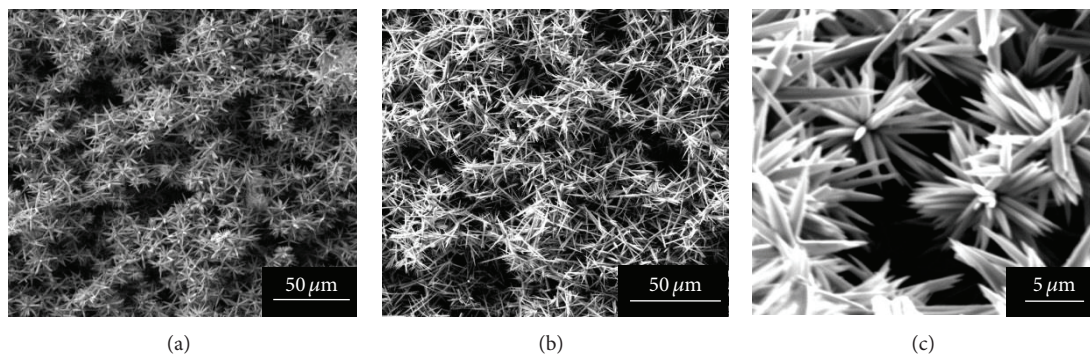


FIGURE 2: SEM pictures of sea-urchin-like ZnO nanoparticles after (a) 2 hr deposition and (b) 8 hr deposition. (c) The detailed structure morphology of the nanoparticle (8 hr deposition).

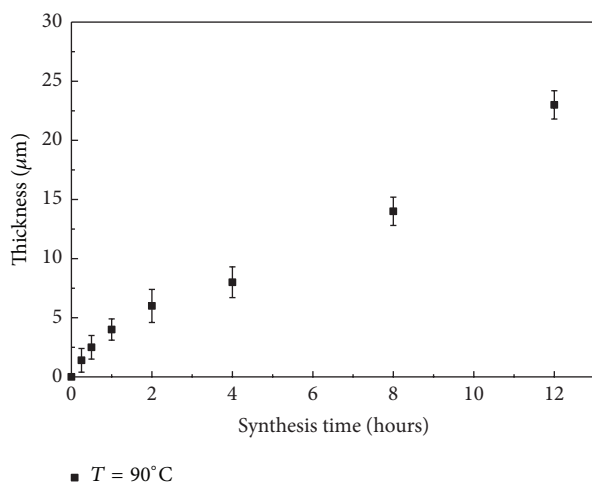


FIGURE 3: Measured relationship of structure thickness versus synthesis time.

and the sea-urchin-like structure becomes more obvious. As the length of the sea-urchin-like structure increases, the effective total surface area of the photoanode also increases, thus enhancing dye absorbance.

Figure 3 depicts the measured relationship of the thickness of the structure versus the synthesis time. A longer deposition time resulted in a thicker nanostructure. The thickness of the synthesized structure increased from 0 to about 25 μm within 12 h. During the early stage of the synthesis process (synthesis time is less than 4 hours), the ZnO particles are relatively small and the branches on each ZnO particle are relatively thin and short. These particles closely pile up to form a ZnO film. However, as the synthesis time is larger than 4 hours, the ZnO particles become thicker and the branches of each ZnO particle become thicker and longer (i.e., stronger). These bigger ZnO particles are relatively difficult to be closely packed and stacked. As a result, these bigger particles with stronger branches uphold the film structure, and the density of the film becomes smaller, as compared with the film formed by smaller particles. Therefore, the film thickness increases faster as the synthesis time is larger than 4 hours.

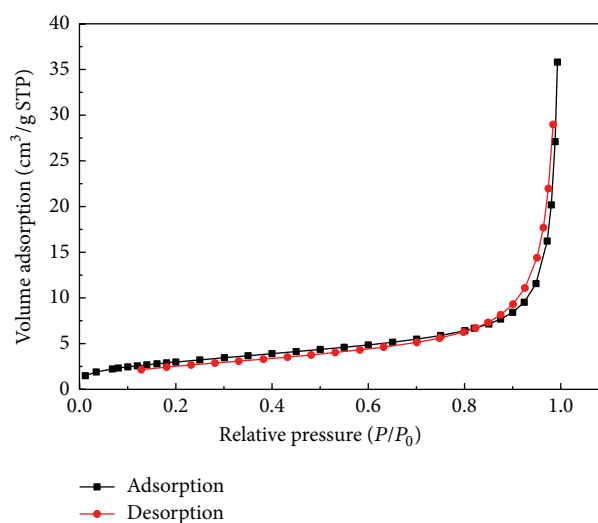


FIGURE 4: Typical N_2 adsorption-desorption isotherms for the sea-urchin-like ZnO film.

As shown in Figures 2(a) and 2(b), the ZnO film of 4-hour synthesis is more packed than the ZnO film of 8-hour synthesis.

The specific surface area and average internal pore morphology of the sea-urchin-like ZnO nanoparticle film were obtained by analyzing nitrogen adsorption and desorption isotherms (Figure 4). According to the results, the sea-urchin-like ZnO film can be categorized as a general Type III isotherm that exhibits no hysteresis. The isotherms indicated that nitrogen adsorption and desorption occur predominantly at $P/P_0 > 0.8$. Figure 5 shows the results of the pore size analysis conducted using the Barrett, Joyner, and Halenda (BJH) method. The specific surface area was calculated using the standard Brunauer-Emmett-Teller (BET) analysis of the adsorption isotherms and was estimated at about 11.09 m^2/g . The surface area-to-volume ratio from this analysis implied an average pore diameter of about 198.8 \AA .

The crystal orientation of the sea-urchin-like ZnO nanoparticles structure was characterized using X-ray diffraction (Rigaku TTRAX 3) (Figure 6). The diffraction

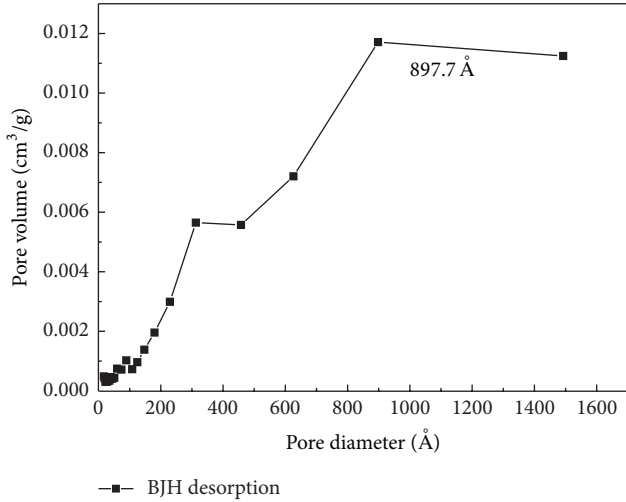


FIGURE 5: BJH pore diameter distribution curve.

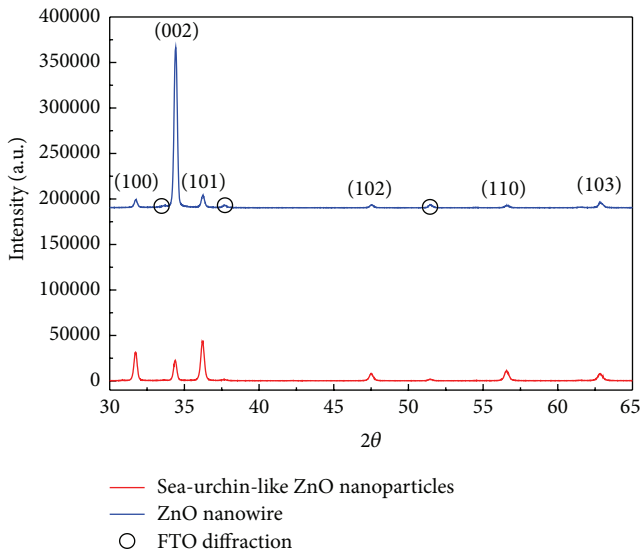


FIGURE 6: XRD patterns of sea-urchin-like ZnO nanoparticles and ZnO nanowires.

peaks can be indexed as a hexagonal wurtzite ZnO phase in contrast to JCPDS Card number 75-1526 [21]. Compared with the XRD patterns of typical ZnO nanowires, the *Z*-direction (002) intensity of the sea-urchin-like ZnO nanoparticles was relatively flat, indicating that the orientations of the ZnO crystal structures in the sea-urchin-like structure are quite random.

3.2. Photocurrent-Voltage and Power Conversion Characteristics. Current-voltage (*I-V*) curve measurements were conducted using a source meter (Keithley 2410). Simulated AM 1.5 G (100 mW/cm^2) illumination was provided by a solar light source (Newport class A), and the light intensity was measured using a calibrated Si solar cell. The total measurement area of the photoanode was 0.25 cm^2 , and the voltage swept from -1 to 1 V in fixed increments of 0.02 V .

TABLE 1: Photovoltaic performance data of the proposed DSSC with different synthesis times.

	J_{SC} (mA/cm^2)	V_{OC} (V)	FF	η (%)
2 hrs	3.37	0.45	53.85	0.81
4 hrs	4.01	0.49	58.00	1.14
8 hrs	4.70	0.59	50.19	1.16
16 hrs	1.24	0.33	70.87	0.29

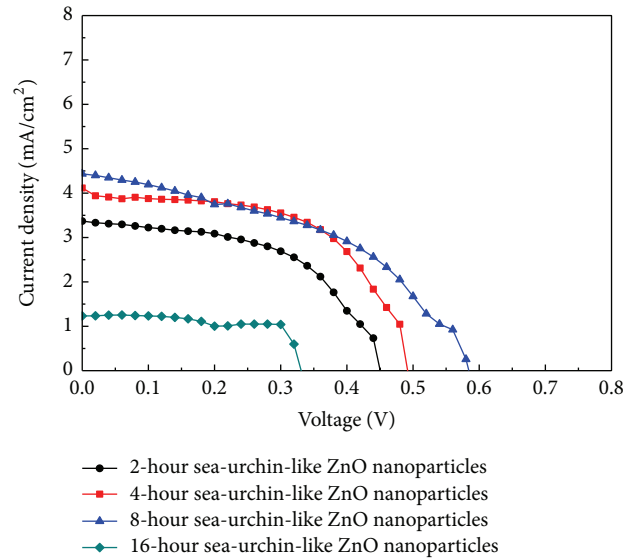


FIGURE 7: *I-V* characteristic curve of the proposed DSSC.

Figure 7 illustrates the *I-V* characteristics of the sea-urchin-like ZnO nanoparticles with dissimilar deposition times. The longer the deposition time was, the higher the photocurrent was. Notably, at a deposition time of 16 h, the photocurrent became extremely low, possibly because overdeposited nanoparticles caused the electron transport pathway to become excessively long, thus substantially reducing the power conversion efficiency. The maximum conversion efficiency was approximately 1.16%. The corresponding photovoltaic parameters are summarized in Table 1.

Incident photo-to-current efficiency (IPCE) spectrum measurements were also conducted using a 300 W xenon lamp and a grating monochromator. In the measurement, the wavelength ranged from 400 to 800 nm with a spectral resolution of 20 nm. The samples fabricated at various deposition times were measured. Figure 8 depicts the results of the IPCE characteristics for different sea-urchin-like ZnO nanoparticles. The results are similar to the adsorption spectrum of N719 dye [22]. In the current study, the highest IPCE value was 15.32%.

The impedance and phase were measured under an illumination of 100 mW/cm^2 . The AC signal parameter was 10 mV, and the scanning range was from 105 to 0.05 Hz. The measured samples were the same as those used in the IPCE measurement. Figure 9 shows the Nyquist plot of two sea-urchin-like ZnO nanoparticles fabricated using different deposition times. Table 2 lists the derived circuit parameters

TABLE 2: Summary of derived circuit parameters: the impedance of transport resistance of the electrons in ZnO (R_t), charge transfer resistance of charge recombination process (R_{ct}), electron lifetime (τ), chemical capacitance of the ZnO (C_μ), electron diffusion coefficient in ZnO (D), and effective diffusion length (L_n).

Cell	$f_{\max,m}$ (s^{-1})	τ (ms)	R_{ct} (Ω)	R_t (Ω)	C_μ (μF)	D (cm^2/s)	L_n (μm)
2 hrs	1.28	124	2247	608.3	55.4	1.186×10^{-4}	38.4
8 hrs	3.17	50.1	2736	1059	18.3	2.06×10^{-4}	32.1

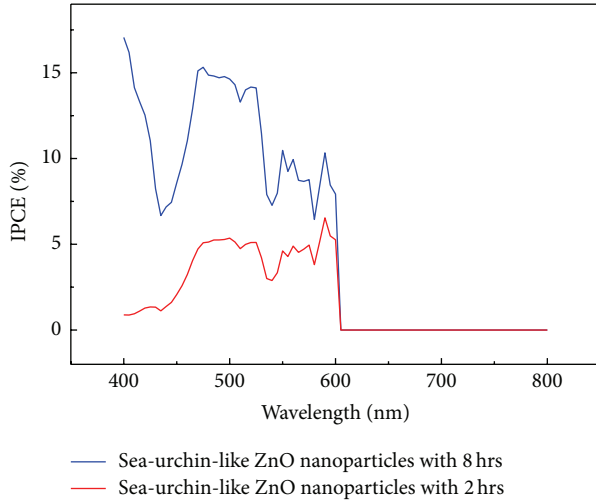


FIGURE 8: IPCE spectra of the proposed DSSCs.

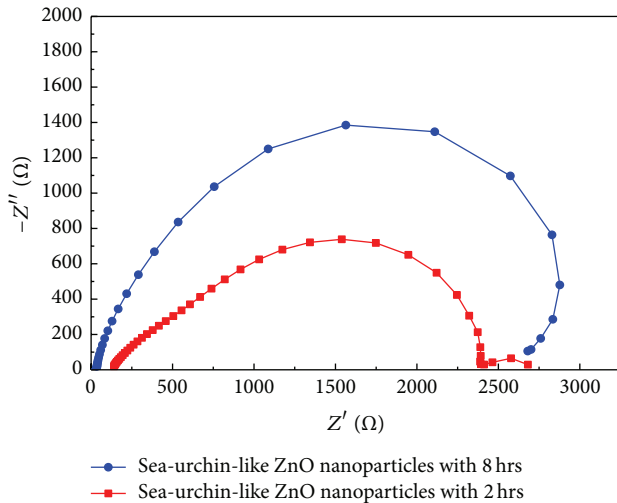


FIGURE 9: Nyquist plot of the proposed DSSC with different synthesis times.

after the data were fitted using a proper equivalent circuit model [23]. The results indicated that a thicker photoanode resulted in a higher electron transport resistance (R_t) and a higher charge transfer resistance of the charge recombination process (R_{ct}). The lifetime (τ) of injected electrons in the ZnO nanoparticles is defined as $\tau = 1/2\pi f$. According to the EIS model, the frequency f can be extracted using the position of the medium-frequency peak shown in Figure 6, where f is

the medium-frequency peak [24]. This figure also shows that thicker photoanodes provide a longer electron lifetime.

4. Conclusion

In this study, we developed novel photoanode material architecture based on sea-urchin-like ZnO nanoparticles and integrated it into a DSSC system. Nanoparticles were synthesized using a simple chemical solution method. The effect of the reaction parameters on the ZnO nanostructure morphology was also studied. BET analysis of the adsorption isotherms was employed to estimate the specific surface area at approximately $11.09 \text{ m}^2/\text{g}$. In addition, the XRD patterns of the ZnO film showed strong intensity in every direction, indicating that the orientations of the ZnO nanostructures are randomly distributed. The sample synthesized using a deposition time of 8 h exhibited a high power conversion efficiency of approximately 1.16% and an IPCE efficiency of approximately 15.32%. The characteristics of DSSCs measured using electrochemical impedance spectroscopy are also presented.

Conflict of Interests

The authors declare that there is no conflict of interests regarding the publication of this paper.

Acknowledgment

This work was supported in part by the National Science Council, Taiwan (Contract no. NSC 100-2221-E-002-074-MY3).

References

- [1] M. Grätzel, "Photoelectrochemical cells," *Nature*, vol. 414, no. 6861, pp. 338–344, 2001.
- [2] S. Gubbala, V. Chakrapani, V. Kumar, and M. K. Sunkara, "Band-edge engineered hybrid structures for dye-sensitized solar cells based on SnO_2 nanowires," *Advanced Functional Materials*, vol. 18, no. 16, pp. 2411–2418, 2008.
- [3] G. K. Mor, K. Shankar, M. Paulose, O. K. Varghese, and C. A. Grimes, "Use of highly-ordered TiO_2 nanotube arrays in dye-sensitized solar cells," *Nano Letters*, vol. 6, no. 2, pp. 215–218, 2006.
- [4] B. O'Regan and M. Grätzel, "A low-cost, high-efficiency solar cell based on dye-sensitized colloidal TiO_2 films," *Nature*, vol. 353, no. 6346, pp. 737–740, 1991.
- [5] Y. G. Seo, K. Woo, J. Kim, H. Lee, and W. Lee, "Rapid fabrication of an inverse opal TiO_2 photoelectrode for DSSC using a binary mixture of TiO_2 nanoparticles and polymer microspheres," *Advanced Functional Materials*, vol. 21, no. 16, pp. 3094–3103, 2011.

- [6] E. S. Kwak, W. Lee, N.-C. Park, J. Kim, and H. Lee, "Compact inverse-opal electrode using non-aggregated TiO₂ nanoparticles for dye-sensitized solar cells," *Advanced Functional Materials*, vol. 19, no. 7, pp. 1093–1099, 2009.
- [7] B. Liu and E. S. Aydil, "Growth of oriented single-crystalline rutile TiO₂ nanorods on transparent conducting substrates for dye-sensitized solar cells," *Journal of the American Chemical Society*, vol. 131, no. 11, pp. 3985–3990, 2009.
- [8] X. Feng, K. Shankar, O. K. Varghese, M. Paulose, T. J. Latempa, and C. A. Grimes, "Vertically aligned single crystal TiO₂ nanowire arrays grown directly on transparent conducting oxide coated glass: synthesis details and applications," *Nano Letters*, vol. 8, no. 11, pp. 3781–3786, 2008.
- [9] G. Yang, C. Miao, Z. Bu, Q. Wang, and W. Guo, "Seed free and low temperature growth of ZnO nanowires in mesoporous TiO₂ film for dye-sensitized solar cells with enhanced photovoltaic performance," *Journal of Power Sources*, vol. 233, pp. 74–78, 2013.
- [10] K. Zhu, T. B. Vinzant, N. R. Neale, and A. J. Frank, "Removing structural disorder from oriented TiO₂ nanotube arrays: reducing the dimensionality of transport and recombination in dye-sensitized solar cells," *Nano Letters*, vol. 7, no. 12, pp. 3739–3746, 2007.
- [11] Q. Zhang, C. S. Dandeneau, X. Zhou, and C. Cao, "ZnO nanostructures for dye-sensitized solar cells," *Advanced Materials*, vol. 21, no. 41, pp. 4087–4108, 2009.
- [12] C.-X. He, B.-X. Lei, Y.-F. Wang, C.-Y. Su, Y.-P. Fang, and D.-B. Kuang, "Sonochemical preparation of hierarchical ZnO hollow spheres for efficient dye-sensitized solar cells," *Chemistry—A European Journal*, vol. 16, no. 29, pp. 8757–8761, 2010.
- [13] M. Law, L. E. Greene, J. C. Johnson, R. Saykally, and P. Yang, "Nanowire dye-sensitized solar cells," *Nature Materials*, vol. 4, no. 6, pp. 455–459, 2005.
- [14] A. B. F. Martinson, J. W. Elam, J. T. Hupp, and M. J. Pellin, "ZnO nanotube based dye-sensitized solar cells," *Nano Letters*, vol. 7, no. 8, pp. 2183–2187, 2007.
- [15] S. H. Ko, D. Lee, H. W. Kang et al., "Nanoforest of hydrothermally grown hierarchical ZnO nanowires for a high efficiency dye-sensitized solar cell," *Nano Letters*, vol. 11, no. 2, pp. 666–671, 2011.
- [16] K. Kakiuchi, M. Saito, and S. Fujihara, "Fabrication of ZnO films consisting of densely accumulated mesoporous nanosheets and their dye-sensitized solar cell performance," *Thin Solid Films*, vol. 516, no. 8, pp. 2026–2030, 2008.
- [17] G.-J. Chang, S.-Y. Lin, and J.-J. Wu, "Room-temperature chemical integration of ZnO nanoarchitectures on plastic substrates for flexible dye-sensitized solar cells," *Nanoscale*, vol. 6, no. 3, pp. 1329–1334, 2014.
- [18] Y. Shi, K. Wang, Y. Du et al., "Solid-state synthesis of ZnO nanostructures for quasi-solid dye-sensitized solar cells with high efficiencies up to 6.46%," *Advanced Materials*, vol. 25, no. 32, pp. 4413–4419, 2013.
- [19] L. Vayssieres, K. Keis, S.-E. Lindquist, and A. Hagfeldt, "Purpose-built anisotropic metal oxide material: 3d highly oriented microrod array of ZnO," *The Journal of Physical Chemistry B*, vol. 105, no. 17, pp. 3350–3352, 2001.
- [20] L. Wang, D. Tsan, B. Stoeber, and K. Walus, "Substrate-free fabrication of self-supporting ZnO nanowire arrays," *Advanced Materials*, vol. 24, no. 29, pp. 3999–4004, 2012.
- [21] P. Yang, H. Yan, S. Mao et al., "Controlled growth of ZnO nanowires and their optical properties," *Advanced Functional Materials*, vol. 12, no. 5, pp. 323–331, 2002.
- [22] M. K. Nazeeruddin, R. Humphry-Baker, P. Liska, and M. Grätzel, "Investigation of sensitizer adsorption and the influence of protons on current and voltage of a dye-sensitized nanocrystalline TiO₂ solar cell," *The Journal of Physical Chemistry B*, vol. 107, no. 34, pp. 8981–8987, 2003.
- [23] M. Adachi, M. Sakamoto, J. Jiu, Y. Ogata, and S. Isoda, "Determination of parameters of electron transport in dye-sensitized solar cells using electrochemical impedance spectroscopy," *The Journal of Physical Chemistry B*, vol. 110, no. 28, pp. 13872–13880, 2006.
- [24] R. Kern, R. Sastrawan, J. Ferber, R. Stangl, and J. Luther, "Modeling and interpretation of electrical impedance spectra of dye solar cells operated under open-circuit conditions," *Electrochimica Acta*, vol. 47, no. 26, pp. 4213–4225, 2002.

Research Article

Functionalised Au Coated Iron Oxide Nanocomposites Based Reusable Immunosensor for AFB1 Detection

Ruchika Chauhan and T. Basu

Amity Institute of Nanotechnology, Amity University, Uttar Pradesh, Noida 201301, India

Correspondence should be addressed to T. Basu; basu002@yahoo.com

Received 17 March 2015; Accepted 14 June 2015

Academic Editor: Tapan Desai

Copyright © 2015 R. Chauhan and T. Basu. This is an open access article distributed under the Creative Commons Attribution License, which permits unrestricted use, distribution, and reproduction in any medium, provided the original work is properly cited.

A reusable sandwiched electrochemical piezoelectric immunosensor has been developed for aflatoxin B1 (AFB1) detection using gold coated iron oxide core-shell (Au-Fe₃O₄) nanostructure. The monoclonal anti-aflatoxin antibody (aAFB1) was immobilized on self-assembled monolayer of 4-aminothiophenol on gold coated quartz crystal to fabricate immunoelectrode (BSA/aAFB1/4-ATP/Au). In addition, secondary rabbit-immunoglobulin antibodies (r-IgGs) functionalized with Au-Fe₃O₄ NPs via cysteamine (r-IgG-Cys-Au-Fe₃O₄) were allowed to interact with AFB1. Both competitive and noncompetitive strategies were employed and a competition between coated AFB1 and free AFB1 was carried out. The competitive mode shows higher linear range (0.05 to 5 ng mL⁻¹) than the noncompetitive one (0.5 to 5 ng mL⁻¹), high sensitivity 335.7 μ A ng⁻¹ mL cm⁻², and LOD 0.07 ng mL⁻¹. The fabricated immunosensor has been tested using cereal samples spiked with different concentrations of AFB1. The developed competitive immunoelectrode displays good reproducibility, and storage stability and regenerated with negligible loss in activity through removal of the r-IgG-Cys-Au-Fe₃O₄ conjugate using a strong external magnet.

1. Introduction

Aflatoxin B1 (AFB1), which is a low molecular mass compound mainly produced by the moulds *Aspergillus flavus* and *Aspergillus parasiticus*, can contaminate several important crops (e.g., corn, sorghum, peanuts, fruits, dried fruits, cocoa, and spices) under favorable environmental conditions [1, 2]. Owing to high toxicity and carcinogenicity, AFB1 is of major concern for food producers, the food processing industry, and consumers [3]. The European Commission has set the maximum permissible residue levels for AFB1 in corn products ready for retail sale at 2 μ g kg⁻¹ [4–7]. Compared to conventional techniques [8–10], immunosensors are an interesting alternative that can be used to quantify and detect selectively toxin molecules [11–14]. Some of the biosensing techniques used for AFB1 detection include electrochemical biosensors [15, 16], surface plasmon resonance [17, 18], fluorescent biosensors [19, 20], and quartz crystal (piezoelectric) microbalance based sensors [21, 22]. Among the signal detection techniques, quartz crystal microbalance (QCM) based detection systems are considered to be the most promising

for immunointeraction owing to their affordable cost and real-time and label-free compatibility with miniaturization, portability, and high sensitivity [23–25].

The immunosensors which employ monoclonal antibody, synthesized from animal source as a receptor, are fast and efficient technique no doubt but are expensive and used for one time only. Therefore it will be advantageous to develop reusable immunosensor which can be regenerated mechanically without any chemical as the chemicals affect biological activity of the receptor antibody [26, 27]. In 2009, Wang and Gan have used magnetic core-shell Fe₃O₄/SiO₂ composite nanoparticles to regenerate the QCM crystal. In this regard, magnetic nanoparticles (MNP) can be considered as one of the potential tools to regenerate immunosensor using strong external magnet [28]. The MNP is commonly used in the coated form to gain biocompatibility and stability [29, 30]. Since AFB1 is a low molecular weight (Mwt. 312) molecule, competitive mode of detection could provide the desired detection limit and sensitivity [31, 32]. The competition occurs between coated toxin (toxin-protein conjugate)

and free toxin. The few binding sides of coated toxin (antigen-protein complex) are partially blocked through the toxin-protein binding. Therefore, the secondary antibody captures free toxin leaving heavy toxin-protein complex.

In this study, a sandwich type electrochemical quartz crystal microbalance (EQCM) based reusable immunosensor (BSA/aAFBI/4-ATP/Au) was fabricated using self-assembled monolayer of 4-aminothiophenol on gold coated quartz crystal. The gold coated magneto nanoparticles attached to the secondary antibody were used as a signal enhancing agent and for regeneration of the immunoelectrode through external magnet. Both competitive and noncompetitive strategy are studied. Here, competition occurs between free AFBI and coated AFBI (with no protein bonded). Interestingly, we have observed that competition mode offers wider linearity, lower detection range, and higher sensitivity. The constructed immunosensor can be used for estimation of aflatoxin B1 from sample and regenerated with negligible loss of activity using a strong external magnet.

2. Experimental Methods

2.1. Chemicals and Reagents. Monoclonal anti-aflatoxin B1 (aAFBI) antibodies, aflatoxin B1 (AFBI), bovine serum albumin (BSA), polyclonal IgG antibodies from rabbit (r-IgG), 4-aminothiophenol (4-ATP), *N*-ethyl-*N*-(3-dimethylaminopropyl) carbodiimide (EDC), *N*-hydroxysuccinimide (NHS), ferrous chloride hexahydrate ($\text{FeCl}_2 \cdot 6\text{H}_2\text{O}$), ferric chloride tetrahydrate ($\text{FeCl}_3 \cdot 4\text{H}_2\text{O}$), sodium hydroxide (NaOH), and chloroauric acid ($\text{HAuCl}_4 \cdot \text{H}_2\text{O}$) were procured from Sigma-Aldrich. All reagents were of analytical grade and used without further purification, and deionized water (18 M Ω cm) was used for the preparation of solutions. The gold coated (diameter: 6.7 mm) quartz resonator (AT cut quartz crystal, 13.7 mm dia, 6 MHz) was procured from Autolab, Netherlands.

2.2. Solution Preparation. Anti-AFBI antibody (1 mg mL⁻¹) solution was prepared in 50 mM phosphate buffer (PBS), 50 mM, pH 7.4, and a 0.15 M NaN₃ was used as a preservative. r-IgG antibody (2 mg mL⁻¹) solution was prepared in 50 mM PBS (pH 7.4). The stock solution of AFBI was prepared in PBS (50 mM, pH 7.4) with 10% methanol and diluted in different working concentrations and stored at -20°C. A solution of bovine serum albumin (BSA, 1 mg mL⁻¹) was prepared in PBS (50 mM, pH 7.0) and used as blocking agent for nonspecific binding sites.

2.3. Pretreatment of Quartz Crystals. The quartz crystals were immersed in 1 M NaOH for 5 min and 1 M HCl for 2 min in a sequence. Then, freshly prepared piranha solution {1:3 (30% v/v) H₂O₂-H₂SO₄} was dropped on the gold surface for 2 min, with special care to avoid the contamination of the electrode leads. The quartz crystals were rinsed twice with deionized water followed by ethanol and dried in a stream of nitrogen after each pretreatment and then the initial resonance frequency (F_0) was recorded. After the above

cleaning procedure, the quartz crystal was ready for surface modification and antibody immobilization.

2.4. Synthesis of Fe₃O₄ and Au Coated Fe₃O₄. Fe₃O₄ NPs were synthesized simply by the coprecipitation method reported earlier [33] with some modification. Solution of 0.07 M FeCl₃·6H₂O and 0.04 M FeCl₂·4H₂O (2:1, w/w ratio) was dissolved in 25 mL deionized water and then this mixture was added dropwise to the 100 mL solution of 0.15 mM NaOH with stirring under N₂ atmosphere at room temperature. A black precipitate of Fe₃O₄ NPs was obtained. The black precipitate of Fe₃O₄ NPs thus obtained was dissolved in 20 mL citrate buffer (1.6 gm citric acid and 0.8 gm trisodium citrate) to stabilize ferrofluid in solution at a pH around 6.3.

The Au-Fe₃O₄ core-shell NPs were prepared using 3 mL of the synthesized colloidal Fe₃O₄ nanosuspension (0.1 M), boiled with 25 mL of ultrapure water under vigorous stirring condition. Then 0.2 mM HAuCl₄ was added, followed by the addition of 10 mM trisodium citrate, and the reaction mixture was kept boiling and stirring for 15 min till the color of the solution turned red from black. The gold coated Fe₃O₄ NPs (Au-Fe₃O₄ NPs) solution was allowed to cool and stored in a dark glass bottle at 4°C before use.

2.5. Synthesis of r-IgG-Cys-Au-Fe₃O₄. Synthesized Au-Fe₃O₄ nanosuspension was treated with 10⁻³ M cysteamine and HCl in 1:15 volume ratio for 12 h at 25°C. Cysteamine functionalized Au-Fe₃O₄ NPs (Cys-Au-Fe₃O₄) were separated and purified by centrifugation at 10,000 rpm for 10 min. The purification and centrifugation process were repeated 4-5 times for removing nonbonded cysteamine. Then cysteamine functionalized Au-Fe₃O₄ core-shell NPs were redispersed in PB (50 mM, pH 7.0) solution. Cysteamine forms a self-assembled layer on Au-Fe₃O₄ NPs which provides NH₂ group to bind favorably with COOH functional group of the polyclonal r-IgG antibodies during immobilization. The r-IgG antibodies are mixed with Cys-Au-Fe₃O₄ solution in 1:3 (v/v ratio) [34], followed by addition of 0.2 M EDC and 0.05 M NHS for the activation of -COOH group present in antibody. Further to block the nonspecific sites on the r-IgG-Cys-Au-Fe₃O₄ conjugates, 100 μ L BSA (1 mg mL⁻¹) was added and incubated for 2 h at 25°C. The mixture was centrifuged at 10,000 rpm for 10 min and washed for 4-5 times. Finally, the r-IgG-Cys-Au-Fe₃O₄ conjugate was resuspended in PB (50 mM, pH 7.4) and stored at 4°C until use.

2.6. Fabrication of AFBI/BSA/aAFBI/4-ATP/Au Immunosensor. Pretreated quartz crystal was immersed in 2 mM solution of 4-ATP in ethanol for 24 h at 25°C for SAM formation. However, a uniform and steady 4-ATP film was obtained [35]. The crystal was subsequently washed with ethanol followed by rinsing with water to remove any unbound ATP molecules. 10 μ L of the monoclonal anti-aflatoxin B1 (aAFBI) antibody, activated with 0.2 M EDC and 0.05 M NHS for about 2 h, was spread over the electrode and incubated overnight at 4°C for the amide bond formation between aAFBI and 4-ATP. In this study, optimized concentration of 40 μ g mL⁻¹ of aAFBI

was used. The nonspecific sites of fabricated immunoelectrodes were blocked with BSA (1 mg mL^{-1}). These fabricated BSA/aAFBI/4-ATP/Au immunoelectrodes were exposed to saturated concentration of AFBI (5 ng mL^{-1}) for 35 min at 25°C .

2.7. Pretreatment and Analysis of Cereal Samples. The cereal samples (corn flakes) were spiked after the treatment. Corn flakes samples were crushed to powder using a hand-held blender. 2 g of powdered cereals was added to methanol: water (7 : 3, v/v) solution on a sonication bath for 45 min. The extract was centrifuged for 7 min at 5000 rpm to remove the solids. The supernatants were collected and allowed to evaporate to dryness under nitrogen at 25°C . The residues were resuspended in 5 mL PBS and filtered through $0.45 \mu\text{m}$ nylon membranes [36]. Finally, extract was spiked with the different concentrations of 0.05, 2, and 5 ng mL^{-1} of aAFBI.

2.8. Instrumentation. The resonant frequency of quartz crystal and electrochemical studies were monitored by Autolab Potentiostat/Galvanostat Model AUT83945 (PGSTAT302N). The electrochemical quartz crystal cyclic voltammetric (EQCM-CV) studies were carried out in a three-electrode cell using modified quartz crystal as the working electrode, gold wire as the auxiliary electrode, and saturated Ag/AgCl as the reference electrode in PBS (50 mM, pH 7.4, 0.9% NaCl) containing 5 mM $[\text{Fe}(\text{CN})_6]^{3-/4-}$ as a redox species. The Au- Fe_3O_4 core-shell magnetic nanoparticles were characterized by scanning electron microscopy (ZEISS EVO-18), vibrating sample magnetometer (VSM) (Microsense, ADE-Model EV9), transmission electron microscopy (JEOL JEM (Model 1200F)), and X-ray diffractometer from Bruker AXS (XRD). The structural and surface morphological characterizations of 4-ATP/Au, aAFBI/4-ATP/Au, BSA/aAFBI/4-ATP/Au, and AFBI/BSA/aAFBI/4-ATP/Au electrode were carried out using Fourier transform infrared spectroscopy (FT-IR, Perkin-Elmer, Model 2000), scanning electron microscopy (ZEISS EVO-18), and Autolab Potentiostat/Galvanostat Model AUT83945 (PGSTAT302N).

3. Results and Discussion

3.1. Characterization of Fe_3O_4 and Au- Fe_3O_4 Core-Shell Structure. Figure 1(a) shows the UV-Visible absorption spectrum of pure magnetic Fe_3O_4 NPs, Au NPs, and Au- Fe_3O_4 (curve (c)) core-shell NPs. Typical absorption spectra of pure Fe_3O_4 NPs (curve (a)) exhibit absorption edge at $\sim 340 \text{ nm}$. The absorption peak seen at 324 nm and the sharp absorption maxima at 527 nm (curve (b)) are assigned for pure Au NPs exhibiting strong absorption that is dependent on the size and shape of particles. For spherical nanoparticles, the absorption band maximum generally falls between about 520 and 532 nm [37]. The UV-Visible absorption spectrum of Au- Fe_3O_4 core-shell (curve (c)) structure shows a broad peak at 532 nm . The shifting of peak position towards longer wavelengths (red shift) and disappearance of peak edge arise due to Fe_3O_4 ,

indicating the formation of bimetallic core-shell structure with the existence of Fe_3O_4 as core. Au covers the Fe_3O_4 NPs surface and provides a broad shifted peak at 532 nm due to inherent surface plasmon resonance property of Au NPs.

The magnetic properties of Fe_3O_4 NPs and Au- Fe_3O_4 core-shell structure were analyzed by vibrating sample magnetometer (VSM) at 17 K . Figure 1(b) shows the hysteresis loop measured for the Fe_3O_4 NPs (curve (a)), Fe_3O_4 NPs in citrate buffer (curve (b)), and Au- Fe_3O_4 core-shell structure (curve (c)). The values of saturated magnetization from the hysteresis curve of the pure Fe_3O_4 NPs and Fe_3O_4 NPs in buffer were found to be 0.0028 and 0.0085 emu/g , respectively, at 17 K . The saturated magnetization of Fe_3O_4 NPs dispersed in citrate buffer was increased by ~ 4 times compared with the precipitated Fe_3O_4 NPs indicating uniform dispersion of Fe_3O_4 particles in citrate buffer. In the dispersed form, each NP acts like a tiny magnet, resulting in a higher magnetic moment density than that of precipitated Fe_3O_4 NPs. The saturated specific magnetization of Au- Fe_3O_4 core-shell structure decreases to 0.0022 emu/g . This decrease may be due to the fact that the gold is a nonmagnetic material, which could decrease the saturated specific magnetization [38] indicating that the gold was successfully coated on Fe_3O_4 NPs to form Au- Fe_3O_4 core shell.

EQCM-CV (Figure 1(c)) of Fe_3O_4 NPs dispersion and Au- Fe_3O_4 NPs were studied in PBS buffer (50 mM, pH 7.4, 0.9% NaCl) containing 5 mM $[\text{Fe}(\text{CN})_6]^{3-/4-}$. $100 \mu\text{L}$ of NPs dispersion was added to buffer to conduct CV at a scan rate of 100 mV/s in the potential range of -0.2 to 0.8 V {Figure 1(c) (a, b, and c)}. Curve (a) represents the EQCM-CV of $[\text{Fe}(\text{CN})_6]^{3-/4-}$ redox system in PBS buffer. The magnitude of the peak current increases after adding Fe_3O_4 NPs (curve (b)) which further increases on adding Au- Fe_3O_4 core shell (curve (c)) showing an enhanced electron transform rate through the medium to surface of electrode and confirming the Au is successfully coated onto Fe_3O_4 NPs.

To confirm the formation of Au- Fe_3O_4 NPs, EDX analysis has been studied for elemental composition in Fe_3O_4 and Au- Fe_3O_4 NPs. Figure 2(a) (images (A) and (B) for Fe_3O_4 and Au- Fe_3O_4 NPs) shows the presence of Fe peak at 6.8 keV and absence of Au peak in image (A), while image (B) shows peaks both for Au at 2.4 keV and 9.5 keV and for Fe at 0.58 keV , 6.5 keV , and 7.1 keV , respectively. The weight percentage of these elements, shown as insets of respective images, indicates the presence of corresponding elements.

Figure 2(b) shows the TEM images of Fe_3O_4 NPs, Fe_3O_4 NPs in citrate buffer, and Au- Fe_3O_4 NPs. The average particle size of Fe_3O_4 NPs, Fe_3O_4 NPs in citrate buffer, and Au- Fe_3O_4 NPs was $\sim 8 \text{ nm}$, $\sim 13 \text{ nm}$, and $\sim 19 \text{ nm}$, respectively. Figure 2(b), image (A), shows Fe_3O_4 NPs overlap each other, while image (B) shows the uniform distribution of Fe_3O_4 NPs in ionic citrate buffer. It reveals that in buffer solution ionic citrate layer surrounds the Fe_3O_4 NPs. Image (C) presents the Au- Fe_3O_4 core-shell NPs having bilayer structure with a dark center surrounded by a lighter layer. The molecular d spacing is 0.48 nm for darker part and 0.23 nm (from ImageJ software) for light part of shell. The lattice distances measured for the shell correspond to the known Au lattice parameters

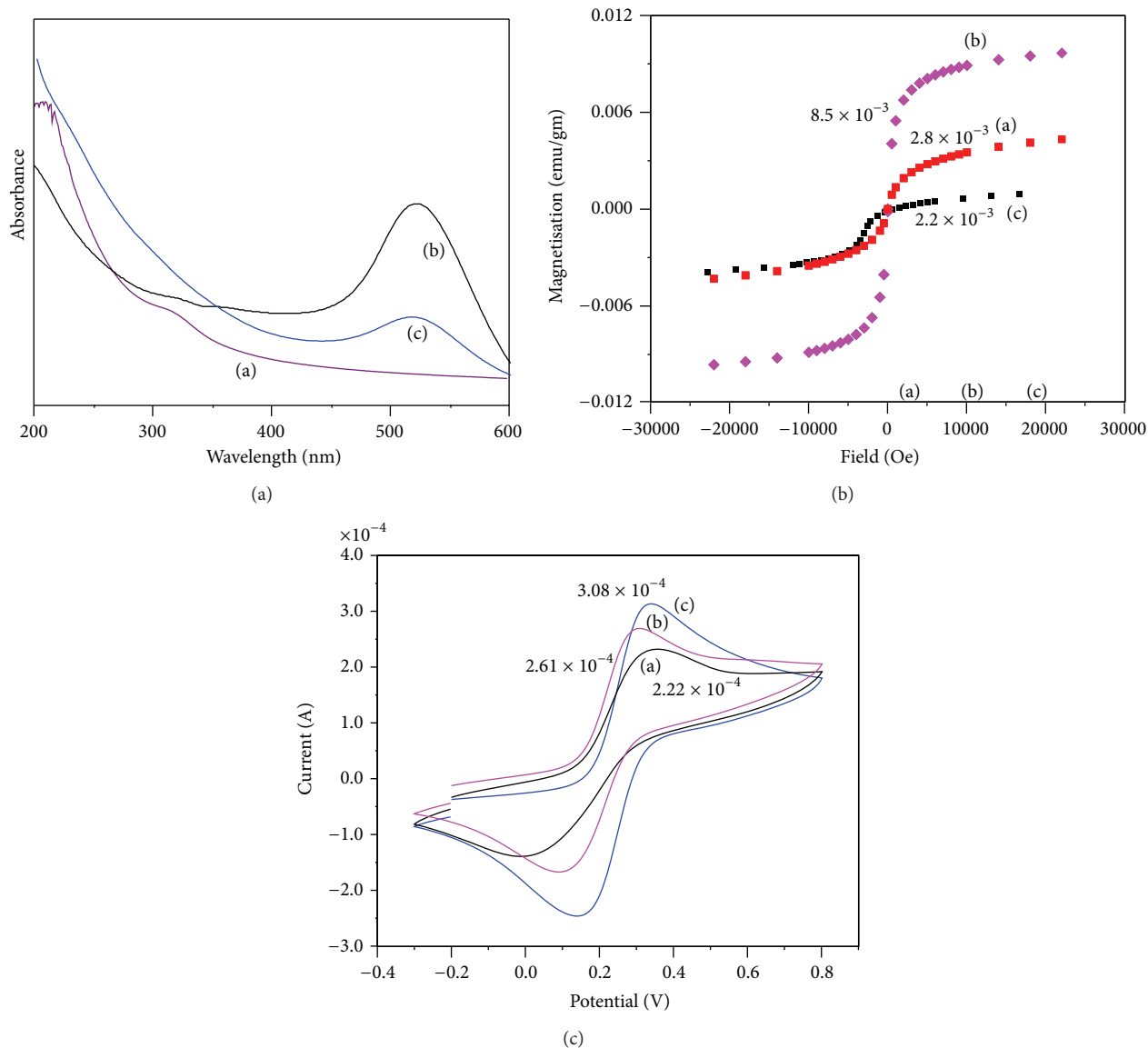


FIGURE 1: (a) UV-Visible spectra of (a) Fe₃O₄, (b) Au NPs, and (c) Au-Fe₃O₄ NPs. (b) VSM of (a) Fe₃O₄, (b) Fe₃O₄ in citrate buffer, and (c) Au-Fe₃O₄ NPs. (c) CV of (a) bare Au crystal, (b) Fe₃O₄, and (c) Au-Fe₃O₄ NPs in PBS containing [Fe(CN)₆]^{3-/4-}.

for the (111) plane and those measured for the core match well the Fe₃O₄ lattice parameters for the (311) plane. The presence of these two phases is also confirmed by X-ray diffraction (XRD) analysis. The XRD pattern of the Fe₃O₄ NPs and Au-Fe₃O₄ core-shell NPs, demonstrated in Figures 2(c) (a) and 2(c) (b), shows diffraction peaks at 2θ 30.15°, 35.76°, 43.2°, 53.6°, 57.6°, and 62.96° for Fe₃O₄ which exhibit indexed (220), (311), (400), (422), (511), and (440). For Au-Fe₃O₄ (graph (b)), the characteristic peaks seen at 38.28°, 44.43°, 59.1°, 64.70°, and 77.81°, marked by their indices (111), (200), (220), (311), and (222), are observed indicating that the Fe₃O₄ in Au-Fe₃O₄ NPs resembles pure Fe₃O₄ with a spinel hexagonal structure [39, 40].

3.2. Characterization of r-IgG-Cys-Au-Fe₃O₄. The conjugate formation of r-IgG-Cys-Au-Fe₃O₄ was confirmed by

UV-absorption spectroscopy (Figure 3(a)). The absorbance maxima for the pure r-IgG antibody solution appear at 250 nm (curve (a)) whereas the r-IgG-Cys-Au-Fe₃O₄ conjugate shows two peaks observed at 258 nm for r-IgG and 529 nm for Au-Fe₃O₄ (curve (b)). Broadening in peaks and slight red shift are also observed in both peaks due to increased size of NPs. These results indicate that the r-IgG antibodies are immobilized onto the surface of the Cys-Au-Fe₃O₄ core-shell structure. Scheme 1 represents the formation of r-IgG-Cys-Au-Fe₃O₄ conjugate.

The EQCM-CV (Figure 3(b)) of cysteamine functionalized Au-Fe₃O₄ NPs and r-IgG-Au-Fe₃O₄ conjugate corroborates the fabrication of secondary antibody conjugate with Au-Fe₃O₄ NPs. EQCM-CV was studied in PBS buffer (50 mM, pH 7.4, 0.9% NaCl) containing 5 mM [Fe(CN)₆]^{3-/4-} at a scan rate of 100 mV/s in the potential range of -0.2

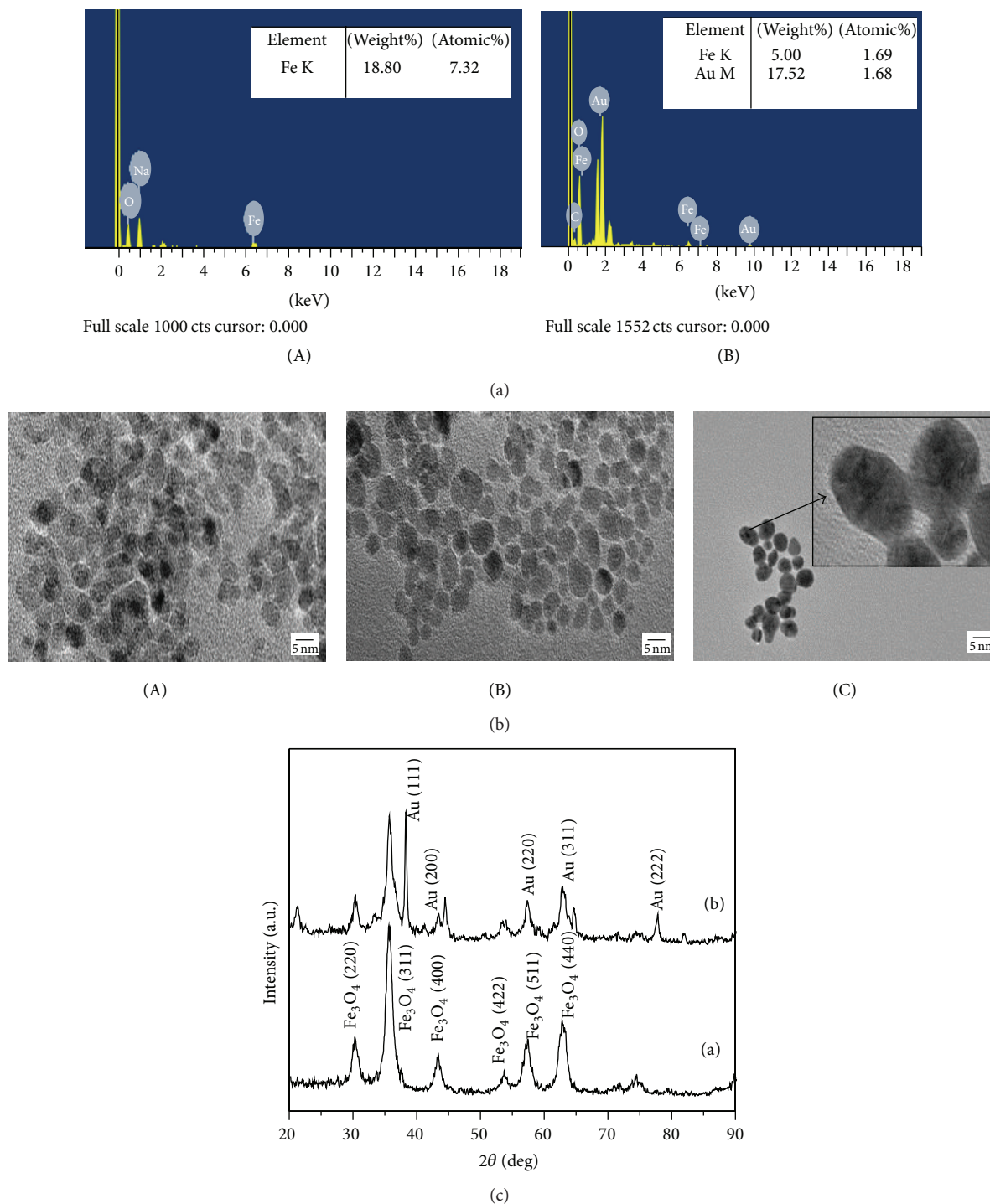


FIGURE 2: (a) EDX of (A) Fe₃O₄ NPs and (B) Au-Fe₃O₄ NPs. (b) TEM image of (A) Fe₃O₄, (B) Fe₃O₄ in buffer, and (C) Au-Fe₃O₄ NPs. (c) XRD of (a) Fe₃O₄ and (b) Au-Fe₃O₄ NPs.

to 0.8 V {Figure 3(b) (a, b, and c)}. 100 μ L of conjugate dispersion was added to the buffer to conduct CV of conjugates. Curve (a) represents the EQCM-CV of Au-Fe₃O₄ nanoparticles in [Fe(CN)₆]^{3-/4-} redox system in PBS buffer. The magnitude of the peak current decreases after functionalization of Au-Fe₃O₄ nanoparticles with cysteamine

(curve (b)); decrease in current occurs due to the insulating nature of cysteamine. The EQCM-CV of r-IgG-Au-Fe₃O₄ conjugate (curve (c)) in [Fe(CN)₆]^{3-/4-} redox system results in increase in current, due to the presence of carboxyl and amine group throughout the IgG antibodies indicating the formation of r-IgG-Cys-Au-Fe₃O₄ conjugates.

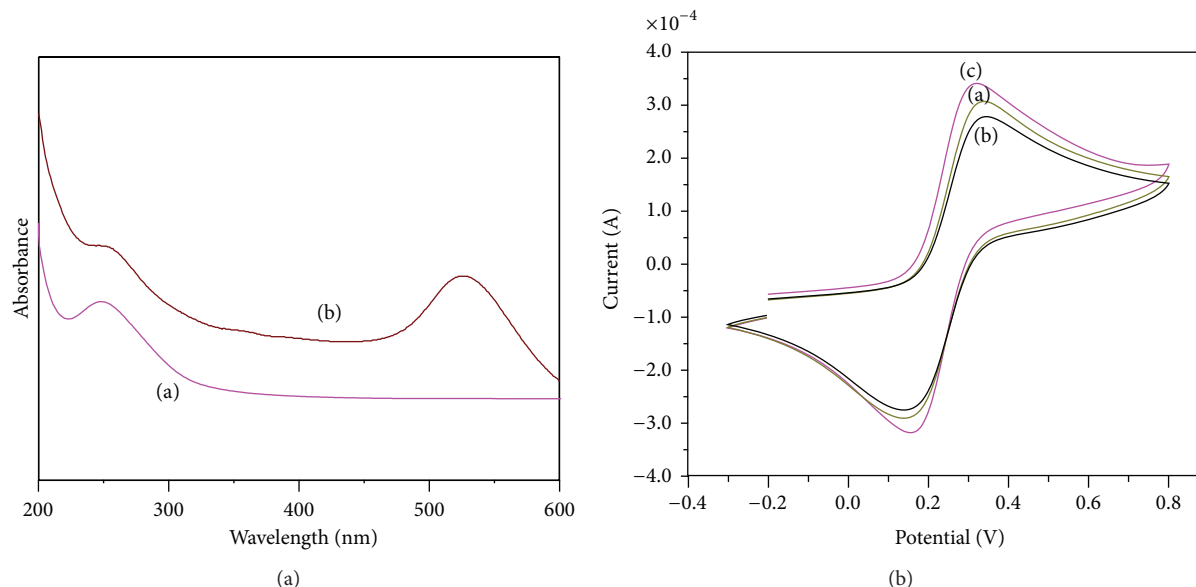
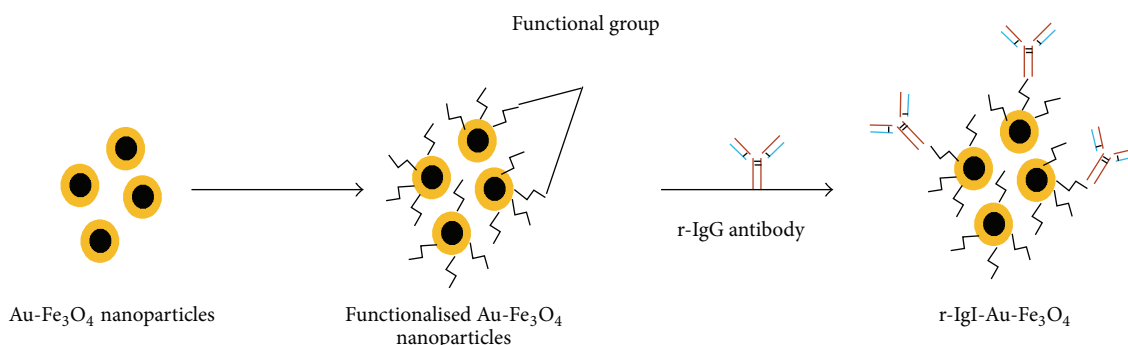


FIGURE 3: (a) UV-Visible spectra of (a) r-IgG antibody and (b) r-IgG-Cys-Au-Fe₃O₄ conjugate. (b) CV of (a) Au-Fe₃O₄ NPs, (b) Cys-Au-Fe₃O₄ NPs, and (c) r-IgG-Cys-Au-Fe₃O₄ conjugate in PBS (pH 7.4) containing [Fe(CN)₆]^{3-/4-}.



SCHEME 1: Scheme representing the formation of r-IgG-Cys-Au-Fe₃O₄ conjugate.

3.3. Characterization of the Immunosensor

3.3.1. Electrochemical Characterization of the Immuno-electrode. EQCM-CV shows both frequency and current changes. Figure 4(a) represents the change in frequency of QCM (ΔF) after the SAM deposition of 4-ATP on the bare gold crystal surface obtained at a scan rate of 100 mV/s in the potential range of -0.2 to 0.8 V. The cleaned bare quartz crystal was taken as a reference. The frequency changes increase as mass increases on the electrode surface; the continuous increase in mass reveals the successive deposition of electrode.

Table 1 shows the list of mass deposition over the electrode at each layer. The successive deposition of various layers on Au quartz crystal is understood by mass change of $206.50 \text{ ng cm}^{-2}$ for 4-ATP, $268.71 \text{ ng cm}^{-2}$ for aAFB1 antibodies, and $396.196 \text{ ng cm}^{-2}$ for BSA/aAFB1/4-ATP/Au electrode, respectively. After the competition the electrode surface mass increases drastically due to the formation of sandwiched between secondary antibody conjugate and monoclonal antibodies (r-IgG-Cys-Au-Fe₃O₄/AFB1/BSA/aAFB1/4-ATP/Au)

TABLE 1: Change in frequency and mass during the fabrication of r-IgG-Cys-Au-Fe₃O₄/AFB1/BSA/aAFB1/4-ATP/Au electrode.

S. number	Electrode name	Frequency change (Hz)	Mass change (ng cm^{-2})
1	4-ATP/Au	16.83	206.50
2	aAFB1/4-ATP/Au	21.19	268.71
3	BSA/aAFB1/4-ATP/Au	32.29	396.19
4	r-IgG-Cys-Au-Fe ₃ O ₄ /AFB1/BSA/aAFB1/4-ATP/Au	136.2	1668.71

over the electrode (Table 1). These results are supported with EQCM-CV.

EQCM-CV (Figure 4(b)) was conducted in PBS (50 mM, pH 7.4, 0.9% NaCl) containing 5 mM [Fe(CN)₆]^{3-/4-} as a redox species at a scan rate of 100 mV/s in the potential range of -0.2 to 0.8 V. Figure 4(b) shows CV of [Fe(CN)₆]^{3-/4-} of

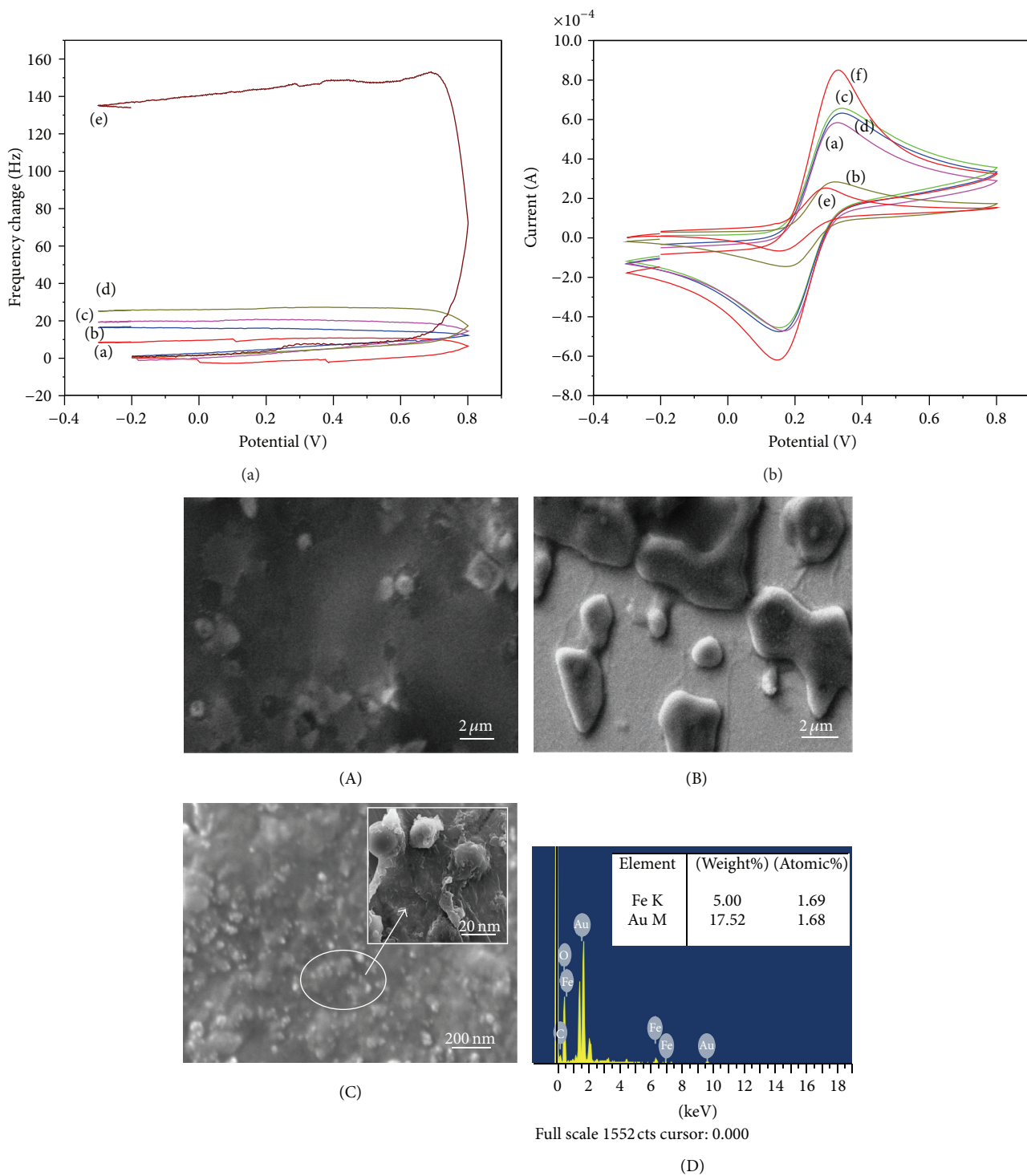


FIGURE 4: ((a) and (b)) Frequency change and CV of (a) bare Au electrode, (b) 4-ATP/Au, (c) aAFB1/4-ATP/Au, (d) BSA/aAFB1/4-ATP/Au, and (e) r-IgG-Cys-Au-Fe₃O₄/AFB1/BSA/aAFB1/4-ATP/Au immunoelectrodes. (c) SEM images of (A) aAFB1/4-ATP/Au, (B) AFB1/BSA/aAFB1/4-ATP/Au, and (C) r-IgG-Cys-Au-Fe₃O₄/AFB1/BSA/aAFB1/4-ATP/Au and (D) EDX of r-IgG-Cys-Au-Fe₃O₄/AFB1/BSA/aAFB1/4-ATP/Au immunoelectrodes.

a bare Au QCM electrode (curve (a)), 4-ATP/Au electrode (curve (b)), aAFBI/4-ATP/Au electrode (curve (c)), and BSA/aAFBI/4-ATP/Au electrode (curve (d)). After the SAM deposition, the magnitude of anodic peak current (2.49×10^{-4} A) decreases (curve (b)), due to the insulating properties of the thin layer of thiol which hinders the electron movement through electrode of the gold surface. The presence of aAFBI over the surface enhances the peak current up to 6.48×10^{-4} A (curve (c)) due to the presence of polar groups of antibody such as carboxyl and amine moieties. There is a slight decrease in the magnitude of current response (6.17×10^{-4} A) after immobilization of BSA onto the surface of AFBI/4-ATP/Au electrode, indicating enhanced electron-transfer barriers introduced upon assembly of BSA layer. After the competition, the magnitude of current increases (8.31×10^{-4}) due to the presence of r-IgG-Cys-Au-Fe₃O₄ conjugate over the surface of AFBI/BSA/aAFBI/4-ATP/Au immunoelectrode. It reveals that the IgG antibodies interact with AFBI coated over the surface.

3.3.2. SEM Studies. The surface morphological studies of aAFBI/4-ATP/Au, AFBI/BSA/aAFBI/4-ATP/Au, and r-IgG-Cys-Au-Fe₃O₄/AFBI/BSA/aAFBI/4-ATP/Au electrodes and immunoelectrodes were examined by scanning electron microscopy (SEM). Figure 4(c) represents the surface morphology of aAFBI/4-ATP/Au electrode (image (A)), showing highly dense globular morphology with bright streaks confirming the immobilization of aAFBI onto 4-ATP/Au surface. Figure 4(c), image (B), shows the surface morphology of AFBI/BSA/aAFBI/4-ATP/Au electrode surface. The morphological changes in the SEM image after incubation of AFBI indicate the binding of AFBI to the aAFBI/4-ATP/Au electrode surface. Image (C) shows the surface morphology of r-IgG-Cys-Au-Fe₃O₄/AFBI/BSA/aAFBI/4-ATP/Au immunoelectrode and the surface is saturated with r-IgG-Cys-Au-Fe₃O₄ conjugate. Inset image (image (C)) shows the morphology of r-IgG-Cys-Au-Fe₃O₄/AFBI/BSA/aAFBI/4-ATP/Au at high magnification. It reveals that the secondary antibody interacts with coated antigen and forms sandwich like structure. Further, this fact is confirmed by EDX of this surface (Figure 4(c), image (D)) containing Fe and Au metal along with other elements and the weight% shown in image (D) (inset table). The presence of these elements confirms the interaction of secondary antibody r-IgG-Cys-Au-Fe₃O₄ conjugate over the AFBI/BSA/aAFBI/4-ATP/Au immunoelectrode.

3.3.3. Atomic Force Microscopy (AFM). Topographic images were taken by AFM in noncontact mode ($1 \mu\text{m} \times 1 \mu\text{m}$ surface). In order to compare the topologies of each surface, surface roughness (R_a) and root mean square roughness (R_q) were estimated from the AFM images [41]. Figure 5 represents surface morphology of the bare Au (Figure 5(a)), 4-ATP/Au (Figure 5(b)), aAFBI/4-ATP/Au (Figure 5(c)), AFBI/BSA/aAFBI/4-ATP/Au (Figure 5(d)), and r-IgG-Cys-Au-Fe₃O₄/AFBI/BSA/aAFBI/4-ATP/Au (Figure 5(e)) based immunosensors. The R_a and R_q values and surface topology for the bare gold surface and 4-ATP/Au electrode are similar.

Therefore, it can be assumed that a highly ordered and densely packed self-assembled layer of 4-ATP appears on the gold surface [42]. The drastic increase of surface roughness of aAFBI/4-ATP/Au (Figure 4(c)) as indicated by the values of R_a (6.669 nm from 0.934 nm) and R_q (2.109 nm from 0.195 nm) clearly demonstrates immobilization of the monoclonal aAFBI antibody onto 4-ATP/Au electrode surface. The increase in R_a and R_q of aAFBI/4-ATP/Au immunosensor is attributed to the configuration and presence of paratope on antibody. After immobilization of BSA to block nonspecific sites, surface roughness further increases as observed by R_a and R_q values of 7.217 nm and 2.6 nm, respectively (image not shown), which was also supported by SEM image. The R_a and R_q values have been found to be reduced to 1.895 nm and 0.563 nm of AFBI/BSA/aAFBI/4-ATP/Au (image 5(d)) after the interaction of antigen with the immobilized antibody. Therefore, sandwiched structure (image 5(e)) of Au NP functionalized secondary antibody, antigen, and monoclonal antibody (r-IgG-Cys-Au-Fe₃O₄/AFBI/BSA/aAFBI/4-ATP/Au) is demonstrated by the rough surface topology and the R_a (5.25 nm) and R_q (6.39 nm) values.

3.3.4. FT-IR Studies. Figure 6 demonstrates FT-IR spectrum of the thiol monolayer between 500 and 3000 cm^{-1} . The formation of a covalent gold-sulfur bond reveals the presence of the large band in the range of 624–640 cm^{-1} assigned to C–S stretching mode (spectrum (a)). The observed bands at 804 cm^{-1} and 1461 cm^{-1} and broad band at 3340 cm^{-1} due to =C–H deformation of the benzene ring, aromatic –C=C– in-plane vibrations, and N–H vibration of NH₂ confirm the presence of 4-ATP on Au surfaces. After immobilization of aAFBI on 4-ATP/Au electrode surface, the appearance of intense amide bands is characteristic of protein adsorption, amide I band at 1687 cm^{-1} corresponding to carbonyl C=O stretching vibration and amide II band at 1594 cm^{-1} due to the coupled C–N stretching, and –N–H bending mode indicates successful immobilization of monoclonal antibodies [43] (Figure 6, spectrum (b)). Figure 6 (spectrum (c)) represents FT-IR spectrum of AFBI/BSA/aAFBI/4-ATP/Au, that is, after recognition of AFBI by BSA/aAFBI/4-ATP/Au immunosensor. The presence of 1474 cm^{-1} for methyl adjacent to epoxy ring, 1308 cm^{-1} for in-plane –CH bending of phenyl in Figure 6 (spectrum (c)), clearly indicates the presence of AFBI on the surface of aAFBI/4-ATP/Au surface [42]. The bands at 1098 cm^{-1} for symmetric stretching of =C–O–C or symmetric bending of phenyl and 938 cm^{-1} for possibly isolated H further confirm interaction between coated AFBI-aAFBI on the immunosensor surface. The band at 3414 cm^{-1} due to –N–H stretching of NH₂ group of the antibody almost disappears in the spectrum of AFBI/BSA/aAFBI/4-ATP/Au (Figure 6, (c)) indicating strong interaction between the antigen epitope and paratope of the antibody.

3.3.5. Response Studies of the Immunosensor. The sensitivity and detection limit of an immunosensor depend on antibody loading. Prior to sensing studies, we have optimized all the parameters like the concentration of aAFBI ($40 \mu\text{g mL}^{-1}$),

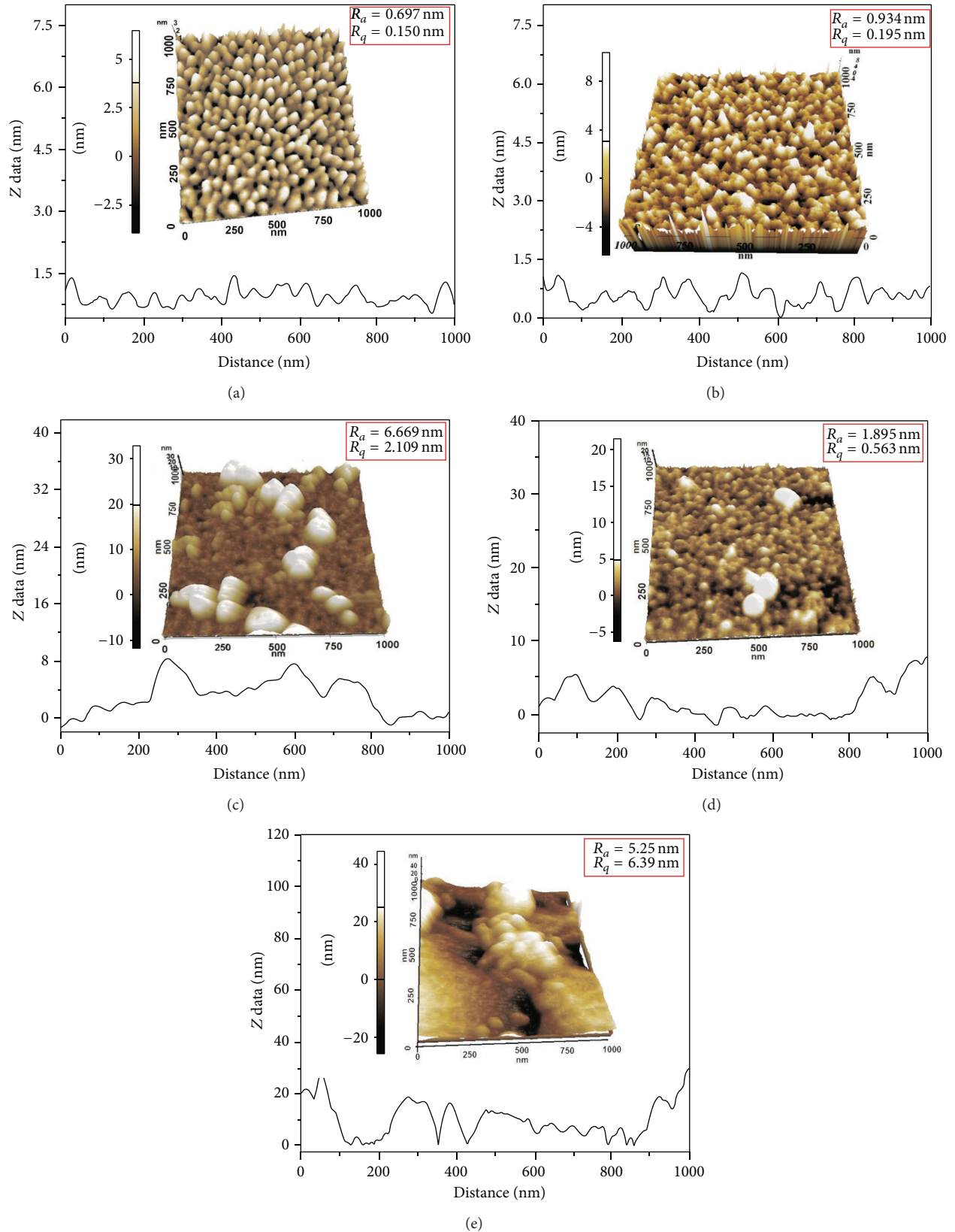


FIGURE 5: AFM images: topography image and height profiles of (a) bare Au, (b) 4-ATP/Au, (c) aAFB1/4-ATP/Au, (d) AFB1/BSA/aAFB1/4-ATP/Au, and (e) r-IgG-Cys-Au-Fe₃O₄/AFB1/BSA/aAFB1/4-ATP/Au immunosensor.

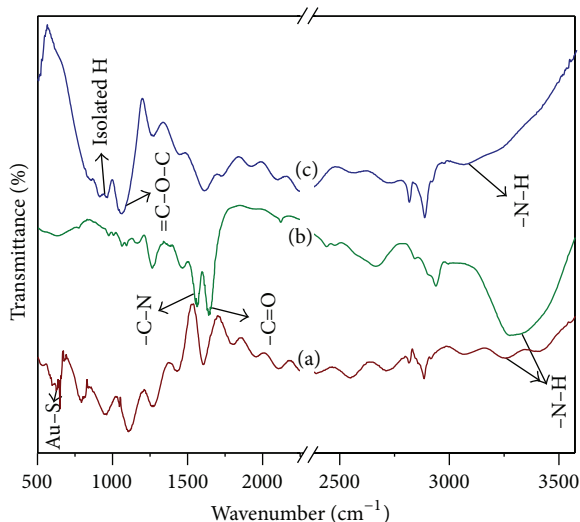


FIGURE 6: FT-IR of (a) 4-ATP/Au, (b) aAFBI/4-ATP/Au, and (c) AFBI/BSA/aAFBI/4-ATP/Au immunoelectrodes.

incubation time (30–35 min), and pH (7.4) in our previous study [35]. Further the concentration of r-IgG antibodies was optimized at $10\text{--}50\ \mu\text{g mL}^{-1}$ (Figure 7(a)). Figure 7(a) shows the current response of AFBI/BSA/aAFBI/4ATP/Au electrode with varying (different solution, $10\text{--}50\ \mu\text{g mL}^{-1}$) concentration of r-IgG-Cys-Au- Fe_3O_4 conjugate, current response increasing from 10 to $30\ \mu\text{g mL}^{-1}$ after that decrease in current was observed, due to steric hindrance of conjugate or overloading of conjugates. Finally, $30\ \mu\text{g mL}^{-1}$ concentration of r-IgG-Cys-Au- Fe_3O_4 conjugate was applied over the AFBI/BSA/aAFBI/4ATP/Au electrode for all the experiments.

Both competitive and noncompetitive strategies have been investigated. In case of competitive mode, the BSA/aAFBI/4-ATP/Au immunoelectrodes were fully covered with saturated concentration of AFBI solution. Then the same (AFBI/BSA/aAFBI/4-ATP/Au) was allowed to interact with optimized concentration ($30\ \mu\text{g mL}^{-1}$) of secondary antibody conjugate (r-IgG-Cys-Au- Fe_3O_4) and free AFBI with varying concentration. Finally, the response in the sandwiched form was recorded with EQCM-CV after washing with PB in N_2 atmosphere. During the competition process, secondary antibodies easily access free AFBI, while the rest of the r-IgG-Cys-Au- Fe_3O_4 conjugates form sandwiched structure with the coated AFBI, respectively. Figure 7(b) shows calibration curve as a function of AFBI concentration, linear range obtained from $0.05\text{--}5\ \text{ng mL}^{-1}$ after which it decreases revealing that at $5\ \text{ng mL}^{-1}$ concentration becomes saturated. The inset of Figure 7(b) shows the peak current intensity of the redox mediator is inversely proportional to the amount of free AFBI in the sample and the peak current decreases with increase in concentration of AFBI. Scheme 2 represents the formation of this competitive sandwich type immunoelectrode. Each value is obtained in triplicate experiments and

regression equation is obtained with a regression coefficient of ca. 0.98:

$$I\ (\text{A}) = (6.93 \times 10^{-4}\ \text{A}) - 9.40 \times 10^{-5}\ \text{A ng}^{-1}\ \text{mL} \times [\text{AFBI}]\ \text{ng mL}^{-1}. \quad (1)$$

This corresponds to the sensitivity of ca. $335.7\ \mu\text{A ng}^{-1}\ \text{mL cm}^{-2}$ for AFBI with a calculated detection limit of $0.07\ \text{ng mL}^{-1}$.

For noncompetitive mode, BSA/aAFBI/4-ATP/Au immunoelectrode was allowed to interact with increasing concentration of AFBI. After the interaction, the same (AFBI/BSA/aAFBI/4-ATP/Au) electrode was again exposed to optimum concentration of r-IgG-Cys-Au- Fe_3O_4 conjugate to form sandwiched structure (r-IgG-Cys-Au- Fe_3O_4 /AFBI/BSA/aAFBI/4-ATP/Au). Figure 7(c) shows calibration curve as a function of AFBI concentration, linear range obtained from $0.5\text{--}5\ \text{ng mL}^{-1}$, after which it decreases revealing that at $5\ \text{ng mL}^{-1}$ concentration it becomes saturated. In this case, the peak current increases (Figure 7(c) inset) with increasing concentration of AFBI as the concentration of r-IgG-Cys-Au- Fe_3O_4 conjugate also increases enhancing the electron transfer through the medium by virtue of the presence of Au- Fe_3O_4 nanoparticles on conjugate. All experiments were performed with triplicate measurements and the temperature was controlled at 25°C . The calibration curve shows range of 0.5 to $5\ \text{ng mL}^{-1}$ with calculated LOD of $0.9\ \text{ng mL}^{-1}$ for the noncompetitive mode. However, the regression coefficient is 0.933 and the linear equation is as follows:

$$(A) = (6.82 \times 10^{-4}\ \text{A}) + 3.47 \times 10^{-5}\ \text{A ng}^{-1}\ \text{mL} \times [\text{AFBI}]\ \text{ng mL}^{-1}. \quad (2)$$

This corresponds to the sensitivity of ca. $123.9\ \mu\text{A ng}^{-1}\ \text{mL cm}^{-2}$. It reveals that the competitive mode offers a wider linear range, higher sensitivity, and lower LOD and corresponds to higher regression coefficient in spite of identical nature of coated AFBI and free AFBI.

3.3.6. Real Sample Testing and Selectivity of Immunoelectrode.

To evaluate the applicability of the developed immunosensor to real sample analysis, corn flakes samples were spiked with various concentrations of AFBI. For this the corn flakes sample extracted with a methanolic solution of potassium bicarbonate was exploited as a real sample. Evaporation to dryness and final reconstitution in PBS buffer were necessary to avoid the inhibition of the antibody-antigen binding caused by methanol. The extract sample was spiked with three different concentrations of AFBI (0.05 , 2 , and $5\ \text{ng mL}^{-1}$) to examine the applicability of the proposed probe. During these experiments, the AFBI/BSA/aAFBI/4-ATP/Au immunosensor was dipped in the cell containing a mixture of different concentration of AFBI spiked extracted sample and fixed amount of r-IgG-Cys/Au- Fe_3O_4 in PBS and incubated for 35 min. The EQCM-CV of AFBI/BSA/aAFBI/4-ATP/Au immunosensor was examined with the corn flakes extract

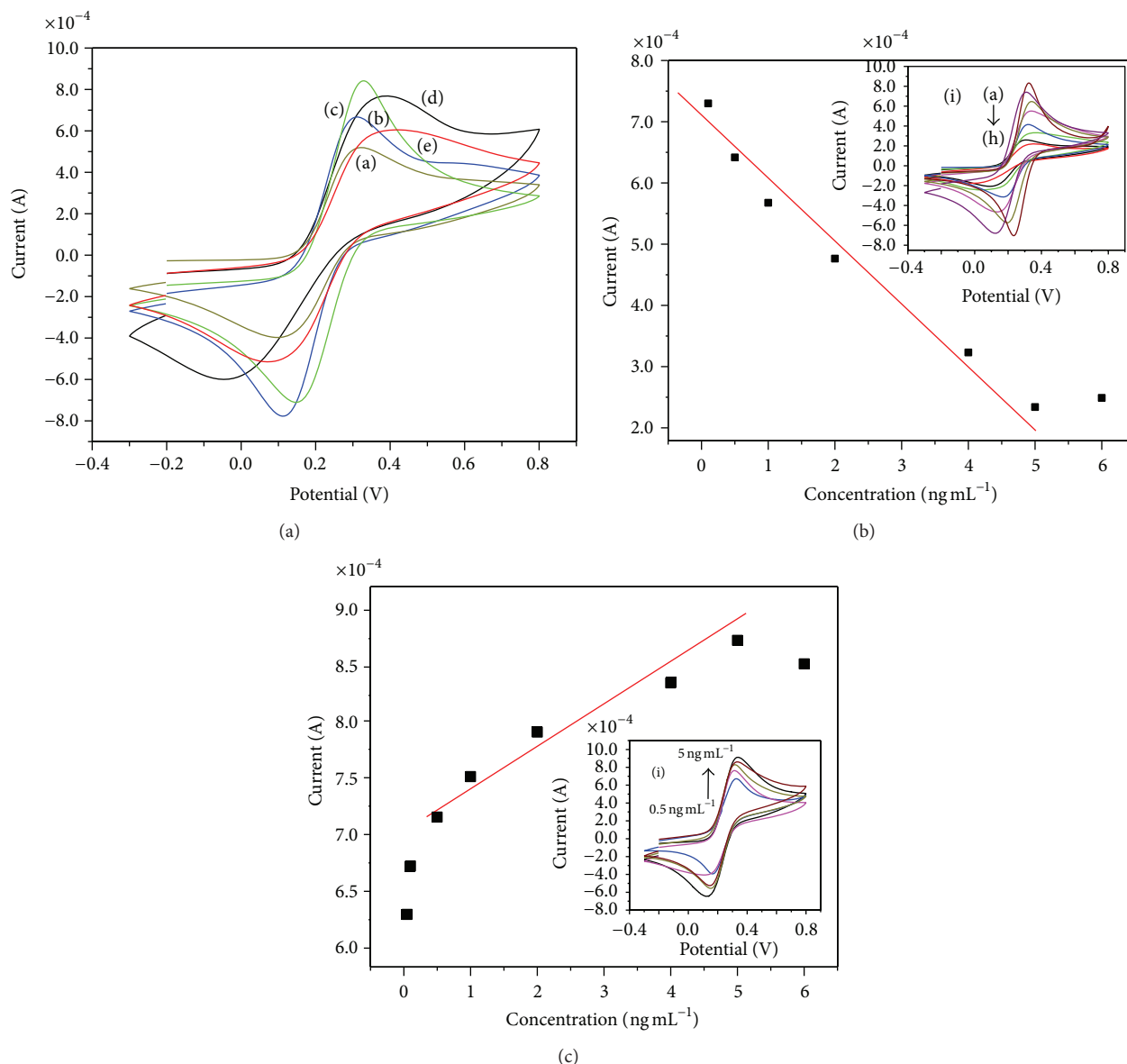


FIGURE 7: (a) CV of the AFB1/BSA/aAFB1/4-ATP/Au immunoelectrode with respect to the r-IgG-Cys-Au-Fe₃O₄ concentration: (a) 10 μg mL⁻¹, (b) 20 μg mL⁻¹, (c) 30 μg mL⁻¹, (d) 40 μg mL⁻¹, and (e) 50 μg mL⁻¹, in PBS (50 mM, pH 7.4, 0.9% NaCl) containing [Fe(CN)₆]^{3-/4-} (5 mM). (b) Calibration curve for competitive detection of AFB1. Inset (b) shows (i) CV of the AFB1/BSA/aAFB1/4-ATP/Au immunoelectrode with respect to the AFB1 concentration (0.05–5 ng mL⁻¹). (c) Calibration curve for noncompetitive detection of AFB1. Inset (c) shows (i) CV of the AFB1/BSA/aAFB1/4-ATP/Au immunoelectrode with respect to the AFB1 concentration (0.5–5 ng mL⁻¹).

3.3.7. Reproducibility, Shelf Life, and Regeneration of Immuno-electrode. The reproducibility of the proposed immunoelectrode was estimated by repetitive measurement of immunoelectrode with current response using 2 ng mL⁻¹ standard AFB1 solutions in PBS (50 mM, pH 7.4, 0.9% NaCl, containing 5 mM [Fe(CN)₆]^{3-/4-}). The results obtained in 5 repeated measurements show a relative standard deviation (RSD) of 2–3%, indicating that the obtained data are reproducible. These results demonstrate the acceptable reproducibility and precision of the proposed immunosensor. In addition, the immunosensor could be stored at 4°C for shelf life study. The stability of the BSA/aAFB1/4-ATP/Au immunoelectrode was

evaluated by EQCM-CV study and the current response in the presence of 2 ng mL⁻¹ standard AFB1 solution in PBS (50 mM, pH 7.4, 0.9% NaCl) was monitored at a regular interval of 7 days (Figure 8(b)). The immunoelectrode retains its activity up to 28 days with 5–7% decrease in activity. 95% of the initial response was left remaining after 1 week and 90% of the initial response was left remaining after 1 month, indicating acceptable stability.

The immunosensor can be regenerated (Scheme 2) using an external strong magnet to remove the immuno-r-IgG-Cys-Au-Fe₃O₄ conjugate (i.e., r-IgG-Cys-Au-Fe₃O₄). It was observed that the reagent-free regeneration method could

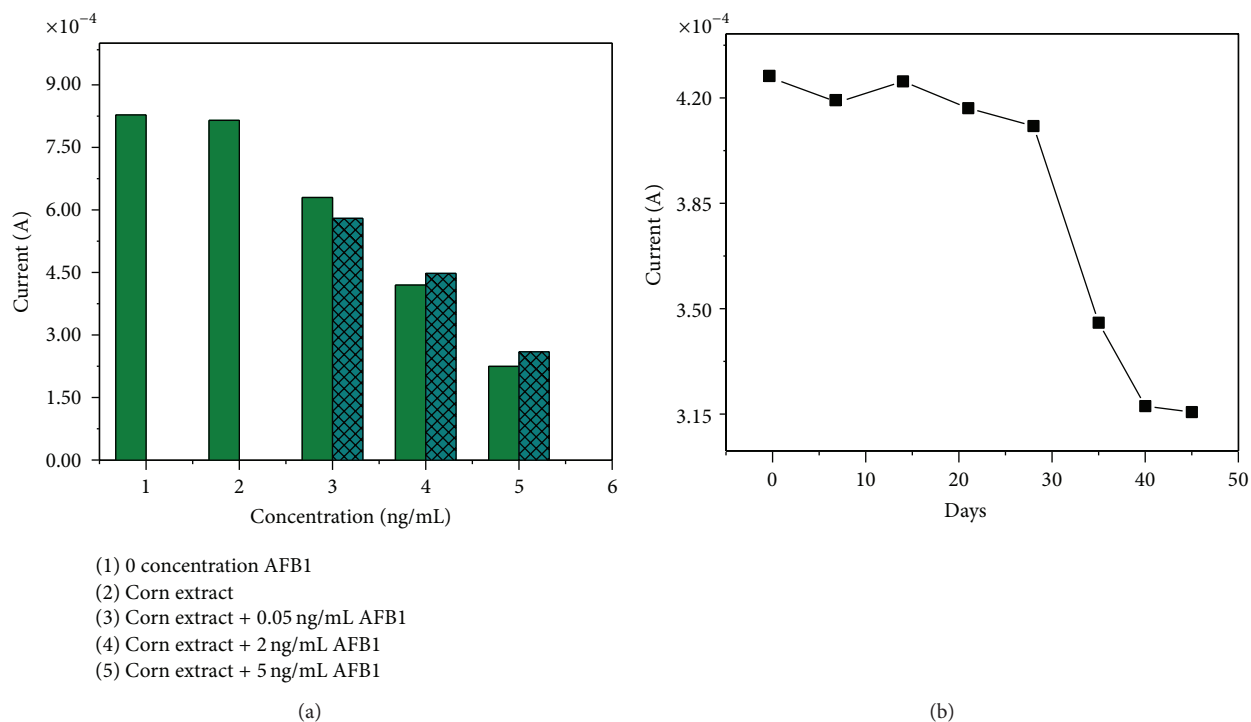


FIGURE 8: (a) Bar chart of frequency change for corn flakes sample with addition of AFB1 concentration. (b) Shelf life study of immunoelectrode with EQCM-CV at 7-day interval.

regenerate the immunosensor up to 15–16 times with 2–3% loss in activity using a fixed concentration of AFB1.

4. Conclusions

In the present study, a reusable immunoelectrode is developed using self-assembled 4-ATP on quartz crystal electrode. EQCM measurement technique is applied to determine the response current of sandwiched structure comprising BSA/aAFB1/4-ATP/Au immunoelectrode, AFB1, and r-IgG-Cys-Au- Fe_3O_4 . The regeneration of the immunoelectrode is done after removing the AFB1 attached with r-IgG-Cys-Au- Fe_3O_4 through external magnet. The immunosensor can be regenerated about 15–16 times with 2–3% loss of activity. We have compared the competitive and noncompetitive methods for the determination of the AFB1. It has been observed that the competitive mode has offered wider linear range of 0.05–5 ng mL^{-1} with the limit of detection of 0.07 ng mL^{-1} and higher sensitivity than the noncompetitive one while coated AFB1 and free AFB1 are identical in chemical structure. This immunosensor is found to be highly promising for detection of AFB1 in corn flakes samples. Therefore, the same principle can be utilized for detection of other food toxins such as OTA, OTB, fumonisins, and zearalenone and other small molecules also.

Conflict of Interests

The authors declare that there is no conflict of interests regarding the publication of this paper.

Acknowledgments

The authors thank Dr. Ashok Kumar Chauhan (Founder President, Amity University, Uttar Pradesh) for providing the facilities. They also thank Dr. (Mrs.) Balvinder Shukla, Vice Chancellor, Amity University, Uttar Pradesh, and Professor L. M. Bharadwaj, Director, AINT. The authors also express their deep gratitude to Ms. Shuvra Singha, Department of Chemistry, University of Hyderabad, India, for her help in conducting the XRD studies.

References

- [1] Y. Li, X. Liu, and Z. Lin, "Recent developments and applications of surface plasmon resonance biosensors for the detection of mycotoxins in foodstuffs," *Food Chemistry*, vol. 132, no. 3, pp. 1549–1554, 2012.
- [2] J. W. Bennett and M. Klich, "Mycotoxins," *Clinical Microbiology Reviews*, vol. 16, no. 3, pp. 497–516, 2003.
- [3] R. G. Digigow, J.-F. Dechézelles, H. Dietsch et al., "Preparation and characterization of functional silica hybrid magnetic nanoparticles," *Journal of Magnetism and Magnetic Materials*, vol. 362, pp. 72–79, 2014.
- [4] International Agency for Research on Cancer, *IARC Monographs on the Evaluation of Carcinogenic Risks to Humans*, vol. 56, IARC, Lyon, France, 1993.
- [5] E. Anklam, J. Stroka, and A. Boenke, "Acceptance of analytical methods for implementation of EU legislation with a focus on mycotoxins," *Food Control*, vol. 13, no. 3, pp. 173–183, 2002.
- [6] D. M. Parkin, F. Bray, J. Ferlay, and P. Pisani, "Estimating the world cancer burden: Globocan 2000," *International Journal of Cancer*, vol. 94, no. 2, pp. 153–156, 2001.

- [7] H. P. Van Egmond, R. C. Schothorst, and M. A. Jonker, "Regulations relating to mycotoxins in food," *Analytical and Bioanalytical Chemistry*, vol. 389, no. 1, pp. 147–157, 2007.
- [8] W. S. Khayoon, B. Saad, B. Salleh, N. H. A. Manaf, and A. A. Latiff, "Micro-solid phase extraction with liquid chromatography-tandem mass spectrometry for the determination of aflatoxins in coffee and malt beverage," *Food Chemistry*, vol. 147, pp. 287–294, 2014.
- [9] F. Hepsag, O. Golge, and B. Kabak, "Quantitation of aflatoxins in pistachios and groundnuts using HPLC-FLD method," *Food Control*, vol. 38, no. 1, pp. 75–81, 2014.
- [10] O. G. Roch, G. Blunden, R. D. Coker, and S. Nawaz, "The validation of a solid phase clean-up procedure for the analysis of aflatoxins in groundnut cake using HPLC," *Food Chemistry*, vol. 52, no. 1, pp. 93–98, 1995.
- [11] D. W. Kimmel, G. Leblanc, M. E. Meschievitz, and D. E. Cliffl, "Electrochemical sensors and biosensors," *Analytical Chemistry*, vol. 84, no. 2, pp. 685–707, 2012.
- [12] J. C. Vidal, L. Bonel, A. Ezquerro, P. Duato, and J. R. Castillo, "An electrochemical immunosensor for ochratoxin A determination in wines based on a monoclonal antibody and paramagnetic microbeads," *Analytical and Bioanalytical Chemistry*, vol. 403, no. 6, pp. 1585–1593, 2012.
- [13] R. Chauhan, Deepshikha, and T. Basu, "Development of a reusable transducer matrix based on nano structured conducting polyaniline and its application to cholesterol biosensor," *Science of Advanced Materials*, vol. 4, no. 1, pp. 96–105, 2012.
- [14] R. Chauhan, B. Nagar, P. R. Solanki, and T. Basu, "Development of triglyceride biosensor based on a platinum nanoparticle and polypyrrole nano composite electrode," *Materials Focus*, vol. 2, no. 4, pp. 316–323, 2013.
- [15] L. Masoomi, O. Sadeghi, M. H. Banitaba, A. Shahrjerdi, and S. S. H. Davarani, "A non-enzymatic nanomagnetic electro-immunosensor for determination of Aflatoxin B1 as a model antigen," *Sensors and Actuators B*, vol. 177, pp. 1122–1127, 2013.
- [16] S. Srivastava, V. Kumar, M. A. Ali et al., "Electrophoretically deposited reduced graphene oxide platform for food toxin detection," *Nanoscale*, vol. 5, no. 7, pp. 3043–3051, 2013.
- [17] M. Puiu, O. Istrate, L. Rotariu, and C. Bala, "Kinetic approach of aflatoxin B1-acetylcholinesterase interaction: a tool for developing surface plasmon resonance biosensors," *Analytical Biochemistry*, vol. 421, no. 2, pp. 587–594, 2012.
- [18] X. Xu, X. Liu, Y. Li, and Y. Ying, "A simple and rapid optical biosensor for detection of aflatoxin B1 based on competitive dispersion of gold nanorods," *Biosensors and Bioelectronics*, vol. 47, pp. 361–367, 2013.
- [19] T. Li, J.-Y. Byun, B. B. Kim, Y.-B. Shin, and M.-G. Kim, "Label-free homogeneous FRET immunoassay for the detection of mycotoxins that utilizes quenching of the intrinsic fluorescence of antibodies," *Biosensors and Bioelectronics*, vol. 42, no. 1, pp. 403–408, 2013.
- [20] B. Prieto-Simón, I. Karube, and H. Saiki, "Sensitive detection of ochratoxin A in wine and cereals using fluorescence-based immunosensing," *Food Chemistry*, vol. 135, no. 3, pp. 1323–1329, 2012.
- [21] K. Spinella, L. Mosiello, G. Palleschi, F. Vitali, and K. Spinella, "Development of a QCM (quartz crystal microbalance) biosensor to the detection of aflatoxin B1," *Open Journal of Applied Biosensor*, vol. 2, no. 4, pp. 112–119, 2013.
- [22] J. Li, X. He, Z. Wu, K. Wang, G. Shen, and R. Yu, "Piezoelectric immunosensor based on magnetic nanoparticles with simple immobilization procedures," *Analytica Chimica Acta*, vol. 481, no. 2, pp. 191–198, 2003.
- [23] J. C. Vidal, P. Duato, L. Bonel, and J. R. Castillo, "Use of polyclonal antibodies to ochratoxin A with a quartz-crystal microbalance for developing real-time mycotoxin piezoelectric immunosensors," *Analytical and Bioanalytical Chemistry*, vol. 394, no. 2, pp. 575–582, 2009.
- [24] A. V. Nabok, A. Tsargorodskaya, A. Holloway, N. F. Starodub, and O. Gojster, "Registration of T-2 mycotoxin with total internal reflection ellipsometry and QCM impedance methods," *Biosensors and Bioelectronics*, vol. 22, no. 6, pp. 885–890, 2007.
- [25] C. I. Cheng, Y.-P. Chang, and Y.-H. Chu, "Biomolecular interactions and tools for their recognition: focus on the quartz crystal microbalance and its diverse surface chemistries and applications," *Chemical Society Reviews*, vol. 41, no. 5, pp. 1947–1971, 2012.
- [26] Y. Zhang, H. Wang, B. Yan et al., "A reusable piezoelectric immunosensor using antibody-adsorbed magnetic nanocomposite," *Journal of Immunological Methods*, vol. 332, no. 1–2, pp. 103–111, 2008.
- [27] Y. Zhuo, P.-X. Yuan, R. Yuan, Y.-Q. Chai, and C.-L. Hong, "Bionzyme functionalized three-layer composite magnetic nanoparticles for electrochemical immunosensors," *Biomaterials*, vol. 30, no. 12, pp. 2284–2290, 2009.
- [28] L. Wang and X.-X. Gan, "Biomolecule-functionalized magnetic nanoparticles for flow-through quartz crystal microbalance immunoassay of aflatoxin B1," *Bioprocess and Biosystems Engineering*, vol. 32, no. 1, pp. 109–116, 2009.
- [29] N. A. Frey, M. H. Phan, H. Srikanth, S. Srinath, C. Wang, and S. Sun, "Interparticle interactions in coupled Au-Fe₃O₄ nanoparticles," *Journal of Applied Physics*, vol. 105, no. 7, Article ID 07B502, 2009.
- [30] R. Costi, A. E. Saunders, and U. Banin, "Colloidal hybrid nanostructures: a new type of functional materials," *Angewandte Chemie International Edition*, vol. 49, no. 29, pp. 4878–4897, 2010.
- [31] X. Jin, X. Jin, L. Chen, J. Jiang, G. Shen, and R. Yu, "Piezoelectric immunosensor with gold nanoparticles enhanced competitive immunoreaction technique for quantification of aflatoxin B1," *Biosensors and Bioelectronics*, vol. 24, no. 8, pp. 2580–2585, 2009.
- [32] X. Jin, X. Jin, X. Liu et al., "Biocatalyzed deposition amplification for detection of aflatoxin B1 based on quartz crystal microbalance," *Analytica Chimica Acta*, vol. 645, no. 1–2, pp. 92–97, 2009.
- [33] S. Banerjee, S. O. Raja, M. Sardar, N. Gayathri, B. Ghosh, and A. Dasgupta, "Iron oxide nanoparticles coated with gold: enhanced magnetic moment due to interfacial effects," *Journal of Applied Physics*, vol. 109, no. 12, Article ID 123902, 2011.
- [34] A. Sharma, Z. Matharu, G. Sumana, P. R. Solanki, C. G. Kim, and B. D. Malhotra, "Antibody immobilized cysteamine functionalized-gold nanoparticles for aflatoxin detection," *Thin Solid Films*, vol. 519, no. 3, pp. 1213–1218, 2010.
- [35] R. Chauhan, P. R. Solanki, J. Singh, I. Mukherjee, T. Basu, and B. D. Malhotra, "A novel electrochemical piezoelectric label free immunosensor for aflatoxin B1 detection in groundnut," *Food Control*, vol. 52, pp. 60–70, 2015.
- [36] B. Prieto-Simón, M. Campàs, J.-L. Marty, and T. Noguier, "Novel highly-performing immunosensor-based strategy for ochratoxin A detection in wine samples," *Biosensors and Bioelectronics*, vol. 23, no. 7, pp. 995–1002, 2008.
- [37] J. Singh, P. Khanra, T. Kuila et al., "Preparation of sulfonated poly(ether-ether-ketone) functionalized ternary

- graphene/AuNPs/chitosan nanocomposite for efficient glucose biosensor,” *Process Biochemistry*, vol. 48, no. 11, pp. 1724–1735, 2013.
- [38] S. Pal, M. Morales, P. Mukherjee, and H. Srikanth, “Synthesis and magnetic properties of gold coated iron oxide nanoparticles,” *Journal of Applied Physics*, vol. 105, no. 7, Article ID 07B504, 2009.
- [39] I. Robinson, L. D. Tung, S. Maenosono, C. Wälti, and N. T. K. Thanh, “Synthesis of core-shell gold coated magnetic nanoparticles and their interaction with thiolated DNA,” *Nanoscale*, vol. 2, no. 12, pp. 2624–2630, 2010.
- [40] C. Zhang, S. Si, and Z. Yang, “A highly selective photoelectrochemical biosensor for uric acid based on core-shell $\text{Fe}_3\text{O}_4@\text{C}$ nanoparticle and molecularly imprinted TiO_2 ,” *Biosensors and Bioelectronics*, vol. 65, pp. 115–120, 2015.
- [41] M. B. Young, B.-K. Oh, W. Lee, H. L. Won, and J.-W. Choi, “Study on orientation of immunoglobulin G on protein G layer,” *Biosensors and Bioelectronics*, vol. 21, no. 1, pp. 103–110, 2005.
- [42] M. Hegner, P. Wagner, and G. Semenza, “Ultralarge atomically flat template-stripped Au surfaces for scanning probe microscopy,” *Surface Science*, vol. 291, no. 1-2, pp. 39–46, 1993.
- [43] P. R. Solanki, A. Kaushik, T. Manaka et al., “Self-assembled monolayer based impedimetric platform for food borne mycotoxin detection,” *Nanoscale*, vol. 2, no. 12, pp. 2811–2817, 2010.

Research Article

Synthesis and Microwave Absorption Properties of Core-Shell Structured Co_3O_4 -PANI Nanocomposites

Hongyan Xu,¹ Zhenyin Hai,² Jiangtao Diwu,¹ Qiang Zhang,² Libo Gao,² Danfeng Cui,² Junbin Zang,³ Jun Liu,² and Chenyang Xue²

¹School of Materials Science and Engineering, North University of China, Taiyuan, Shanxi 030051, China

²Key Laboratory of Instrumentation and Dynamic Measurement of Ministry of Education, North University of China, Taiyuan, Shanxi 030051, China

³North University of China, Shuozhou, Shanxi 036000, China

Correspondence should be addressed to Chenyang Xue; xuechenyang@foxmail.com

Received 16 May 2015; Accepted 16 August 2015

Academic Editor: Themis Matsoukas

Copyright © 2015 Hongyan Xu et al. This is an open access article distributed under the Creative Commons Attribution License, which permits unrestricted use, distribution, and reproduction in any medium, provided the original work is properly cited.

The core-shell structured Co_3O_4 -PANI nanocomposites have been successfully prepared using an in situ polymerization method, while the core Co_3O_4 nanoparticles were synthesized by carbon-assisted method using degreasing cotton as a template. The obtained samples were characterized by XRD, TEM, FTIR, and XPS. The results indicated that the amorphous PANI was well covered on the surface of the spinel Co_3O_4 and the Co_3O_4 -PANI with core-shell structure was formed with particle size of about 100 nm. The interfacial interaction of the core-shell nanocomposite greatly enhances the microwave absorption properties. The maximum reflection loss of Co_3O_4 -PANI is up to -45.8 dB at 11.7 GHz with a thickness of 2.5 mm and the adsorption bandwidth with the reflection loss below -10 dB reaches 14.1 GHz ranging from 3.9 to 18 GHz when the thickness is between 2 and 5.5 mm. Therefore, the facilely synthesized and low-cost Co_3O_4 -PANI nanocomposite with superior microwave absorption properties can be a promising nanomaterial for high efficient microwave absorption.

1. Introduction

With the wide use of electronic devices, the electromagnetic pollution has been a growing threat to the stable running of electronically controlled systems and more importantly to our healthy life [1, 2]. Considerable attention has been attracted to the study on the high efficient and inexpensive microwave absorbing materials [3, 4]. Of all the discovered microwave absorbing materials, due to its electric conductivity, lightweight, flexibility, stability, and ease of synthesis, polyaniline (PANI), as a traditional practical polymer, has been extensively employed in the synthesis of promising microwave absorbers, for instance, PANI-NiZn, PANI- CoFe_2O_4 , PANI- Fe_3O_4 -graphene, and PANI- Fe_3O_4 -MWCNTs [5–8].

Co_3O_4 is a normal spinel structured crystal with Co^{3+} occupying octahedral sites and Co^{2+} in tetrahedral sites

within the lattice [9]. Co_3O_4 can act as a functional material in various fields, such as catalysts, lithium ion batteries, supercapacitor, and chemical sensors [10–15]. Recent studies have demonstrated that Co_3O_4 can also be used as excellent microwave absorption material. The porous $\text{Co-Co}_3\text{O}_4$ hybrid hollow spheres synthesized by Wu et al. can absorb microwave with maximum reflection loss of -18.5 dB at 6.5 GHz when the thickness is 5.00 mm [16]. The 2D Co_3O_4 @C@PGC fabricated by Wen et al. shows better microwave absorption properties [2]. The maximum reflection loss is -32.3 dB at 11.4 GHz with thickness of 2.3 mm. The CoO_x /CFs composite investigated by Liu et al. exhibits excellent microwave absorption performances [17]. The lowest reflectivity is -45.16 dB at 13.41 GHz with 1.5 mm in thickness. The RGO- Co_3O_4 , PANI-RGO- Co_3O_4 , and PPy-RGO- Co_3O_4 nanocomposites researched by Liu et al. have maximum reflection losses of -43.7 dB at 13.8 GHz (with a thickness

of 3.3 mm), -32.6 dB at 6.3 GHz (with a thickness of 3 mm), and -33.5 dB at 15.8 GHz (with a thickness of 2.5 mm), respectively [18–20].

In this work, we report a core-shell structured Co_3O_4 -PANI nanocomposite with a maximum reflection loss of up to -45.8 dB at 11.7 GHz when its thickness is 2.5 mm. The core-shell Co_3O_4 -PANI was synthesized by a facile, inexpensive, and scalable method and characterized by XRD, TEM, FTIR, and XPS. The behaviors of microwave absorption of Co_3O_4 -PANI were investigated and the microwave absorbing mechanisms were also discussed.

2. Experimental

2.1. Preparation of Co_3O_4 -PANI Nanocomposites. The spinel Co_3O_4 was synthesized by carbon-assisted method using degreasing cotton as a template. 17.46 g $\text{Co}(\text{NO}_3)_2 \cdot 6\text{H}_2\text{O}$ was dissolved in 20 mL deionized water with magnetic stirring for 10 min. Then 1.5 g degreasing cotton was immersed in the blood red solution and ultrasonicated for 10 min to disperse the ions on the degreasing cotton homogeneously. Then the treated degreasing cotton was transferred into a quartz Petri dish in the tube furnace (OTF-1200X-III, Heifei, China) and calcined at 600°C for 2 h in air to obtain Co_3O_4 nanoparticles.

The core-shell Co_3O_4 -PANI nanocomposite was prepared by an in situ polymerization method. 0.9 g preprepared Co_3O_4 was added into 5 mL of 2 mol/L HCl diluted by 50 mL deionized water and kept for 1 h in an ultrasonic bath. Then 1.6 mL aniline was mixed in the solution and stirred vigorously for 30 min. The aqueous solution of $(\text{NH}_4)_2\text{S}_2\text{O}_8$ (APS, 4.56 g was dissolved in 50 mL deionized water) was slowly added to the above mixture and stirred for 10 h. The obtained precipitate was filtered and washed with HCl, methanol, and deionized water in sequence repeatedly until the precipitate is neutral. Finally, the precipitate was dried at 60°C for 24 h and the Co_3O_4 -PANI nanocomposite was obtained.

2.2. Characterization. The X-ray powder diffraction (XRD) was carried out using a Bruker D8 with $\text{Cu K}\alpha$ ($\lambda = 1.5406 \text{ \AA}$) radiation at 40 eV in the 2θ of 20 – 80° . The morphology was observed by transmission electron microscopy (TEM, JEOL JEM-2011). Fourier transform infrared spectroscopy (FTIR) was recorded from KBr pellets in the range of 500 – 4000 cm^{-1} on an Avatar 360 spectrometer. X-ray photoelectron spectroscopy (XPS) was measured on an ESCALAB 250Xi spectrometer with a standard Al $\text{K}\alpha$ radiation with the binding energies calibrated based on the contaminant carbon (C1s = 284.6 eV).

In order to measure the electromagnetic parameters, the samples were prepared by uniformly mixing the prepared nanomaterials with a paraffin matrix in the mass ratio of 1 : 1 and then pressing the mixture into a toroidal shaped compact ($\Phi_{\text{outer}} = 7.00 \text{ mm}$ and $\Phi_{\text{inner}} = 3.04 \text{ mm}$). The electromagnetic parameters of the as-obtained samples were measured in the frequency range of 2.0–18.0 GHz by an Agilent HP-8722ES vector network analyzer.

3. Results and Discussions

The XRD patterns of Co_3O_4 and Co_3O_4 -PANI are shown in Figure 1. In the pattern of Co_3O_4 , it can be observed that the diffraction peaks of Co_3O_4 at $2\theta = 31.3, 36.9, 38.5, 44.8,$

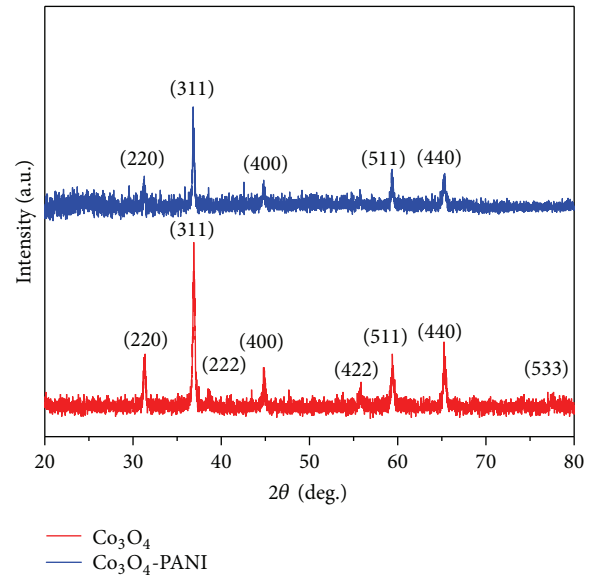


FIGURE 1: XRD patterns of Co_3O_4 and Co_3O_4 -PANI.

55.6, 59.3, 65.2, and 77.3 can be assigned to the (220), (311), (222), (400), (422), (511), (440), and (533) planes of Co_3O_4 , respectively, which is in accordance with JCPDS card of the standard spinel cubic Co_3O_4 (JCPDS number 42-1467) [21]. The crystallite size with respect to (311) peak of Co_3O_4 has been calculated by the Scherrer relation and is estimated to be 56.6 nm. In the pattern of Co_3O_4 -PANI, comparing to pure Co_3O_4 , all peaks of Co_3O_4 become weaker and the peaks at $2\theta = 38.5, 55.6,$ and 77.3 are even too weak to be observed, which is on account of the PANI coating. There is a small hump when 2θ is below 30. This is due to the periodicity parallel and perpendicular to the polymer chains which indicates the polyaniline is amorphous [22, 23]. The absence of the peaks of PANI in Co_3O_4 -PANI nanocomposites is due to the presence of Co_3O_4 which has a great effect on forming PANI during the coating process. The interaction of PANI and Co_3O_4 in the interface blocks the crystallization of PANI [24]. Both the weakness of Co_3O_4 peaks and the lack of the PANI peaks in Co_3O_4 -PANI prove that Co_3O_4 nanoparticles are well coated by PANI.

To investigate the morphology and structure of the products, TEM images were taken for Co_3O_4 and Co_3O_4 -PANI and the corresponding results are presented in Figure 2. Figure 2(a) shows that the Co_3O_4 nanoparticles with a relatively small size are obtained. The edges are clear and round. It indicates that the particles are approximately spherical or ellipsoidal. The average size of nanoparticles is about 60 nm, which is consistent with the calculation from XRD mentioned above. From Figure 2(b), we can see that a lot of wrinkled forms cover on the Co_3O_4 dark cores. The edges of particles are quite blur and amorphous, which is attributed to PANI. The formation of amorphous PANI supports the explanation about the lack of PANI peaks in Co_3O_4 -PANI discussed before. After coating with PANI, the particle sizes of the core-shell nanocomposites are around 100 nm. It can be observed in Figures 2(c) and 2(d) that the measured lattice spacing

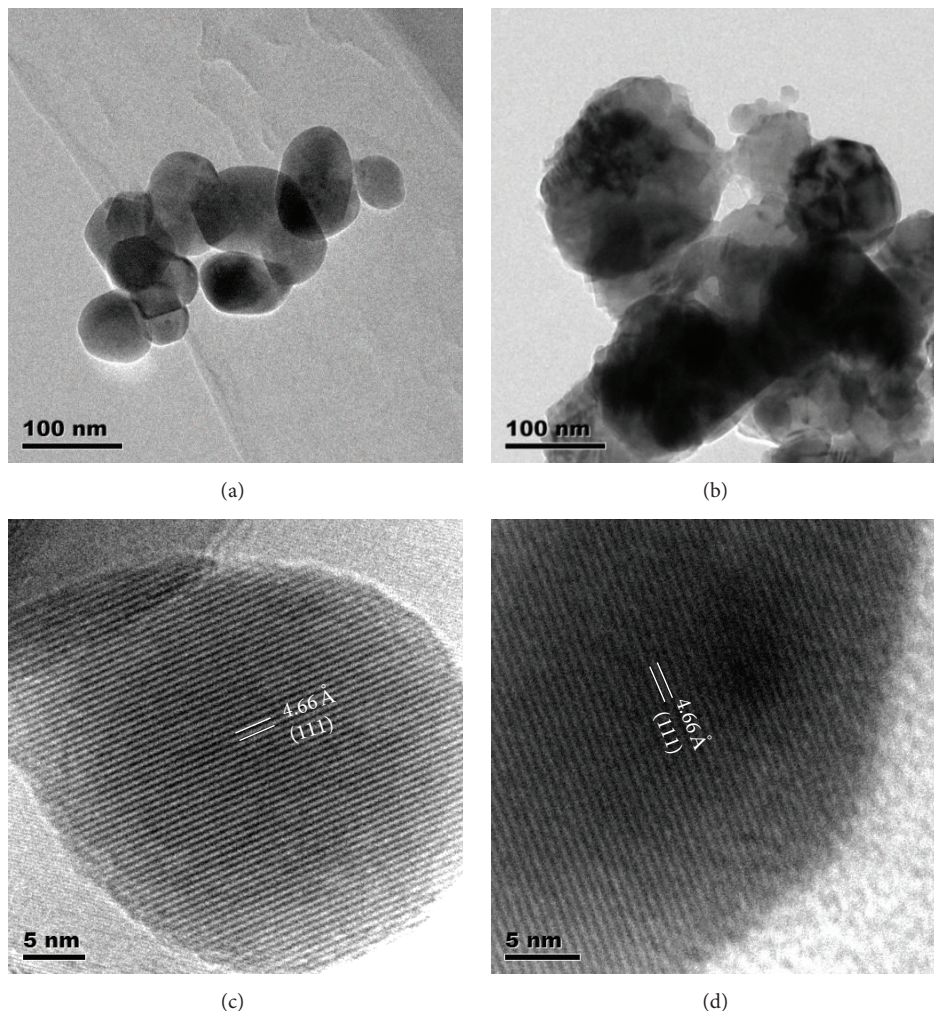


FIGURE 2: TEM images of Co_3O_4 (a) and Co_3O_4 -PANI (b). HRTEM images of Co_3O_4 (c) and Co_3O_4 -PANI (d).

is 4.66 Å which is in line with the (111) interplanar distance of the Co_3O_4 [12]. The HRTEM analysis shows clear and continuous lattice fringes which further confirm the good crystal structure of prepared Co_3O_4 .

The FTIR spectra of Co_3O_4 and Co_3O_4 -PANI are shown in Figure 3. The sharp peaks at 572 and 661 cm^{-1} in the spectrum of Co_3O_4 are associated with the OB_3 (B represents Co^{3+} in an octahedral hole) and the ABO (A represents the Co^{2+} in a tetrahedral hole) vibrations in the spinel lattice, respectively [25, 26]. Both Co_3O_4 and Co_3O_4 -PANI have two peaks at 1118 and 1398 cm^{-1} . The peak at 1118 cm^{-1} is attributed to the stretching vibrations of C–O and CO_3^{2-} anions. They are introduced by the burn of degreasing cotton during the preparation procedure of Co_3O_4 . The peak at 1398 cm^{-1} is corresponding to the stretching vibration of NO_3^- , which is due to the residue of $\text{Co}(\text{NO}_3)_3$ [12]. The peaks at 1642 and 3465 cm^{-1} in the spectrum of Co_3O_4 are assigned to molecular water and O–H [27]. In the spectrum of Co_3O_4 -PANI, other than the influence of molecular water and O–H, the bands at 1644 and 3446 cm^{-1} are also affected by the quinoid ring and N–H stretching of PANI, separately [24, 28, 29]. In the spectrum of Co_3O_4 -PANI, the very small

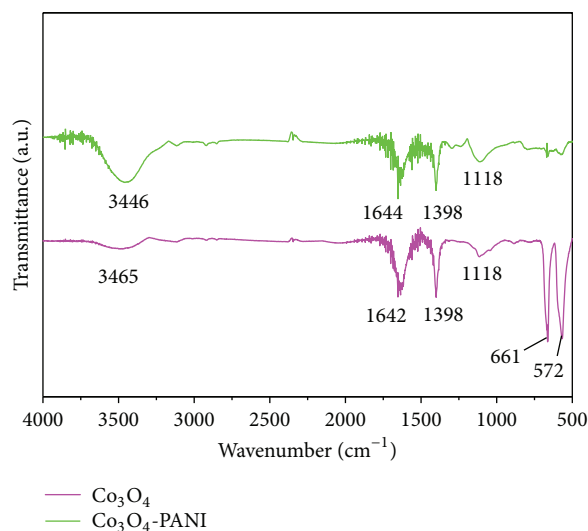


FIGURE 3: FT-IR spectra of Co_3O_4 and Co_3O_4 -PANI.

peaks between 1118 and 1644 cm^{-1} are due to the existence of PANI. The absence of the characteristic peaks of Co_3O_4

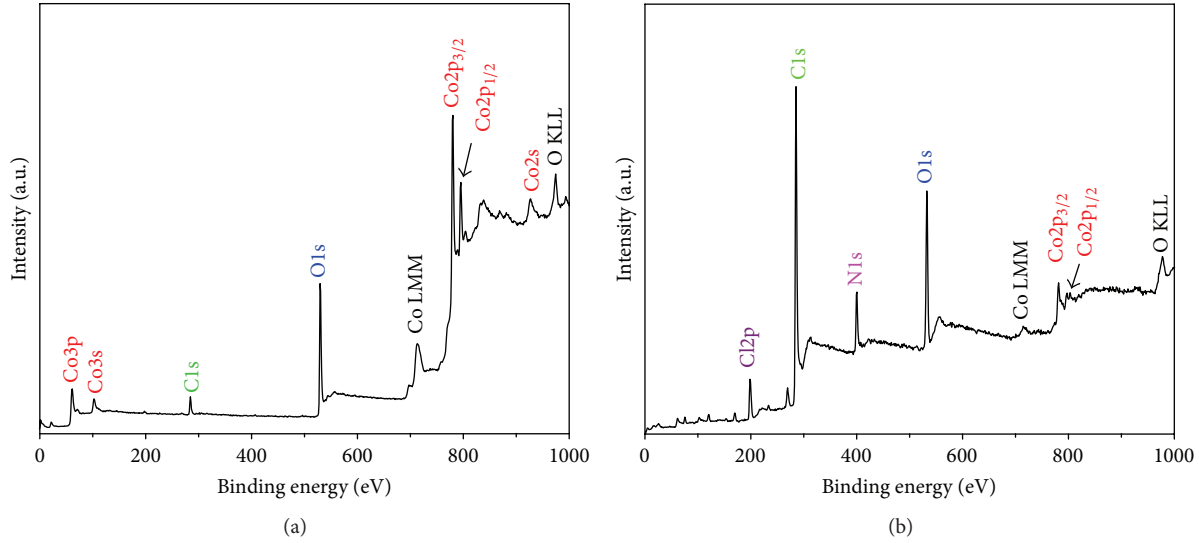


FIGURE 4: XPS spectra of Co₃O₄ (a) and Co₃O₄-PANI (b).

shows that the PANI is completely coated on the Co₃O₄ and has an impact on the surface of Co₃O₄. The analysis above suggests that it is not a simple mix between Co₃O₄ and PANI but rather an interaction existing at the interfaces of Co₃O₄ nanoparticles and PANI [30].

The XPS spectra of Co₃O₄ and Co₃O₄-PANI nanoparticles are presented in Figure 4. In Figure 4(a), the spectrum of Co₃O₄ samples shows the existence of cobalt, oxygen, and carbon elements at the surface. Two peaks at 780.4 and 795.4 eV correspond to Co2p_{3/2} and Co2p_{1/2} spin-orbit peaks of Co₃O₄, which are characteristic of the Co₃O₄ phase [31]. The O1s peak centered at 529.8 eV is assigned to the lattice oxygen in the Co₃O₄ phase. The relatively small peak Cl1s at 284.6 eV is ascribed to elemental carbon which results from the insufficient burning of degreasing cotton. In Figure 4(b), it can be observed that there are chlorine, carbon, nitrogen, oxygen, and cobalt elements presented at the surface of Co₃O₄-PANI samples. The Cl2p peak at 198.4 eV indicates the existence of Cl⁻ which is due to the HCl solution used in the synthesis of Co₃O₄-PANI [32]. The Cl1s and N1s peaks at 285.5 and 400.2 eV are attributed to the C-N and -NH- from the PANI backbone [33, 34]. The O1s peak at 532.4 eV is ascribed to hydroxide ions adsorbed on the surface. The characteristic peaks of Co₃O₄ at 780.4 and 795.4 eV are very weak. It can be inferred that Co₃O₄ core is well covered by PANI and the core-shell Co₃O₄-PANI nanocomposite is well synthesized.

To study the microwave absorption properties, reflection loss (R_L) can be used to characterize the microwave absorption capacity, which is affected by morphology, dielectric and magnetic properties, electromagnetic impedance match, and chemical stability of the absorber. R_L is calculated according to the transmission line theory [35]:

$$R_L \text{ (dB)} = 20 \log \left| \frac{Z_{\text{in}} - Z_0}{Z_{\text{in}} + Z_0} \right|, \quad (1)$$

$$Z_{\text{in}} = Z_0 \sqrt{\frac{\mu_r}{\epsilon_r}} \tanh \left[j \left(\frac{2\pi f d}{c} \right) \sqrt{\mu_r \epsilon_r} \right],$$

where Z_{in} is the input impedance of the absorber, Z_0 is the input impedance of air, μ_r and ϵ_r are, respectively, the relative complex permeability and permittivity, f is the frequency of the electromagnetic waves, d is the thickness of the absorber, c is the velocity of electromagnetic waves in free space, and R_L (dB) is the reflection loss of the absorber.

Figure 5 shows the relationship between reflection loss and frequency in different thickness for the obtained samples. In Figure 5(a), it can be observed that the R_L of Co₃O₄ is no more than -6 dB when its thickness ranges from 2 to 5.5 mm, and the maximum R_L is only -6.0 dB at the frequency of 8.3 GHz with a thickness of 5.5 mm. This demonstrates that the Co₃O₄ sample exhibits a very weak ability to absorb microwave. In Figure 5(b), it can be found that the microwave absorption properties of Co₃O₄ are significantly enhanced by PANI coating. The reflection loss of Co₃O₄-PANI is less than -10 dB (90% of microwave absorption) over the frequency range of 3.9–18 GHz when the thickness of sample is between 2 mm and 5.5 mm. The maximum R_L of Co₃O₄-PANI is up to -45.8 dB at 11.7 GHz and the absorption bandwidths corresponding to the R_L values below -10 dB are 5.8 GHz (from 9.6 to 14.4 GHz) when its thickness is 2.5 mm. It is well known that microwave absorption capability relies on the nature shape and size of an absorber [36]. The excellent microwave absorption properties may be due to the special structure and geometrical morphology of the nanocomposite prepared by applying PANI coating on Co₃O₄. Furthermore, the thickness of the samples is another critical factor affecting the intensity and the position of the frequency at the maximum reflection losses [37]. It can be seen that the maximum R_L values obviously shift to the lower frequency as the thickness increases from 2 to 5.5 mm. They also move to the smaller intensity except the maximum R_L value with a thickness of 2.5 mm, which has the maximal intensity of all.

To investigate the microwave absorption mechanism of the Co₃O₄-PANI, the relative complex permittivity, permeability, and loss tangent of Co₃O₄ and Co₃O₄-PANI are

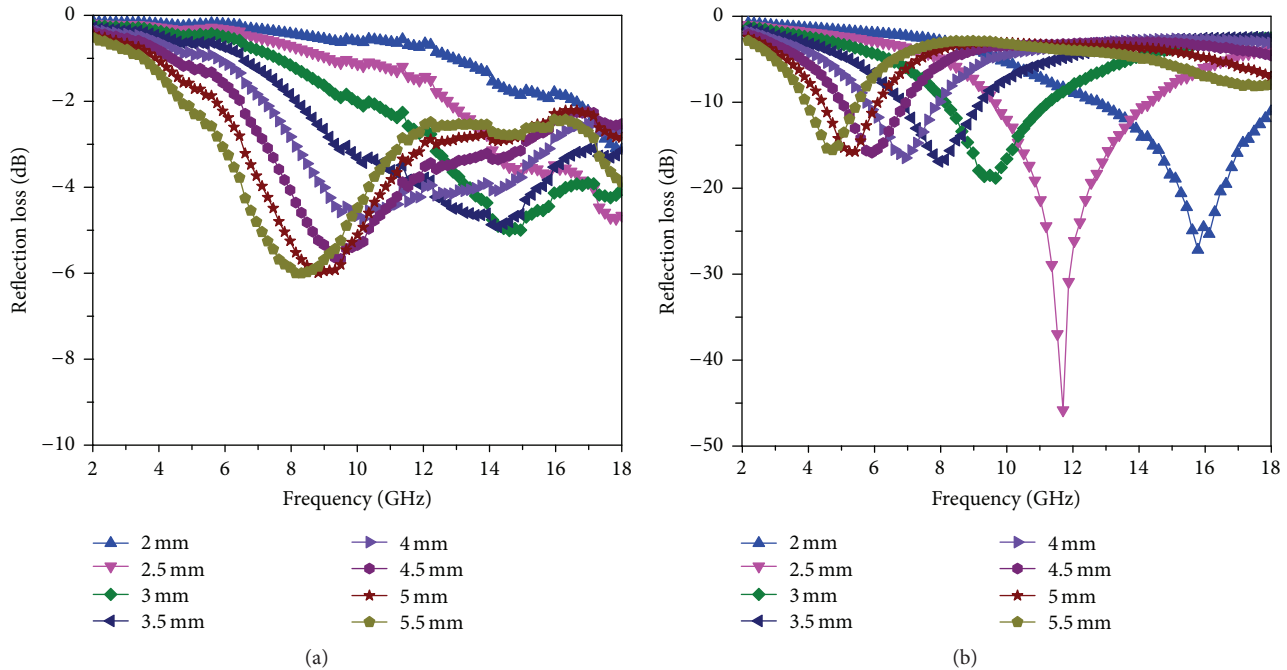


FIGURE 5: Microwave reflection loss of Co₃O₄ (a) and Co₃O₄-PANI (b).

presented in Figure 6 to characterize dielectric loss and magnetic loss properties of absorbers. In Figure 6(a), the real (ϵ') and imaginary (ϵ'') parts of relative permittivity of Co₃O₄ are around 3.5 and 0.5, respectively, and both of the two parameters change slowly as the frequency increases. They decrease relatively fast when frequency increases from 2 to 6 GHz and then tend to stabilize with some fluctuations. The fluctuations are related to the resonance behavior caused by the charge polarization of Co₃O₄ [38]. Comparing to Co₃O₄, Co₃O₄-PANI has much higher and more unstable ϵ' and ϵ'' values (Figure 6(b)). The high values are partially due to the strong polarization in PANI generated from polaron/bipolaron and other bound charges [3]. But PANI itself cannot improve the permittivity that much [30, 39]. The interfacial interaction between the PANI and Co₃O₄ core has a great effect on the permittivity, which is attributed to a large number of interfacial polarization charges [2, 40]. Both the ϵ' and ϵ'' values decrease rapidly with frequency increasing from 2 to 6 GHz. ϵ' keeps declining until the frequency reaches 18 GHz, but ϵ'' stops decreasing at the frequency of 12 GHz and then has a slight rise. The variation of permittivity with frequency can be explained by the interfacial relaxation between Co₃O₄ cores and PANI shells, as well as the Debye relaxation of PANI [3, 41]. As the applied field alters, the charges redistribute alternatively between Co₃O₄ cores and PANI shells, and the dipoles in nanocomposites cannot reorient themselves along with the field.

By comparing the relative permeability of Figures 6(c) and 6(d), it is clearly shown that PANI coating almost has no influence on the permeability of Co₃O₄-PANI nanocomposite. The real (μ') and imaginary (μ'') parts of relative permittivity of Co₃O₄ are slightly above 1.0 and below 0.1,

respectively. Being almost identical to those of Co₃O₄, the real and imaginary parts of relative permittivity of Co₃O₄-PANI fluctuate around 1.0 and 0.1, separately. The small difference may be caused by the interfacial interaction where the motion of charges produces an induced magnetic field. The small values indicate that both Co₃O₄ and Co₃O₄-PANI show a very weak magnetic loss.

Figures 6(e) and 6(f) show the loss tangent of Co₃O₄ and Co₃O₄-PANI. Apparently, the dielectric loss tangent ($\tan \delta_\epsilon = \epsilon''/\epsilon'$) is much larger than the magnetic loss tangent ($\tan \delta_\mu = \mu''/\mu'$) for both Co₃O₄-PANI and Co₃O₄. This indicates that the main absorption mechanism of Co₃O₄-PANI and Co₃O₄ is dielectric loss. The dielectric loss of Co₃O₄-PANI is nearly four times as high as that of Co₃O₄. The interfacial interaction between the Co₃O₄ cores and PANI shells greatly affects the dielectric loss of Co₃O₄-PANI as discussed above. So it can be concluded that the core-shell structure makes a major contribution to the excellent microwave absorption properties of Co₃O₄-PANI.

4. Conclusion

The Co₃O₄ nanoparticle has been synthesized by carbon-assisted method using degreasing cotton as a template and coated with PANI using an in situ polymerization method. The XRD, TEM, FTIR, and XPS characterizations show that the Co₃O₄ nanoparticle prepared is the spinel structure with average size of around 60 nm and the Co₃O₄-PANI nanocomposite is the core-shell structure with particle size of about 100 nm. Comparing to Co₃O₄, the core-shell structured Co₃O₄-PANI exhibits greatly enhanced microwave absorption properties. The optimal absorption peak of Co₃O₄-PANI

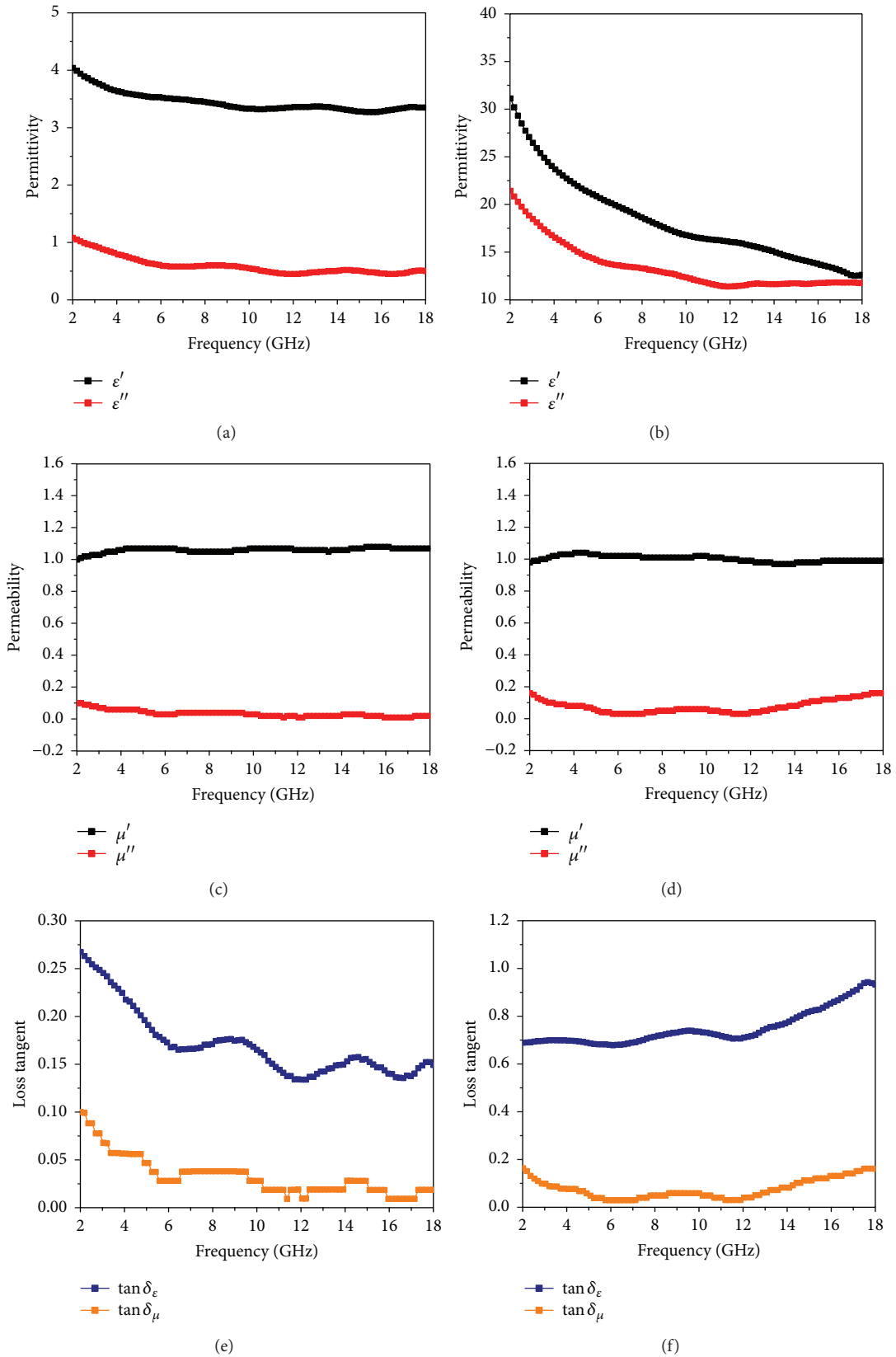


FIGURE 6: The complex relative permittivity of Co_3O_4 (a) and $\text{Co}_3\text{O}_4\text{-PANI}$ (b), the complex relative permeability of Co_3O_4 (c) and $\text{Co}_3\text{O}_4\text{-PANI}$ (d), and the loss tangent of Co_3O_4 (e) and $\text{Co}_3\text{O}_4\text{-PANI}$ (f).

reaches -45.8 dB at 11.7 GHz with a thickness of 2.5 mm and the adsorption bandwidth corresponding to the reflection loss below -10 dB is 14.1 GHz (from 3.9 to 18 GHz) when the thickness is between 2 and 5.5 mm. This is believed to be due to the interfacial interaction of the core-shell structure. The microwave absorption properties of Co_3O_4 -PANI may be further optimized by varying the ratio of Co_3O_4 core and PANI shell during the synthesis process in the future work. The superior microwave absorption properties demonstrate that the core-shell structured Co_3O_4 -PANI nanocomposite can be a promising nanomaterial for high efficient microwave absorption.

Conflict of Interests

The authors declare that there is no conflict of interests regarding the publication of this paper.

Acknowledgments

This work was financially supported by the National Natural Science Foundation of China for Distinguished Young Scholar (Grant no. 51225504) and the National High-Tech Research and Development (863) Program of China (Grant no. 2015AA042600).

References

- [1] J. Qiu and T. Qiu, "Fabrication and microwave absorption properties of magnetite nanoparticle-carbon nanotube-hollow carbon fiber composites," *Carbon*, vol. 81, no. 1, pp. 20–28, 2015.
- [2] F. Wen, H. Hou, J. Xiang et al., "Fabrication of carbon encapsulated Co_3O_4 nanoparticles embedded in porous graphitic carbon nanosheets for microwave absorber," *Carbon*, vol. 89, pp. 372–377, 2015.
- [3] K. Singh, A. Ohlan, A. K. Bakhshi, and S. K. Dhawan, "Synthesis of conducting ferromagnetic nanocomposite with improved microwave absorption properties," *Materials Chemistry and Physics*, vol. 119, no. 1-2, pp. 201–207, 2010.
- [4] T. Zhang, B. Zhong, J. Q. Yang, X. X. Huang, and G. Wen, "Boron and nitrogen doped carbon nanotubes/ Fe_3O_4 composite architectures with microwave absorption property," *Ceramics International*, vol. 41, no. 6, pp. 8163–8170, 2015.
- [5] T. H. Ting, R. P. Yu, and Y. N. Jau, "Synthesis and microwave absorption characteristics of polyaniline/NiZn ferrite composites in 2–40 GHz," *Materials Chemistry and Physics*, vol. 126, no. 1-2, pp. 364–368, 2011.
- [6] N. Gandhi, K. Singh, A. Ohlan, D. P. Singh, and S. K. Dhawan, "Thermal, dielectric and microwave absorption properties of polyaniline- CoFe_2O_4 nanocomposites," *Composites Science and Technology*, vol. 71, no. 15, pp. 1754–1760, 2011.
- [7] K. Singh, A. Ohlan, V. H. Pham et al., "Nanostructured graphene/ Fe_3O_4 incorporated polyaniline as a high performance shield against electromagnetic pollution," *Nanoscale*, vol. 5, no. 6, pp. 2411–2420, 2013.
- [8] M.-S. Cao, J. Yang, W.-L. Song et al., "Ferroferric oxide/multi-walled carbon nanotube vs polyaniline/ferroferric oxide/multi-walled carbon nanotube multiheterostructures for highly effective microwave absorption," *ACS Applied Materials & Interfaces*, vol. 4, no. 12, pp. 6949–6956, 2012.
- [9] S. C. Petitto and M. A. Langell, "Surface composition and structure of $\text{Co}_3\text{O}_4(110)$ and the effect of impurity segregation," *Journal of Vacuum Science & Technology A: Vacuum, Surfaces and Films*, vol. 22, no. 4, pp. 1690–1696, 2004.
- [10] B. Bai, H. Arandiyani, and J. Li, "Comparison of the performance for oxidation of formaldehyde on nano- Co_3O_4 , 2D- Co_3O_4 , and 3D- Co_3O_4 catalysts," *Applied Catalysis B: Environmental*, vol. 142–143, pp. 677–683, 2013.
- [11] D. Su, X. Xie, P. Munroe, S. Dou, and G. Wang, "Mesoporous hexagonal Co_3O_4 for high performance lithium ion batteries," *Scientific Reports*, vol. 4, article 6519, 8 pages, 2014.
- [12] X.-H. Xia, J.-P. Tu, Y.-J. Mai, X.-L. Wang, C.-D. Gu, and X.-B. Zhao, "Self-supported hydrothermal synthesized hollow Co_3O_4 nanowire arrays with high supercapacitor capacitance," *Journal of Materials Chemistry*, vol. 21, no. 25, pp. 9319–9325, 2011.
- [13] L. Wang, Y. Ye, Y. Shen et al., "Hierarchical nanocomposites of Co_3O_4 /polyaniline nanowire arrays/reduced graphene oxide sheets for amino acid detection," *Sensors and Actuators, B: Chemical*, vol. 203, pp. 864–872, 2014.
- [14] Q. Zhang, L. Gao, X. Chou, J. Diwu, H. Xu, and C. Xue, "Synthesis of octahedral Co_3O_4 via carbon-assisted method," *Micro & Nano Letters*, vol. 10, no. 2, pp. 85–87, 2015.
- [15] L. Gao, J. Diwu, Q. Zhang et al., "A green and facile synthesis of carbon-incorporated Co_3O_4 nanoparticles and their photocatalytic activity for hydrogen evolution," *Journal of Nanomaterials*, vol. 2015, Article ID 618492, 7 pages, 2015.
- [16] H. Wu, Q. Wu, and L. Wang, "Design and wide range microwave absorption of porous Co- Co_3O_4 hybrid hollow sphere with magnetic multi-resonance mechanisms," *Materials Characterization*, vol. 103, pp. 1–10, 2015.
- [17] Y. Liu, Z. Zhang, S. Xiao, C. Qiang, L. Tian, and J. Xu, "Preparation and properties of cobalt oxides coated carbon fibers as microwave-absorbing materials," *Applied Surface Science*, vol. 257, no. 17, pp. 7678–7683, 2011.
- [18] P. Liu, Y. Huang, L. Wang, M. Zong, and W. Zhang, "Hydrothermal synthesis of reduced graphene oxide- Co_3O_4 composites and the excellent microwave electromagnetic properties," *Materials Letters*, vol. 107, pp. 166–169, 2013.
- [19] P. Liu, Y. Huang, L. Wang, and W. Zhang, "Preparation and excellent microwave absorption property of three component nanocomposites: polyaniline-reduced graphene oxide- Co_3O_4 nanoparticles," *Synthetic Metals*, vol. 177, pp. 89–93, 2013.
- [20] P. Liu, Y. Huang, L. Wang, and W. Zhang, "Synthesis and excellent electromagnetic absorption properties of polypyrrole-reduced graphene oxide- Co_3O_4 nanocomposites," *Journal of Alloys and Compounds*, vol. 573, pp. 151–156, 2013.
- [21] K. R. Reddy, K. P. Lee, and A. I. Gopalan, "Self-assembly approach for the synthesis of electro-magnetic functionalized Fe_3O_4 /polyaniline nanocomposites: effect of dopant on the properties," *Colloids and Surfaces A: Physicochemical and Engineering Aspects*, vol. 320, no. 1–3, pp. 49–56, 2008.
- [22] B. Thakur, C. A. Amarnath, S. H. Mangoli, and S. N. Sawant, "Polyaniline nanoparticle based colorimetric sensor for monitoring bacterial growth," *Sensors and Actuators, B: Chemical*, vol. 207, pp. 262–268, 2014.
- [23] C. A. Amarnath, N. Venkatesan, M. Doble, and S. N. Sawant, "Water dispersible Ag@polyaniline-pectin as supercapacitor electrode for physiological environment," *Journal of Materials Chemistry B*, vol. 2, no. 31, pp. 5012–5019, 2014.

- [24] B. H. Shambharkar and S. S. Umare, "Production and characterization of polyaniline/ Co_3O_4 nanocomposite as a cathode of Zn-polyaniline battery," *Materials Science and Engineering B: Solid-State Materials for Advanced Technology*, vol. 175, no. 2, pp. 120–128, 2010.
- [25] Y. Liu, G. Zhu, B. Ge, H. Zhou, A. Yuan, and X. Shen, "Concave Co_3O_4 octahedral mesocrystal: polymer-mediated synthesis and sensing properties," *CrystEngComm*, vol. 14, no. 19, pp. 6264–6270, 2012.
- [26] T. He, D. Chen, X. Jiao, Y. Xu, and Y. Gu, "Surfactant-assisted solvothermal synthesis of Co_3O_4 hollow spheres with oriented-aggregation nanostructures and tunable particle size," *Langmuir*, vol. 20, no. 19, pp. 8404–8408, 2004.
- [27] S. Vijayakumar, A. Kiruthika Ponnalagi, S. Nagamuthu, and G. Muralidharan, "Microwave assisted synthesis of Co_3O_4 nanoparticles for high-performance supercapacitors," *Electrochimica Acta*, vol. 106, pp. 500–505, 2013.
- [28] P. Boomi, H. G. Prabu, P. Manisankar, and S. Ravikumar, "Study on antibacterial activity of chemically synthesized PANI-Ag-Au nanocomposite," *Applied Surface Science*, vol. 300, pp. 66–72, 2014.
- [29] W. Zheng, M. Angelopoulos, A. J. Epstein, and A. G. MacDiarmid, "Experimental evidence for hydrogen bonding in polyaniline: mechanism of aggregate formation and dependency on oxidation state," *Macromolecules*, vol. 30, no. 10, pp. 2953–2955, 1997.
- [30] F. Xu, L. Ma, Q. Huo, M. Gan, and J. Tang, "Microwave absorbing properties and structural design of microwave absorbers based on polyaniline and polyaniline/magnetite nanocomposite," *Journal of Magnetism and Magnetic Materials*, vol. 374, pp. 311–316, 2015.
- [31] Z.-S. Wu, W. Ren, L. Wen et al., "Graphene anchored with Co_3O_4 nanoparticles as anode of lithium ion batteries with enhanced reversible capacity and cyclic performance," *ACS Nano*, vol. 4, no. 6, pp. 3187–3194, 2010.
- [32] H. Cui, Q. Li, Y. Qian, R. Tang, H. An, and J. Zhai, "Defluoridation of water via electrically controlled anion exchange by polyaniline modified electrode reactor," *Water Research*, vol. 45, no. 17, pp. 5736–5744, 2011.
- [33] S. Golczak, A. Kancierzewska, M. Fahlman, K. Langer, and J. J. Langer, "Comparative XPS surface study of polyaniline thin films," *Solid State Ionics*, vol. 179, no. 39, pp. 2234–2239, 2008.
- [34] J. Zhang, D. Shu, T. Zhang et al., "Capacitive properties of PANI/ MnO_2 synthesized via simultaneous-oxidation route," *Journal of Alloys and Compounds*, vol. 532, pp. 1–9, 2012.
- [35] L. Yan, J. Wang, X. Han, Y. Ren, Q. Liu, and F. Li, "Enhanced microwave absorption of Fe nanoflakes after coating with SiO_2 nanoshell," *Nanotechnology*, vol. 21, no. 9, Article ID 095708, 2010.
- [36] P. Liu and Y. Huang, "Decoration of reduced graphene oxide with polyaniline film and their enhanced microwave absorption properties," *RSC Advances*, vol. 21, no. 5, pp. 1–5, 2014.
- [37] T. Chen, F. Deng, J. Zhu et al., "Hexagonal and cubic Ni nanocrystals grown on graphene: phase-controlled synthesis, characterization and their enhanced microwave absorption properties," *Journal of Materials Chemistry*, vol. 22, no. 30, pp. 15190–15197, 2012.
- [38] H. Wu, L. Wang, Y. Wang, and S. Guo, "Microwave absorption properties of CeO_2 and Zn-modified CeO_2 microstructures," *Applied Surface Science*, vol. 258, no. 24, pp. 10047–10052, 2012.
- [39] M. Oyharçabal, T. Olinga, M.-P. Foulc, S. Lacomme, E. Gontier, and V. Vigneras, "Influence of the morphology of polyaniline on the microwave absorption properties of epoxy polyaniline composites," *Composites Science and Technology*, vol. 74, pp. 107–112, 2013.
- [40] H. Qin, Q. Liao, G. Zhang, Y. Huang, and Y. Zhang, "Microwave absorption properties of carbon black and tetrapod-like ZnO whiskers composites," *Applied Surface Science*, vol. 286, pp. 7–11, 2013.
- [41] S. S. S. Afghahi and A. Shokuhfar, "Two step synthesis, electromagnetic and microwave absorbing properties of FeCo@C core-shell nanostructure," *Journal of Magnetism and Magnetic Materials*, vol. 370, pp. 37–44, 2014.

Research Article

The Effect of NaCl/pH on Colloidal Nanogold Produced by Pulsed Spark Discharge

Kuo-Hsiung Tseng, Chin-Liang Hsieh, Jen-Chuen Huang, and Der-Chi Tien

Department of Electrical Engineering, National Taipei University of Technology, Taipei 10608, Taiwan

Correspondence should be addressed to Kuo-Hsiung Tseng; khtseng@ee.ntut.edu.tw

Received 20 May 2015; Revised 8 August 2015; Accepted 16 August 2015

Academic Editor: Themis Matsoukas

Copyright © 2015 Kuo-Hsiung Tseng et al. This is an open access article distributed under the Creative Commons Attribution License, which permits unrestricted use, distribution, and reproduction in any medium, provided the original work is properly cited.

A green method, using pulsed spark discharge (PSD) to synthesize colloidal gold, is studied in this thesis. PSD uses spark discharge to synthesize gold nanoparticles (AuNPs) in deionized water (DIW) and/or ethanol (EtOH). While gold nanoparticles have widespread applications in many fields, especially for the human body, in use they must overcome the influence of NaCl and pH value; therefore, this study adds NaCl into PSD-AuNPs to simulate the human body to study its stability. Furthermore, a variety of protectants are added in an attempt to determine the best protectant for AuNPs and improve biologically compatible potency. From the results of this study, adding the long-chain-polymer Carboxymethyl cellulose (CMC) or Polyvinyl pyrrolidone (PVP-k30) can prevent nanogold from aggregation and precipitation in NaCl or different pH value and maintain the characteristic of nanogold dispersion by raising the repulsive force between the particles. The results of this study can be a reference of nanogold applying in biomedical science.

1. Introduction

The pulse spark discharge (PSD) method is developed and used to fabricate the AuNPs solution [1–5], which involves a pulse current being passed through two gold electrodes [6–8], which are submerged in deionized water or ethanol. Many methods of producing AuNPs include the introduction of surfactants in order to improve the suspension of the gold particles. However, gold nanoparticles fabricated by the pulse spark discharge (PSD) method in deionized water or ethanol without any surfactants or stabilizers are characterized as a stable colloid, which can be stored for a long term in a glass container at room temperature without visible sedimentation (no apparent precipitate). The DIW_nanogold is safe for the human body, such as target therapy and drug carriers; this study will propose the experiments and simulate results of the colloidal gold [9–13] within the NaCl and pH test.

Gold nanoparticles are widely applied in the human body but require overcoming the impacts of NaCl and pH value. Gold number [14] is defined as the amount (mg) of polymer required to prevent the aggregation of 10 cm^3 of gold solution with 1 cm^3 10% NaCl added. This study

also proposes an effective gold number method (a more efficient version of Zsigmondy's [15] method is conducted in the experiment performed here) in order to determine the gold number of potential colloidal gold stabilizers. Instead of varying the amount of surfactant added, increasing amounts of NaCl are added into a solution of colloidal gold with 0.1 mg of stabilizer, thus simulating continuous titrations. Also, the photothermal effect of AuNPs can also be used as a cancer treatment [16]. The superior biological piezoelectric biosensors can be produced, through biocompatibility, the electrical conductivity and the high surface area of nanogold particles [17]. The properties of nanoparticles can apply to metal to produce beneficial reaction of catalytic [18]. This study simulates the human body or normal saline in NaCl in order to discuss the impacts on gold nanoparticles of DIW_nanogold, under various biologically compatible protective agents, for improving biologically compatible potency. The impacts on, and variations in, suspension of pH value of gold nanoparticles (DIW_nanogold, chem_nanogold, and ethanol nanogold) fabricated by other methods, as well as the changes of absorbance and wavelength, are compared.

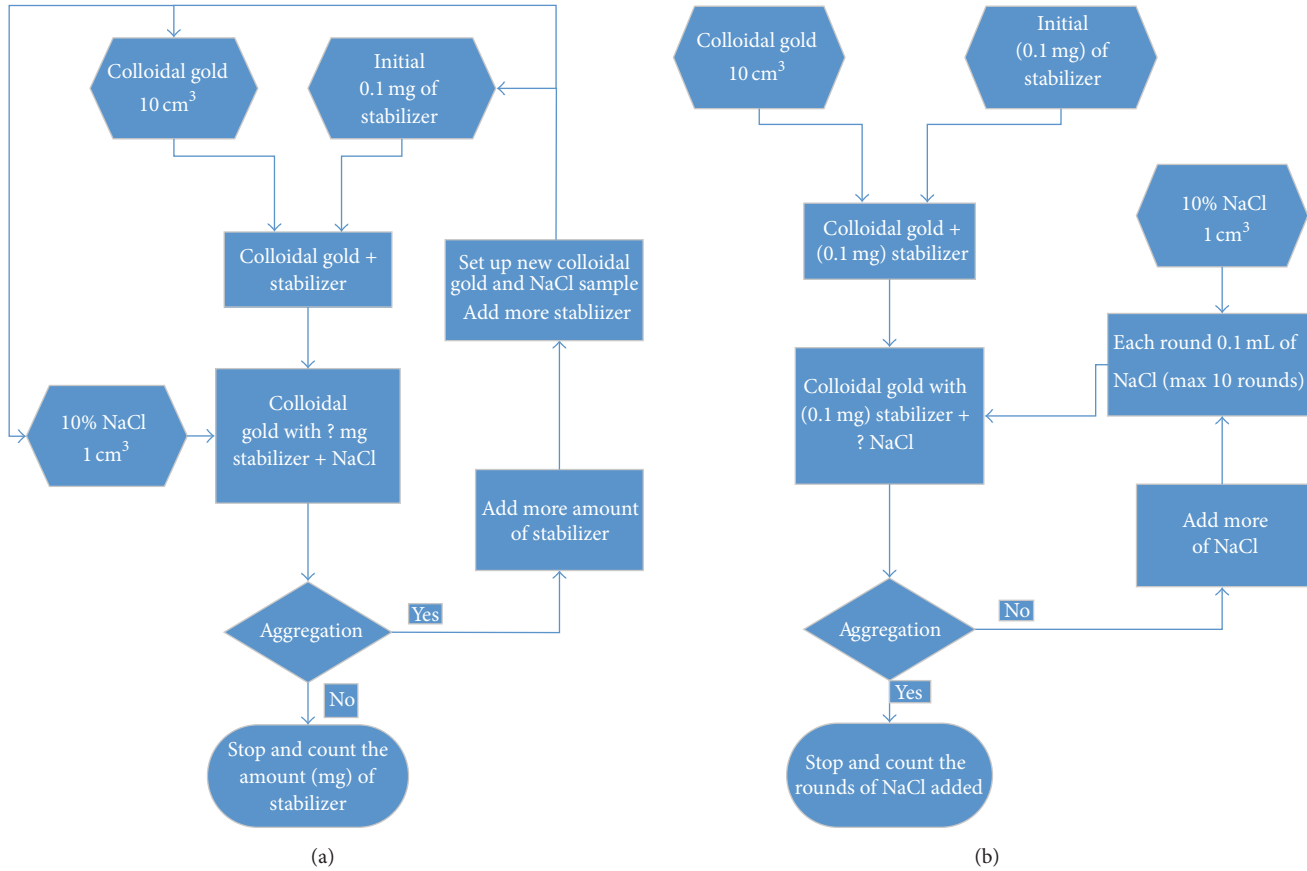


FIGURE 1: Flow chart of (a) Zsigmondy's method and (b) more efficient version of Zsigmondy's method.

2. Experimental Setup

This study utilizes the developed PSD system as a preparation method; the principle is to use a bar material (Au), which will be generated into nanometal material as top and bottom electrodes; there exists no direct contact between the two electrodes; thus, there is no physical force produced between the two; however, by using electricity converted into heat energy, a kind of hot melting method of electrode rapidly melting is created. The chamber is the main processing center. Deionized water, which has good insulativity, or ethanol, is used as dielectric liquid. The top and bottom electrodes are submerged into dielectric liquid to cause the generated nanoparticles to spread evenly and be directly stored in the dielectric liquid.

2.1. Preparation for NaCl Test. The fourteen agents listed in Table 1 were tested for their ability to maintain gold colloidal suspension. With the simulation of NaCl in proportions similar to those in human body fluids (0.9%), or the proportion of NaCl in normal saline, colloidal gold is mixed with a highly concentrated NaCl solution, which results in Na⁺ and Cl⁻ ions attacking the surface electric potential of the AuNPs. With the loss of their zeta potential, the nanoparticles lose their mutual repulsion and agglomerate. In order to avoid the destruction of zeta potential, the use of an adequate protecting agent is required so that the gold colloid can

TABLE 1: Types of stabilizing agents.

Item #	Name
S(1)	Propylene glycol alginate
S(2)	Sodium alginate
S(3)	Animal glue
S(4)	Gelatin L-150
S(5)	Guar gum S-200
S(6)	Xanthan gum
S(7)	CMC (carboxymethyl cellulose)
S(8)	Pectin
S(9)	CMC (carboxymethyl cellulose, antiacid)
S(10)	Carrageenan
S(11)	SDS (sodium dodecyl sulfate)
S(12)	PVP-k30 (polyvinyl pyrrolidone)
S(13)	Citric acid
S(14)	Glycine

survive in such an ion-rich solution. This study analyzed the impacts of various protecting agents (must be biocompatible for use in medicinal applications) on the agglomerate of PSDAuNPs-DIW and the agent can be used as protecting agent for PSD-AuNPsDIW.

First, 10 mL of the 30 ppm colloidal gold solution is placed into each of the 15 containers, numbered Au(0)~Au(14); then,

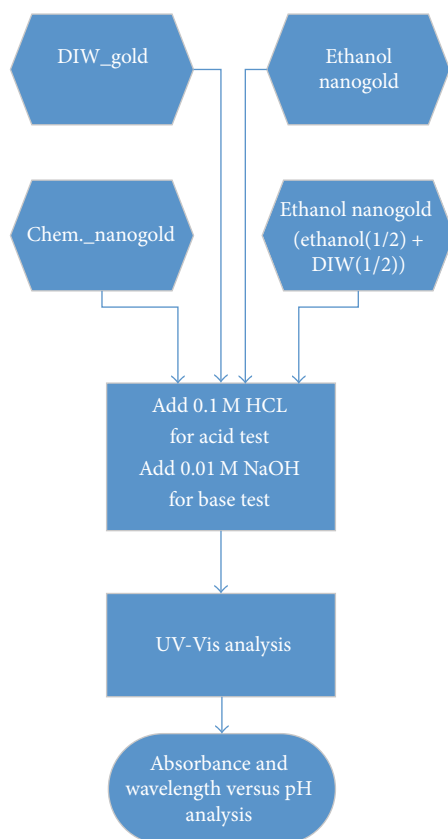


FIGURE 2: Flow chart of pH effect analysis for DIW_nanogold, chem._nanogold, and ethanol nanogold.

a second set is prepared by placing 10 mg of the 14 stabilizers into 10 mL of DIW for a 0.1% (w/v) concentration, which are labeled S(1)~S(14). Then, 0.1 mL is taken from each of S(1)~S(14) and placed into Au(1)~Au(14) so that 0.1 mg of the agent is present. No agents are added into Au(0), the control solution. A mixture of 1 g anhydrous salt, with 10 mL of water, is used for titrations in the amount of 0.1 mL (per round), and color change is noted after each titration. Add 0.1 mL of the 10% NaCl solution in each round. After the tenth round, the proportion of NaCl (1/11) is the amount seen, on average, in human body fluids (0.9%); therefore, the experiment can be stopped at that point. The continuous titrations will show, through level of color change, which stabilizer is the most effective. Figure 1 presents the flow chart of (a) Zsigmondy's method and (b) presents the more efficient version of Zsigmondy's method.

2.2. Preparation of pH Test. For ethanol nanogold, ethanol nanogold (ethanol(1/2) + DIW(1/2)), DIW_nanogold, and chem._ nanogold, six bottles of 10ml of each kind are used as a sample group. Each sample group adds HCl for acid tests and NaOH for base tests, and then the change of pH, visual observation of sample group, color changes, and agglomerate are observed. UV-Vis analysis is conducted for nonagglomerated samples and the pH effects on absorbance and wavenumber are analyzed, in order to gain further understanding of the relationships between the suspension

of various gold nanoparticles and pH. Figure 2 presents the flow chart of pH effect analysis for DIW_nanogold, chem._nanogold, and ethanol nanogold.

3. Results and Discussion

3.1. Results and Discussion of NaCl Test. Table 2 displays the number of rounds each surfactant required before a major color change was observed. Once one was observed, no more rounds of NaCl were added.

Reference is round 0: if color change is observed after the stabilizer is mixed with colloidal gold, but before any NaCl is added, round 0 is recorded. The statues are analyzed as follows:

- (1) Nanogold particles which change color just after the salt solution is added: Au(6) and Au(10).
- (2) Nanogold particles that aggregated, precipitated, or turned white: Au(2) and Au(11).
- (3) Nanogold particles that turned blue-violet: Au(1), Au(3), Au(4), Au(5), Au(8), Au(9), Au(13), and Au(14).
- (4) Nanogold particles which did not agglomerate: Au(7) and Au(12).

It is therefore determined that CMC and PVP-k30 solutions provide the best protection against agglomeration in colloidal

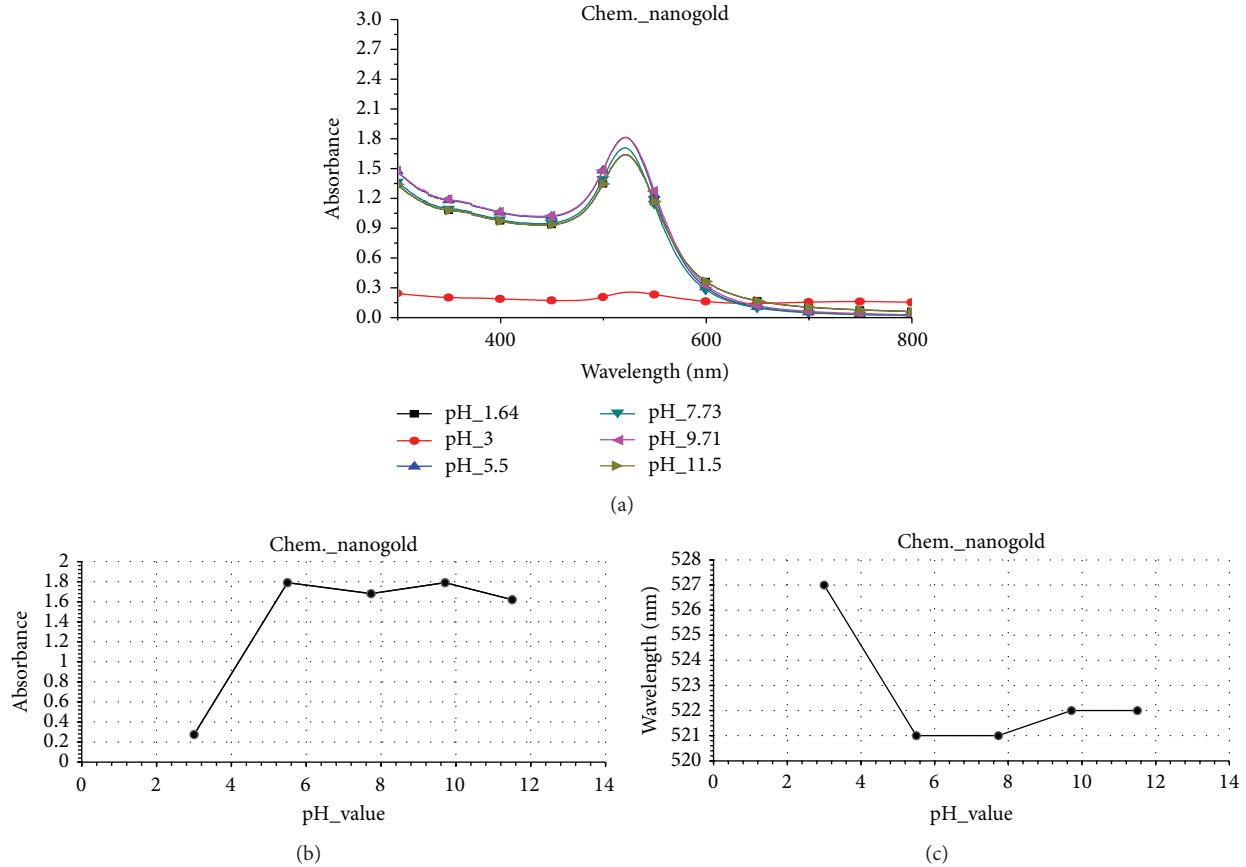


FIGURE 3: (a) SPR, (b) absorbance, and (c) wavelength versus pH of chem..nanogold.

TABLE 2: Number of NaCl rounds.

Item #	Surfactant (0.1 mg)	NaCl (10^{-1} mL)
Au(0)	No surfactant	1
Au(1)	Propylene glycol alginate	6
Au(2)	Sodium alginate	1
Au(3)	Animal glue	3
Au(4)	Gelatin L-150	5
Au(5)	Guar gum S-200	8
Au(6)	Xanthan gum	0
Au(7)	CMC (carboxymethyl cellulose)	10
Au(8)	Pectin	7
Au(9)	CMC (antiacid)	7
Au(10)	Carrageenan	0
Au(11)	SDS (sodium dodecyl sulfate)	2
Au(12)	PVP-k30 (polyvinyl pyrrolidone)	10
Au(13)	Citric acid	2
Au(14)	Glycine	2

nanogold. Of these, CMC is the safer choice, as it presents no harm to the human body and is even used in some food items to maintain a food-particle suspension.

3.2. Results and Discussion of pH Test. Chem..nanogold at HCl and NaOH condition, the relation of absorbance and wavelength with pH, as shown in Figures 3(a), 3(b), and 3(c). AuNPs-DIW at HCl and NaOH condition, the relation of absorbance and wavelength with pH, as shown in Figures 4(a), 4(b), and 4(c). Ethanol nanogold at HCl and NaOH condition, the relation of absorbance and wavelength with pH, as shown in Figures 5(a), 5(b), and 5(c). Table 3 shows absorbance and wavelength deviation at different nanogold versus pH.

In pH test, the higher pH will cause the optical property of AuNPs to have a blue shift of the peak wavelength, indicating that the suspension capacity can be improved when the gold nanoparticles are in an alkalic environment.

Table 3 shows absorption and wavelength of colloidal nanogold in different pH value. As shown in Figures 3(c), 4(c), 5(c), and 6(c), in acid liquid, the wavelength of colloidal nanogold is longer, which is red shifting. The zeta potential is lower and also the Debye Length is shorter. These cause the nanogold particles to assemble and precipitate. In alkalic liquid, the wavelength of colloidal nanogold is shorter, which is blue shifting. The absorption of UV-Vis is higher and the zeta potential is higher. Also, the Debye Length is longer. These cause the nanogold particles to disperse. As the results show, in alkali liquid, the nanogold particles are more separated. Under the circumstances of pH 13 and 2, the UV

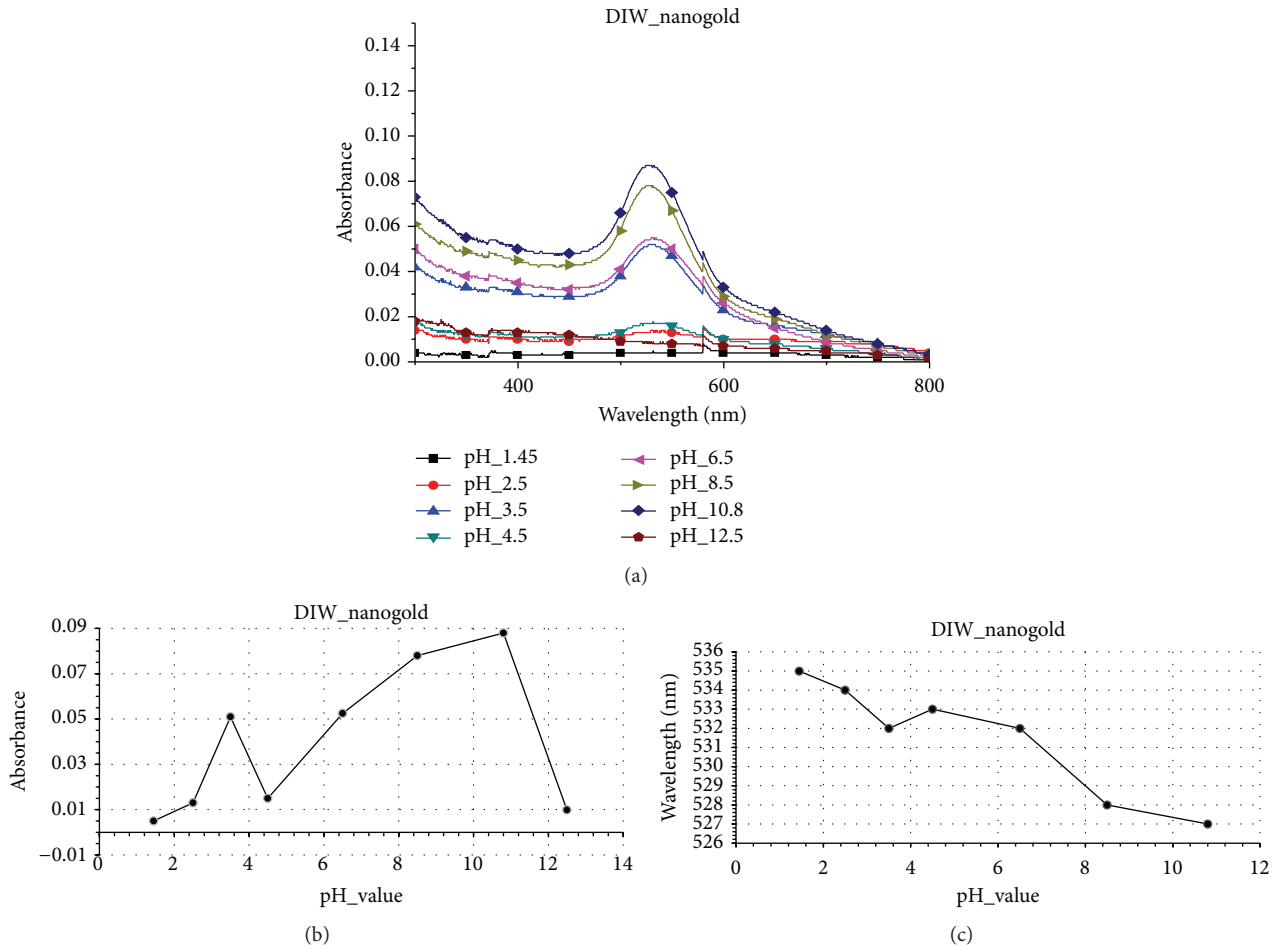


FIGURE 4: (a) SPR, (b) absorbance, and (c) wavelength versus pH of AuNPs-DIW.

absorption value of colloidal nanogold is 0 where it appears that the AuNPs drop to the bottom of the container.

4. Conclusions

A method of spark discharge (PSD) for producing gold nanoparticles in organic or inorganic medium (ethanol/water) without additives is proposed. The most significant contribution of this PSD method research is the capability to directly fabricate gold nanoparticles with different particle sizes and shapes in different medium. Moreover, the gold nanoparticles produced through PSD method were well-dispersed and form a stable suspension for an extended period of time. Generally, to obtain stable suspension of colloidal gold, the chemical preparation method requires posttreatments (e.g., heating, dialysis, and purification), as well as long preparation and waiting time. This PSD technique does not require complicated pretreatment or any chemical additive and can instantly achieve stable suspension of gold colloid solution.

In this study, adding or not adding different kinds of surfactant and adding different concentration of NaCl to see the different color changes are discussed. It is determined

TABLE 3: Absorbance and wavelength deviation at different nanogold versus pH.

Nanogold/item	pH value	Absorbance	Wavelength (nm)
Chem._nanogold	3.1~11.5	Increase	From 527 to 522
AuNPs-DIW	2.5~10.8	Increase	From 534 to 527
Ethanol nanogold	7.1~11.5	Increase	From 544 to 534
Ethanol nanogold (1/2 ethanol + 1/2 DIW)	3.1~10.5	No change	From 540 to 520

under what condition the colloidal nanogold is better in the combination of surfactant and NaCl. The result of NaCl test by using the modified gold 15 number method is therefore determined that CMC and PVP-k30 solutions provide the best protection against agglomeration in colloidal nanogold. Of these, CMC is the safer choice as it presents no harm to the human body and is even used in some food items to maintain a food-particle suspension. This study uses the UV-Vis to observe the absorption of the different pH value. The results

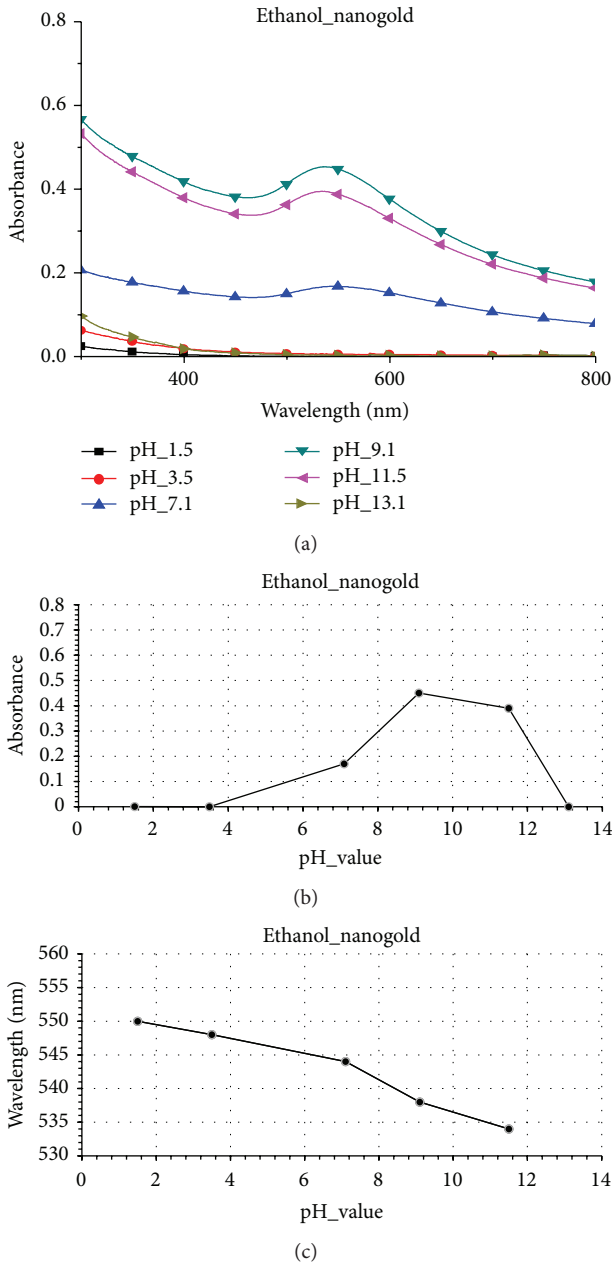


FIGURE 5: (a) SPR, (b) absorbance, and (c) wavelength versus pH of ethanol nanogold.

show that, in acid liquid, the wavelength of colloidal nanogold is longer, which is red shifting. The absorption of UV-Vis is lower. Also, the Debye Length is shorter. These cause the nanogold particles to assemble and precipitate. In alkalic liquid, the wavelength of colloidal nanogold is shorter, which is blue shifting. The absorption of UV-Vis is higher. Also, the Debye Length is longer. These cause the nanogold particles to disperse. In addition, the result of pH test shows that a higher pH will cause the optical property of AuNPs to have a blue shift of the peak wavelength, indicating that the suspension capacity can be improved when the gold nanoparticles are in an alkalic environment. The results of this study can be a reference of nanogold applying in biomedical science.

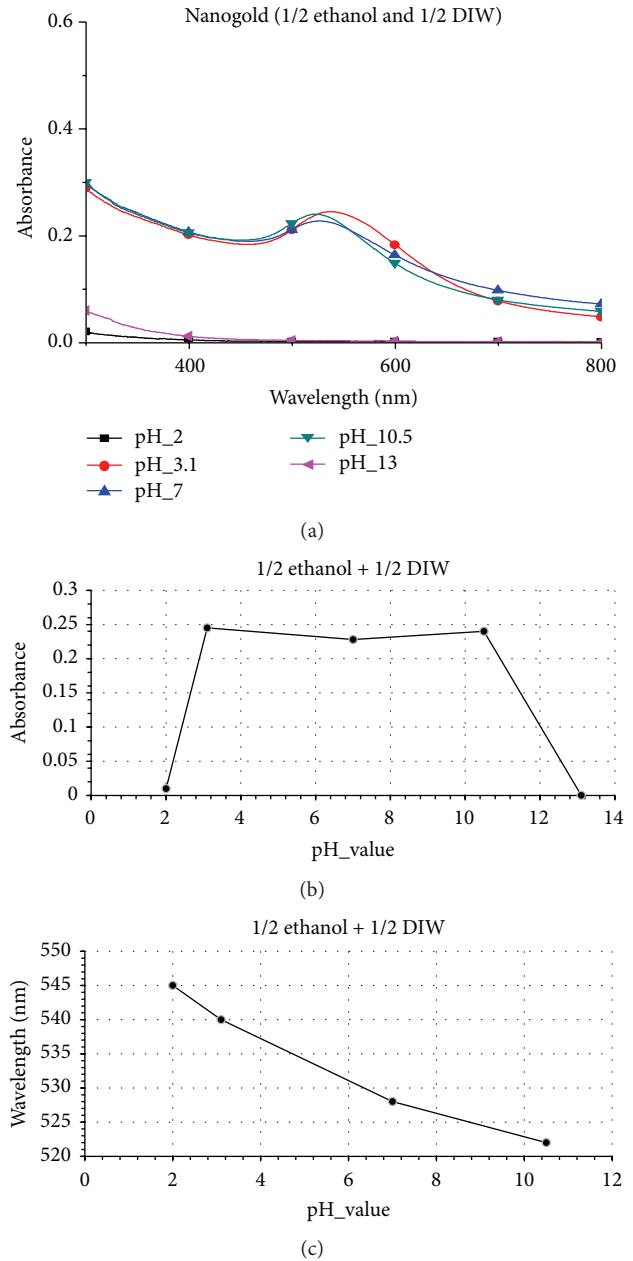


FIGURE 6: (a) SPR, (b) absorbance, and (c) wavelength versus pH of ethanol nanogold (1/2 ethanol + 1/2 DIW).

Conflict of Interests

The authors declare that there is no conflict of interests regarding the publication of this paper.

References

- [1] A. Lazcano and J. L. Bada, "The 1953 Stanley L. Miller experiment: fifty years of prebiotic organic chemistry," *Origins of Life and Evolution of the Biosphere*, vol. 33, no. 3, pp. 235–242, 2003.
- [2] K.-H. Tseng, H.-L. Lee, D.-C. Tien, Y.-L. Tang, and Y.-S. Kao, "A study of antibioactivity of nanosilver colloid and silver ion solution," *Advances in Materials Science and Engineering*, vol. 2014, Article ID 371483, 6 pages, 2014.

- [3] K.-H. Tseng and J.-C. Huang, "Pulsed spark-discharge assisted synthesis of colloidal gold nanoparticles in ethanol," *Journal of Nanoparticle Research*, vol. 13, no. 7, pp. 2963–2972, 2011.
- [4] K.-H. Tseng, J.-C. Huang, C.-Y. Liao, D.-C. Tien, and T.-T. Tsung, "Preparation of gold ethanol colloid by the arc discharge method," *Journal of Alloys and Compounds*, vol. 472, no. 1-2, pp. 446–450, 2009.
- [5] K.-H. Tseng, C.-Y. Liao, J.-C. Huang, D.-C. Tien, and T.-T. Tsung, "Characterization of gold nanoparticles in organic or inorganic medium (ethanol/water) fabricated by spark discharge method," *Materials Letters*, vol. 62, no. 19, pp. 3341–3344, 2008.
- [6] H. Kawaguchi, "The determination of temperature of light sources for spectroscopic analysis from spectra," *Spectroscopic Research*, vol. 13, no. 1, pp. 1–6, 1964.
- [7] W. Natsu, M. Shimoyamada, and M. Kunieda, "Study on expansion process of EDM arc plasma," *JSME International Journal, Series C: Mechanical Systems, Machine Elements and Manufacturing*, vol. 49, no. 2, pp. 600–605, 2006.
- [8] N. Moriyama, J. Sekikawa, and T. Kubono, "Spectroscopic temperature measurement of breaking arcs near cathode and anode surfaces of copper contacts," *IEICE Transactions on Electronics*, vol. 89, no. 8, pp. 1141–1146, 2006.
- [9] H. Gay-Lussac, "Ueber den Cassius'schen Goldpurpur," *Annalen der Physik*, vol. 101, no. 8, pp. 629–630, 1832.
- [10] J. J. Berzelius, "Ueber den Cassius' schen Goldpurpur," *Annalen der Physik und Chemie*, vol. 98, no. 6, pp. 306–308, 1831.
- [11] V. R. Reddy, "Gold nanoparticles: synthesis and applications," *Synlett*, no. 11, pp. 1791–1792, 2006.
- [12] M. Faraday, "The bakerian lecture: experimental relations of gold (and other metals) to light," *Philosophical Transactions of the Royal Society of London*, vol. 147, no. 0, pp. 145–181, 1857.
- [13] V. Sharma, K. Park, and M. Srinivasarao, "Colloidal dispersion of gold nanorods: historical background, optical properties, seed-mediated synthesis, shape separation and self-assembly," *Materials Science and Engineering R: Reports*, vol. 65, no. 1-3, pp. 1–38, 2009.
- [14] B. Papaconstantinou, "The protective action of soaps on zsigmondy's gold sols," *The Journal of Physical Chemistry*, vol. 29, no. 3, pp. 319–322, 1924.
- [15] R. Zsigmondy, "Die hochrothe Goldlösung als Reagens auf Colloide," *Zeitschrift für Analytische Chemie*, vol. 40, no. 11, pp. 697–719, 1901.
- [16] E. C. Dreaden, M. A. MacKey, X. Huang, B. Kang, and M. A. El-Sayed, "Beating cancer in multiple ways using nanogold," *Chemical Society Reviews*, vol. 40, no. 7, pp. 3391–3404, 2011.
- [17] Y. Li, H. J. Schluesener, and S. Xu, "Gold nanoparticle-based biosensors," *Gold Bulletin*, vol. 43, no. 1, pp. 29–41, 2010.
- [18] M.-C. Daniel and D. Astruc, "Gold nanoparticles: assembly, supramolecular chemistry, quantum-size-related properties, and applications toward biology, catalysis, and nanotechnology," *Chemical Reviews*, vol. 104, no. 1, pp. 293–346, 2004.

Research Article

Effect of Nanostructure on Thermal Conductivity of Nanofluids

Saba Lotfizadeh and Themis Matsoukas

Department of Chemical Engineering, Pennsylvania State University, University Park, PA 16802, USA

Correspondence should be addressed to Themis Matsoukas; matsoukas@enr.psu.edu

Received 26 May 2015; Revised 5 August 2015; Accepted 24 August 2015

Academic Editor: Wei Chen

Copyright © 2015 S. Lotfizadeh and T. Matsoukas. This is an open access article distributed under the Creative Commons Attribution License, which permits unrestricted use, distribution, and reproduction in any medium, provided the original work is properly cited.

The presence of colloidal particles is known to increase the thermal conductivity of base fluids. The shape and structure of the solid particles are important in determining the magnitude of enhancement. Spherical particles—the only shape for which analytic theories exist—produce the smallest enhancement. Nonspherical shapes, including clusters formed by colloidal aggregation, provide substantially higher enhancements. We conduct a numerical study of the thermal conductivity of nonspherical structures dispersed in a liquid at fixed volume fraction in order to identify structural features that promote the conduction of heat. We find that elongated structures provide high enhancements, especially if they are long enough to create a solid network (colloidal gel). Cross-linking further enhances thermal transport by directing heat in multiple directions. The most efficient structure is the one formed by hollow spheres consisting of a solid shell and a core filled by the fluid. In both dispersed and aggregated forms, hollow spheres provide enhancements that approach the theoretical limit set by Maxwell's theory.

1. Introduction

Common fluids used in heating/cooling processes have very low thermal conductivity in comparison to solid materials [1]. Adding nanoparticles results in considerable improvement of the fluid thermal properties [2, 3]. While solid particles of any size will increase the thermal conductivity of the base fluid, there is a great interest in nanoparticles due to practical considerations associated with the production of stable suspensions that resist precipitation. Adding to this practical concern is a number of experimental reports of unusually large but often inconsistent increases of the thermal conductivity when working with nanoparticles [3], which have motivated various hypotheses as to the microscopic origins of these behaviors [4, 5]. Large enhancements of the thermal conductivity have recently been associated with aggregation [6–8]; however, analytical theories are not equipped to address the conductivity of aggregated structures quantitatively. The standard theoretical tool for conduction in inhomogeneous media such as colloidal dispersions is Maxwell's mean field theory [9]. Maxwell's result, originally developed in the context of electrical conduction, gives the

conductivity of a dispersion of spheres in a continuous medium:

$$k = k_f \frac{2k_f + k_p + 2\phi_p(k_p - k_f)}{2k_f + k_p - \phi_p(k_p - k_f)}, \quad (1)$$

where k is the conductivity of the dispersion, k_p is the conductivity of the particles, k_f is the conductivity of the fluid, and ϕ_p is the volume fraction of the particles. As the conductivity of solids is typically higher to much higher than that of liquids, this equation predicts that the conductivity of the dispersion is higher than that of the fluid. An even higher conductivity is obtained if the roles of the solid and liquid are inverted to produce a dispersion of liquid droplets inside a continuous solid matrix with the same volume fraction. The result is obtained by swapping k_p and k_f in (1) and replacing ϕ_p by $1 - \phi_p$:

$$k' = k_p \frac{k_f(3 - 2\phi_p) + 2\phi_p k_p}{k_f \phi_p + k_p(3 - \phi_p)}. \quad (2)$$

Equations (1) and (2) establish two limits for the thermal conductivity of an inhomogeneous system composed of two

phases at fixed volume fraction. The lower limit, (1), refers to a dispersion of the more conductive phase in a medium of low conductivity, whereas (2) refers to a dispersion of the less conductive phase in a continuum formed by the more conductive phase. Eapen et al. [7] suggested that (2) can be viewed as an upper limit for a colloidal gel, whose structure consists of a continuous solid network with regions of liquid dispersed in the interior. The two bounds may be taken then to represent the limits of fully dispersed particles (lower limit) and a fully gelled colloid (upper limit), with finite clusters falling in the space between these bounds. Recently, Lotfizadeh et al. [8] confirmed this hypothesis by showing that the thermal conductivity of a suspension at fixed volume fraction of primary particles increases monotonically with cluster size and reaches the upper limit of Maxwell's theory in the gel state. In a subsequent study, this behavior was quantified via an analytic model based on Maxwell's theory [10]. This model, however, depends on a parameter that reflects the structure of the cluster and which cannot be obtained by analytic means.

Structural details of colloidal clusters are important in determining the conductivity of the dispersion. While Maxwell's theory provides a baseline calculation for two idealized limits, that of fully dispersed and that of fully gelled states, for nearly all other cases theory is inadequate and one must resort to numerical simulations. To evaluate thermal conductivity of colloidal suspensions with different properties including particles shape and size along with investigating the effect of aggregation and cluster structure using model configurations, we need to go beyond experimental limitations and employ an accurate numerical model to avoid colloidal complications. In macroscopic simulations, large-scale structural effects can be captured. These simulations can be done by different standard models to solve the macroscopic conduction equation; however Monte Carlo method is both fast and accurate and especially well suited for complex geometries.

In this study we present a systematic investigation on the thermal conductivity of nonspherical particles with special interest in identifying structures that maximize conductivity at fixed volume fraction of the solid and approach the upper limit of the theory. We explore the range of validity of Maxwell's theory for different particle shapes, evaluate thermal conductivity of solid particles, hollow particles as well as rods, and other nonspherical shapes, and identify the structures that produce maximum enhancement at fixed volume fraction of the dispersed phase.

2. Monte Carlo Method for the Thermal Conductivity of Clusters

Of the several methods available for the conductivity of heterogeneous structures, Monte Carlo is particularly useful because it allows the study of systems with arbitrarily complex geometries. In Monte Carlo we obtain the thermal conductivity of a two-phase system via the statistics of a biased random walk along sites with different thermal conductivities. The method as implemented here ignores the motion of the

particle through the fluid medium as well as all fluid-mediated interactions between particles. We justify omitting these factors for two reasons. The first one is that Maxwell's theory itself only considers conduction and neglects all other mechanisms of heat transfer. In this respect the simulation provides a direct comparison to the predictions of Maxwell's theory. The second reason is based on the previous experimental and theoretical studies that show the enhancement of the thermal conductivity of clustered dispersions is fully captured by the conduction of heat along the solid backbone of the cluster and that other mechanisms, if present, make contributions that are at best within the error bounds of the experimental measurements [6–8, 10–13].

The Monte Carlo method used here is based on the work of Van Siclen [14]. The volume of the system (cluster in a fluid) is discretized in cubic elements of equal size, each element representing either fluid or particle. Heat walkers are launched randomly inside the system and take unit steps in one of 6 directions that exist in the discretized $3d$ lattice chosen at random. Movement of the walker is biased by the conductivity of the sites the walker is leaving from and moving to with transition probability:

$$p_{i \rightarrow j} = \frac{k_j}{k_i + k_j}, \quad (3)$$

where k_i is the conductivity of the current site and k_j the conductivity of the neighbor. Time is advanced by $1/k_i$ and the process is repeated to produce a trajectory in time, $\mathbf{r}(t)$. The thermal diffusivity D of the composite material is obtained from the Einstein relationship [15]:

$$D = \lim_{\tau \rightarrow \infty} \frac{1}{6\tau} \langle |\mathbf{r}(t + \tau) - \mathbf{r}(t)|^2 \rangle, \quad (4)$$

and the conductivity is finally calculated from its relationship with the thermal diffusivity, $k = \rho C_p D$, where C_p is the heat capacity. The implementation of the method is straightforward even for very complex solid structures and has been used by many others in the study of the thermal conduction in inhomogeneous media [15–19].

The dimensionless parameter that controls the conductivity of the suspension is the ratio of the solid-to-liquid thermal conductivity. Oxide materials in typical fluids have conductivity ratios in the range 2–50, and metallic particles can reach values of the order of 100. The ratio $k_p/k_f = 1$ is trivial and in this case the conductivity of the suspension is identical to that of the fluid for all particle structures and solid volume fractions. In the limit $k_p/k_f \rightarrow \infty$, heat conduction is entirely governed by the least conducting phase (liquid) and is independent of the conductivity of the solid [10, 20]. In this study we use ratios in the range 2 to 50, roughly corresponding to a range between aqueous dispersions of silica (lower limit) and alumina (upper limit). The results are qualitatively very similar to other ratios.

3. Results and Discussion

3.1. Validation of Numerical Simulation against Maxwell's Theory. An important element of the simulation is the discretization size of a unit element relative to the size of the spherical

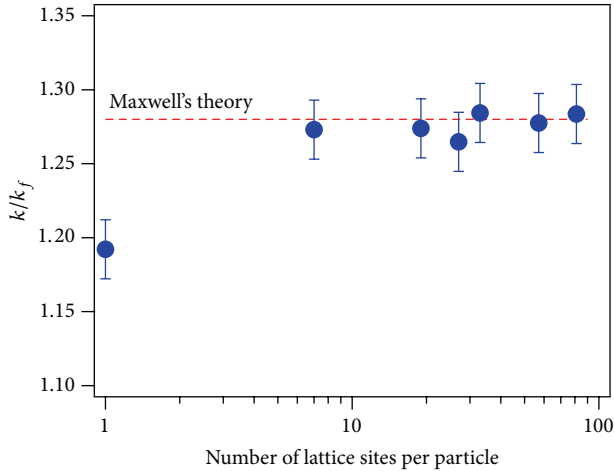


FIGURE 1: Effect of the number of lattice sites: a single spherical particle is composed of numerical simulations on thermal conductivity of the suspensions with $k_p/k_f = 20$ at constant solid volume fraction of $\phi_p = 0.1$. The dashed line represents conductivity predicted by Maxwell's theory.

particle. In general, the smaller the discretization size, the more accurate the simulation but also more computationally intensive. It is common to represent primary solid particles by a single lattice site [11, 21]; however, the numerical accuracy of this simplification has not been reported in the literature. Thus the first test is evaluating the thermal conductivity of a single sphere within a unit lattice as a function of the discretization size. The results are shown in Figure 1. As the number of sites increases, the thermal conductivity of the dispersion, reported as a ratio over the conductivity of the fluid (we refer to this ratio as enhancement), increases and converges to the value predicted by Maxwell's theory. The most coarse representation of the sphere by a single lattice site underestimates the conductivity of the dispersion by 7%. Approximating the sphere with 7 sites (three orthogonal rows of 3 sites, each with a common center) produces results with the same accuracy as a sphere composed of 100 sites. In all subsequent simulations we use at least 7 lattice sites to represent each primary particle. As further validation we compute the conductivity of the dispersion as a function of volume fraction up to a maximum fraction of 25%, shown in Figure 2. These results are in excellent agreement with Maxwell's theory and further corroborate the findings of Belova and Murch [21] who reported very good agreement between simulation and Maxwell's theory for all volume fractions up to the point that particles begin to touch.

Figure 3 shows the conductivity of a dispersion at fixed volume fraction of solid as a function of size of the dispersed particles. The smaller particles are made of less primary lattice sites with maintaining the minimum sites required to keep the simulation accurate. The conductivity in all cases is the same and independent of the size of the dispersed spheres. This behavior, an important element of Maxwell's theory, is reproduced accurately by the simulation. We also show results for a dispersion of cubical particles at the same volume

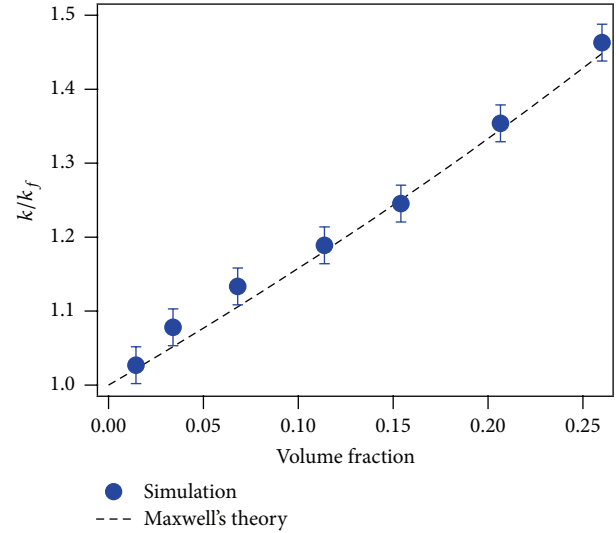


FIGURE 2: Comparison of thermal conductivity between simulations (points) and Maxwell's theory (dashed line) for a well-dispersed suspension of spherical particles at different volume fractions with $k_p/k_f = 4$. The dispersion consists of spherical particles each represented by 7 lattice sites.

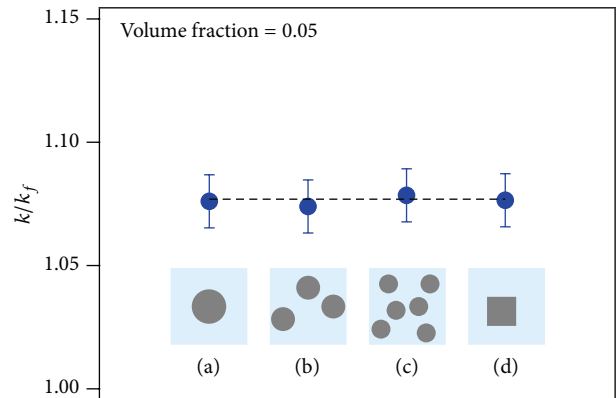


FIGURE 3: Effect of particle size of spherical particles on thermal conductivity of the solution at fixed volume fraction of $\phi_p = 0.05$ and $k_p/k_f = 4$. (a), (b), and (c) refer to spherical particles with different sizes at fixed volume fraction; (d) is a dispersion of cubical particles with the same volume fraction. The dashed line is Maxwell's theory for spheres.

fraction and observe that their thermal conductivity is within error indistinguishable from that of spherical particles.

3.2. Hollow Particles: A First-Order Model for Clusters. Maxwell's original derivation is based on a concentric core-shell model in which the core represents one phase (the dispersed solid) and the shell the other one (liquid) [9]. Maxwell showed that this arrangement has the same conductivity as a dispersion of spheres with the same volume fraction, a result confirmed in Figure 3. The upper bound of Maxwell's theory is obtained by inverting the order of the phases; the least conducting phase is now in the core and the most

conductive one in the shell. This allows us to calculate the conductivity of a suspension of *hollow* particles consisting of a solid shell and a core that is filled with the suspending fluid. The conductivity of a dispersion of hollow particles is calculated analytically from Maxwell's theory. First, the conductivity of a single hollow particle with outer and inner radii R_0 and R_i , respectively, is obtained from Maxwell's upper bound, (2), with ϕ_p being replaced by the solid fraction in the hollow particle, $\phi_i = 1 - (R_i/R_0)^3$:

$$k_h = k_p \frac{k_f (3 - 2\phi_i) + 2\phi_i k_p}{k_f \phi_i + k_p (3 - \phi_i)}, \quad (5)$$

where ϕ_i is the volume fraction of solid material inside the hollow particle. The conductivity of a dispersion of these hollow spheres at bulk volume fraction ϕ_h (based on the outer radius R_0) is given by the lower bound of Maxwell's theory with k_p being replaced by k_h and ϕ_p by ϕ_h :

$$k = k_f \frac{2k_f + k_h + 2\phi_h (k_h - k_f)}{2k_f + k_h - \phi_h (k_h - k_f)}. \quad (6)$$

The hollow sphere represents the simplest model of a colloidal cluster. This model views the cluster as a "microgel" structure consisting of an extended solid network that is modeled by the solid shell and pockets of liquid within the cluster that are represented by the core.

To test (6) by simulation, we calculate numerically the conductivity of a dispersion of hollow spheres at a fixed volume fraction of solid $\phi = 0.0656$ with $k_p/k_f = 20$ as a function of the ratio R_i/R_0 . With $R_i = 0$ we obtain a dispersion of solid spheres at volume fraction $\phi_p = 0.0656$. As we increase the outer radius the thickness of the shell is decreased to conserve the total amount of solid and the corresponding volume fraction of the dispersed hollow spheres is $\phi_h = \phi/\phi_i$, corresponding to fixed volume fraction of the solid phase $\phi = 0.0656$. The results are shown in Figure 4. The theoretical conductivity increases starting from the lower Maxwell limit ($k/k_f = 1.1801$) for spherical particles at $\phi_p = 0.0656$, $k_p/k_f = 20$, to the upper Maxwell limit ($k/k_f = 1.868$) at $(R_i/R_0)^3 = 1 - \phi = 0.934$. The Monte Carlo simulation tracks this profile closely.

In inhomogeneous two-phase systems, thermal conduction is dominated by the phase that provides the longest uninterrupted paths to heat transport. Given two materials of different conductivities layered in a core-shell arrangement, maximum conductivity is obtained when the most conductive material surrounds the least conductive phase. The smallest possible conductivity is achieved by reversing this order. In fact, if the less conductive phase is a perfect insulator, a core-shell particle with the insulator fully encapsulated will still conduct heat, whereas the inverted structure (insulator on the outside) is a perfect insulator. Generalizing this principle, structures that place the most conductive phase at the exterior while shielding the less conductive phase are expected to produce enhanced thermal conductivity relative to uniform dispersion of the more conductive phase. The hollow sphere is an exact analytic model that bridges the

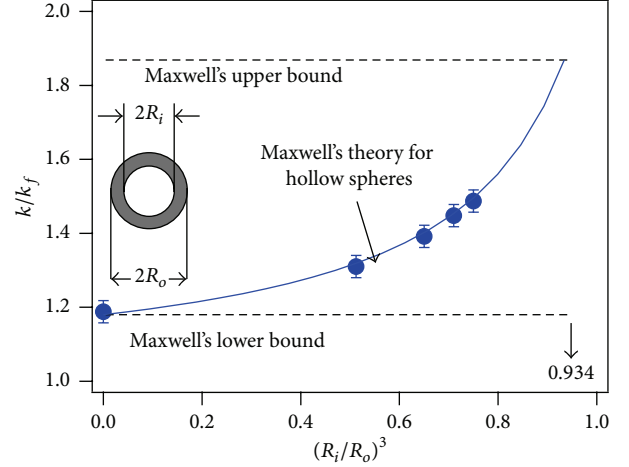


FIGURE 4: Thermal conductivity of hollow particles as the core radius increases while the volume fraction of the solid shell is constant at $\phi = 6.5\%$ with $k_p/k_f = 20$ (the maximum possible value of $(R_i/R_0)^3$ is $1 - \phi = 0.934$ and is reached when the entire fluid is encapsulated in the core of a hollow sphere). The line represents conductivity predicted by Maxwell's theory as explained in the text.

entire range of conductivities between the two bounds of Maxwell's theory. At the lower limit we have a colloidal system of fully dispersed spheres. The upper limit represents an idealized system in which the entire fluid is found inside the core of a single hollow sphere. Such system cannot be made experimentally using primary spherical particles as its building blocks. Nonetheless, one does not need to reach this limit exactly to achieve high conductivity. With $(R_i/R_0)^3 = 0.75$ (corresponding to a hollow particle whose core is 25% of the total volume and the shell is 75%), the conductivity of the suspension is $k/k_f \approx 1.79$, about 30% above the lower bound and within 60% of the upper limit. Therefore, significant enhancements can be achieved with structures that are within experimental reach.

3.3. Rods. Among the many other structures that have been studied, nanotubes and nanofibers are of special interest as model structures for nonspherical particles. They can be made out of materials with high thermal conductivity and their anisotropic shape makes them potentially excellent additives to thermal fluids [22–33]. Maxwell's theory fails to predict thermal behavior of these suspensions. For compact nonspherical particles, the most common model is that of Hamilton and Crosser [34], which is based on the work of Fricke [35]. This model modifies Maxwell's lower limit as follows:

$$k = \frac{(n-1)k_f + k_p + (n-1)\phi_p(k_p - k_f)}{(n-1)k_f + k_p - \phi_p(k_p - k_f)}. \quad (7)$$

The shape of the particle is incorporated into the parameter n , whose general form is

$$n = \frac{3}{\psi^a}. \quad (8)$$

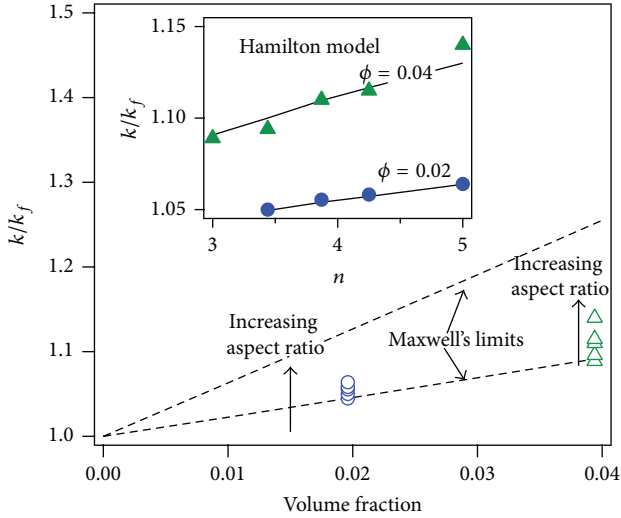


FIGURE 5: Thermal conductivity of suspensions of rods with aspect ratios in the range of $L/2R = 0.5$ to $L/2R = 5$ and, therefore, shape factors between $n = 3$ and $n = 6$ in comparison to Maxwell's limiting bounds (dashed lines) at volume fractions of $\phi_p = 0.019$ and $\phi_p = 0.039$. The inset graph shows the comparison between these simulated values (point) and Hamilton's model (line).

Here, ψ is the sphericity of the particle, defined as the surface area of an equal volume sphere over the surface area of the particle. In [35] the exponent a is 1 for spheres, 2 for prolate ellipsoids, and 1.5 for oblate ellipsoids. It is noted, however, that the experiments of Hamilton and Crosser [34] were better described with $a = 1$ regardless of shape.

For nonspherical particles ($\psi < 1$) (7) gives conductivities that are higher than that of spheres. To study Maxwell's range of validity for asymmetric particles, investigating thermal behavior of these particles and also validating Hamilton's model, simulations were established on rods with different aspect ratios ranging from $L/2R = 0.5$ to $L/2R = 5$. The conductivity ratio in these simulations is $k_p/k_f = 10$ and rods are made of discretized cells.

The results in Figure 5 show that enhancement at fixed volume fractions of $\phi_p = 0.019$ and $\phi_p = 0.039$ depends on the aspect ratio of the rods and that as the aspect ratio increases (sphericity decreases), conductivity increases above Maxwell's lower limit. Elongated particles such as rods and fibers facilitate heat transport along their primary axis. Upon increasing the aspect ratio, conductivity along the main axis increases substantially, and even though transport along the other two axes is decreased, the overall conductivity of the suspension is higher than that of spheres at the same volume fraction. Maximum enhancement is reached when the rod becomes long enough to connect two opposite sides of the cubic lattice. In our simulations, this occurs at $L/2R = 5$. While the conductivity increases above that of the lower limit in Maxwell's theory, it stays below the upper limit, even when the rod makes thermal contact between opposite ends of the simulation volume. The simulation results are compared to Hamilton's model in the inset in Figure 5. Excellent agreement was observed with $a = 1$.

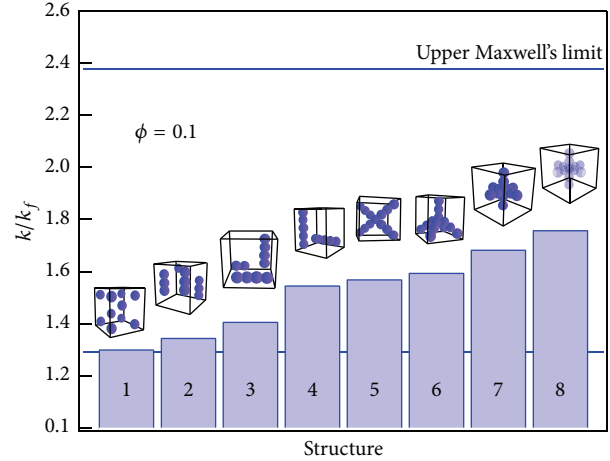


FIGURE 6: Effect of aggregation state and cluster configuration on conductivity enhancement. Thermal conductivity of different model aggregates at $k_p/k_f = 20$ and solid volume fraction of $\phi_p = 0.1$ are presented. The last bar of the chart represents a structure created from hollow particles with the same solid volume fraction as all other structures. Structures 5–8 make contact with opposite walls.

The general conclusion from these investigations is that Maxwell's lower limit can be employed for suspension of monomers as long as we have symmetric shaped particles such as cubes and spheres, including core-shell structures. Anisotropic shapes, such as rods, cylinders, and ellipsoids, enhance conductivity above Maxwell's lower limit. Nonetheless, the enhancement is always found to lie below the maximum limit of Maxwell's theory.

3.4. Linear and Nonlinear Aggregates. Colloidal particles are susceptible to aggregation, especially in nanofluids prepared by dispersing dry particles in the fluid. Clusters are more complex in structure than the cases considered so far because of the random nature of contacts between the primary particles that make up the cluster. As a result, clusters with the same size (e.g., hydrodynamic radius) can have quite different structures, for example, linear, packed, fractal, and highly cross-linked. Although many studies have investigated different ways to create assemblies with controlled geometries [36, 37], controlling cluster configuration is an experimental challenge. MC simulations on the other hand enable us to create model aggregates and investigate thermal conductivity of such systems. This capability provides not only a tool to find the exact conductivity in systems with complex structures and different sizes but also a way to investigate the effect of configuration and geometry in aggregated structures on the conductivity.

Figure 6 shows thermal conductivity of different model aggregates with $\phi_p = 0.1$ and $k_p/k_f = 20$. The first four bars of this figure show thermal conductivity of suspensions containing linear clusters ranging from monomers to pentamers. The linear pentamer is the largest linear aggregate to fit in the simulation volume and makes thermal contact between opposite sides of the simulation box. The other clusters are formed by cross-linking linear chains in various

symmetric forms. The Maxwell bounds are also marked in this figure, the lower limit corresponding to the conductivity of dispersed spheres (structure #1 in the graph). Conductivity increases as the linear dimension increases, with pentameric chains reaching a value that is about 20% above Maxwell's lower limit. As with rods, maximum enhancement is reached when the chain makes thermal contact between opposite sides of the simulation volume. While linear clusters can increase conductivity significantly, the maximum enhancement remains well below that maximum allowed by Maxwell's upper limit. The next level of structural complexity involves cross-linking between linear branches, shown as structures #5 through #7. The X-shaped cluster, formed by cross-linking two chains (structure 5) and a tetrahedral cluster with four branches emanating from a common link, offers marginally higher enhancement than the linear pentamer. Structure 7, formed by cross-linking three chains aligned along the x -, y -, and z -axes, provides higher enhancement that is 30% above the lower bound. This result is somewhat unexpected because this structure has higher concentration of mass at the center and is closer to the structure of a sphere compared to the other structures. Its enhanced conductivity suggests that while linear branches are important in providing long pathways for heat transfer, the density of cross-linking is important as well and provides a locally high density of the more conducting phase that distributes heat to the branches. The last structure (8) is identical to 7, but the primary particles are hollow spheres (the volume fraction of the solid phase is $\phi = 0.1$, as in all of the cases in this figure). Hollow spheres in a suspension, as we established already, provide higher conductivity compared to solid spheres with the same volume fraction of solid, a trait carried over to aggregated structures. Indeed, the aggregate formed by hollow spheres exhibits the largest enhancement of thermal conductivity, 35% above the lower limit of Maxwell's theory.

4. Conclusions

We have studied by systematic numerical simulation the effect of nanostructure on the thermal properties of nanofluids. At fixed volume fractions, spherical particles exhibit the lowest possible thermal conductivity. Structures formed by creating contacts between primary particles always have higher conductivity compared to fully dispersed spheres. Structural elements that contribute to enhanced conductivity are linear branches, which facilitate heat transport along uninterrupted paths, and cross-links, which help distribute the transport to multiple directions. Both elements are needed to produce large enhancements. Structures that encapsulate the fluid within regions that are more or less thermally isolated from the main fluid exhibit the maximum enhancement. The ideal structure is a solid spherical shell that is filled with the suspending fluid. Colloidal aggregates are reasonable approximations of this highly conducting structure. In all cases, the conductivity of the nanofluid is found to lie between the two limits of Maxwell's theory. This adds further support to the suggestion that both the unusually large conductivities that have been reported in some studies and the inconsistencies as to the precise magnitude of

the enhancement of the thermal conductivity of colloidal suspensions can be attributed to the presence of nonspherical particles/aggregates in the nanofluid.

Conflict of Interests

The authors declare that there is no conflict of interests regarding the publication of this paper.

Acknowledgment

This work was supported by the National Science Foundation under Grant no. CBET GOALI no. 1132220.

References

- [1] W. M. Haynes, *CRC Handbook of Chemistry and Physics*, CRC Press, Taylor & Francis, Boca Raton, Fla, USA, 2013.
- [2] R. Taylor, S. Coulombe, T. Otanicar et al., "Small particles, big impacts: a review of the diverse applications of nanofluids," *Journal of Applied Physics*, vol. 113, no. 1, Article ID 011301, 2013.
- [3] S. K. Das, S. U. S. Choi, and H. E. Patel, "Heat transfer in nanofluids—a review," *Heat Transfer Engineering*, vol. 27, no. 10, pp. 3–19, 2006.
- [4] B.-X. Wang, L.-P. Zhou, and X.-F. Peng, "A fractal model for predicting the effective thermal conductivity of liquid with suspension of nanoparticles," *International Journal of Heat and Mass Transfer*, vol. 46, no. 14, pp. 2665–2672, 2003.
- [5] R. Prasher, P. Bhattacharya, and P. E. Phelan, "Thermal conductivity of nanoscale colloidal solutions (nanofluids)," *Physical Review Letters*, vol. 94, no. 2, Article ID 025901, 2005.
- [6] P. Keblinski, R. Prasher, and J. Eapen, "Thermal conductance of nanofluids: is the controversy over?" *Journal of Nanoparticle Research*, vol. 10, no. 7, pp. 1089–1097, 2008.
- [7] J. Eapen, R. Rusconi, R. Piazza, and S. Yip, "The classical nature of thermal conduction in nanofluids," *Journal of Heat Transfer*, vol. 132, no. 10, Article ID 102402, 2010.
- [8] S. Lotfizadeh, T. Desai, and T. Matsoukas, "The thermal conductivity of clustered nanocolloids," *APL Materials*, vol. 2, no. 6, Article ID 066102, 2014.
- [9] J. K. Maxwell, *Treatise on Electricity and Magnetism*, vol. 2, Dover, 1954.
- [10] S. Lotfizadeh and T. Matsoukas, "A continuum Maxwell theory for the thermal conductivity of clustered nanocolloids," *Journal of Nanoparticle Research*, vol. 17, no. 6, 2015.
- [11] R. Prasher, W. Evans, P. Meakin, J. Fish, P. Phelan, and P. Keblinski, "Effect of aggregation on thermal conduction in colloidal nanofluids," *Applied Physics Letters*, vol. 89, no. 14, Article ID 143119, 2006.
- [12] J. Eapen, J. Li, and S. Yip, "Beyond the Maxwell limit: thermal conduction in nanofluids with percolating fluid structures," *Physical Review E*, vol. 76, no. 6, Article ID 062501, 2007.
- [13] J. Eapen, W. C. Williams, J. Buongiorno et al., "Mean-field versus microconvection effects in nanofluid thermal conduction," *Physical Review Letters*, vol. 99, no. 9, Article ID 095901, 2007.
- [14] C. D. Van Siclen, "Walker diffusion method for calculation of transport properties of composite materials," *Physical Review E*, vol. 59, no. 3, pp. 2804–2807, 1999.

- [15] W. Evans, R. Prasher, J. Fish, P. Meakin, P. Phelan, and P. Keblinski, "Effect of aggregation and interfacial thermal resistance on thermal conductivity of nanocomposites and colloidal nanofluids," *International Journal of Heat and Mass Transfer*, vol. 51, no. 5-6, pp. 1431-1438, 2008.
- [16] D. C. Hong, H. E. Stanley, A. Coniglio, and A. Bunde, "Random-walk approach to the two-component random-conductor mixture: perturbing away from the perfect random resistor network and random superconducting-network limits," *Physical Review B*, vol. 33, no. 7, pp. 4564-4573, 1986.
- [17] Y. Shoshany, D. Prialnik, and M. Podolak, "Monte Carlo modeling of the thermal conductivity of porous cometary ice," *Icarus*, vol. 157, no. 1, pp. 219-227, 2002.
- [18] I. V. Belova and G. E. Murch, "Calculation of the effective conductivity and diffusivity in composite solid electrolytes," *Journal of Physics and Chemistry of Solids*, vol. 66, no. 5, pp. 722-728, 2005.
- [19] T. Fiedler, A. Öchsner, N. Muthubandara, I. V. Belova, and G. E. Murch, "Calculation of the effective thermal conductivity in composites using finite element and Monte Carlo methods," *Materials Science Forum*, vol. 553, pp. 51-56, 2007.
- [20] S. Lotfizadeh and T. Matsoukas, "Colloidal thermal fluids," in *Encyclopedia of Surface and Colloid Science*, Taylor & Francis, 2014.
- [21] I. Belova and G. Murch, "Monte Carlo simulation of the effective thermal conductivity in two-phase material," *Journal of Materials Processing Technology*, vol. 153-154, pp. 741-745, 2004, Proceedings of the International Conference in Advances in Materials and Processing Technologies.
- [22] H. Xie, H. Lee, W. Youn, and M. Choi, "Nanofluids containing multiwalled carbon nanotubes and their enhanced thermal conductivities," *Journal of Applied Physics*, vol. 94, no. 8, pp. 4967-4971, 2003.
- [23] M. J. Assael, C.-F. Chen, I. Metaxa, and W. A. Wakeham, "Thermal conductivity of suspensions of carbon nanotubes in water," *International Journal of Thermophysics*, vol. 25, no. 4, pp. 971-985, 2004.
- [24] D. Wen and Y. Ding, "Effective thermal conductivity of aqueous suspensions of carbon nanotubes (carbon nanotube nanofluids)," *Journal of Thermophysics and Heat Transfer*, vol. 18, no. 4, pp. 481-485, 2004.
- [25] M.-S. Liu, M. Ching-Cheng Lin, I.-T. Huang, and C.-C. Wang, "Enhancement of thermal conductivity with carbon nanotube for nanofluids," *International Communications in Heat and Mass Transfer*, vol. 32, no. 9, pp. 1202-1210, 2005.
- [26] M. J. Assael, I. N. Metaxa, J. Arvanitidis, D. Christofilos, and C. Lioutas, "Thermal conductivity enhancement in aqueous suspensions of carbon multi-walled and double-walled nanotubes in the presence of two different dispersants," *International Journal of Thermophysics*, vol. 26, no. 3, pp. 647-664, 2005.
- [27] S. Kumar, J. Y. Murthy, and M. A. Alam, "Percolating conduction in finite nanotube networks," *Physical Review Letters*, vol. 95, no. 6, 2005.
- [28] B. Yang and Z. H. Han, "Temperature-dependent thermal conductivity of nanorod-based nanofluids," *Applied Physics Letters*, vol. 89, no. 8, Article ID 083111, 2006.
- [29] Y. Yang, E. A. Grulke, Z. G. Zhang, and G. Wu, "Thermal and rheological properties of carbon nanotube-in-oil dispersions," *Journal of Applied Physics*, vol. 99, no. 11, Article ID 114307, 2006.
- [30] X. Zhang, H. Gu, and M. Fujii, "Effective thermal conductivity and thermal diffusivity of nanofluids containing spherical and cylindrical nanoparticles," *Journal of Applied Physics*, vol. 100, no. 4, Article ID 044325, 2006.
- [31] S. Jana, A. Salehi-Khojin, and W.-H. Zhong, "Enhancement of fluid thermal conductivity by the addition of single and hybrid nano-additives," *Thermochimica Acta*, vol. 462, no. 1-2, pp. 45-55, 2007.
- [32] L. Chen, H. Xie, Y. Li, and W. Yu, "Nanofluids containing carbon nanotubes treated by mechanochemical reaction," *Thermochimica Acta*, vol. 477, no. 1-2, pp. 21-24, 2008.
- [33] R. Zheng, J. Gao, J. Wang et al., "Thermal percolation in stable graphite suspensions," *Nano Letters*, vol. 12, no. 1, pp. 188-192, 2012.
- [34] R. L. Hamilton and O. K. Crosser, "Thermal conductivity of heterogeneous two-component systems," *Industrial & Engineering Chemistry Fundamentals*, vol. 1, no. 3, pp. 187-191, 1962.
- [35] H. Fricke, "A mathematical treatment of the electric conductivity and capacity of disperse systems I. The electric conductivity of a suspension of homogeneous spheroids," *Physical Review*, vol. 24, no. 5, pp. 575-587, 1924.
- [36] Y. Ofir, B. Samanta, and V. M. Rotello, "Polymer and biopolymer mediated self-assembly of gold nanoparticles," *Chemical Society Reviews*, vol. 37, no. 9, pp. 1814-1825, 2008.
- [37] M. Grzelczak, J. Vermant, E. M. Furst, and L. M. Liz-Marzán, "Directed self-assembly of nanoparticles," *ACS Nano*, vol. 4, no. 7, pp. 3591-3605, 2010.

Research Article

Influence of Monodisperse Fe_3O_4 Nanoparticle Size on Electrical Properties of Vegetable Oil-Based Nanofluids

Bin Du, Jian Li, Feipeng Wang, Wei Yao, and Shuhan Yao

State Key Laboratory of Power Transmission Equipment & System Security and New Technology, Chongqing University, Chongqing 400044, China

Correspondence should be addressed to Jian Li; lijian@cqu.edu.cn

Received 21 January 2015; Accepted 24 May 2015

Academic Editor: Themis Matsoukas

Copyright © 2015 Bin Du et al. This is an open access article distributed under the Creative Commons Attribution License, which permits unrestricted use, distribution, and reproduction in any medium, provided the original work is properly cited.

Insulating oil modified by nanoparticles (often called nanofluids) has recently drawn considerable attention, especially concerning the improvement of electrical breakdown and thermal conductivity of the nanofluids. In this paper, three sized monodisperse Fe_3O_4 nanoparticles were prepared and subsequently dispersed into insulating vegetable oil to achieve nanofluids. The dispersion stability of nanoparticles in nanofluids was examined by natural sedimentation and zeta potential measurement. The electrical breakdown strength, space charge distribution, and several dielectric characteristics, for example, permittivity, dielectric loss, and volume resistivity of these nanofluids, were comparatively investigated. Experimental results show that the monodisperse Fe_3O_4 nanoparticles not only enhance the dielectric strength but also uniform the electric field of the nanofluids. The depth of electrical potential well of insulating vegetable oils and nanofluids were analyzed to clarify the influence of nanoparticles on electron trapping and on insulation improvement of the vegetable oil.

1. Introduction

Recent research works have shown that conductive and semiconductive nanoparticles can be dispersed in mineral and vegetable insulating oils to enhance dielectric strength or thermal conductivity of the insulating oils. Magnetic Fe_3O_4 nanoparticles have been proved of increasing the AC breakdown voltage of insulating oils for the case that the nanoparticles were well dispersed in oil [1–5]. It is also documented that both mineral and vegetable insulating oils are possible to show enhanced AC breakdown voltages and partial-discharge-inception voltages after the oils are modified by semiconductive TiO_2 nanoparticles [6, 7]. The electrical properties and dispersion stability of three nanofluids that are prepared by dispersing Fe_3O_4 , TiO_2 , and Al_2O_3 nanoparticles, respectively, in transformer oils have been discussed at a certain level [8]. The main process of charge transport in nanofluids is considered as the trapping and detrapping of electrons in shallow traps which has been argued in [7, 9].

It is already clarified that the dielectric performance of nanofluids is critically determined by nanoparticles' size

[10, 11]. However, comparative and systematic studies on the influence of nanoparticle size on the breakdown and the dielectric properties of vegetable oil-based nanofluids are still an open issue, which is becoming more important for applying such nanofluids in large power transformers. Moreover, nanoparticles often tend to agglomerate in oil because of nanoparticle's high surface-energy. It is technically difficult to prepare sufficiently good nanoparticles (single-crystalline, well-shaped, and narrow size-distribution) for analyzing the relationship between nanoparticle size and nanofluids' dielectric responses. Recently, several models are proposed to explain the improving breakdown characteristics of nanofluids [9, 12]. However, these mechanisms are always hard to explain influence of nanoparticle size on breakdown voltages and dielectric properties of nanofluids.

Our work aims to explore how the size of monodisperse nanoparticles generates various dielectric performances of nanofluids. The insulating vegetable oil-based nanofluids were prepared by adding three sized monodisperse Fe_3O_4 nanoparticles. Their basic physical and chemical properties are first presented briefly. The dispersion stability of nanofluids was determined by comparison of zeta potential

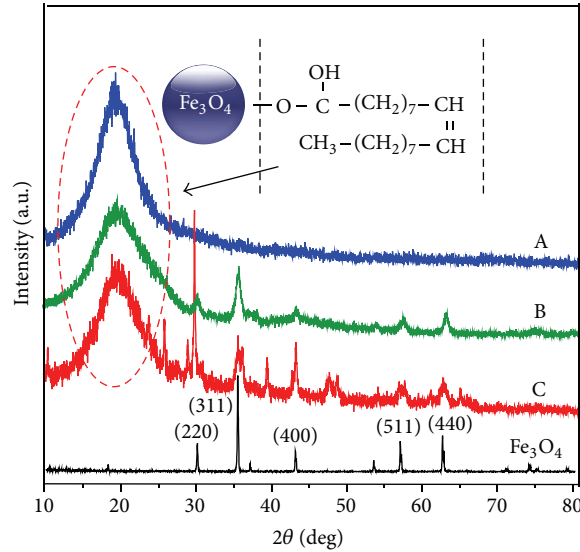


FIGURE 1: XRD patterns of pure Fe_3O_4 and Fe_3O_4 nanoparticle at different reaction time: (A) 12 hours, (B) 24 hours, and (C) 48 hours.

measurement. Next, the different dielectric properties of nanofluids are presented and discussed. The space charge distribution and electrical potential well depth were analyzed for the explanation of different breakdown voltages between the nanofluids and insulating vegetable oils.

2. Experimental

2.1. Materials. All reagents used in the experiment were of analytical grade without further purification.

2.2. Preparation of Nanofluids. The insulating vegetable oil-based nanofluids are obtained via three main procedures: preparation of the iron oleate precursor, preparation of the monodisperse Fe_3O_4 nanoparticle, and synthesis of the nanofluids.

2.2.1. Iron Oleate Precursor. 6.48 g of iron (III) chloride hexahydrate was dissolved in the mixture of 48 mL ethanol and 84 mL N-hexane. The obtained solution was slowly added by 21.9 g sodium-oleate-vigorous with magnetic string at 60°C for 12 h. The precipitated iron oleate was washed twice with methanol and was redissolved in hexane afterwards. The solution was additionally washed three times with warm ($\sim 60^\circ\text{C}$) deionized water in a separatory funnel and subsequently dried in vacuum at 80°C for 24 h.

2.2.2. Fe_3O_4 Nanoparticles. 2.1 g iron oleate precursor and 0.64 mL oleic acid were mixed in 10 mL octadecene followed by transferring into a three-neck-round-bottom flask and drying at 120°C for 30 min under nitrogen protection to remove water and oxygen. Then, the resulting mixture was heated to 320°C with 12 h, 24 h, and 48 h, respectively, to realize Fe_3O_4 nanoparticles with varied sizes. After cooling down to room temperature, the nanoparticles were

TABLE 1: Basic physical and chemical properties of the FR3 and the insulating vegetable oil-based nanofluids.

Parameter	FR3	Nanofluids
Appearance	Light yellow	Dark yellow
Density ($\text{kg}\cdot\text{m}^{-3}$, 20°C)	0.90	0.90
Kinematic viscosity ($\text{mm}^2\cdot\text{s}^{-1}$, 40°C)	43.0	44.0
Pour point ($^\circ\text{C}$)	-18	-18
Flash point ($^\circ\text{C}$)	325	325
Acid value ($\text{mg}\cdot\text{KOH}\cdot\text{g}^{-1}$)	0.03	0.03
Interfacial tension (mN/m)	30	30

subsequently centrifuged and washed several times with ethanol and cyclohexane before drying in air at 70°C .

2.2.3. Preparation of Nanofluids. The three Fe_3O_4 nanoparticles obtained by different reaction time were dispersed in the insulating vegetable oil through ultrasonic treatment. They were tagged by samples A, B, and C, respectively. The FR3 natural ester was used as received [13]. Before electrical characterization, three nanofluids and the FR3 were dried at 85°C under 50 Pa for 72 h. Some physical and chemical parameters of the FR3 and nanofluids are listed in Table 1.

2.3. Nanoparticle Characterization. The X-ray diffraction (XRD) pattern was obtained by using a powder X-ray diffraction meter equipped with a rotating anode and a $\text{Cu}\cdot\text{K}\alpha$ radiation source. The scan step was 0.02° . Figure 1 shows the XRD results of typical Fe_3O_4 nanoparticle according to [5] and different samples were obtained by high temperature decomposition method. It can be seen from the figure that the XRD patterns of Fe_3O_4 nanoparticle near 20° have a very wide amorphous peak; this is because the nanoparticles surface

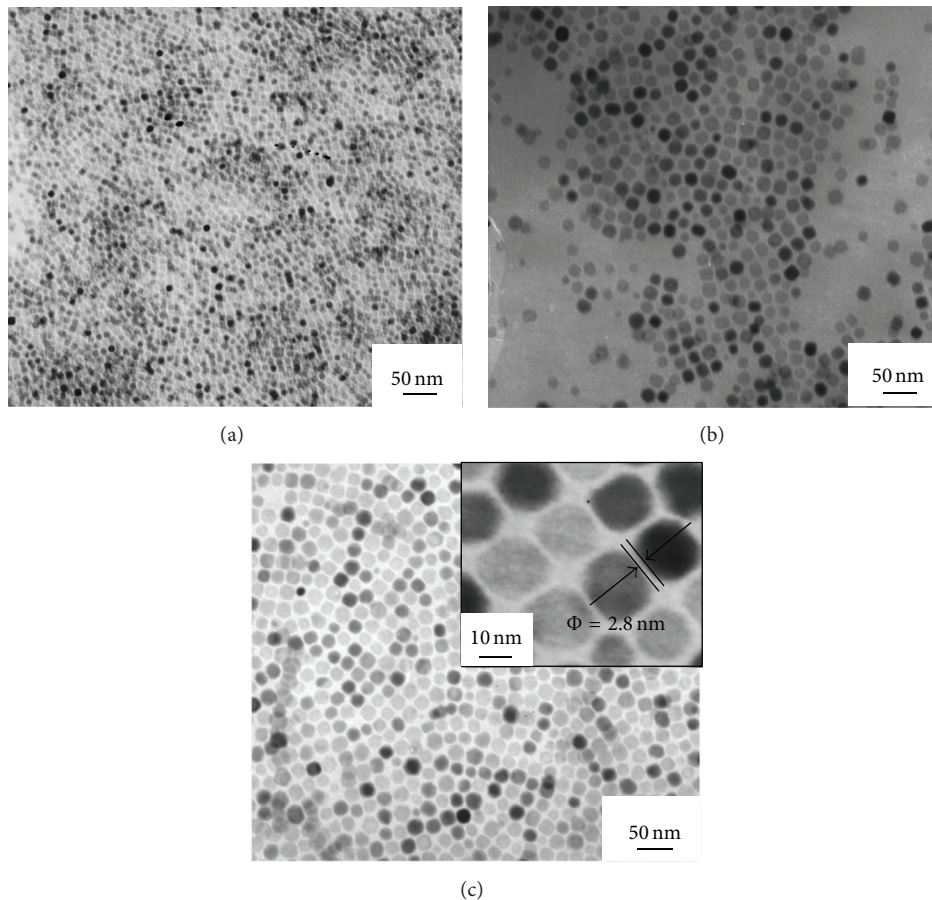


FIGURE 2: TEM images of monodisperse Fe_3O_4 nanoparticles at different reaction times (a) 12 hours, (b) 24 hours, and (c) 48 hours and the high resolution TEM image of monodisperse Fe_3O_4 (top right).

was coated with a large number of oleic acid. As the reaction time of sample A is not sufficient and the size is too small, there was no peak corresponding with Fe_3O_4 observed. The sharp peaks of samples B and C reveal that the nanoparticles have high crystallinity. According to JCPDS card number 65-3107, the 2θ values of 30.1° , 35.5° , 43.1° , 56.9° , and 62.6° are signatures of (220), (311), (400), (511), and (440) crystal face for Fe_3O_4 , respectively. Therefore, these XRD patterns may be indicative of the spinel structure of the Fe_3O_4 nanoparticles.

The morphologies of the three sized nanoparticles were observed by transmission electron microscopy (TEM), as shown in Figure 2. It is seen that the nearly spherical Fe_3O_4 nanoparticles prepared by high temperature decomposition (at 320°C) have achieved monodispersity. Each nanoparticle consists of two differentiated contrast regions. The darker central-core is the Fe_3O_4 crystal, which is surrounded by a lower-density shell, that is, the oleic acid. The covalent bonding between oleic acid and Fe_3O_4 prevents agglomeration of Fe_3O_4 nanoparticles but also improves the compatibility between nanoparticles and vegetable insulating oil [14].

The average size of the Fe_3O_4 crystal in Figure 2(a) is estimated as ~ 6.6 nm. Here the size represents the diameter of Fe_3O_4 crystal without the shell. With longer reaction time, that is, from 12 to 48 h, the thickness of oleic acid

shell grows slightly from ~ 2 to ~ 3 nm. Therefore sized Fe_3O_4 nanoparticles are obtained with varying diameter from ~ 8.6 (Figure 2(a)) to ~ 24.4 nm (Figure 2(c)) via ~ 15.2 nm (Figure 2(b)). The zoomed TEM image (inset in Figure 2(c)) better indicates the border between oleic acid shell and Fe_3O_4 crystal.

3. Results and Discussion

3.1. Dispersion Stability of Nanofluids. Natural sedimentation is an indicator of the dispersion stability for nanoparticles in nanofluids. Three sized Fe_3O_4 nanoparticles were dispersed in the vegetable oil, to realize nanofluids that are recognized as 1, 2, and 3 to examine their storage-time dependent dispersion stability. As shown in Figure 3, nanofluids show no visible agglomeration for the nanoparticles in oil after 6 months standing in ambient condition.

The zeta potential measurement is another method to evaluate stability of the nanofluids. As the stabilization theory [15] describes, the electrostatic repulsion among nanoparticles should increase prominently for the case that the zeta potential stands at a high level which signifies good suspension stability [16]. Table 2 lists several key zeta potential values that indexed the suspension stability of nanofluids.

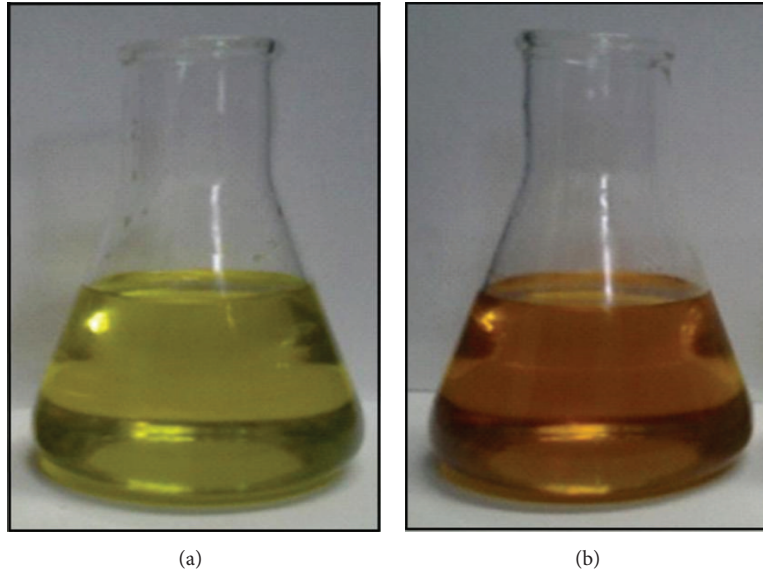


FIGURE 3: (a) FR3 and (b) vegetable oil-based nanofluids.

TABLE 2: Zeta potential and associated suspension stability.

Z potential (mV)	Stability
0	Little or no stability
15	Some stability but settling lightly
30	Moderate stability
45	Good stability, possible settling
60	Very good stability, little settling likely

The zeta potential for all the three nanofluids 1, 2, and 3 display values above 30 mV, that is, 74.0, 60.7, and 47.4 mV, respectively. It has been well accepted that a zeta potential which is great than 30 mV should mark a sufficiently good dispersion stability [15]. As a general rule, the smaller nanoparticles in nanofluids, the higher the zeta potential and certainly the more stable the nanofluids.

3.2. Breakdown Voltage of Nanofluids. The absolute moisture content of all nanofluids was controlled at a value below 200 mg/kg. The AC breakdown voltages of each nanofluid were characterized in accordance with IEC 60156 [17]. All the measurements were made on 9 nanofluids samples. The FR3 oil was also included in measurements for comparison.

The lightning-impulse breakdown voltages for nanofluids were obtained by means of a configuration consisting of a container and an electrode in Figure 4. The high-voltage electrode and the grounding electrode were a steel needle and a 13 mm diameter steel sphere, respectively. The gap between the needle tip and the sphere was 15 mm. These dimensions comply with IEC 60897 [18] for liquid dielectrics. 1.2/50 μ s standard lightning-impulse voltages are employed to determine the lightning-impulse breakdown voltages

Figure 5 lists the AC breakdown voltages of the three nanofluids and the FR3 oil, in which the oil was marked as

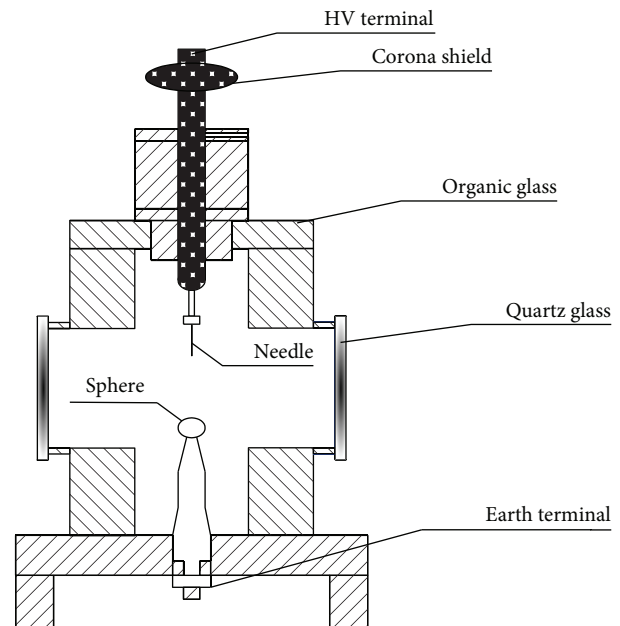


FIGURE 4: Sketch of electrode setup and oil vessel for lightning-impulse breakdown experiments on insulating oils.

0 ppm nanoparticles added. It is seen that the breakdown strength of each nanofluids increases to a top value and slightly decreases afterwards with higher nanoparticle content. For example, the breakdown strength enhances by 23% from 55.1 kV for FR3 to 67.8 kV for nanofluids C that was added with 200 ppm nanoparticles. On the other hand, the breakdown strength tends to increase for nanofluids with larger size nanoparticles added.

The lightning-impulse breakdown voltages of the three nanofluids and FR3 oil for both polarities are summarized in

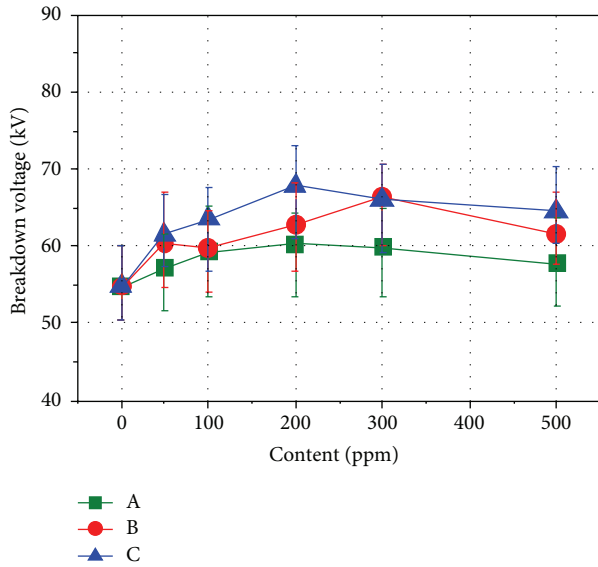


FIGURE 5: Influence of contents and sizes of Fe_3O_4 nanoparticles on the AC breakdown voltage of the vegetable oil-based nanofluids.

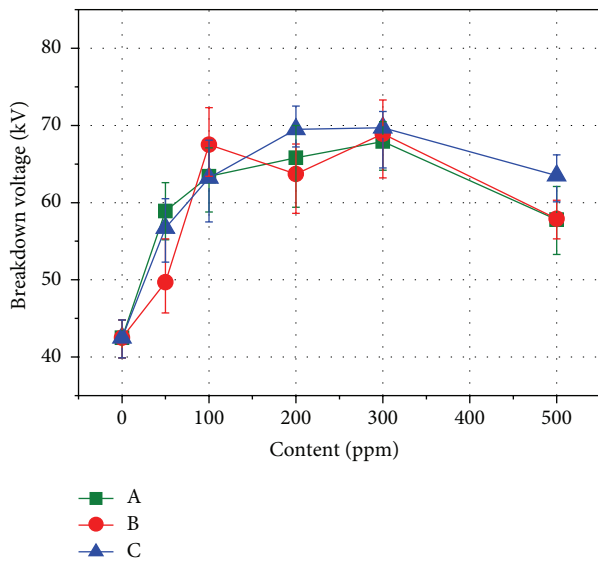


FIGURE 6: Influence of contents and size of nanoparticles on the positive lightning breakdown voltage of the vegetable oil-based nanofluids.

Figures 6 and 7. For negative lightning-impulse the nanofluids provide insignificant effects, but for the AC profile or for the positive lightning-impulse the attained improvement is significant. Here the positive lightning-impulse leads to strongly increased breakdown voltages. The nanofluid C, which contains 300 ppm nanoparticles, exhibits the highest breakdown voltage of 69.7 kV for positive lightning-impulse. This is a significantly higher voltage which is enhanced by 64% compared to that of FR3 oil. However the nanofluids show only slightly improved (7%) breakdown behavior for the case of negative lightning-impulse application. The increases of the positive lightning breakdown voltages are greater than

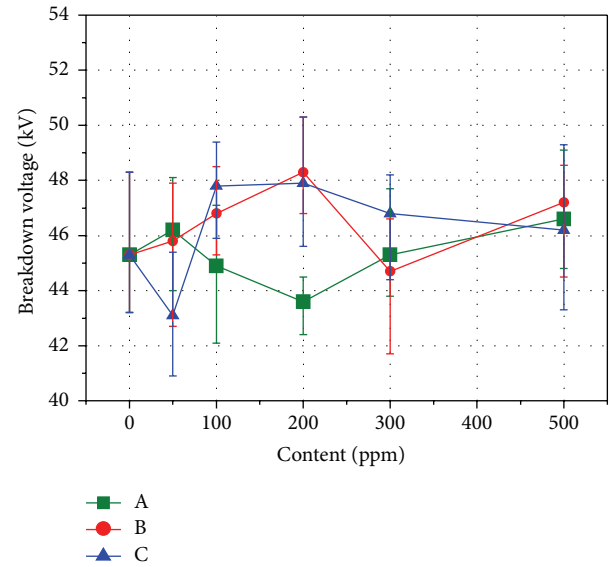


FIGURE 7: Influence of contents and size of nanoparticles on the negative lightning breakdown voltage of the vegetable oil-based nanofluids.

that of the negative lightning-impulse breakdown voltages. For positive lightning-impulse, nanoparticles in nanofluids will weaken the field strength and extremely increase positive breakdown voltages. However, the effect is inconspicuous for negative lightning-impulse [4]. Our results point out an opposite tendency with the breakdown behavior that has been observed in mineral oil-based nanofluids [1, 8]. This should be attributed to the much different molecular conformation of insulating vegetable oil, which certainly generates different streamer development.

From the results in Figures 5–7, one can note that the measured breakdown voltage of nanofluids follows a sequence $A < B < C$ with nearly no influence from polarity or nanoparticle content. This encourages us to conclude that the breakdown strength of nanofluids is mainly determined by the size of nanoparticles.

3.3. Dielectric Properties of Nanofluids. The frequency dependences of permittivity between 10^{-2} and 10^6 Hz for FR3 oil and the three nanofluids are summarized in Figure 8. There is no big difference over the frequency range among samples. As well known, the relative permittivity of Fe_3O_4 nanoparticles is ca. 80 [12], which is much greater than that of FR3 oil. Therefore nanoparticles may contribute more to the permittivity of nanofluids than FR3 oil. Furthermore, at 50 Hz, the relative permittivity decreases with increasing nanoparticle size and the relative permittivity of sample A has a maximum value of 3.06.

It is obvious that the permittivity values of nanofluids varied with the size of nanoparticles. Considerable results have confirmed that smaller sized nanoparticles usually possess higher permittivity than that of larger ones. The reason can be found from an internal-stress model which has been introduced by Buessem et al. [19]; that is, the permittivity of

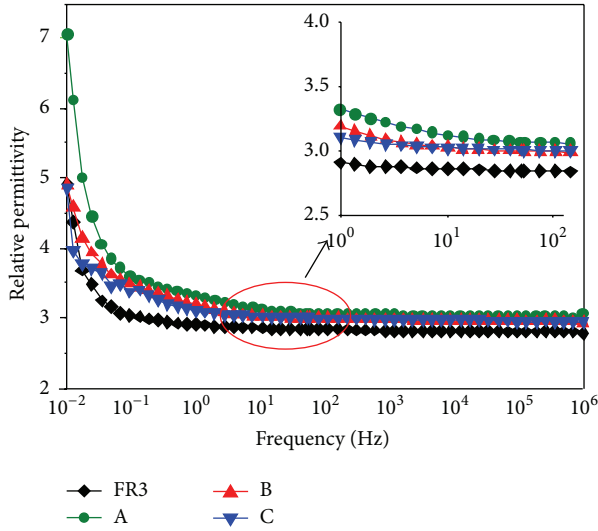


FIGURE 8: Variation of the relative permittivity of vegetable oil modified by Fe_3O_4 nanoparticles with different sizes at different frequencies.

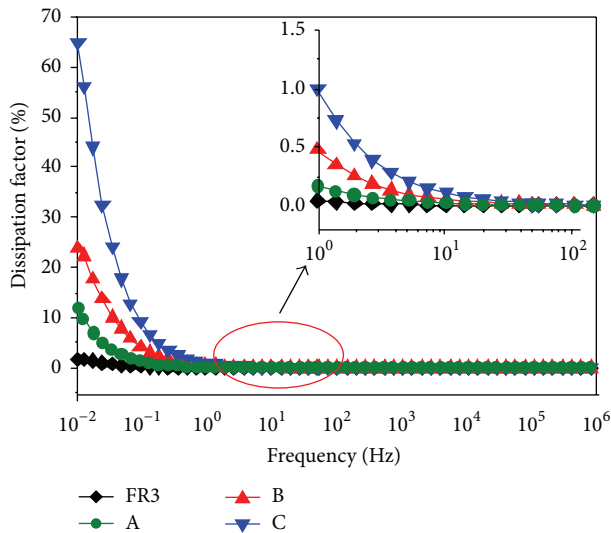


FIGURE 9: Variation of the dielectric loss of vegetable oil modified by Fe_3O_4 nanoparticles with different sizes at different frequencies.

a nanoparticle is determined by the relatively strong internal-stress which is the result of free-energy balance.

The dielectric loss of nanofluids and FR3 oil shows a decrease with increasing frequency as the results shown in Figure 9. However the nanofluids' loss decreases for larger sized Fe_3O_4 nanoparticles. The three nanofluids and the FR3 oil behave almost identical between 1 and 10^6 Hz. They present obvious difference at the range of 10^{-2} –1 Hz.

The loss of a fluid is composed of two contributions, that is, conductance loss and polarization loss. Vegetable insulating oil (e.g., FR3 oil in this work) is a weak polar liquid dielectric, which implies that the conductance loss dominants at low frequency [20]. The crystal defects within nanoparticles, which are unavoidable and usually are brought

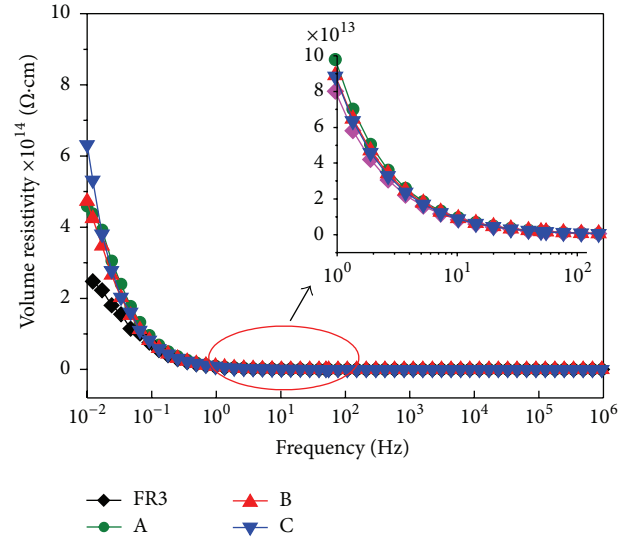


FIGURE 10: Variation of the volume resistivity of vegetable oil modified by Fe_3O_4 nanoparticles with different sizes at different frequencies.

during chemical preparation, emerge more for larger sized nanoparticles. The high conductivity of these nanoparticles certainly leads to much increased dielectric loss.

Figure 10 gives the frequency dependence of the volume resistivity for FR3 oil and the three nanofluids. There is no visible difference among nanofluids and FR3 oil at a frequency above 0.1 Hz. When frequency downs below 0.1 Hz, the curves start to diverge, with a changeless tendency that the volume resistivity of nanofluids is always higher than that of FR3 oil.

Nanoparticles dispersed in nanofluids are polarized when the nanofluids are subjected to an externally applied electric field [12]. These nanoparticles provide traps free electrons, thereby decreasing the concentration of highly mobile electrons in the nanofluids and increasing the concentration of low-mobility negatively charged nanoparticles. As a result, the volume resistivity of the nanofluids is larger than that of the vegetable insulating oil. Increasing the frequency decreases both the duration of each half cycle of the electrical field and the probability of electron capture by the nanoparticles. These phenomena explain the smaller difference in volume resistivity between the FR3 oil and the nanofluids at frequencies greater than approximately 0.1 Hz.

3.4. Space Charge Distribution of Nanofluids. In order to investigate the influence of sizes of monodisperse Fe_3O_4 nanoparticle on charge carriers transport characteristics of the vegetable oil and vegetable oil-based nanofluids, the pulse electroacoustic (PEA) tests were carried out to investigate the space charge density of all samples, stressed 15 kV/mm for varying time (0.5, 1, 5, 10, and 30 min). As shown in Figure 11, the charge density in vegetable oil is increasing with time and the maximum charge density was about 34.2 C/m^3 . However, the charge density in nanofluids was first increased and then decreased with time, less than half of that in vegetable oil. The

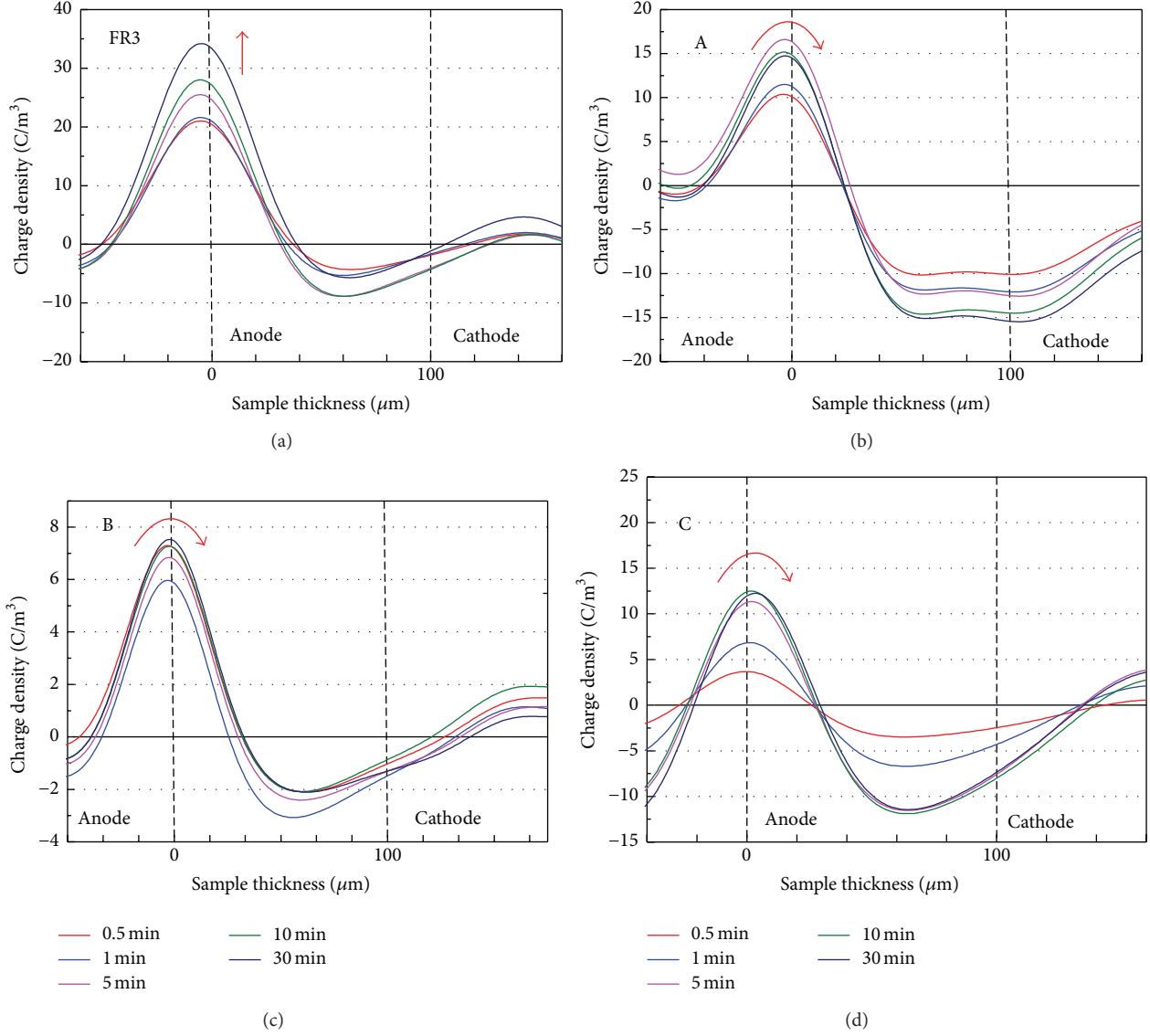


FIGURE 11: Charge density of the samples vegetable oil modified by Fe_3O_4 nanoparticles with different sizes.

maximum charge density of the three nanofluids was about 16.6, 12.5, and 7.5 C/m^3 , respectively.

The similar results also can be found in [7, 21, 22]. Interaction between nanoparticles and vegetable oil molecule will significantly improve the charge mobility of nanofluids. And the rapid charge mobility may inhibit space charge accumulation, resulting in uniform electric field of nanofluids.

3.5. Possible Mechanism. To understand why the breakdown voltage of nanomodified insulating vegetable oil is higher than that of pure vegetable oil, a dipole model of nanoparticles in [23] is proposed. The charge relaxation time constant of nanoparticles has a major bearing on the extent to which the electrodynamic processes in the liquid are modified. If the nanoparticles' charge relaxation time constant is short, then the timescales of interest for streamer growth and their

presence in the oil will significantly modify the electro-dynamics.

The spherical nanoparticles (diameter $2a$, relative dielectric constant ϵ_2) were dispersed in the insulating oils (relative dielectric constant ϵ_1) as shown in Figure 12, and an external electric field E_0 was applied to the vegetable oil-based nanofluids consisting of ϵ_1 and ϵ_2 dielectrics. According to the calculation, the relaxation time constant of the nanoparticle Fe_3O_4 used in the test is less than the propagation time of the streamer [4]. Electric charges will be induced by the electric field E_0 at the surface of the spherical body. As a result, the dipole surface charge density, $\sigma_p(\theta_p, \varphi_p)$, given by (1), is induced by the applied electric field E_0 at the interface between the ϵ_1 and ϵ_2 dielectrics:

$$\delta_p = \epsilon_0 E_0 \left(1 - \frac{3\epsilon_1}{2\epsilon_1 + \epsilon_2} \right) \cos \varphi_p \sin \theta_p. \quad (1)$$

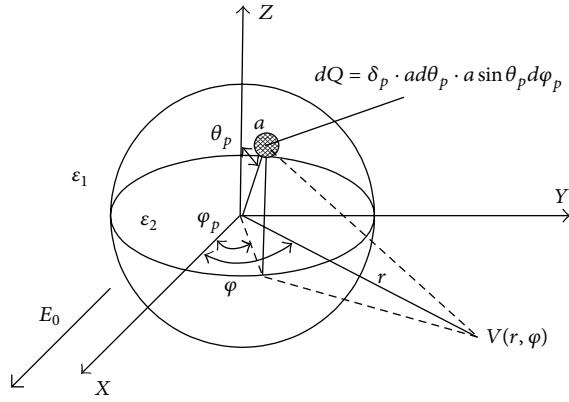


FIGURE 12: Diagram depicting the dipole surface charge density, $\sigma_p(\theta_p, \varphi_p)$, and the electrical potential, $V(r, \varphi)$, in spherical coordinates.

As the direction of E_0 was set in the direction of the x -axis, angle $\varphi = 0$, the positive dipole surface charge, $+\sigma_p(\theta_p, \varphi_p)$, was induced within the angle range $-\pi/2 < \varphi_p < +\pi/2$, and the negative dipole surface charge, $-\sigma_p(\theta_p, \varphi_p)$, was induced within the angle range $\pi/2 < \varphi_p < 3\pi/2$. The electrical potential distribution, $V(r, \varphi)$, induced by the dipole surface charge density, $\sigma_p(\theta_p, \varphi_p)$, expressed as (1), is given by (2). Equation (2) is normalized by the potential difference aE_0 :

$$V(r, \varphi) = \frac{aE_0}{4\pi} \left(1 - \frac{3\varepsilon_1}{2\varepsilon_1 + \varepsilon_2} \right) \int_{-\pi}^{+\pi} \int_0^{+\pi} \frac{\sin^2 \theta_p d\theta_p \cos \varphi_p d\varphi_p}{\sqrt{1 + (r/a)^2 - 2(r/a) \sin \theta_p \cos(\varphi - \varphi_p)}} \quad (2)$$

Figure 13 showed the electrical potential well distribution, $V(r)$, at $\varphi = 0$ which was obtained from (2). The size of nanoparticle was $a = 10, 20$ and 30 nm, respectively, and the external electric field is $E_0 = 200$ kV/mm. Furthermore, the relative dielectric constant of the Fe_3O_4 nanoparticle was $\varepsilon_1 = 80$ and vegetable insulating oil was $\varepsilon_2 = 3.2$.

In Figure 13, it can be seen that the maximum electrical potential well occurred at the surface of the nanoparticle. The maximum electrical well of nanoparticle grows linearly with increasing the nanoparticle size. When the nanoparticle size was 10 nm, 20 nm, and 30 nm, the maximum electrical potential well depth was 5.86, 11.73, and 17.59 eV, respectively. The electrical potential well depth was much higher than that of insulating oil (about 0.45 eV) [23]. The increased electrical potential well depth in nanofluids could inhibit the free charge spread and enhance the capability of breakdown performance of nanofluids.

4. Conclusion

- (1) The nanofluids were developed by dispersing Fe_3O_4 nanoparticles with different sizes in insulating vegetable oil to enhance its breakdown strength. For negative lightning-impulse the nanofluids provide

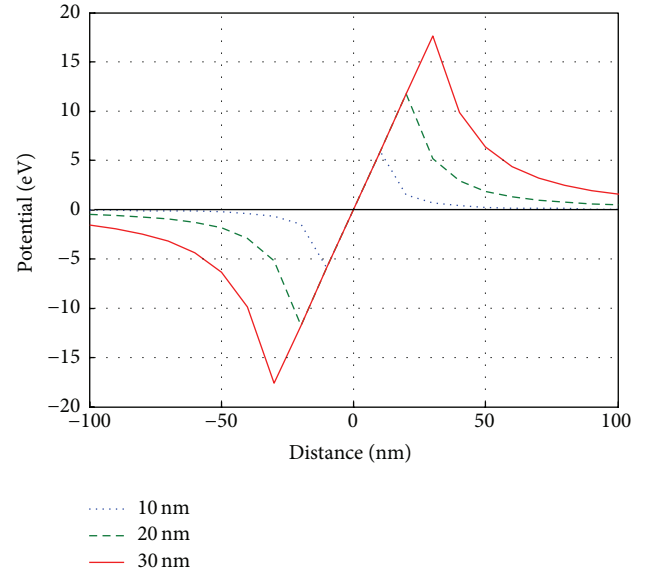


FIGURE 13: Dependence on size of nanoparticle induced trapped depth.

insignificant effects, but for the AC profile or for the positive lightning-impulse the attained improvement is significant. Meanwhile, the increasing nanoparticle size will improve the breakdown performance of nanofluids.

- (2) With increasing the nanoparticle size, the volume resistivities of the nanofluids are almost equal and their dissipation factors increase at frequencies below 0.1 Hz. The relative permittivities of the nanofluids are greater than that of the FR3 oil between 10^{-2} and 10^7 Hz, probably because of the much higher relative permittivity of the Fe_3O_4 nanoparticles.
- (3) The addition of monodisperse Fe_3O_4 nanoparticle into vegetable insulating oil will increase the electrical potential well depth and nanoparticle size could significantly influence the electrical potential well depth. The increased electrical potential well depth could enhance the capability of breakdown performance of nanofluids.

Conflict of Interests

The authors declare that they have no financial or personal relationship with any people or any organization that may inappropriately influence their work and there is no professional or commercial interest of any kind in all of the commercial entities mentioned in our paper.

Acknowledgments

The authors acknowledge the National Science Foundation of China (nos. 51321063 and 51377176) and the 111 Project of the Ministry of Education, China (B08036). A visiting scholarship provided by the State Key Lab of Power Equipment &

System Security and New Technology at Chongqing University (no. 2007DA10512713408) and the Doctoral Program of Higher Education of China (SRFDP) (20110191110017) are also appreciated for supporting this work.

References

- [1] J. A. Mergos, M. D. Athanassopoulou, T. G. Argyropoulos, and C. T. Dervos, "Dielectric properties of nanopowder dispersions in paraffin oil," *IEEE Transactions on Dielectrics and Electrical Insulation*, vol. 19, no. 5, pp. 1502–1507, 2012.
- [2] V. Segal, A. Rabinovich, D. Nattrass, K. Raj, and A. Nunes, "Experimental study of magnetic colloidal fluids behavior in power transformers," *Journal of Magnetism and Magnetic Materials*, vol. 215, pp. 513–515, 2000.
- [3] P. Zou, J. Li, C. Sun, Z. Zhang, and R. Liao, "Dielectric properties and electrodynamic process of natural ester-based insulating nanofluid," *Modern Physics Letters B*, vol. 25, p. 2021, 2011.
- [4] J. Li, Z. Zhang, P. Zou, B. Du, and R. Liao, "Lightning impulse breakdown characteristics and electrodynamic process of insulating vegetable oil-based nanofluid," *Modern Physics Letters B*, vol. 26, no. 15, Article ID 1250095, 13 pages, 2012.
- [5] J. Li, Z. Zhang, P. Zou, S. Grzybowski, and M. Zahn, "Preparation of a vegetable oil-based nanofluid and investigation of its breakdown and dielectric properties," *IEEE Electrical Insulation Magazine*, vol. 28, no. 5, pp. 43–50, 2012.
- [6] D. Yue-Fan, L. Yu-Zhen, L. Cheng-Rong et al., "Effect of electron shallow trap on breakdown performance of transformer oil-based nanofluids," *Journal of Applied Physics*, vol. 110, p. 104, 2011.
- [7] Y.-F. Du, Y.-Z. Lv, C. Li et al., "Effect of semiconductive nanoparticles on insulating performances of transformer oil," *IEEE Transactions on Dielectrics and Electrical Insulation*, vol. 19, no. 3, pp. 770–776, 2012.
- [8] W.-X. Sima, X.-F. Cao, Q. Yang, H. Song, and J. Shi, "Preparation of three transformer oil-based nanofluids and comparison of their impulse breakdown characteristics," *Nanoscience and Nanotechnology Letters*, vol. 6, no. 3, pp. 250–256, 2014.
- [9] Y.-X. Zhong, Y.-Z. Lv, C.-R. Li et al., "Insulating properties and charge characteristics of natural ester fluid modified by TiO₂ semiconductive nanoparticles," *IEEE Transactions on Dielectrics and Electrical Insulation*, vol. 19, pp. 770–776, 2012.
- [10] P. Kopčanský, L. Tomččo, K. Marton, M. Koneracká, M. Timkoa, and I. Potočová, "The DC dielectric breakdown strength of magnetic fluids based on transformer oil," *Journal of Magnetism and Magnetic Materials*, vol. 289, pp. 415–418, 2005.
- [11] J.-C. Lee, W.-H. Lee, S.-H. Lee, and S. Lee, "Positive and negative effects of dielectric breakdown in transformer oil based magnetic fluids," *Materials Research Bulletin*, vol. 47, no. 10, pp. 2984–2987, 2012.
- [12] J. G. Hwang, M. Zahn, F. M. O'Sullivan, L. A. A. Pettersson, O. Hjortstam, and R. Liu, "Effects of nanoparticle charging on streamer development in transformer oil-based nanofluids," *Journal of Applied Physics*, vol. 107, no. 1, Article ID 014310, 2010.
- [13] Q. Liu and Z. D. Wang, "Streamer characteristic and breakdown in synthetic and natural ester transformer liquids under standard lightning impulse voltage," *IEEE Transactions on Dielectrics and Electrical Insulation*, vol. 18, no. 1, pp. 285–294, 2011.
- [14] Y. Ren, K.-I. Iimura, and T. Kato, "Structure of barium stearate films at the air/water interface investigated by polarization modulation infrared spectroscopy and $\pi - A$ isotherms," *Langmuir*, vol. 17, no. 9, pp. 2688–2693, 2001.
- [15] J.-H. Lee, K. S. Hwang, S. P. Jang et al., "Effective viscosities and thermal conductivities of aqueous nanofluids containing low volume concentrations of Al₂O₃ nanoparticles," *International Journal of Heat and Mass Transfer*, vol. 51, no. 11-12, pp. 2651–2656, 2008.
- [16] L. Vandsburger, *Synthesis and Covalent Surface Modification of Carbon Nanotubes for Preparation of Stabilized Nanofluid Suspensions*, Department of Chemical Engineering, McGill University, Montreal, Canada, 2009.
- [17] *Insulating Liquids—Determination of the Breakdown Voltage at Power Frequency—Test Method*, IEC 60156, 1995.
- [18] *Methods for the determination of the lightning impulse breakdown voltage of insulating liquids*, IEC 60897, 1987.
- [19] W. Buessem, L. Cross, and A. Goswami, "Phenomenological theory of high permittivity in fine-grained barium titanate," *Journal of the American Ceramic Society*, vol. 49, no. 1, pp. 33–36, 1966.
- [20] R. Richert, A. Agapov, and A. P. Sokolov, "Appearance of a Debye process at the conductivity relaxation frequency of a viscous liquid," *The Journal of Chemical Physics*, vol. 134, no. 10, Article ID 104508, 2011.
- [21] J. K. Nelson and J. C. Fothergill, "Internal charge behaviour of nanocomposites," *Nanotechnology*, vol. 15, no. 5, pp. 586–595, 2004.
- [22] T. Tanaka, "Dielectric nanocomposites with insulating properties," *IEEE Transactions on Dielectrics and Electrical Insulation*, vol. 12, no. 5, pp. 914–928, 2005.
- [23] T. Takada, Y. Hayase, and Y. Tanaka, "Space charge trapping in electrical potential well caused by permanent and induced dipoles for LDPE/MgO nanocomposite," *IEEE Transactions on Dielectrics and Electrical Insulation*, vol. 15, no. 1, pp. 152–160, 2008.

Review Article

Recent Advances in FePt Nanoparticles for Biomedicine

Yujuan Shi,^{1,2} Mei Lin,¹ Xingmao Jiang,³ and Shuai Liang³

¹Taizhou People's Hospital Affiliated to Nantong University, No. 210 Yingchun Road, Taizhou, Jiangsu 225300, China

²Medical School of Nantong University, Nantong, Jiangsu 226001, China

³Key Laboratory of Advanced Catalytic Material and Technology, Changzhou University, Changzhou, Jiangsu 213000, China

Correspondence should be addressed to Mei Lin; l.mei@163.com

Received 26 March 2015; Revised 30 May 2015; Accepted 21 June 2015

Academic Editor: Kangtaek Lee

Copyright © 2015 Yujuan Shi et al. This is an open access article distributed under the Creative Commons Attribution License, which permits unrestricted use, distribution, and reproduction in any medium, provided the original work is properly cited.

FePt nanoparticles have great potential for biomedical applications due to their superior characteristics, including superparamagnetism, resistance to oxidation, and high chemical stability. The present paper reviews the methods used to prepare FePt nanoparticles, surface modifications, and their applications in the biomedical field, such as biosensing, magnetic resonance imaging (MRI), targeted drug delivery, and therapy.

1. Introduction

In the past several decades, the biomedical applications of magnetic nanoparticles (MNPs), including their use as MRI contrast agents and carriers for targeted drug delivery and in magnetic fluid hyperthermia (MFH), biological separation, and immunodetection, have become the topic of considerable research, and significant progress has been made in these fields [1–5]. MNPs mainly include metallic oxide nanoparticles (e.g., Fe_3O_4 and $\gamma\text{-Fe}_2\text{O}_3$), metallic nanoparticles (e.g., Fe and Co), and metal alloys (e.g., FePt and FeCo). Among them, iron oxide nanoparticles (IONP) are the most frequently investigated due to their advantages of superparamagnetism, good biocompatibility, being biodegradable, and easy synthesis. They have been used for the purposes of diagnosis and therapy [6–12]. Branca et al. [7] reported that the cancer-binding ligands functionalized IONP combined with hyperpolarized ^3He MRI could detect early-stage metastatic lung tumors in mice. Andreas et al. [8] demonstrated the citrate-coated superparamagnetic iron oxide nanoparticles (SPIONs) as MRI contrast agents could be employed in human mesenchymal stem cell labeling and tracking. Mahmoudi et al. [9] reported that drug-loaded SPIONs could potentially be guided to the desired target site under an external magnetic field. However, metal alloy nanoparticles, such as FePt nanoparticles, with better magnetic properties, have also

attracted increasing attention from many researchers. The FePt nanoparticles can show excellent superparamagnetic property and be chemically stable against oxidation [13]. In addition, the FePt nanoparticles can be prepared with tunable size and shape and could be modified for diverse biomedical applications [14]. The present paper reviews advances in FePt nanoparticle preparation, surface modification, and biomedical applications in recent years and their future prospects.

2. Preparation and Properties of FePt MNPs

FePt nanoparticles mainly include two structures. One structure consists of a disordered face centered cubic (FCC) structure (cf. Figure 1(a)). The other structure consists of an ordered face centered tetragonal (FCT) or ordered L1_0 phase (cf. Figure 1(b)). Due to their good magnetocrystalline anisotropy, high coercivity, high magnetic energy product, specific Curie temperature, and low superparamagnetic critical size, FePt nanoparticles are suitable for applications such as ultrahigh density magnetic recording media and vertical magnetic tunnel junctions [15–20]. In addition, superparamagnetic FePt nanoparticles, which have good biocompatibility and high X-ray absorption, have potential applications in biomedicine [21, 22].

Various methods are available for the preparation of FePt MNPs, including mechanical cold deformation [23],

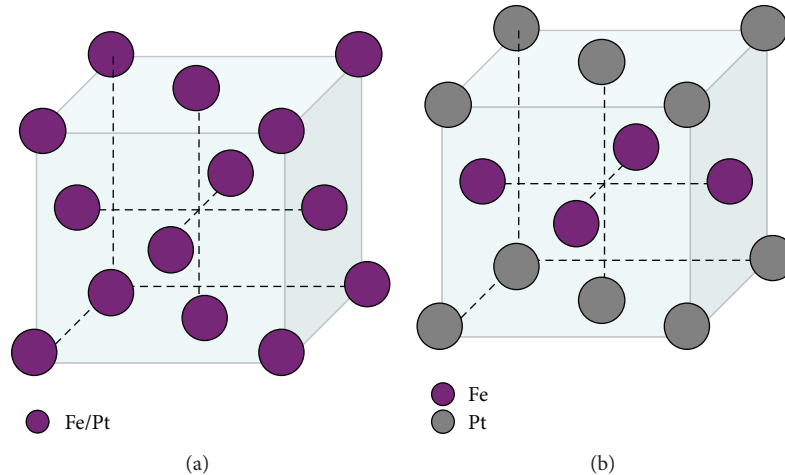


FIGURE 1: FePt crystal structure: (a) FCC structure; (b) FCT structure.

magnetron sputtering [18, 24, 25], vacuum deposition [26], and some chemical techniques.

2.1. Physical Methods

2.1.1. Mechanical Cold Deformation Method. The general mechanical cold deformation procedure consists of cold drawing, rolling, and extrusion. Using this method, Hai et al. [23] obtained ordered FePt material with high anisotropy by heating Fe and Pt metals, which were circularly rolled, in a sealed vacuum quartz tube. This strategy can be used for large-scale production due to its relatively simple technique. However, it is not easy to control the mutual diffusion of Pt and Fe, and the properties of the product are also difficult to control.

2.1.2. Magnetron Sputtering Method. In a vacuum with an appropriate amount of inert gas (typically Ar) and a certain voltage, Ar⁺ can impact the Fe target, Pt target, or other alloy targets to cause the Fe and Pt atoms on the surface of the targets to be sputtered out. Under the influence of the magnetic and electric fields, the sputtered Fe and Pt atoms may be transferred to the substrate and deposit to form a FePt nanomaterial. This process is called magnetron sputtering and is one of most widely used methods. FePt films have been successfully prepared by this method [18, 24, 25]. Weller et al. [24] used high-temperature sputtering to prepare highly chemically ordered L1₀ FePt films in a glass dish coated with adhesion, heat sinks, and a deformation layer by adding Ag to reduce the required deposition temperature and Cu to reduce the Curie temperature.

2.1.3. Vacuum Evaporation Deposition Method. The vacuum evaporation deposition method is described as follows. First, the reaction chamber is placed in a strong vacuum. After heating, the objective material can evaporate and deposit on the smooth substrate. Then, the desired nanomaterials are obtained. Yu et al. [26] reported the production of FePt films

grown on a MgO (110) single-crystal substrate (where the temperature was heated to 700°C) by electron-beam coevaporation. Castaldi et al. [27] prepared FePt nanoparticles, which were thermally deposited on oxidized Si substrates (substrate temperatures of 300–700°C) by electron-beam coevaporation of Fe and Pt.

2.2. Chemical Methods. However, when using these physical methods, it is not easy to specify the morphology, particle size, and size distribution of FePt MNPs. To overcome these shortcomings, several chemical methods have been developed in the past decades in which the stoichiometry, size, and shape of FePt MNPs can be controlled. The general chemical strategies used to obtain FePt MNPs include high-temperature thermal decomposition reduction, polyol reduction, microemulsion methods, and electrochemical deposition methods.

2.2.1. Thermal Decomposition Reduction. Thermal decomposition deacidizing is another method used to prepare MNPs through heating and reducing the organic metal compound (precursor) in a high-boiling-point solvent with a surfactant. This method can yield particles with a tunable size and high crystallinity. In 2000, using oleic acid and oleylamine as surfactant, Sun et al. [28] prepared monodispersed FePt nanoparticles with a 4 nm diameter by thermally decomposing iron pentacarbonyl (Fe(CO)₅) and deacidizing platinum acetylacetonate (Pt(acac)₂) in a solvent of octyl ether. Subsequently, Wang et al. [29] synthesized 4.5 and 12 nm monodispersed FePt nanoparticles by thermal decomposition of Fe(CO)₅ and reduction of Pt(acac)₂ in a benzyl ether solvent using oleic acid as a surfactant. Bian et al. [30] obtained single-crystal FePt nanoparticles with a controllable size and isotropic shape using a complex of Fe(CO)₅-oleylamine and Pt(acac)₂ as the precursors of Fe and Pt, respectively, and adjusting the ratio and temperature of oleylamine and Fe(CO)₅.

However, thermal decomposition has the shortcoming of requiring nocuous precursors, such as Fe(CO)₅, during

preparation [31]. $\text{Fe}(\text{CO})_5$, a metal organic compound with strong volatility, can produce the toxic gas CO during thermal decomposition, which makes the technique difficult to perform and also causes side effects in the composition, particle size, and size distribution of the FePt particles. Therefore, using relatively low-toxicity precursors, such as iron fatty acids, $\text{Fe}(\text{acac})_2$ and $\text{Na}_2\text{Fe}(\text{CO})_4$, to replace $\text{Fe}(\text{CO})_5$ has recently attracted considerable interest [1, 31, 32]. Taylor et al. [31] synthesized superparamagnetic FePt nanoparticles (SIPPs) by utilizing a “green” thermal decomposition method. They used iron-fatty acid and $\text{Pt}(\text{acac})_2$ as the precursors of Fe and Pt, respectively, octadecene (ODE) or tetracosane (TCA) as solvents, and fatty amine as a ligand. The carbon length of fatty amine ranges from 12 to 18. They compared the effects of fatty amine ligands with different lengths on the composition, uniformity, magnetic properties, shape, and structure of the SIPPs. The results showed that the use of 1-tetradecylamine (TDA) and a 30-min reflux reaction could produce the optimal particles. These TDA-SIPPs exhibited the best properties of saturation magnetization, iron content, monodispersity, and stability and could be a promising MRI contrast agent for cancer detection.

2.2.2. Polyol Reduction Method. Polyol is often used in the preparation of various metal and alloy nanoparticles due to its ability to simultaneously act as a surface active agent, solvent, and reducing agent. The so-called polyol reduction method refers to the use of diol or polyol as a reductant to deacidize a metallic salt to obtain the corresponding nanoparticles. Based on this method, Chou et al. [21] prepared FePt nanoparticles with 3, 6, and 12 nm diameters by heating a reaction mixture of $\text{Pt}(\text{acac})_2$, $\text{Fe}(\text{CO})_5$, 1,2-hexadecanediol, dioctyl ether, oleylamine, and oleic acid to 297°C and then using ethanol to extract the resultant material. Sahu et al. [33] obtained nanoparticles of diverse sizes with different stoichiometric compositions using an equimolar ratio of an Fe precursor ($\text{Fe}(\text{acac})_3$) and Pt precursors ($\text{Pt}(\text{acac})_2$, PtCl_2 , PtCl_4 , and $\text{H}_2\text{PtCl}_6 \cdot \text{H}_2\text{O}$) and the reducing agent 1,2-hexadecanediol in the presence of octyl ether.

2.2.3. Microemulsion Method. Microemulsions are transparent, isotropic, and thermodynamically stable liquid mixtures that consist of oil, water, surfactant, and cosurfactant. Depending on the ratio of water and oil, microemulsions can be divided into three basic types: the oil dispersed in water type (O/W type), water dispersed in oil type (W/O type), and multiple microemulsion type (W/O/W or O/W/O type). The most commonly used type for MNP preparation is the W/O type microemulsion method (also called the reverse micelle method). The nanoparticles obtained by this method are uniform with a controllable size and stable in a colloid solution. Hyie and Yaacob [34] successfully prepared disordered FCC soft magnetic FePt nanoparticles with 4.7 and 8.4 nm diameters in a water/glycol octyl phenyl ether/cyclohexane (water-in-oil) microemulsion system using NaBH_4 as a reducing agent, FeCl_2 as the Fe source, and H_2PtCl_6 as the Pt source.

2.2.4. Electrochemical Deposition Method. The electrochemical deposition method is widely used due to its simple equipment requirements and low cost and controllability of the particle properties. Using a single-tank system (relative electrode: Pt tablets; reference electrode: saturated calomel electrode; working electrode: plating conductive layer Si film), Fe/Pt multilayer films were prepared by Leistner et al. [35]. Then, L_{10} -phase FePt was obtained by heating the multilayer films to 600°C in H_2 .

3. Surface Functionalization of FePt Nanoparticles

As a rule, the MNPs for biomedical applications must have high chemical stability, excellent dispersion, and biocompatibility. Therefore, surface modifications, such as ligand additions, ligand exchange, chemical conjugation, and bioconjugation, become necessary. Good surface modification not only can effectively reduce the surface energy needed to obtain MNPs with excellent dispersion but also can improve the biocompatibility of the MNPs. Furthermore, introduction of reactive functional groups to the surface for further conjugation can produce multifunctional nanoparticles. The materials currently used for surface modification of MNPs include organic micromolecular compounds (e.g., 2-amino ethyl mercaptan, aspartic acid, glutamic acid, citric acid, phosphorus acid, vitamin B, and gamma cyclodextrin), organic polymer compounds (e.g., glucose, starch, polyethylene glycol (PEG), polyethyleneimine (PEI), polypeptides, proteins, and polyvinyl alcohol (PVA)), SiO_2 , and inorganic nanomaterials (e.g., Au). Among these substances, the characteristics and applications of some materials have been reported in the literature [36–38]. These materials can be attached to the surface of MNPs using ligand addition or ligand exchange [39].

Recently, great progress has been made in the study of FePt nanoparticle surface functionalization. By conducting ligand exchange from oleic acid to aminoethanethiol (AET), the AET-modified FePt nanoparticles showed excellent water-solubility [40] and no aggregation in stock dispersion [41]. Further bioconjugation with any antibody, peptide, or another nanoparticle can be achieved through ligand exchange. Chou et al. [21] conjugated cysteamine-FePt MNPs with an anti-Her2 antibody and confirmed that the modified nanoparticles for the imaging contrast had excellent biocompatibility and hemocompatibility. Employing cysteamine for ligand exchange, Chen et al. [42] obtained cysteamine surface functionalized FePt nanoparticles (fcc-FePt-A) with good biocompatibility and high chemical stability. Silica and (3-aminopropyl) triethoxysilane were also used in this study to functionalize the surface of FCC FePt nanoparticles. Similarly, the silica-coated and (3-aminopropyl) triethoxysilane surface-functionalized FCC FePt nanoparticles (fcc-FePt-silica-A) showed good biocompatibility and stability.

Using tetraglycol for surface modification, Yang et al. [43] obtained 4 nm FePt nanoparticles that could be engulfed by HeLa cells and cause the T_2 magnetic resonance signal to be significantly decreased.

3-Mercaptopropionic acid (MPA) has been employed to replace the original surfactants on the surface nanoparticles to form nanoparticles with carboxyl groups for further conjugation [44]. Chen et al. [44] used MPA to produce COOH-terminated, water-dispersible FePt nanoparticles. Then, after activating the COOH-FePt nanoparticles with N-ethyl-N 8-(dimethylaminopropyl)-carbodiimide (EDC), folic acid was used to conjugate to the previously produced nanoparticles. The final FePt nanoparticles had excellent biocompatibility and photothermal transduction efficiency.

Using a polyol method, Fuchigami et al. [45] utilized poly(diallyldimethylammonium chloride)- (PDDA-) modified silica particles as a template and produced PDDA-modified silica particles coated with FePt nanoparticles. Subsequently, they dissolved the silica particles in a NaOH solution to obtain FePt-nanoparticles/polycation hybrid capsules, which had a superior capacity to carry drugs and genes.

After introducing poly(L)lysine (PLL) to modify the surface of FePt-folate nanoparticles, PEG, HVGSSV peptide, and an Alexa fluor 750 fluorescent probe were successively conjugated to nanoparticles by Hariri et al. [46]. This multifunctional nanoparticle had good stability and biocompatibility and could potentially be applied for the radiation-guided targeting and imaging of tumors.

Liu et al. [47] used PEG to functionalize their synthesized FePt@Fe₂O₃ core-shell nanoparticles and conjugated folic acid to the surface of the FePt@Fe₂O₃-PEG nanoparticles. The final products were confirmed to be highly stable in diverse physiological solutions.

4. Biocompatibility and Safety

Good biocompatibility and lack of harm to the human body are prerequisites for FePt nanoparticle applications in clinical practice. The toxicity of FePt nanoparticles is a key factor to consider when estimating their potential in biomedicine. The *in vitro* cytotoxicity of FePt nanoparticles can be observed in diverse cell lines using colorimetric assays [48], and the kinetics and toxicology can be tested using *in vivo* animal experiments. In addition, to understand the *in vivo* toxicity of FePt nanoparticles, precise understanding of the *in vivo* biodistribution might be crucial.

Chen et al. [42] used an MTS assay to investigate the cytotoxicity of their synthesized fcc-FePt-A nanoparticles in A375M, MCF7, and U2OS cell lines. The result of their biocompatibility study showed that, after undergoing 168 hours of incubation, no cytotoxicity was observed at nanoparticle concentrations below 30 $\mu\text{g/mL}$.

Chou et al. [21] used an MTT assay, hemolysis test, and biodistribution analysis to evaluate the biocompatibility of their prepared 3, 6, and 12 nm FePt nanoparticles. The results showed no noticeable cytotoxicity (cell viability >90%) at Fe concentrations below 10 mM, and the cell viability was as high as 75% at the highest concentration of nanoparticles (100 mM). No significant hemolysis (<5%) occurred at 0.0001–100 mM Fe concentrations of FePt nanoparticles. Additionally, the biodistribution analysis in 6-week-old male C3H/HeN mice demonstrated that most of the particles

were mainly accumulated within the spleen followed by lung and liver and could be gradually removed from the organs with time (approximately one week). Among these three sizes of nanoparticles, the 12 nm FePt nanoparticles displayed the highest serum concentration and circulation half-life. And, the 3 nm-FePt had the highest brain concentration. These results of biocompatibility, hemocompatibility, and biodistribution make FePt nanoparticles potential vectors for *in vivo* applications.

Liu et al. [47] employed an MTT assay to evaluate the cytotoxicity of FePt@Fe₂O₃-PEG core-shell nanoparticles and the lactate dehydrogenase (LDH) leakage assay to determine the cell membrane integrity. The results revealed no noticeable cytotoxic response in KB cells, even at a high concentration (160 $\mu\text{g/mL}$), after 3 days of incubation and no clear cell membrane damage induced by the synthesized nanoparticles. Subsequently, they performed studies in mice to observe the potential toxicity of nanoparticles *in vivo*. For FePt@Fe₂O₃-PEG nanoparticle-treated mice, death and notable abnormalities were absent at the tested dose of 34 mg/kg of Fe for 20 days and no obvious damage, lesion, or inflammation in major organs was observed from Hematoxylin and Eosin (H&E) stained tissue slices. The results of various serum biochemistry analysis showed no notable hepatic toxicity or kidney dysfunction induced by nanoparticles. Compared with the control groups, the hematology analysis was not abnormal. The *in vitro* and *in vivo* studies indicated that their synthesized nanoparticles could be a promising multifunctional platform for MRI and targeted drug delivery.

Seemann et al. [49] used the trypan blue exclusion test to evaluate the cell viability of rat cortical astrocytes and applied flow cytometry (FCM) to assess the potential of the nanoparticles to induce apoptosis. The results indicated that the cell viability was not influenced at physiological concentrations of nanoparticles. They concluded that the high degree of biocompatibility, good dispersibility in aqueous solutions, and high magnetic susceptibility at room temperature made these magnetic core-shell nanoparticles potential tools for applications in cancer treatment.

Liang et al. [50] used an MTT assay to evaluate the cytotoxicity of their synthesized FePt-Cys nanoparticles in the ECV304, L929, and HEK293 cell lines. Compared to the control group, no striking differences in cell viability were observed in the FePt-Cys nanoparticle-treated group. After 72 h of treatment with FePt-Cys nanoparticles at a concentration of 100 $\mu\text{g/mL}$, the viability of ECV304 cells was approximately 110.2%, and no clear decrease in cell viability was observed in L929 cells or HEK293 cells. The good biocompatibility of FePt-Cys nanoparticles was revealed by this study.

Sahu et al. [51] employed an SRB assay to evaluate the cytotoxicity of PEGylated FePt-Fe₃O₄ composite nanoassemblies (CNAs) in the L929 and HeLa cell lines. After 24 h of incubation with CNAs at concentrations of up to 2.0 mg mL⁻¹, low cytotoxicity was observed in L929 cells, and more than 20% of the HeLa cells died. The results demonstrated that CNAs had no effect on cell proliferation of L929 cells but had toxic effects on HeLa cells.

Cytotoxicity studies of FePt nanoparticles that have been previously reported are shown in Table 1.

TABLE I: Cytotoxicity studies on FePt nanoparticles.

Material	Fe precursor	Surface coating	NP concentration	Cell line	Test	t (h)	Toxicity	Reference
FePt-SiO ₂ -A	Na ₂ Fe(CO) ₄	SiO ₂ shell	200 µg/mL ([Fe]: ~2 µg/mL)	A375M, MCF7, U2OS	MTS	168	V: no loss	[42]
FePt-A	Na ₂ Fe(CO) ₄	Cysteamine	30 µg/mL ([Fe]: ~5.3 µg/mL) 60 µg/mL ([Fe]: ~10.5 µg/mL)	A375M, MCF7, U2OS	MTS	168 72	V: no loss V: ~10% loss	[42]
FePt	Fe(CO) ₅	Cysteamine; conjugated with anti-Her2 antibody	[Fe]: 0.01–100 mM	Vero	MTT	24	V: >90% (below 10 mM); V: 75% (at 100 mM)	[21]
PEGylated FePt@Fe ₂ O ₃	Fe(CO) ₅	Fe ₂ O ₃ shell, PEG, FA	160 µg/mL	KB, HeLa, HL 7702	MTT LDH	24	No significant cytotoxicity No obvious cell membrane damage	[47]
FePt	Fe(CO) ₅	Folate-conjugated	5–100 µg/mL	EMT-6	MTT	24, 48	No adverse toxicity effects	[44]
SiW ₁₁ O ₃₉ -FePt	C ₁₀ H ₁₄ FeO ₄	Silicone-tungsten- oxide	0.015 mg/mL 0.25 mg/mL	Rat cortical brain astrocytes	Trypan blue exclusion, flow-cytometric annexin/PI apoptosis	24	V: 80%, a: 5.4% V: 23%, a: 28.5%	[49]
SiW _x O _y -FePt	C ₉ H ₉ FeO ₆	Hydrophilic SiW _x O _y first shell	0.015 mg/mL 0.25 mg/mL	Rat cortical brain astrocytes	Trypan blue exclusion, flow-cytometric annexin/PI apoptosis	24	V: 81%, a: 7.6% V: 35.7%, a: 26.2%	[49]
FePt-Cys	FeCl ₂ ·H ₂ O	L-Cysteine	100 µg/mL	ECV304, HEK293, L929	MTT	72	V: ~110.2% (ECV304); V: no obvious decrease (HEK293 or L929)	[50]
PEGylated FePt-Fe ₃ O ₄ composite nanoassemblies (CNAs)	FeCl ₂ ·4H ₂ O	Fe ₃ O ₄ , PEGylated	2.0 mg mL ⁻¹	L929, HeLa	SRB assay	24	Low cytotoxicity to L929; over 20% of HeLa cells died	[51]

NP is nanoparticle; t is the incubation time; [Fe] is the Fe concentration; D is the cell damage; V is the cell viability; a is the cell apoptosis.

5. Biomedical Applications of FePt Nanomaterials

After surface functionalization, FePt nanomaterials have been employed in biosensing, targeted drug delivery, MRI, fluorescence imaging, and therapy experiments. Some biomedical applications of functionalized FePt MNPs are shown in Figure 2.

5.1. FePt Nanoparticles as Contrast Agents in MRI. As a powerful noninvasive medical imaging technique, MRI is extensively used in clinical medicine. Its signal is mainly produced by the protons in the water molecules. By collecting the body's most abundant signal, the water molecule, high-quality soft tissue images, and high-resolution anatomical images can be obtained. Compared with computed tomography (CT) or X-rays, MRI has several advantages, such as no radiation and high spatial resolution. However, the sensitivity of MRI is still low. Therefore, in addition to designing a special pulse sequence, MRI contrast agents must be injected to improve the image contrast and sensitivity. MRI contrast agents are a class of material that can enhance the MRI signal contrast between normal and diseased tissues as well as within normal tissues. According to their different properties, MRI contrast agents are classified into two types: T_1 contrast agents, which mainly shorten the longitudinal relaxation time, and T_2 contrast agents, which mainly shorten the transverse relaxation time. The typical representatives of T_2 contrast agents include some superparamagnetic nanoparticles. Under an external magnetic field, the unpaired electrons spin and generate a local magnetic field, which can shorten the relaxation time of surrounding protons in the water molecules and can effectively shorten the T_2 time [52], resulting in a dark image and negative enhancement effect [53]. The contrast effect can be evaluated by the relaxivity (r_2). A higher r_2 value typically indicates a stronger contrast effect [13].

Due to their superior characteristics, FePt MNPs have recently been one of the hotspots in MRI research. Gao et al. [54] described FePt@Fe₂O₃ core-shell nanoparticles for MR imaging. Compared to MION ($r_2 = 2.778 (\mu\text{g}/\text{mL})^{-1} \text{s}^{-1}$) and Sinerem ($r_2 = 2.450 (\mu\text{g}/\text{mL})^{-1} \text{s}^{-1}$), commercial MRI contrast agents, as-synthesized FePt@Fe₂O₃ yolk-shell nanoparticles ($r_2 = 3.462 (\mu\text{g}/\text{mL})^{-1} \text{s}^{-1}$) exhibited stronger contrast enhancement and could act as a potential MRI contrast agent.

Chen et al. [42] investigated the effectiveness of fcc-FePt-A and fcc-FePt-silica-A nanoparticles as MRI contrast agents. The r_2 values were $887 \text{ mM}^{-1} \cdot \text{s}^{-1}$ and $210 \text{ mM}^{-1} \cdot \text{s}^{-1}$ for fcc-FePt-A and fcc-FePt-silica-A nanoparticles, respectively, in the MRI magnetic field (7 T), whereas the r_2 value of commercial Feridex was $148 \text{ mM}^{-1} \cdot \text{s}^{-1}$. Their work demonstrated that the FePt-based T_2 contrast agents were superior to commercial Feridex with respect to MRI contrast enhancement.

Chou et al. [21] synthesized size-tunable superparamagnetic FePt nanoparticles and investigated their potential as a dual-modality contrast agent for CT/MRI. Their studies showed that superparamagnetic FePt nanoparticles could enhance shortening of the T_2 of proton relaxation and produce efficient CT contrast enhancement. In a further in

vivo imaging experiment, selective contrast enhancement of Her2/neu overexpression cancer lesions was achieved in both CT and MRI in tumor-bearing animals injected with nanoparticles.

At 4.7 Tesla, the relaxivities of the SIPPs prepared by Taylor et al. [55] were higher than commercial SPIONs. The relaxivities were 62.2 and 21.37 Hz/mM Fe for SIPPs and SPIONs, respectively. The results indicated that the SIPPs may be superior T_2 -weighted MRI contrast agents.

5.2. Fluorescence Imaging Probes. The so-called fluorescent nanoparticles refer to a variety of nanoparticles with fluorescent properties. Fluorescent nanoparticles can be sorted into two types according to the light-emitting principle. One type can emit fluorescence after it is excited by external energy, for example, semiconductor nanocrystals with unique optical and electronic properties, also known as quantum dots (quantum dot, QD). The other type can emit fluorescence after exposure to a labeled fluorescent substance, for example, fluorescent magnetic nanoparticles and quantum dots wrapped silica nanoparticles. Both particles can achieve highly sensitive detection of biological molecules, such as nucleic acids, proteins, and pathogenic microorganisms. Based on the advantages of strong fluorescence emission and antiphotobleaching, fluorescent nanoparticles may also be a promising fluorescence imaging marker.

In recent years, many scholars have prepared fluorescent magnetic nanospheres using FePt nanoparticles. Gu et al. [56] prepared composite nanoparticles containing FePt nanoparticles and amorphous CdS (semiconductor colloids (quantum dots)). These nanoparticles were less than 10 nm in diameter and exhibited good superparamagnetism and fluorescence. Using a one-pot synthesis procedure, Gao et al. [57] obtained superparamagnetic FePt@CdX core-shell nanocrystals ($X = \text{S}$ or Se), which could show fluorescence with quantum yields of 2.3–9.7%.

Using the fluorescent dye NOPS to label magnetic FePt core-shell nanoparticles, Seemann and Kuhn [58] observed the fluorescence of these labeled nanoparticles in ethanol (EtOH) and the bright luminescence of the magnetic core-shell nanoparticles (containing labeled and unlabeled particles) with multiphoton excitation (cf. Figure 3). They reported that these bright magnetic core-shell nanoparticles could be employed for in vivo multiphoton imaging in the mouse neocortex as far inward as cortical layer 5.

Taylor et al. [59] encapsulated superparamagnetic FePt nanoparticles with PEGylated phospholipids to generate stealth immunomicelles that could be specifically targeted to human prostate cancer cells and detected by MRI and fluorescence imaging.

These multifunctional FePt nanoparticles with both magnetic and fluorescent properties may be used for multimodal imaging for the diagnosis of diseases.

5.3. Photothermal Therapy. Photothermal therapy is an emerging treatment modality for cancer. By using near-infrared (NIR) light to locally irradiate tumor cells, the light energy can be transformed into heat energy, which can

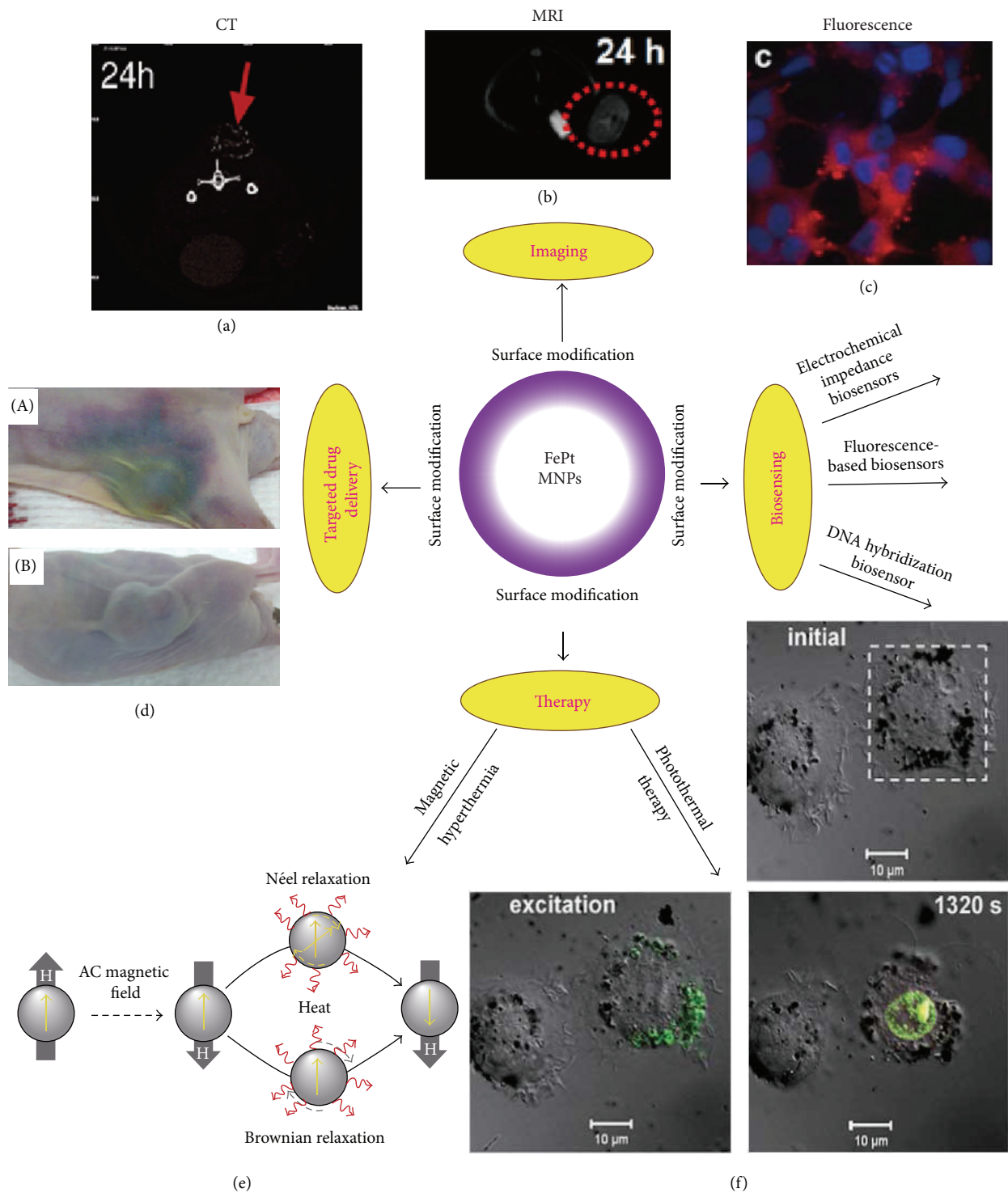


FIGURE 2: Biomedical applications of functionalized FePt MNPs: (a) a CT image of the MBT2 tumor-bearing mice 24 h after being injected with anti-Her2 antibody-FePt nanoparticles [21]; (b) T_2 -weighted MRI of KB tumor-bearing nude mice 24 h after being injected with FePt@Fe₂O₃-PEG-FA nanoparticles [47]; (c) fluorescence image of C4-2 PSMA-positive after 10 min of incubation with J591-DSPE-SIPPs [59]; (d) extensive hematoma around the tumors on PTX alone injected mice (A), no such side effect on mice injected with J591-SPMs (B) [1]; (e) the principle of magnetic heat induction [2]; (f) photothermolysis images of the EMT-6 cancer cell induced by FePt nanoparticles under $10 \text{ mJ}/\text{cm}^2$ [44].

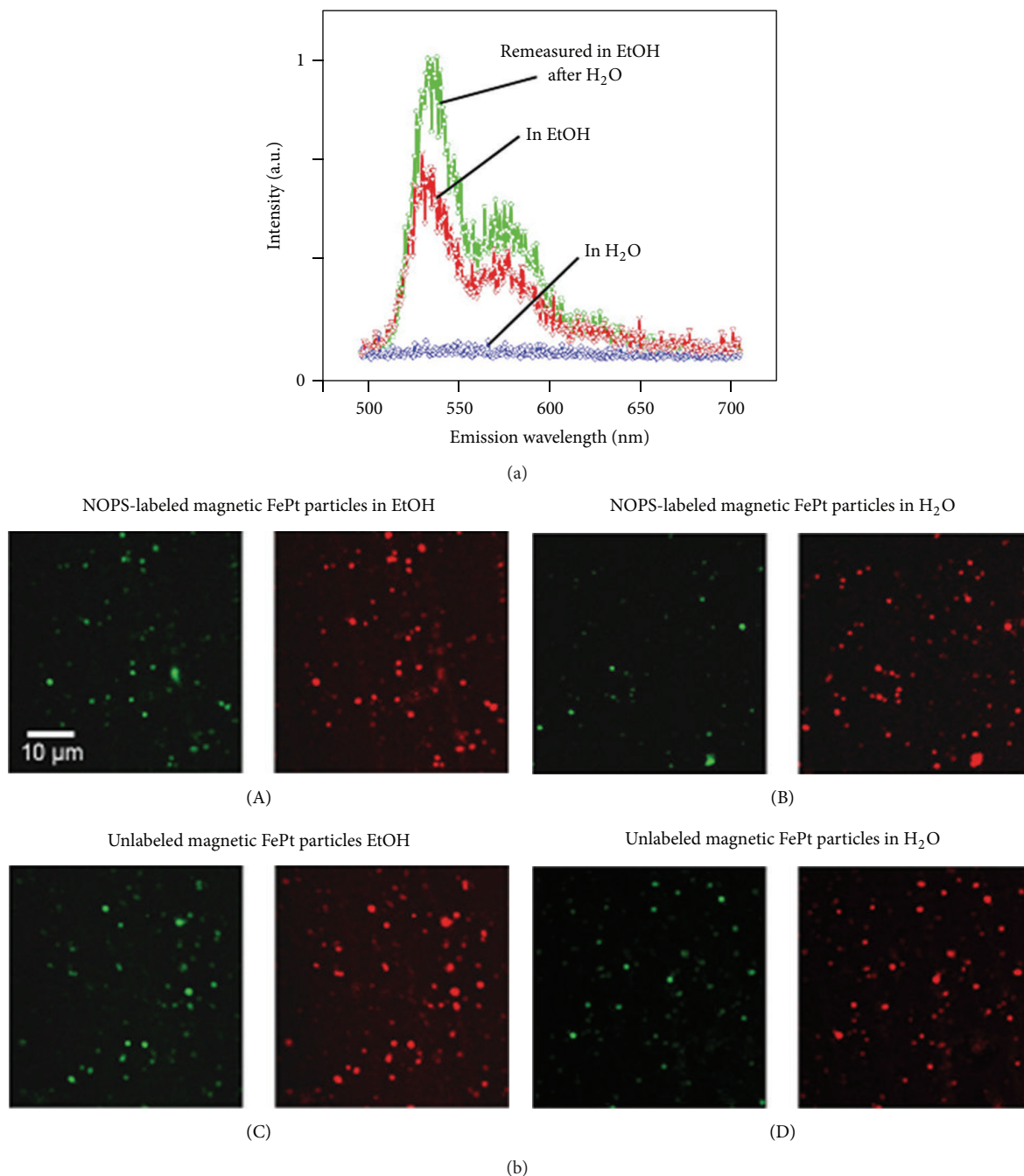


FIGURE 3: Fluorescence data (a) of the NOPS-labeled FePt nanoparticles (1-photon excitation, wavelength: 488 nm). Bright luminescence (b) of the NOPS-labeled and unlabeled FePt core-shell nanoparticles (multiphoton excitation, two wavelength intervals (green: bandpass 490 nm–560 nm, red: bandpass 570 nm–640 nm)) [58].

degenerate tumor cells and cause necrosis at a certain temperature. Due to the performance of strongly absorbing NIR light, nanometer material can be applied for photothermal treatment of tumor cells after surface functionalization. This process is illustrated in Figure 4 [44].

The photothermal effect of folate functionalized FePt nanoparticles activated by a NIR femtosecond laser has been examined by Chen et al. [44]. Due to their superior photothermal transduction efficiency, these nanoparticles can be

heated up to several hundred degrees Celsius in picoseconds under laser irradiation. The threshold laser energy required to damage EMT-6 cells was comparable to that of previously reported gold nanoparticles. These findings suggest various applications for FePt nanoparticles in targeted cancer therapy.

5.4. Magnetic Carriers for Targeted Drug Delivery. MNPs are commonly used as vectors for encapsulated drugs or other therapeutic agents for targeted therapy. After specific target

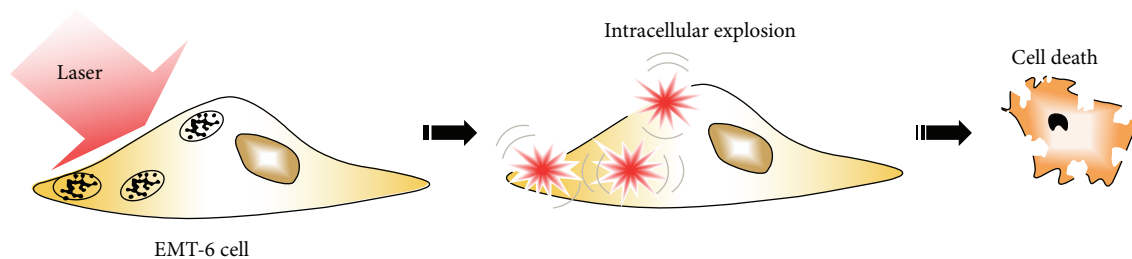


FIGURE 4: An illustration of photothermal lysis of tumor cells mediated by laser-activated MNPs [44].

molecules are conjugated to the surface, these drug-loaded nanoparticles can enter target cells. As a result, targeted drug treatment can be achieved. Taylor and Sillerud [1] encapsulated paclitaxel into SIPPs to produce multifunctional SIPP-PTX micelles (SPMs). Subsequently, they combined SPMs with an antibody against a prostate-specific membrane antigen (PSMA) for the specific targeting, MRI, and therapy of human prostate cancer-bearing mice. The results showed that PSMA-targeted SPMs could effectively prevent C4-2 prostate cancer xenografts from growing in nude mice. In addition, compared to nontargeted SPM-injected and paclitaxel-injected mice, more paclitaxel and platinum was observed in tumors in mice injected with PSMA-targeted SPMs.

Due to the superior magnetic response, MNP carriers may be collected in the lesion under an external magnetic field to achieve targeted drug delivery. Fuchigami et al. [60] performed in vitro application of porous FePt capsules in a magnetically targeted drug delivery system. After the introduction of an anticancer drug and coating with a lipid membrane to avoid leaking of the agents, the magnetic capsules arrived at lung cancer cells and gastric cancer cells within 15 min under a NdFeB magnet (0.2 T), resulting in greater than 70% cancer cell death. As magnetic carriers, FePt magnetic capsules could be effectively utilized for drug delivery systems.

The pH value of tumor interstitial fluid is lower than that of normal tissue. In a low-pH environment, nanoparticles wrapped with pH sensitive lipids can increase the rate of drug release. This is favorable for the application of multifunctional FePt nanomaterials for drug delivery and controlled release [47]. Liu et al. [47] prepared DOX loaded FePt@Fe₂O₃-PEG-FA nanoparticles and incubated them in buffers with pH values of 7.4 and 5.0 to assess their drug release behaviors. After 24 h of incubation, they observed approximately 1.5% DOX release at pH 7.4 and approximately 20% DOX release at pH 5.0, indicating accelerated release at a lower pH value.

5.5. Biosensors. The biosensor is an analytical device that can identify, convert, and detect various substances, such as enzymes, nucleic acids, antibodies, and antigens. Due to their advantages of surface effects, small size effect, quantum size effect, macroscopic quantum tunneling effect, and quantum confinement effect, nanomaterials are attractive prospects for biosensor applications.

Through modification, carbon-decorated FePt nanoparticles have been used as new ultra-high-resolution DNA

electrochemical impedance biosensors that can improve the detection of the PML-RARA fusion gene in acute promyelocytic leukemia [61]. Amide ligand-modified FePt/carbon nanotube (CNT) nanocomposite paste electrodes have been employed for the simultaneous determination of tryptophan (Trp), glutathione (GSH), and nicotinamide adenine dinucleotide (NADH) levels [62]. The modified N-(4-hydroxyphenyl)-3, 5-dinitrobenzamide-FePt/CNTs carbon paste electrode can be used as a highly sensitive biosensor to simultaneously determine GSH and piroxicam (PXM) levels [63]. FePt nanoparticles with three different compositions (Fe₂₅Pt₇₅, Fe₃₀Pt₇₀, and Fe₃₅Pt₆₅) displayed higher electrocatalytic activity than Pt nanoparticles for vitamin C electrooxidation [64]. The linear range, sensitivity, and detection limit of the Fe₃₀Pt₇₀ NPs/Si nanowire sensors were 0.01–1 mM, 4.347 mA cm⁻² mM⁻¹, and 0.1 μM (S/N = 3), respectively. The sensitivity was more than 10-fold higher than the best performance that has been previously reported for sensor materials (e.g., Pd nanowires: 166.5 μA cm⁻² mM⁻¹). These FePt nanoparticles could be a superior sensing material for a fast-response vitamin C sensor. Recently, researchers have employed FePt nanoparticles for arsenic detection. Among FePt, FeAu, and FePd nanoparticles, the FePt nanoparticles (detection limit: 1.2 ppb; sensitivity: 1.23 μA ppb⁻¹) showed the best performance and might be an effective, high-performance electrochemical sensor for the detection of ultratrace quantities of arsenic [65].

5.6. Magnetic Fluid Hyperthermia (MFH)/Magnetic Hyperthermia (MH). Using arteriovenous or direct injection, magnetic fluid modified by a specific antibody can selectively penetrate tumor tissue or cells. Under an external alternating magnetic field (AMF), the magnetic fluid in tumor tissue or cells is heated through the main mechanisms of Brownian and Néel relaxation, and then the produced heat kills the tumor. This process is called MFH or MH. This therapy is highly specific; that is, only tissue or cells with MNPs can be heated and killed, whereas the surrounding normal tissues without MNPs are not subject to thermal damage. Simultaneously, this therapy also successfully resolves the difficulty of temperature control in hyperthermia. Generally, tumor cells are more likely to die at temperatures ranging from 39 to 45°C [66]. The MH effect is related to the size, Curie temperature and magnetization of the particles, the intensity and frequency of AMF, and the heat dissipation from the tumor [67].

The use of FePt nanoparticles as a medium for MH has been explored in the last two decades. Marnosono and Saita [66] reported a theoretical assessment of MH using fcc FePt MNPs. These fcc FePt MNPs displayed great superiority to magnetite, maghemite, FeCo, and $L1_0$ FePt MNPs in MH. At $H_0 = 50$ mT and $f = 300$ kHz, the energy dissipation of 9 nm fcc FePt MNPs was $P = 3.97 \times 10^5$ W/m, while the energy dissipation of 19 nm magnetite MNPs was only $P = 1.95 \times 10^5$ W/m.

Seemann et al. [49] successfully demonstrated the magnetocaloric heating effect of as-synthesized tungsten-oxide coated biocompatible FePt core-shell nanoparticles. An approximately 3°C increase in the aqueous suspension was recorded after 15 min in an 831 kHz high-frequency AMF of 250 Gauss field strength (25 mT) at a moderate nanoparticle concentration (0.5 mg/mL).

Hyperthermia combined with ionizing radiation could enhance the tumor damage and thereby enhance the therapeutic effect. Seemann et al. [49] reported that their designed novel nanoparticles had a convenient decay time. Utilization of cold neutrons could activate the content of tungsten atoms in the nanoparticles, resulting in a transformation into the radioisotope W-187, which could provide potentially beneficial 1.3 MeV kinetic energy β -radiation. The specific activity value reached 0.6 MBq/mg. These features make these FePt core-shell nanoparticles promising candidates for advanced radiopharmaceutical applications.

Sahu et al. [51] found that the CNAs with a concentration of 2 mg mL^{-1} could produce a hyperthermic temperature of approximately 43°C . They investigated the MH therapeutic effect of CNAs on HeLa cells. The results demonstrated that approximately $53 \pm 2.1\%$ of HeLa cells were alive after treatment with 2 mg mL^{-1} of CNAs in presence of an alternating current magnetic field (ACMF) ($f = 250$ kHz, applied field = 460 Oe), and less than 20% of HeLa cells were alive after incubation with CNAs + DOX in the presence of an ACMF, whereas the control cells without an ACMF showed no obvious decrease in cell viability. Their work showed that DOX loaded CNAs could produce more damage in HeLa cells in hyperthermic conditions.

5.7. Anticancer Agents. Studies have shown that FePt MNPs can suppress the proliferation of some cancer cells. Gao et al. [68] reported that, according to an MTT assay, FePt@CoS₂ yolk-shell nanocrystals showed an IC₅₀ of 35.5 ± 4.7 ng of Pt/mL in HeLa cells, which was considerably lower than that of cisplatin (230 ng of Pt/mL). This abnormally high toxicity might suggest that these FePt@CoS₂ yolk-shell nanocrystals could be a new anticancer nanomedicine. Xu et al. [69] reported that FePt nanoparticles functionalized with the *luteinizing hormone-releasing hormone (LHRH)* peptide could take precedence in binding to A2780 and suppress the proliferation of these tumor cells. Their work demonstrated that these functionalized FePt nanoparticles could be a new agent for controlled cancer therapy. Sun et al. [70] observed that oleic acid/oleylamine-coated FePt nanoparticles could notably suppress the proliferation of U251, U87, and H4 glioma cell lines in time- and dose-dependent manners. Their

work demonstrated that surface-coated FePt nanoparticles could potentially be used as novel therapeutic agents for malignant gliomas.

6. Future Perspectives

Many methods have been used to prepare FePt MNPs. However, the technology used must be further improved to produce FePt nanoparticles to obtain nanoparticles with more controllable and uniform sizes and increased stability. To improve their biocompatibility and application for biomedicine, FePt MNPs require further surface modifications and functionalization with organic functional groups or heterostructures. FePt MNP applications in the biomedical field are increasing and include MRI contrast enhancement, biosensors, and magnetic carriers for targeted drug delivery systems. However, most studies are still in the laboratory phase and far from clinical application. Moreover, the research period has not been sufficiently long to determine the long-term efficacy, toxicity, and metabolism of FePt MNPs in vivo. In addition, other applications in biomedicine, including their use as gene transfer vectors and radionuclide carriers and in MFH, need to be further explored.

However, with further research of FePt MNP technology and the further development of nanomaterial science, larger-scale experimental and clinical studies on FePt MNPs and their application are expected to be conducted, which will play a greater role in biomedicine.

Conflict of Interests

The authors declare that they have no conflict of interests in this work.

Acknowledgments

The work is financially supported by the National Natural Science Foundation, China (21373034); the 333 Plan Foundation of Jiangsu, China (BRA2014183); the Six Talents Peak Foundation of Jiangsu, China (2011-WS-023); the Key Talent's Foundation in Science and Education of Jiangsu, China (RC2011212); the Specially Hired Professorship-Funding of Jiangsu province (SCZ1211400001); Social Development Plan of Taizhou (TS201345); Changzhou Sci & Tech Program for Changzhou Key Laboratory of Respiratory Medical Engineering (CM20133005); and Changzhou Science and Technology Bureau for Changzhou Key Laboratory of Respiratory Medical Engineering (CM20133005). The authors also sincerely appreciate Key Laboratory of Fine Petrochemical Engineering and PAPD of Jiangsu Higher Education Institutions for giving supports for this work.

References

- [1] R. M. Taylor and L. O. Sillerud, "Paclitaxel-loaded iron platinum stealth immunomicelles are potent MRI imaging agents that prevent prostate cancer growth in a PSMA-dependent manner,"

- International Journal of Nanomedicine*, vol. 7, pp. 4341–4352, 2012.
- [2] J.-H. Lee, J.-W. Kim, and J. Cheon, “Magnetic nanoparticles for multi-imaging and drug delivery,” *Molecules and Cells*, vol. 35, no. 4, pp. 274–284, 2013.
- [3] M. Lin, J. Huang, and M. Sha, “Recent advances in nanosized Mn-Zn ferrite magnetic fluid hyperthermia for cancer treatment,” *Journal of Nanoscience and Nanotechnology*, vol. 14, no. 1, pp. 792–802, 2014.
- [4] S. Laurent, D. Forge, M. Port et al., “Magnetic iron oxide nanoparticles: synthesis, stabilization, vectorization, physico-chemical characterizations and biological applications,” *Chemical Reviews*, vol. 108, no. 6, pp. 2064–2110, 2008.
- [5] F. M. Kievit, Z. R. Stephen, O. Veisoh et al., “Targeting of primary breast cancers and metastases in a transgenic mouse model using rationally designed multifunctional SPIONs,” *ACS Nano*, vol. 6, no. 3, pp. 2591–2601, 2012.
- [6] Wahajuddin and S. Arora, “Superparamagnetic iron oxide nanoparticles: magnetic nanoplateforms as drug carriers,” *International Journal of Nanomedicine*, vol. 7, pp. 3445–3471, 2012.
- [7] R. T. Branca, Z. I. Cleveland, B. Fubara et al., “Molecular MRI for sensitive and specific detection of lung metastases,” *Proceedings of the National Academy of Sciences of the United States of America*, vol. 107, no. 8, pp. 3693–3697, 2010.
- [8] K. Andreas, R. Georgieva, M. Ladwig et al., “Highly efficient magnetic stem cell labeling with citrate-coated superparamagnetic iron oxide nanoparticles for MRI tracking,” *Biomaterials*, vol. 33, no. 18, pp. 4515–4525, 2012.
- [9] M. Mahmoudi, M. A. Sahraian, M. A. Shokrgozar, and S. Laurent, “Superparamagnetic iron oxide nanoparticles: promises for diagnosis and treatment of multiple sclerosis,” *ACS Chemical Neuroscience*, vol. 2, no. 3, pp. 118–140, 2011.
- [10] A. S. Arbab, B. Janic, J. Haller, E. Pawelczyk, W. Liu, and J. A. Frank, “In vivo cellular imaging for translational medical research,” *Current Medical Imaging Reviews*, vol. 5, no. 1, pp. 19–38, 2009.
- [11] C. Xu, D. Miranda-Nieves, J. A. Ankrum et al., “Tracking mesenchymal stem cells with iron oxide nanoparticle loaded poly(lactide-co-glycolide) microparticles,” *Nano Letters*, vol. 12, no. 8, pp. 4131–4139, 2012.
- [12] E. Y. Egawa, N. Kitamura, R. Nakai, Y. Arima, and H. Iwata, “A DNA hybridization system for labeling of neural stem cells with SPIO nanoparticles for MRI monitoring post-transplantation,” *Biomaterials*, vol. 54, pp. 158–167, 2015.
- [13] D. Ho, X. Sun, and S. Sun, “Monodisperse magnetic nanoparticles for theranostic applications,” *Accounts of Chemical Research*, vol. 44, no. 10, pp. 875–882, 2011.
- [14] S.-W. Chou, C.-L. Zhu, S. Neeleshwar, G.-L. Chen, Y.-Y. Chen, and C.-C. Chen, “Controlled growth and magnetic property of fept nanostructure: cuboctahedron, octapod, truncated cube, and cube,” *Chemistry of Materials*, vol. 21, no. 20, pp. 4955–4961, 2009.
- [15] Y. F. Xu, M. L. Yan, and D. J. Sellmyer, “FePt nanocluster films for high-density magnetic recording,” *Journal of Nanoscience and Nanotechnology*, vol. 7, no. 1, pp. 206–224, 2007.
- [16] B. Zhang and W. A. Soffa, “Structure and properties of rapidly-solidified iron-platinum and iron-palladium alloys,” *IEEE Transactions on Magnetics*, vol. 26, no. 5, pp. 1388–1390, 1990.
- [17] D. Weller and A. Moser, “Thermal effect limits in ultrahigh-density magnetic recording,” *IEEE Transactions on Magnetics*, vol. 35, no. 6, pp. 4423–4439, 1999.
- [18] A. Martins, M. C. A. Fantini, N. M. Souza-Neto, A. Y. Ramos, and A. D. Santos, “Alternate monatomic layer sputter deposition of FCT (L₁₀-type) ordered FePt and CoPt films,” *Journal of Magnetism and Magnetic Materials*, vol. 305, no. 1, pp. 152–156, 2006.
- [19] J. Lyubina, O. Gutfleisch, R. Skomski, K.-H. Müller, and L. Schultz, “Phase transformations and thermodynamic properties of nanocrystalline FePt powders,” *Scripta Materialia*, vol. 53, no. 4, pp. 469–474, 2005.
- [20] D. Weller, A. Moser, L. Folks et al., “High K_u materials approach to 100 Gbits/in²,” *IEEE Transactions on Magnetics*, vol. 36, no. 1, pp. 10–15, 2000.
- [21] S.-W. Chou, Y.-H. Shau, P.-C. Wu, Y.-S. Yang, D.-B. Shieh, and C.-C. Chen, “In vitro and in vivo studies of fept nanoparticles for dual modal CT/MRI molecular imaging,” *Journal of the American Chemical Society*, vol. 132, no. 38, pp. 13270–13278, 2010.
- [22] X. Jiang, S. Weise, M. Hafner et al., “Quantitative analysis of the protein corona on FePt nanoparticles formed by transferrin binding,” *Journal of the Royal Society Interface*, vol. 7, supplement 1, pp. S5–S13, 2010.
- [23] N. H. Hai, N. M. Dempsey, M. Veron, M. Verdier, and D. Givord, “An original route for the preparation of hard FePt,” *Journal of Magnetism and Magnetic Materials*, vol. 257, no. 2-3, pp. L139–L145, 2003.
- [24] D. Weller, O. Mosendz, G. Parker, S. Pisana, and T. S. Santos, “L₁₀ FePtX-Y media for heat-assisted magnetic recording,” *Physica Status Solidi (A)*, vol. 210, no. 7, pp. 1245–1260, 2013.
- [25] Y. F. Ding, J. S. Chen, E. Liu, B. C. Lim, J. F. Hu, and B. Liu, “Effect of carbon additive on microstructure evolution and magnetic properties of epitaxial FePt (001) thin films,” *Thin Solid Films*, vol. 517, no. 8, pp. 2638–2647, 2009.
- [26] M. Yu, H. Ohguchi, A. Zambano et al., “Orientation and magnetic properties of FePt and CoPt films grown on MgO(1 1 0) single-crystal substrate by electron-beam coevaporation,” *Materials Science and Engineering B*, vol. 142, no. 2-3, pp. 139–143, 2007.
- [27] L. Castaldi, K. Giannakopoulos, A. Travlos et al., “Engineering of FePt nanoparticles by e-beam co-evaporation,” *Nanotechnology*, vol. 19, no. 13, Article ID 135702, 2008.
- [28] S. Sun, C. B. Murray, D. Weller, L. Folks, and A. Moser, “Monodisperse FePt nanoparticles and ferromagnetic FePt nanocrystal superlattices,” *Science*, vol. 287, no. 5460, pp. 1989–1992, 2000.
- [29] H. B. Wang, H. Wang, J. Zhang, F. J. Yang, Y. M. Xu, and Q. Li, “Study on composition distribution and ferromagnetism of monodisperse fept nanoparticles,” *Nanoscale Research Letters*, vol. 5, no. 3, pp. 489–493, 2010.
- [30] B. Bian, W. Xia, J. Du et al., “Growth mechanisms and size control of FePt nanoparticles synthesized using Fe(CO)_x (x < 5)-oleylamine and platinum(II) acetylacetonate,” *Nanoscale*, vol. 5, no. 6, pp. 2454–2459, 2013.
- [31] R. M. Taylor, T. C. Monson, and R. R. Gullapalli, “Influence of carbon chain length on the synthesis and yield of fatty amine-coated iron-platinum nanoparticles,” *Nanoscale Research Letters*, vol. 9, no. 1, article 306, 2014.
- [32] F. Zhao, M. Rutherford, S. Y. Grisham, and X. Peng, “Formation of monodisperse FePt alloy nanocrystals using air-stable precursors: fatty acids as alloying mediator and reductant for Fe 3+ Precursors,” *Journal of the American Chemical Society*, vol. 131, no. 14, pp. 5350–5358, 2009.

- [33] N. K. Sahu, A. Prakash, and D. Bahadur, "Role of different platinum precursors on the formation and reaction mechanism of FePt nanoparticles and their electrocatalytic performance towards methanol oxidation," *Dalton Transactions*, vol. 43, no. 12, pp. 4892–4900, 2014.
- [34] K. M. Hyie and I. I. Yaacob, "Preparation of iron-platinum nanoparticles in water/triton/cyclohexane microemulsions," *Journal of Materials Processing Technology*, vol. 191, no. 1–3, pp. 48–50, 2007.
- [35] K. Leistner, S. Fähler, H. Schlörb, and L. Schultz, "Preparation and characterization of electrodeposited Fe/Pt multilayers," *Electrochemistry Communications*, vol. 8, no. 6, pp. 916–920, 2006.
- [36] M. Mahmoudi, S. Sant, B. Wang, S. Laurent, and T. Sen, "Superparamagnetic iron oxide nanoparticles (SPIONs): development, surface modification and applications in chemotherapy," *Advanced Drug Delivery Reviews*, vol. 63, no. 1–2, pp. 24–46, 2011.
- [37] L. Li, W. Jiang, K. Luo et al., "Superparamagnetic iron oxide nanoparticles as MRI contrast agents for non-invasive stem cell labeling and tracking," *Theranostics*, vol. 3, no. 8, pp. 595–615, 2013.
- [38] E. Amstad, M. Textor, and E. Reimhult, "Stabilization and functionalization of iron oxide nanoparticles for biomedical applications," *Nanoscale*, vol. 3, no. 7, pp. 2819–2843, 2011.
- [39] C. Xu and S. Sun, "Superparamagnetic nanoparticles as targeted probes for diagnostic and therapeutic applications," *Dalton Transactions*, no. 29, pp. 5583–5591, 2009.
- [40] Y. Tanaka and S. Maenosono, "Amine-terminated water-dispersible FePt nanoparticles," *Journal of Magnetism and Magnetic Materials*, vol. 320, no. 19, pp. L121–L124, 2008.
- [41] S. Maenosono, R. Yoshida, and S. Saita, "Evaluation of genotoxicity of amine-terminated water-dispersible FePt nanoparticles in the Ames test and in vitro chromosomal aberration test," *The Journal of Toxicological Sciences*, vol. 34, no. 3, pp. 349–354, 2009.
- [42] S. Chen, L. Wang, S. L. Duce et al., "Engineered biocompatible nanoparticles for *in vivo* imaging applications," *Journal of the American Chemical Society*, vol. 132, no. 42, pp. 15022–15029, 2010.
- [43] H. Yang, J. Zhang, Q. Tian et al., "One-pot synthesis of amphiphilic superparamagnetic FePt nanoparticles and magnetic resonance imaging *in vitro*," *Journal of Magnetism and Magnetic Materials*, vol. 322, no. 8, pp. 973–977, 2010.
- [44] C.-L. Chen, L.-R. Kuo, S.-Y. Lee et al., "Photothermal cancer therapy via femtosecond-laser-excited FePt nanoparticles," *Biomaterials*, vol. 34, no. 4, pp. 1128–1134, 2013.
- [45] T. Fuchigami, R. Kawamura, Y. Kitamoto, M. Nakagawa, and Y. Namiki, "Ferromagnetic FePt-nanoparticles/polycation hybrid capsules designed for a magnetically guided drug delivery system," *Langmuir*, vol. 27, no. 6, pp. 2923–2928, 2011.
- [46] G. Hariri, M. S. Wellons, W. H. Morris III, C. M. Lukehart, and D. E. Hallahan, "Multifunctional FePt nanoparticles for radiation-guided targeting and imaging of cancer," *Annals of Biomedical Engineering*, vol. 39, no. 3, pp. 946–952, 2011.
- [47] Y. Liu, K. Yang, L. Cheng et al., "PEGylated FePt@Fe₂O₃ core-shell magnetic nanoparticles: potential theranostic applications and *in vivo* toxicity studies," *Nanomedicine: Nanotechnology, Biology and Medicine*, vol. 9, no. 7, pp. 1077–1088, 2013.
- [48] N. Lewinski, V. Colvin, and R. Drezek, "Cytotoxicity of nanoparticles," *Small*, vol. 4, no. 1, pp. 26–49, 2008.
- [49] K. M. Seemann, M. Luysberg, Z. Révay et al., "Magnetic heating properties and neutron activation of tungsten-oxide coated biocompatible FePt core-shell nanoparticles," *Journal of Controlled Release*, vol. 197, pp. 131–137, 2015.
- [50] S. Liang, Q. Zhou, M. Wang, Y. Zhu, Q. Wu, and X. Yang, "Water-soluble l-cysteine-coated FePt nanoparticles as dual MRI/CT imaging contrast agent for glioma," *International Journal of Nanomedicine*, vol. 10, pp. 2325–2333, 2015.
- [51] N. K. Sahu, J. Gupta, and D. Bahadur, "PEGylated FePt-Fe₃O₄ composite nanoassemblies (CNAs): *in vitro* hyperthermia, drug delivery and generation of reactive oxygen species (ROS)," *Dalton Transactions*, vol. 44, no. 19, pp. 9103–9113, 2015.
- [52] Y.-W. Jun, J.-W. Seo, and J. Cheon, "Nanoscaling laws of magnetic nanoparticles and their applicabilities in biomedical sciences," *Accounts of Chemical Research*, vol. 41, no. 2, pp. 179–189, 2008.
- [53] Y.-W. Jun, J.-H. Lee, and J. Cheon, "Chemical design of nanoparticle probes for high-performance magnetic resonance imaging," *Angewandte Chemie*, vol. 47, no. 28, pp. 5122–5135, 2008.
- [54] J. Gao, G. Liang, J. S. Cheung et al., "Multifunctional yolk-shell nanoparticles: a potential MRI contrast and anticancer agent," *Journal of the American Chemical Society*, vol. 130, no. 35, pp. 11828–11833, 2008.
- [55] R. M. Taylor, D. L. Huber, T. C. Monson, V. Esch, and L. O. Sillerud, "Structural and magnetic characterization of superparamagnetic iron platinum nanoparticle contrast agents for magnetic resonance imaging," *Journal of Vacuum Science and Technology B: Nanotechnology and Microelectronics*, vol. 30, no. 2, Article ID 02C101, 2012.
- [56] H. Gu, R. Zheng, X. Zhang, and B. Xu, "Facile one-pot synthesis of bifunctional heterodimers of nanoparticles: a conjugate of quantum dot and magnetic nanoparticles," *Journal of the American Chemical Society*, vol. 126, no. 18, pp. 5664–5665, 2004.
- [57] J. Gao, B. Zhang, Y. Gao, Y. Pan, X. Zhang, and B. Xu, "Fluorescent magnetic nanocrystals by sequential addition of reagents in a one-pot reaction: a simple preparation for multifunctional nanostructures," *Journal of the American Chemical Society*, vol. 129, no. 39, pp. 11928–11935, 2007.
- [58] K. M. Seemann and B. Kuhn, "Multi-photon excited luminescence of magnetic FePt core-shell nanoparticles," *Biomedical Optics Express*, vol. 5, no. 7, pp. 2446–2457, 2014.
- [59] R. M. Taylor, D. L. Huber, T. C. Monson, A.-M. S. Ali, M. Bisoffi, and L. O. Sillerud, "Multifunctional iron platinum stealth immunomicelles: targeted detection of human prostate cancer cells using both fluorescence and magnetic resonance imaging," *Journal of Nanoparticle Research*, vol. 13, no. 10, pp. 4717–4729, 2011.
- [60] T. Fuchigami, R. Kawamura, Y. Kitamoto, M. Nakagawa, and Y. Namiki, "A magnetically guided anti-cancer drug delivery system using porous FePt capsules," *Biomaterials*, vol. 33, no. 5, pp. 1682–1687, 2012.
- [61] L. Wang, X. Zheng, W. Zhang et al., "One-pot synthesis of carbon-decorated FePt nanoparticles and their application for label-free electrochemical impedance sensing of DNA hybridization," *RSC Advances*, vol. 3, no. 23, pp. 9042–9046, 2013.
- [62] R. Moradi, S. A. Sebt, H. Karimi-Maleh et al., "Synthesis and application of FePt/CNTs nanocomposite as a sensor and novel amide ligand as a mediator for simultaneous determination

- of glutathione, nicotinamide adenine dinucleotide and tryptophan,” *Physical Chemistry Chemical Physics*, vol. 15, no. 16, pp. 5888–5897, 2013.
- [63] H. Karimi-Maleh, F. Tahernejad-Javazmi, A. A. Ensafi, R. Moradi, S. Mallakpour, and H. Beitollahi, “A high sensitive biosensor based on FePt/CNTs nanocomposite/*N*-(4-hydroxyphenyl)-3,5-dinitrobenzamide modified carbon paste electrode for simultaneous determination of glutathione and piroxicam,” *Biosensors & Bioelectronics*, vol. 60, pp. 1–7, 2014.
- [64] N. Moghimi and K. T. Leung, “FePt alloy nanoparticles for biosensing: enhancement of vitamin C sensor performance and selectivity by nanoalloying,” *Analytical Chemistry*, vol. 85, no. 12, pp. 5974–5980, 2013.
- [65] N. Moghimi, M. Mohapatra, and K. T. Leung, “Bimetallic nanoparticles for arsenic detection,” *Analytical Chemistry*, vol. 87, no. 11, pp. 5546–5552, 2015.
- [66] S. Maenosono and S. Saita, “Theoretical assessment of FePt nanoparticles as heating elements for magnetic hyperthermia,” *IEEE Transactions on Magnetics*, vol. 42, no. 6, pp. 1638–1642, 2006.
- [67] J. Verma, S. Lal, and C. J. F. van Noorden, “Nanoparticles for hyperthermic therapy: synthesis strategies and applications in glioblastoma,” *International Journal of Nanomedicine*, vol. 9, no. 1, pp. 2863–2877, 2014.
- [68] J. Gao, G. Liang, B. Zhang, Y. Kuang, X. Zhang, and B. Xu, “FePt@CoS₂ yolk-shell nanocrystals as a potent agent to kill HeLa cells,” *Journal of the American Chemical Society*, vol. 129, no. 5, pp. 1428–1433, 2007.
- [69] C. Xu, Z. Yuan, N. Kohler, J. Kim, M. A. Chung, and S. Sun, “FePt nanoparticles as an Fe reservoir for controlled Fe release and tumor inhibition,” *Journal of the American Chemical Society*, vol. 131, no. 42, pp. 15346–15351, 2009.
- [70] H. Sun, X. Chen, D. Chen et al., “Influences of surface coatings and components of FePt nanoparticles on the suppression of glioma cell proliferation,” *International Journal of Nanomedicine*, vol. 7, pp. 3295–3307, 2012.

Research Article

Incorporation of Nanohybrid Films of Silica into Recycled Polystyrene Matrix

Genoveva Hernández-Padrón,¹ Domingo Rangel-Miranda,²
Gerardo Cedillo,³ and Alejandra Blanco-Hernández⁴

¹Departamento de Nanotecnología, Centro de Física Aplicada y Tecnología Avanzada, Universidad Nacional Autónoma de México, Campus Juriquilla, 76230 Querétaro, QRO, Mexico

²Departamento de Ingeniería Molecular de Materiales, Centro de Física Aplicada y Tecnología Avanzada, Universidad Nacional Autónoma de México, Campus Juriquilla, 76230 Querétaro, QRO, Mexico

³Instituto de Investigaciones en Materiales, Universidad Nacional Autónoma de México, Ciudad Universitaria, Circuito Exterior s/n, 04510 México City, DF, Mexico

⁴Facultad de Química, Universidad Autónoma de Querétaro, Cerro de las Campanas s/n, 76010 Santiago de Querétaro, QRO, Mexico

Correspondence should be addressed to Genoveva Hernández-Padrón; genoveva@unam.mx

Received 22 May 2015; Revised 1 July 2015; Accepted 28 July 2015

Academic Editor: Kangtaek Lee

Copyright © 2015 Genoveva Hernández-Padrón et al. This is an open access article distributed under the Creative Commons Attribution License, which permits unrestricted use, distribution, and reproduction in any medium, provided the original work is properly cited.

An alternative for the reutilization of polystyrene waste containers consisting in creating a hybrid material made of SiO₂ nanoparticles embedded in a matrix of recycled polystyrene (PSR) has been developed. Recycled polystyrene functionalized (PSRF) was used to influence the morphological and antifog properties by the sol-gel synthesis of nanohybrid silica. To this end, silica nanoparticles were produced from alkoxide precursors in the presence of recycled polystyrene. The functionalization of this polymeric matrix was with the purpose of uniting in situ carboxyl and silanol groups during the sol-gel process. In this way, opaque or transparent solid substrates can be obtained, with each of these endowed with optical conditions that depend on the amount of reactants employed to prepare each nanohybrid specimen. The nanohybrids were labelled as SiO₂/PSR (HPSR) and SiO₂/PSRF (HPSRF) and their properties were then compared to those of commercial polystyrene (PS). All the prepared samples were used for coating glass substrates. The hydrophobicity of the resultant coatings was determined through contact angle measurement. The nanohybrid materials were characterized by FT-IR and ¹H-NMR techniques. Additionally, TGA and SEM were employed to determine their thermal and textural properties.

1. Introduction

In the recent decades, the development of new plastics has been a great challenge for the scientific and technological community, because of the harmful influence of plastics on the environment and the accumulation of polymeric materials. Additionally, the degradation time of these materials is very long and nonrenewable resources have been declining in tandem with the growth of plastics engineering [1]. This situation has forced society to diminish the use of plastic materials in the immediate future and so, now, these substances must be recycled [2].

Inorganic-organic hybrids [3, 4] are rapidly emerging as alternatives to traditional antifog, self-cleaning, and UV

protected materials, since they combine the chemical and mechanical properties of both inorganic and organic components [5–7]. In another sense, human health protection and environmental remediation have been constantly deteriorated. In the following work we propose an application for reusing polystyrene, which is commonly used for transporting fast food disposables, food trays, and beverage containers and as a general packaging product.

Polymers can be reused as intelligent window coatings with water repellent properties, antifogging agents, UV protectors, or self-cleaning products. It is known that polymers such as HDPE, LDPE, PS, or PP are used for these applications; the PS surface can be modified with a hydrophobic group to improve these characteristics [8–10]. Also, nano- or

microsilica particles incorporated into the polymer matrix combine the useful polystyrene features. The incorporation of these SiO₂ particles can be performed via the sol-gel method [11]; this process allows a better control of the hydrophobic coating properties. The initial conditions can be manipulated to improve the mechanical, optical, thermal, antifog, and other properties of new materials [12, 13].

Coatings are used to indicate the deposition of a material on the surface of another one; the purpose is to provide on the covered area some characteristic that the material has not yet attained by itself [14]. Organic coatings are those applied in liquid state form on a surface after drying and usually result in a continuous solid covering layer. The drying processes involve chemical reactions or simple evaporation of the solvent, such as in paints, lacquers, enamels, and varnishes [11]. The effect of the coating is to provide some type of insulation, protection by adding a surface or interfacial property, while keeping the original properties of the covered material [15, 16].

Inorganic-organic hybrid composites are rapidly emerging as alternatives to traditional self-cleaning, antifog, or UV protection materials [17] since coatings alone usually exhibit no sufficient wear protection properties due to their low densities, thickness the wear and stress resistance of lining materials, but they can be improved with the incorporation of new hybrid composites.

There is particular interest in the functionalized polymers from the technological and scientific points of view; therefore, the inclusion of nanoparticles to improve the properties of polymers or resins [17] and even recycled polymers is a highly appreciated alternative.

In this work hybrid materials were prepared by incorporating silica nanoparticles (SiO₂) into recycled polystyrene matrices (PSR). Recycled polystyrene was functionalized (PSRF) by using abietic acid. The functionalization of the recycled polymeric matrix has the purpose of uniting carboxyl with silanol groups in situ during the sol-gel process. Infrared and ¹H-NMR spectroscopies were used to verify the functionalization of polystyrene and incorporation into it of silica particles. The prepared nanohybrids were labeled as SiO₂/PSR (HPSR) and SiO₂/PSRF (HPSRF), respectively, and then were compared to commercial crystal polystyrene (PS) and their corresponding hybrids.

2. Experimental Procedure

2.1. Materials and Methods. The materials used in this work were (a) tetraethyl orthosilicate (TEOS) (Aldrich Chem.), (b) CO₂-free triple distilled water, (c) toluene (reactive grade) (J. T. Baker), (d) polystyrene containers that were used as the recycled polymer, (e) commercial crystal polystyrene (Resirene Co.), (f) benzoyl peroxide (Sigma-Aldrich 99%), and (g) abietic acid (Sigma-Aldrich 70%).

2.2. Functionalization of Polystyrene (Commercial and Recycled). The functionalization of commercial or recycled polystyrene was made from a solution of toluene subjected to mechanical stirring. In order to prepare the PSF or PSRF

substrates, abietic acid (AA) and benzoyl peroxide employed as initiator (i) (i.e., an i/AA molar ratio of 0.376) were added to the PS or PSR materials and refluxed for 1 h under mechanical stirring. The method of synthesis and the preparation conditions for preparing the modified polystyrene (PSF) materials have been described elsewhere [18].

2.3. Hybrid Materials Preparation. The PS-SiO₂, PSR-SiO₂, PSF-SiO₂, and PSRF-SiO₂ hybrid materials were prepared from solutions of nonfunctionalized or functionalized recycled polystyrene (PSR or PSRF, resp.). Previously, the PS or PSF commercial solids were dissolved in toluene. TEOS was dissolved in another glass beaker containing a volume of toluene equal to the quantity employed to prepare the above PS or PSR solutions. Afterward, PS, PSF, PSR, or PSRF solutions were added sequentially to the beaker containing the TEOS/toluene mixture. The reactant mixture was kept under stirring and refluxing conditions for 2 h. The TEOS molar ratios employed in the above preparations corresponded to 2.5 and 6.3 × 10⁻⁵ mol of initiator and were added to the PS and PSR polymers.

2.4. Substrates Coating. Clean glass plates of 4 × 1 in. and 4.8 × 10⁻² ± 0.00005 in. thickness were coated with PS, PSF, PSR, PSRF, HPS, HPSF, HPSR, and HPSRF films, respectively. The surface of each glass plate was immersed (at a rate of 5 mms⁻¹) inside the polymers solutions under study.

2.5. Characterization Techniques. The characterization of the obtained hybrid materials was carried out by FT-IR spectroscopy. Infrared analysis (FT-IR) was performed on a Bruker Vector 33 spectrometer, by using the transmittance technique. The samples were prepared as thin films.

The ¹H-NMR spectra were recorded on a Bruker Avance 400 spectrometer, with a BBI 400 MHz SB 5 mm with z-gradient probe and TOPSPIN 2.1 software; all samples were previously dissolved in CDCl₃ at room temperature.

In turn, TGA/DTA analyses were carried out in a DuPont 951 instrument operated in an air atmosphere at a rate of 10 K min⁻¹.

The contact angle was measured on the surface of the coated material that was prepared on the glass surface. One drop of water (1 μL) was placed on the surface and then a photograph was taken of the solid-liquid interface with a camera Cannon Power Shot Sx30 IS. These images were transformed to gray scale and analyzed with the MatLab 6 program, version 6.0.0.88, and five measurements of each sample were made.

Scanning Electron Microscopy (SEM) observations were carried out in a Jeol JSM-5200 scanning microscope. The samples were coated with carbon by vacuum evaporation.

3. Results and Discussion

PS, PSF, HPS, and HPSF FT-IR spectra are shown in Figures 1 and 2, in the ranges of 3300 to 2600 cm⁻¹ and 2000 to 400 cm⁻¹, respectively.

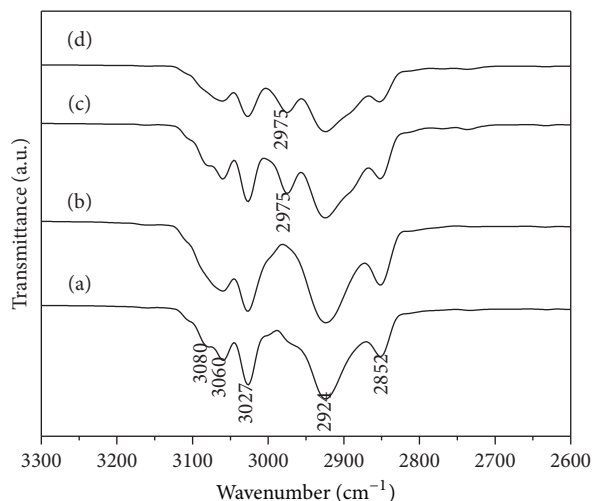


FIGURE 1: FT-IR spectra in the range of 3300–2600 cm^{-1} of (a) PS, (b) PS-F, (c) HPS, and (d) HPSF materials.

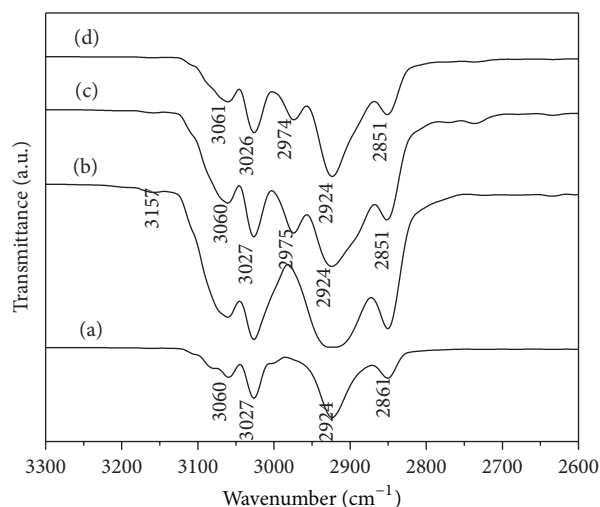


FIGURE 3: FT-IR spectra in the range of 3300–2600 cm^{-1} of (a) PSR, (b) PSRF, (c) HPSR, and (d) HPSRF materials.

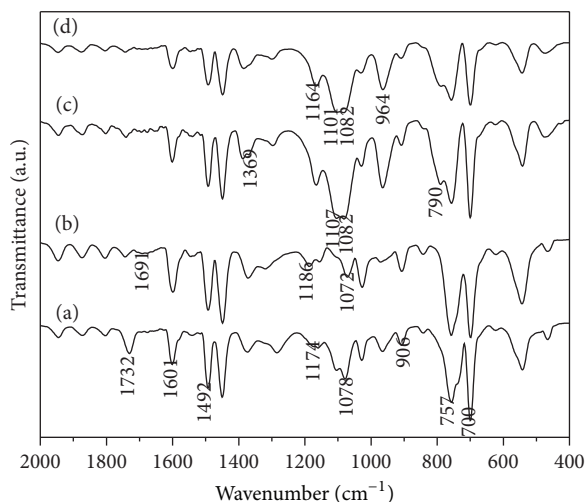


FIGURE 2: FT-IR spectra in the range of 2000–400 cm^{-1} for (a) PS, (b) PS-F, (c) HPS, and (d) HPSF substrates.

Polystyrene (PS) presents characteristic absorption bands at 3080, 3060, and 3027 cm^{-1} corresponding to aromatic CH groups; likewise signals from the aromatic hydrogen present in $^1\text{H-NMR}$ spectra of polystyrene and recycled polystyrene (PSR) appear between 6 and 7.5 ppm (Figures 5(a) and 6(a)). Polystyrene presents bands at 2924 and 2852 cm^{-1} proceeding from CH_2 asymmetric and symmetric vibration, respectively [19] (Figure 1(a)). On the other hand, the signals appearing at 2.4 ppm in Figures 5(a) and 6(a) correspond to aliphatic hydrogen while that of the region between 1 and 2.3 ppm corresponds to methine (CH) and methylene groups (CH_2) [20].

Figure 2(a) shows aromatic ring absorption bands at 1601, 1492, and 700 cm^{-1} [19].

The spectrum of the functionalized polystyrene (PSF) containing abietic acid (Figure 1(b)) shows a broadband in the

range of 3100 to 3000 cm^{-1} due to the overlapping of bands proceeding from aromatic groups.

The presence of abietic acid was identified in Figure 2(b) through the signal of carboxyl group ($\text{C}=\text{O}$) in 1691 cm^{-1} , aromatic rings at 1186 cm^{-1} , and CH bonds at 842 cm^{-1} . The spectrum also shows overlapping bands of PS aliphatic groups and of the initiator in the range of 720 to 800 cm^{-1} (Figure 2(b)).

Figure 1(c) shows the hybrid polystyrene (HPS) FT-IR spectrum. Vibration of the asymmetric methyl groups (CH_3) was identified at 2975 cm^{-1} and symmetric vibration of the CH_3 groups appeared in the range of 2960 to 2860 cm^{-1} . Absorption bands at 1107 and 790 cm^{-1} (Figure 2(c)) correspond to Si-O-Si asymmetric and symmetric vibrations, respectively [21, 22].

The hybrid materials prepared from the recycled polystyrene (HPSR) present the same absorption bands (Figures 3(c) and 4(c)).

The FT-IR spectrum of functionalized hybrid polystyrene (HPSF) shows a broadband at the range of 3200 to 2800 cm^{-1} (Figure 1(d)) which is associated with the overlapping of the bands due to the aromatic ring present in PS and abietic acid, as well as by the absorption bands of CH_2 group at 2925 and 2852 cm^{-1} [19].

The presence of the Si-O-Si group was identified at 1101 and 964 cm^{-1} (Figure 2(d)), while the absorption band of the $\text{C}=\text{O}$ group of abietic acid disappears; this same behavior was observed for the functionalized hybrid of recycled polystyrene (HPSRF) in Figures 3(c) and 4(c) [21].

Figures 3 and 4 show the PSR, PSRF, HPSR, and HPSRF spectra in a range of 3300 to 2600 cm^{-1} and 2000 to 400 cm^{-1} , respectively. Recycled polystyrene (PSR) presents the same characteristic bands of polystyrene (Figures 3(a) and 4(a)). In the respective $^1\text{H-NMR}$ spectrum, a band appears at 5.4 ppm, which is associated with other compounds that are present in the recycled material (Figure 6(a)).

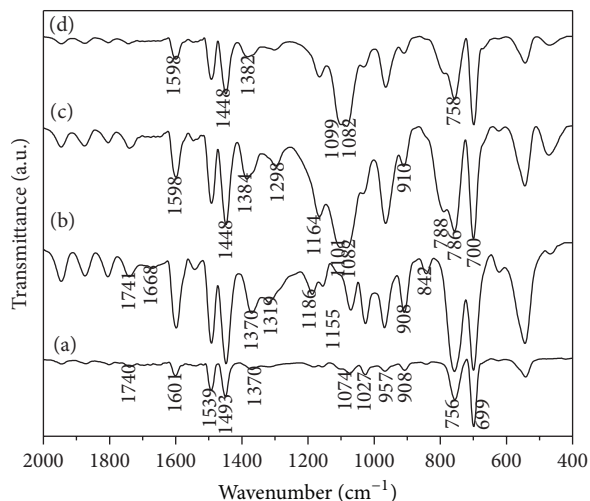


FIGURE 4: FT-IR spectra in the range of 2000–400 cm^{-1} of (a) PSR, (b) PSRF, (c) HPSR, and (d) HPSRF samples.

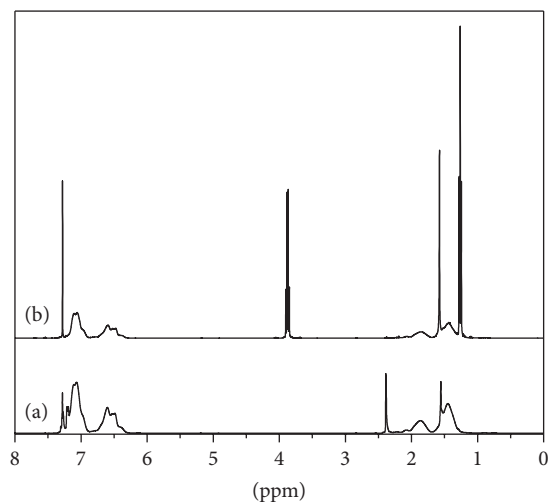


FIGURE 5: ^1H -NMR spectra of (a) PS and (b) HPSF materials.

Deformations in the ranges of 2850 to 2980 cm^{-1} and 2850 to 2980 cm^{-1} in the FT-IR spectrum of functionalized recycled polystyrene (PSRF) were found (Figure 3(b)). These deformation bands can be associated with the presence of abietic acid. The signals located at 1688 and 1319 cm^{-1} correspond to carboxyl group (Figure 4(b)).

Figures 5(b) and 6(b) show the ^1H -NMR spectra of HPSF and HPSRF, respectively. TEOS signals appear at 3.8 ppm and 1.25 ppm for methylene and methyl groups, respectively [$\text{CH}_2(\text{q})$ and $\text{CH}_3(\text{t})$] [20].

In both spectra, it is not possible to distinguish abietic acid signals due to the overlap between the aliphatic signals of polystyrenes (PS and PSR). On the other hand, the signals originally located at 2.4 ppm in PS and PSR spectra disappear altogether, thus suggesting an interaction between the functionalized polymers and TEOS.

The TGA and DSC results of these materials show an increase in the amount of silica and functionalization of

TABLE 1: Degradation and glass transition temperatures and contact angle measurements of the studied materials.

Material	Degradation temperature ($^{\circ}\text{C}$)	Glass transition temperature T_g ($^{\circ}\text{C}$)	Contact angle on glass
PS	299.19	54.36	85.9623 $^{\circ}$
PSR	346.55	59.17	82.0304 $^{\circ}$
PSF	308.04	62.07	77.4712 $^{\circ}$
PSRF	339.24	59.72	77.4712 $^{\circ}$
HPS	221.45	56.08	81.5966 $^{\circ}$
HPSR	318.59	57.60	87.6863 $^{\circ}$
HPSF	338.05	76.99	88.1720 $^{\circ}$
HPSRF	325.26	65.24	89.2098 $^{\circ}$
Substrate			37.6262 $^{\circ}$

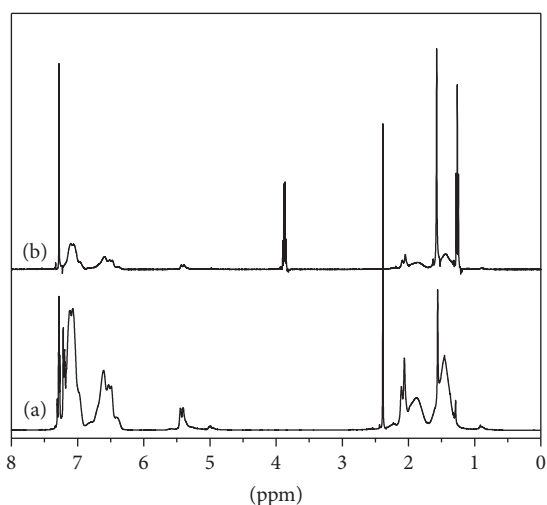


FIGURE 6: ^1H -NMR spectra of (a) PSR and (b) HPSRF materials.

the surface improve the thermal stability of these hybrid materials. The glass transition temperature (T_g) of the hybrid materials increases slightly with the functionalization and amount of silica particles; see Table 1.

The hydrophobicity of the coatings was evaluated by measurement of the contact angle, while establishing the following criteria for having a hydrophilic surface $<40^{\circ}$ and for an acceptable hydrophobic surface $>70^{\circ}$ [14].

The silica nanoparticles incorporated into the polystyrene matrix and combined with the features of the abietic acid allowed obtaining better hydrophobic properties. One manifestation of this hydrophobic surface is the contact angle, which was rather similar in value for the functionalized hybrid materials. All the obtained hybrid materials have a contact angle $>80^{\circ}$. The hybrids of functionalized polystyrene films present an increased contact angle if compared to PS and PSR. This is possible due to the presence of abietic acid, which is an amphiphilic, that is, hydrophobic and hydrophilic, compound and due to the presence of silica particles in the hybrid materials. However, no significant changes in contact angle were observed (Table 1).

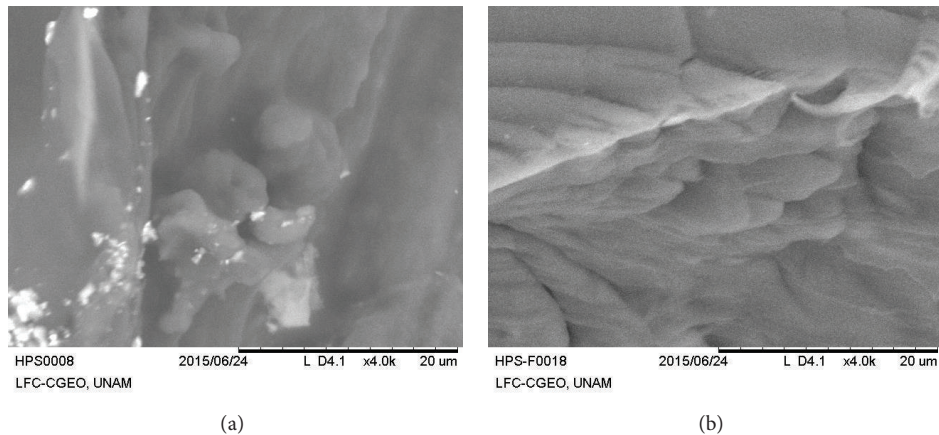


FIGURE 7: SEM photographs of (a) HPS and (b) HPSF.

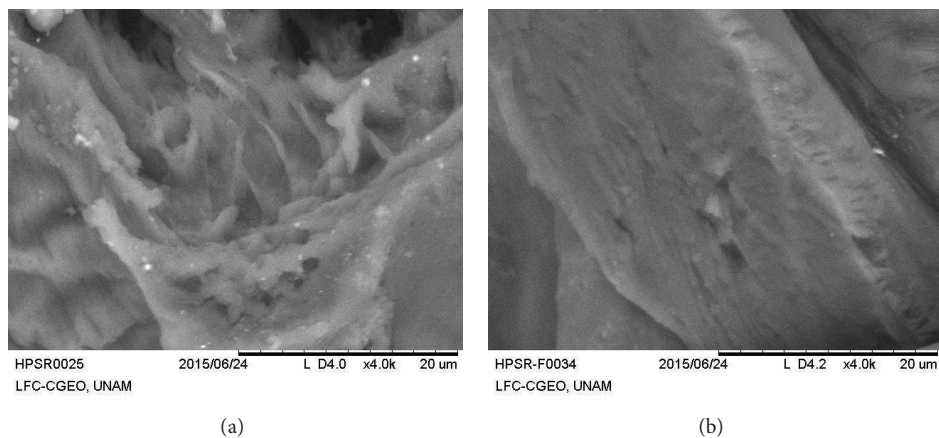


FIGURE 8: SEM photographs of (a) HPSR and (b) HPSRF.

In order to know the homogeneity related to the distribution of silica particles on the surface of the hybrid materials, SEM photographs were taken. Figure 7(a) shows aggregates of silica particles on HPS, which indicates that the sample is not homogenous; in the case of HPSF (Figure 7(b)), this sample presents a homogenous surface, thus suggesting an interaction existing between TEOS and functionalized polystyrene.

Hybrid materials micrographs of recycled polystyrene (Figure 8(b)) present a better homogeneity between silica particles and PSR. This suggests that the presence of abietic acid allows silica particles to be dispersed in the polymer matrix, then forming a free surface of aggregates. HPSR depicts smaller aggregates than HPS (Figures 7(a) and 8(a)).

The homogeneous repartition of silica particles is important since it determines the visual transparency or opacity of the final films to finally apply these hybrids as coatings [7].

4. Conclusions

Hybrid materials were successfully prepared from recycled polystyrene matrices by introducing silica particles to the

polymer matrix by the sol-gel method. Carboxyl groups were identified in the functionalized materials (PSF and PSRF), although this species is absent in the functionalized hybrids (HPSF and HPSRF), thus suggesting that there exists an interaction between carboxyl group and SiO_2 . $^1\text{H-NMR}$ analysis shows the presence of other compounds in PSR, which is attributed to recycled material; however, this did not affect the preparation process and neither the hydrophobicity nor the homogeneity properties of functionalized hybrids.

Hybrids of PS and PSR presented segregation of the silica particles on the material surface, while the functionalized hybrids (HPSF and HPSRF) showed a homogeneous surface, thus improving the visual transparency of the coatings. Also, vitreous temperature (T_g) was increased in these materials and the contact angles on the surface of recycled polystyrene were very similar to those found in commercial polystyrene samples.

The properties of recycled polystyrene analyzed in this work are comparable to those ascribed to commercial polystyrene with the possibility that these materials can be used as hydrophobic coatings. Therefore, this study proposes

a new alternative to the use of recycled polystyrene matrices based on the approach presented.

Conflict of Interests

The authors declare that there is no conflict of interests regarding the publication of this paper.

Acknowledgments

The authors thank Dra. Marina Vega for SEM technical support, M. C. Miguel A. Canseco for TGA/DSC technical support, and M. C. Guillermo Vázquez-Sánchez for computational data processing.

References

- [1] T. Maharana, Y. S. Negi, and B. Mohanty, "Review article: recycling of polystyrene," *Polymer-Plastics Technology and Engineering*, vol. 46, pp. 729–736, 2014.
- [2] E. M. Ilgenenfriz, "Plastics waste handling practices in solid waste management," *Water, Air, & Soil Pollution*, vol. 4, no. 2, pp. 191–198, 1975.
- [3] H. Zou, S. Wu, and J. Shen, "Polymer/silica nanocomposites: preparation, characterization, properties, and applications," *Chemical Reviews*, vol. 108, no. 9, pp. 3893–3957, 2008.
- [4] C. Sanchez, P. Belleville, M. Popall, and L. Nicole, "Applications of advanced hybrid organic-inorganic nanomaterials: from laboratory to market," *Chemical Society Reviews*, vol. 40, no. 2, pp. 696–753, 2011.
- [5] V. A. Gerasin, E. M. Antipov, V. V. Karbushev et al., "New approaches to the development of hybrid nanocomposites: from structural materials to high-tech applications," *Russian Chemical Reviews*, vol. 82, no. 4, pp. 303–332, 2013.
- [6] H. S. Vaziri, M. Abadyan, M. Nouri, I. A. Omaraei, Z. Sadredini, and M. Ebrahimnia, "Investigation of the fracture mechanism and mechanical properties of polystyrene/silica nanocomposite in various silica contents," *Journal of Materials Science*, vol. 46, no. 17, pp. 5628–5638, 2011.
- [7] G. Hernández-Padrón, F. Rojas, M. García-Garduño, M. A. Canseco, and V. M. Castaño, "Development of hybrid materials consisting of SiO₂ microparticles embedded in phenolic-formaldehydic resin polymer matrices," *Materials Science and Engineering A*, vol. 355, pp. 338–347, 2003.
- [8] W. Stevenson and J. R. White, "Photo-sensitivity of recycled photo-degraded polystyrene," *Journal of Materials Science*, vol. 37, pp. 1091–1100, 2012.
- [9] C. Borsoia, K. H. Berwigg, L. C. Scienzac, B. C. D. A. Zoppas, R. N. Brandalisea, and A. J. Zatteraa, "Behavior in simulated soil of recycled expanded polystyrene/waste cotton composites," *Materials Research*, vol. 17, no. 1, pp. 275–283, 2014.
- [10] D. R. Hwang, J. Hong, J. Lee, and S. E. Shim, "In-situ synthesis of PS/(–)silica composite particles in dispersion polymerization using an (±) amphoteric initiator," *Macromolecular Research*, vol. 16, no. 4, pp. 329–336, 2008.
- [11] G. Hernández-Padrón, M. García-Garduño, and F. Rojas-González, "Hybrid materials based on functionalised epoxy resin networks," *Pigment & Resin Technology*, vol. 39, no. 4, pp. 195–202, 2010.
- [12] T. Kotoky and S. K. Dolui, "Synthesis of polystyrene/silica hybrid composites by the sol-gel method: effect of introduction of a flexible component (butyl acrylate) into the silylated polystyrene backbone," *Colloid and Polymer Science*, vol. 284, no. 10, pp. 1163–1169, 2006.
- [13] B. Ou and D. Li, "Preparation of polystyrene/silica nanocomposites by radical copolymerization of styrene with silica macromonomer," *Science in China Series B: Chemistry*, vol. 50, no. 3, pp. 385–391, 2007.
- [14] J. A. Howarter and J. P. Youngblood, "Self-cleaning and next generation anti-fog surfaces and coatings," *Macromolecular Rapid Communications*, vol. 29, no. 6, pp. 455–466, 2008.
- [15] U. C. Nwaogu and N. S. Tiedje, "Foundry coating technology: a review," *Materials Sciences and Applications*, vol. 2, no. 8, pp. 1143–1160, 2011.
- [16] M. C. Wilkinson, J. Hearn, and P. A. Steward, "The cleaning of polymer colloids," *Advances in Colloid and Interface Science*, vol. 81, no. 2, pp. 77–165, 1999.
- [17] G. Hernández-Padrón, F. Rojas, and V. M. Castaño, "Ordered SiO₂-phenolic formaldehyde resin in situ nanocomposite," *Nanotechnology*, vol. 15, no. 1, pp. 98–103, 2004.
- [18] G. Hernández-Padrón, T. Gómez-Quintero, and A. Blanco-Hernández, "Development antifog nanohybrid consisting of polystyrene recycled matrix by sol-gel process," in *Proceedings of the Nanotechnology: Technical Proceedings of the NSTI Nanotechnology Conference and Expo*, vol. 1, pp. 218–219, Washington, DC, USA, May 2014.
- [19] B. C. Smith, *Infrared Spectral Interpretation A Systematic Approach*, CRC Press, 1998.
- [20] R. M. Silverstein, C. G. Bassler, and T. C. Morrill, *Spectrometric Identification of Organic Compounds*, chapter 4, John Wiley & Sons, New York, NY, USA, 3rd edition, 1974.
- [21] N. B. Colthup, L. H. Daly, and S. E. Wiberley, *Introduction to Infrared and Raman Spectroscopy*, Academic Press, San Diego, Calif, USA, 3rd edition, 1990.
- [22] G. Orcel, J. Phalippou, and L. Hench, "Structural changes of silica xerogels during low temperature dehydration," *Journal of Non-Crystalline Solids*, vol. 88, no. 1, pp. 114–130, 1986.